Flow physics of pulsed-jet actuation

Enhancing the efficiency in active separation control through adjustment of the duty cycle

vorgelegt von
M.Sc.
Ben Steinfurth
ORCID: 0000-0002-6857-5359

von der Fakultät V - Verkehrs- und Maschinensysteme
der Technischen Universität Berlin
zur Erlangung des akademischen Grades

Doktor der Ingenieurwissenschaften
-Dr.-Ing.-

genehmigte Dissertation

Promotionsausschuss:

Vorsitzender:	Prof. Dr.-Ing. Flávio Silvestre
Gutachter:	Prof. Dr.-Ing. Julien Weiss
Gutachter:	Prof. Dr.-Ing. Christian Oliver Paschereit
Gutachter:	Dr. René Woszidlo

Tag der wissenschaftlichen Aussprache: 14. November 2022

Berlin 2022

Zusammenfassung

Das gepulste Ausblasen in eine Grenzschicht stellt eine effektive Maßnahme zur Verhinderung von Strömungsablösung dar. Trotz zahlreicher Demonstrationen ist ein Durchbruch dieser Methode im industriellen Kontext jedoch bisher ausgeblieben, was zum Teil auf einen übermäßigen Energiebedarf zurückgeführt werden kann. In dieser Arbeit wird eine Dimension der extern zugeführten Energie adressiert, nämlich der benötigte Massenstrom. Das übergeordnete Ziel ist es, einen Ansatz zur Effizienzsteigerung zu entwickeln, der zu Einsparungen des Massenstroms bei Gewährleistung der erforderlichen Kontrollautorität führt. Zu diesem Zweck werden Strömungsfelder experimentell untersucht, die durch gepulste Jets beeinflusst werden.

Ausgehend von der Hypothese, dass großskalige Wirbelstrukturen maßgeblich für die Kontrollautorität gepulster Jets verantwortlich sind, wird zunächst deren Formierung in ruhender Umgebung untersucht. Trotz der schlitzförmigen Austrittsgeometrie werden runde Wirbelringe mit dickeren Wirbelkernen als in früheren Studien festgestellt. Dies wird mit dem hohen Seitenverhältnis des Auslasses einerseits und einem temporären Überdruck in der Jet-Austrittsebene andererseits erklärt. Bei Überlagerung der gepulsten Jets mit einer senkrecht zu ihnen orientierten Querströmung entstehen, abhängig vom Geschwindigkeitsverhältnis, entweder *hairpin vortices* oder asymmetrische Wirbelringe. Die im Sinne der Ablösekontrolle geeignetere Betriebsweise wird jedoch durch eine Neigung der Jet-Achse in Strömungsrichtung erreicht, da hier, bezogen auf den eingesetzten Massenstrom, eine stärkere Erhöhung der mittleren kinetischen Energie im wandnahen Bereich erfolgt. Folgende Mechanismen wurden diesbezüglich identifiziert: (1) radiale Verdrängung von Fluid mit niedrigem Impuls durch den *leading vortex*, (2) direkte Erhöhung des Impulsstroms durch den Wandstrahl und (3) *entrainment* von Fluid mit hohem Impuls durch den *stopping vortex*. Insbesondere der Wandstrahl, für den in dieser Arbeit Möglichkeiten der Modellierung aufgezeigt werden, ist von großer relativer Bedeutung. Daher muss die Pulsweite so gewählt sein, dass dieser, zusätzlich zu dem *leading vortex*, erzeugt wird. Der Zeitverzug zwischen einzelnen Fluidpulsen sollte dagegen an eine charakteristische Zeitskala angepasst werden, die das Wiederauftreten von Rückströmung bestimmt.

Der in dieser Arbeit entwickelte Ansatz zur Auswahl von Aktuationsparametern sieht eine Implementierung strömungsabhängiger Zeitskalen vor, welche an die Stelle der sonst herangezogenen reduzierten Aktuationsfrequenz treten. Dabei können systematische Effizienzsteigerungen erzielt werden, indem der Betriebszyklus im Vergleich zu bisherigen Arbeiten reduziert wird. Zukünftige Studien müssen sich mit der Beantwortung von Fragen auseinandersetzen, die bei der Übertragung auf weniger generische Konfigurationen auftreten, einschließlich der Anforderungen bezüglich des Versorgungsdruckes, der Kontrolle transienter aerodynamischer Lasten und der Interaktion benachbarter Jets.

Abstract

The injection of pulsed jets into a cross-flowing boundary-layer is well known to prevent or delay flow separation. Although the effectivity of this method has been demonstrated in a variety of academic investigations, a break-through in the aerodynamics industry has so far remained elusive, which may in part be ascribed to excessive energy requirements of the control devices involved. In this thesis, one dimension of the external energy is addressed, namely the supplied mass flow. The overriding objective is to develop an approach that leads to mass flow savings while retaining the control authority. To this end, flow fields forced by a pulsed-jet actuator are studied experimentally in a series of five articles pertaining to this dissertation.

Hypothesising that the control authority in such flows is mainly governed by dominant vortex structures, emphasis is first put on their formation in quiescent environment. Despite the considered slit-shaped outlet geometry, almost spherical vortex rings are revealed through tomographic reconstructions of time-dependent velocity fields. Much thicker vortex cores, hence smaller non-dimensional energies, than in previous studies are noted, which is explained by the specific outlet geometry and a temporary occurrence of over-pressure in the jet exit plane. When transverse pulsed jets are superimposed with a cross-flow, two regimes of vortex appearance can be distinguished: for small velocity ratios, hairpin vortices develop whereas for large velocity ratios, asymmetric vortex rings emerge. However, a more effective operation is argued to be at hand when the jet axis is tilted towards the surface downstream of the outlet as the near-wall flow is energised by three mechanisms: (1) radial displacement of low-momentum fluid by the leading vortex, (2) direct increase of momentum flux by the wall jet, for which models are provided and (3) entrainment of high-momentum fluid on the jet trailing part. Applying inclined pulsed jets to counter boundary-layer separation in a generic diffuser setup, the wall-attached jet is shown to be of overriding importance. Therefore, the pulse width needs to exceed characteristic formation times so that in addition to the leading vortex, a wall jet is generated. The time delay between successive pulses, on the other hand, should be adapted to a flow-inherent separation time that governs the recurrence of reverse-flow subsequent to individual jets.

Following the guidelines established in this work is equivalent to recasting the reduced actuation frequency into flow-dependent time scales. Furthermore, it is shown that a systematic efficiency enhancement is achieved by applying smaller duty cycles than in previous separation control applications. Future studies must address the transferability of the presented approach to less generic flow configurations while answering practical issues that arise in such applications, including supply pressure requirements, the control of transient loads and the interaction between neighbouring pulsed jets.

Table of Contents

List of Figures

1

Introduction

The purpose of this chapter is to provide a brief, yet comprehensive, overview, thereby setting the stage for the research articles inserted subsequently. The current state of the art is presented before the major objectives and limitations of this study are summarised.

1.1 Active separation control

Flow separation (i.e., the detachment of the boundary-layer from a solid surface) is often accompanied by effects that are considered detrimental to the purpose of the respective application. Mainly attributed to a deformation of the flow geometry, this phenomenon is typically accompanied by an alteration of the aerodynamic load, which can be exacerbated by the dynamics of the separated flow region. The implications of such flow states include, but are not limited to, noise emissions impairing the driving comfort in passenger vehicles, reduced efficiency levels of turbines as well as plane crashes due to a loss of lift. Fluid dynamicists therefore seek to avoid, delay or prevent flow separation. This can be facilitated by shunning geometric singularities potentially provoking geometry-induced separation during the design process of flow bodies. Furthermore, it can be attempted to avoid boundary conditions leading to large adverse pressure gradients, thereby precluding pressure-induced flow separation. However, off-design operation is often inevitable as, for instance, the cruising flight of a plane ride is embedded by take-off and landing procedures, either by necessity or by preference.

In the following, I will provide an introductory overview of techniques to counter boundary-layer separation, restricting ourselves to *active* methods where an external energy source is required.

1.1.1 An overview

The target pursued in active separation control is to *energise* the boundary-layer [1–3], which is motivated by knowledge that an insufficient mean kinetic energy makes it more susceptible to separation [4]. This insight goes back more than one hundred years to the seminal work concerning viscous flows carried out by Prandtl [5] who, among many other issues, studied the

manipulation of a cylinder flow. The photogram shown in Figure 1.1 indicates that separation is observed further upstream on the lower side of the cylinder whereas the flow follows the upper side for a longer distance, which Prandtl achieved by removing fluid from the near-wall region through a slot in the cylinder surface on the upper side.

Figure 1.1: Active separation control conducted by Ludwig Prandtl - the figure shows the flow around a cyclinder where suction is applied on the upper surface; photogram taken by Prandtl (1904), based on figure in Ref. [5]

In the following decades, attempts have been made to analytically approximate the effect of boundary-layer suction [6–8], and further successful demonstrations have been reported for generic flow bodies [9, 10] as well as airfoils [11–15].

As an alternative to boundary-layer suction where low-momentum fluid is removed, the near-wall flow can also be energised by the addition of momentum through outlets in the surface. Although this method is typically less efficient in comparison, the design effort to provide the required ducting is considered less elaborate [16]. In its simplest form, a constant mass flow is supplied to the flow through discrete jet outlets. For such *steady blowing* applications, a twofold function principle can be ascertained. First, the boundary-layer profile is modified directly due to the vectorial addition of momentum flux. Second, the interaction between steady jets and the cross-flow leads to the generation of longitudinal vortex structures that transfer high-momentum fluid from the outer flow towards the wall [17–23]. *Unsteady blowing*, on the other hand, is often considered an even more robust method of active separation control [24]. Here, flow-inherent instabilities can be triggered when the forcing dynamics are adapted to the receptivity of the flow. Thus, entrainment into mixing layers is enhanced and the risk of flow separation reduced [25]. The foundation of this approach was arguably laid by Schubauer & Skramstad (1947) discovering that boundary-layer transition can be controlled by acoustic excitation [26]. The same method was then employed to manipulate the spreading rate of turbulent shear-layers [27] which could be related to the initiation of large coherent flow structures [28], especially when forcing was applied near sub-harmonics of the most-amplified frequency [29, 30]. These findings gave rise to a number of investigations where sound was used to counter flow separation [31–34]. Considering that acoustic forcing amplitudes are relatively small, one may conceive that an adequate excitation frequency is the major prerequisite to exploit flow instabilities. In the case of a larger momentum addition, on the other hand, the sensitivity towards the frequency is reduced [35]. Along these lines, a second category of active separation control can be identified, namely one where an amplification of instabilities is not necessarily intended. Here, the momentum is typically supplied to the flow in the form of fluid jets that fluctuate in time. The main advantage over their steady counterpart

lies in the potential to enhance the efficiency since a given mean momentum input can be achieved with a reduced mass flow consumption [36]. Or, the other way around, the forcing intensity is larger than for steady blowing at an equal mass flow rate. In addition to affecting near-wall turbulence properties [37, 38], unsteady jets have been proven to reliably prevent boundary-layer separation in various configurations, for instance in axial compressors [39, 40] or multi-component high-lift configurations [41–44]. It has been confirmed that the effectivity is not as dependent on the excitation frequency as in the acoustic forcing applications addressed above. However, a frequency resulting in perturbations with an average wave-length of a similar order as the length of the control region is often considered best-practice [45, 46], more on that in §1.1.3.

Along with the large body of literature dedicated to experimental efforts concerned with unsteady blowing, its suitability in terms of reliable active separation control has also been attested in numerical studies [47–50]. In addition to that, our understanding of this technique has been advanced through low-order modelling [51] as well as closed-loop [52, 53], multi-variable [54] and visual feedback control [55], surely benefitting from rapid developments in the fields of computer technology and digital evaluation methods. There is no doubt that further progress can be expected thanks to the mutually amplifying developments towards ever-growing data bases on the one hand and methods subsumed under the buzzword that is *Machine Learning* on the other [56]. Whether this progress is sufficient to overcome persistent issues associated with the integration of active separation control in technical applications [57, 58] remains to be seen.

1.1.2 Actuators

In the following, a brief overview of some devices that are employed to facilitate unsteady blowing as a means of active separation control, namely synthetic jet, sweeping jet and pulsed-jet actuators (PJAs), is provided. Although only the latter type of device is used in the experiments carried out in this work, the obtained findings may also be valuable for other means of generating unsteady jets as will be explained in due course. Devices that are not covered in detail include plasma [59–61] and combustion actuators [62]. For an in-depth review of these and other actuators, the interested reader is referred to Ref. [63].

Belonging to the category of *fluidics* initially developed to substitute electronic components [66, 67], sweeping jet actuators can be employed to control boundary-layer separation by ejecting spatially oscillating jets. Along with the double-feedback type displayed in Figure 1.2 (a), there are also devices that exhibit one or zero feedback channels. In the case of the feedback-free design, two steady jets are introduced into a mixing chamber where instabilities associated with the resulting shear-layer eventually lead to a sweeping stream of fluid leaving the actuator [68, 69]. As for one-channel devices, the jet initially attaches on one side of the internal chamber where it induces a low-pressure impulse at the inlet of a feedback channel that is then transported to the other side where it attracts the jet before the cycle is repeated [70]. A similar function principle is at hand in the case of two feedback channels [71]. But instead of sound, the jet deflection is brought about by scooping a portion of the volumetric flow rate and reintroducing it near the inlet of the device. It is clear that the sweeping frequency therefore depends on the supplied mass flow and the actuator dimensions [72]. In summary,
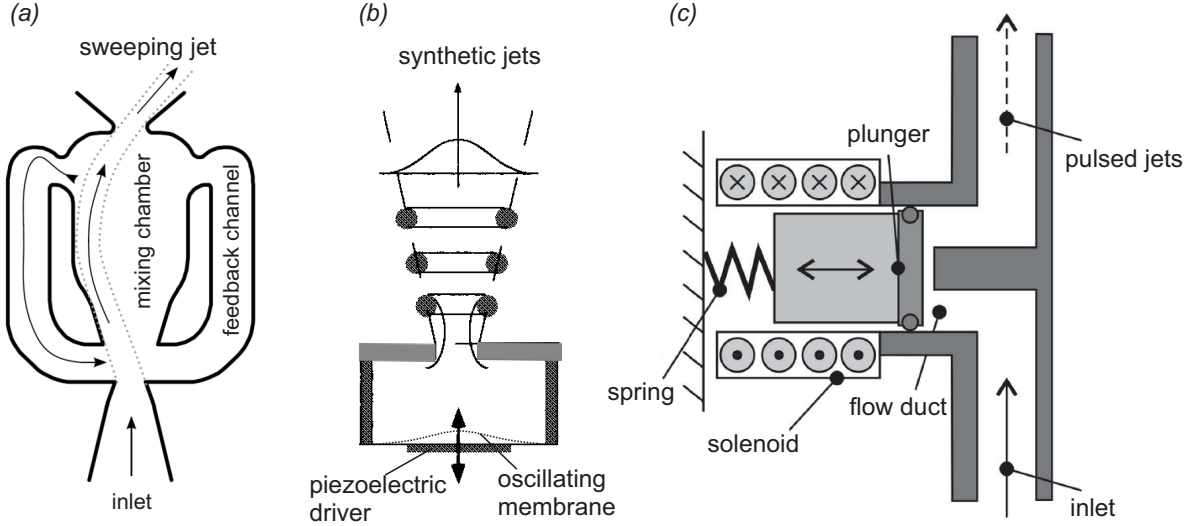
Figure 1.2: A selection of actuators to generate unsteady jets - (a) sweeping jet actuator, based on figure in Ref. [64]; (b) synthetic jet actuator, based on figure in Ref. [65] and (c) pulsed-jet actuator (PJA), based on figure in Ref. [43]

the common feature inherent to all types of sweeping jet actuators is the conversion of a steady fluid supply into a spatially oscillating jet through some kind of bi-stable switching mechanism. The main advantage of such devices is a lack of moving parts rendering them relatively robust. They are also scalable, thus covering a large frequency range. Successful active separation control has been reported on numerous occasions (e.g., in Refs. [73–77]).

Synthetic jet actuators, as shown in Figure 1.2 (b), consist of cavities with time-dependent volumes due to the deformation of a portion of their encasing boundary. This is typically achieved with an oscillating diaphragm controlled by a piezoelectric driver or an electrically driven piston. During the expansion of the cavity volume, surrounding fluid is sucked in before being ejected during the subsequent contraction phase. Owing to the impulsive nature of fluid ejection, vortex structures with mixing characteristics assumedly beneficial in active separation control are generated [65, 78]. However, these vortices may also be ingested when they have not propagated sufficiently far away from the outlet prior to the next ingestion phase. Criteria for a successful 'vortex escape' are provided in Refs. [79, 80]. To reach particularly large forcing intensities, synthetic jet actuators rely on resonance phenomena, either related to the cavity volume or to the oscillating diaphragm. The corresponding frequency bands are, however, relatively small which limits the operating conditions of such devices. This shortcoming is exacerbated by the necessity for moving parts prone to attrition and a low energy conversion efficiency. Since they do not require an external source of fluid supply, synthetic jet actuators are still widely used in active separation control [35, 81–84].

The third category on display in Figure 1.2 comprises PJAs relying on mechanical valves to intercept the mass flow. Here, an external supply of compressed air is required. Periodic closure of the flow duct can either be facilitated by means of rotary valves [85, 86] or plungers [44], the latter being implemented in readily available fast-switching solenoid valves. In this case, an externally generated signal is provided to drive the plunger motion, allowing for a broad range of forcing frequencies up to $\mathcal{O}(f) = 1\,\mathrm{kHz}$. Furthermore, the mass flow rate and frequency are decoupled which is typically not the case for the devices discussed above. On

the downside, the integration of PJAs arguably increases the system weight more than other actuators while also requiring moving parts, making them more prone to failure than fluidic actuators. Nonetheless, they have been used frequently in active separation control [87, 88] where a tendency towards small-scale outlet dimensions can be noted to generate *microjets* associated with a reduced mass flow rate at a maintained jet momentum [89–93].

To conclude this section, a variety of field-tested devices is available to counter flow separation. As described above, they differ in terms of their function principles as well as their advantages and disadvantages. Although all of them can be employed to introduce unsteady perturbations, the detailed nature of flow manipulation varies. A quasi-constant total mass flow supply is only facilitated by sweeping jet actuators but the momentum addition to given spatial locations is still unsteady given the oscillatory jet motion. Synthetic jet actuators and PJAs, on the other hand, only add momentum to the flow during confined time intervals on the order of the contraction phase and the valve opening time, respectively.

1.1.3 Parameters governing the efficacy

In a series of articles, Wygnanski & Greenblatt illustrate the great degree of complexity inherent to the design of effective active separation control systems [24, 94, 25, 95]. A large number of mostly independent parameters needs to be considered where two broad categories can be distinguished. The first comprises parameters defining the flow configuration, such as the incidence angle, the dimensions of the control domain and fluid properties. The second group is related to the separation control system and will be discussed in more detail in the following.

Great importance can be attributed to the location where momentum is introduced to the flow. To optimise this parameter, one needs to consider that the reattachment of a separated mixing layer requires much more energy than the prevention of boundary-layer separation [46]. It may therefore be considered detrimental to place actuators too far downstream of the mean separation point although an upstream effect of actuation manifested in flow acceleration can be expected. On the other hand, an actuator located too far upstream may result in an unnecessary increase of the control length that is commonly defined as the distance between jet outlet and the downstream end of the surface where separation needs to be prevented, for instance the trailing edge [96]. Then, flow structures may dissipate prematurely, thus not imposing a beneficial effect throughout the flow field under consideration. For these reasons, an actuator location near the mean separation line can be viewed as a reasonable choice [95]. Next, the orientation of the actuator needs to be set. To distribute the ejected momentum to the near-wall region, jets are usually inclined towards the wall [97] while a non-zero pitch angle may help to enhance the lateral spreading [98, 99, 88]. Furthermore, the spanwise spacing between neighbouring actuators needs to be chosen as to effectively prevent separation while not using excessive mass flow [100, 101].

Contrasting with these geometric considerations that eventually result in a fixed set-up, the magnitude of momentum input is typically variable. To communicate this quantity, the momentum coefficient

$$c_\mu(t) = \frac{I_{u,\text{jet}}(t)}{qL_\text{c}} \tag{1.1}$$

has been established [102] where $I_{u,\text{jet}}(t)$ is the momentum flow rate per unit width, q is the reference dynamic pressure and L_c the control length. As already indicated above, sound has been used initially as a means of active separation control, associated with small-amplitude forcing levels on the order of $\mathcal{O}(c_\mu) = 0.01\%$ [31]. This is in strong contrast to the $c_\mu = 8\%$ application on a military aircraft reported in Ref. [103], suggesting that the range of effective forcing intensities is relatively broad and depends on the respective control scenario. It is also important to note that an excessive c_μ results in saturation whereas particularly small values may even have detrimental effects [45]. Leading over to the parameter discussed next, it is worth mentioning that the minimum momentum coefficient required to prevent flow separation depends on the forcing frequency, exemplified by experiments where flow separation is initiated by changing the frequency at constant c_μ [24].

The actuation frequency f is usually stated in its non-dimensional form

$$F^+ = fL_\text{c}/U_\text{ref}. \tag{1.2}$$

While the frequency is coupled to the mass flow rate in the case of sweeping jet actuators, it can be adjusted by external signals for synthetic jet actuators and PJAs. To enable an educated guess for the optimum reduced frequency, the wave-length of harmonic perturbations $\lambda = L_\text{c}/F^+$ can be considered, which should be on the same order as the vertical dimension of the control region according to Wygnanski (1997). Assuming that the phase velocity of perturbations is $U_\Phi = U_\text{ref}/2$ and the inclination of the control surface corresponds to $\alpha = 30\,^\circ$, a reduced frequency on the order of unity is determined [24]. An alternative derivation is based on observations suggesting that frequencies on this order lead to enhanced spreading rates of excited shear-layers [104, 27]. Despite the abstract character of these explanations, reduced frequencies of $F^+ \approx 1$ have indeed been proven to be most effective in the reattachment of a separated shear-layer [46, 24]. To prevent flow separation, however, higher frequencies of $1 \leq F^+ \leq 4$ are suggested [94, 35, 105, 106]. While even larger frequencies up to $\mathcal{O}(F^+) = 10$ have been employed effectively on some occasions [107], this often results in the generation of small-scale flow structures that dissipate quickly and thus do not cover the entire control range [94]. However, one may argue that this effect is not explicitly due to a high frequency but rather the resulting short time interval t_p where momentum is added to the flow. Only when the duty cycle is fixed, the pulse duration is defined by a given frequency. Indeed, this is true for most devices used in active separation control where a 50% duty cycle is typically set. However, PJAs represent an exception to this rule. Here, t_p as well as the time delay between successive pulses t_off can be adjusted independently. This allows to investigate their individual influence as well as the effect of a varied duty cycle $DC = t_\text{p}/(t_\text{p} + t_\text{off})$ which has only been done in a relatively small number of studies, for instance in Refs. [87, 108, 109].

1.2 Pulsed jets

The periodic momentum input caused by synthetic jet actuators and PJAs can be viewed as the fundamental flow of starting jets consisting of fluid that is forced from an initial state of rest. This process is accompanied by the generation of leading vortices capable of transporting momentum over long distances [110, 111]. To lay the ground for the investigation

of fundamental properties of such starting, or pulsed, jets carried out in this thesis, we provide a further overview with an emphasis on characteristics relevant to active separation control in the following.

1.2.1 Vortex rings generated in quiescent environment

When a column of fluid is pushed through an outlet featuring a sufficiently large turning angle and into a larger volume of quiescent ambience, a roll-up of vortex sheets can be observed (Figure 1.3). This process can be described in self-similar coordinates, only requiring knowledge of the turning angle [112]. To an extent, this takes into account the effect of secondary vorticity that occurs between the primary vortex and the outlet edge [113, 114], thereby giving rise to robust models for the time-dependent size and circulation of vortex rings.
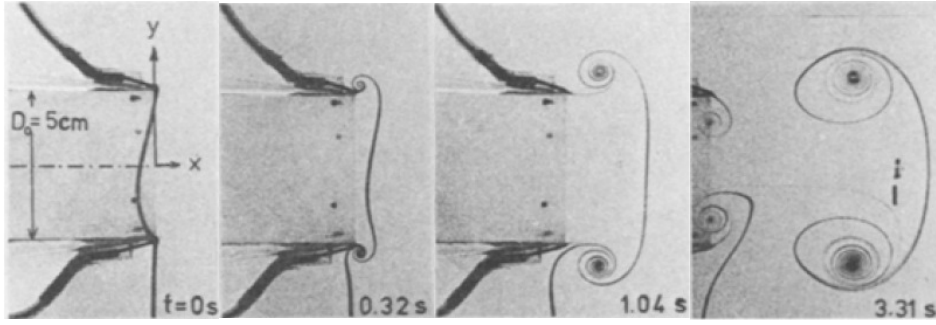

Figure 1.3: The initiation of a pulsed jet, based on figure in Ref. [113]

A quantity maximising these two parameters (size and circulation) for a single vortex ring has been established by Gharib et al. (1998) by considering the aspect ratio of fluid columns L/D ejected with a piston-cylinder apparatus where L is the stroke length and D the outlet diameter [115]. Up to a ratio of $L/D \approx 4$, they noted an increase of the eventual circulation associated with the vortex ring whereas no further enhancement is found for larger amounts of ejected fluid. The characteristic value of $L/D \approx 4$, often referred to as *formation number*, is essentially based on the experimental finding that the vortex core thickness is limited as the non-dimensional vortex ring energy $\alpha = E/(\Gamma^{3/2}I^{1/2})$ does not drop below $\alpha_{\lim} \approx 0.33$. Note that α is based on the kinetic energy E, the circulation Γ and the hydrodynamic impulse I of the vortex ring, and a thicker vortex core coincides with a smaller non-dimensional energy. Since the *formation number* has since been confirmed analytically [116], numerically [117, 118] and experimentally [119, 120], a certain degree of universality can be ascribed to the empirical parameter that is $\alpha_{\lim}$.

The assumption of a uniform velocity profile in the jet exit plane is a common simplification for pulsed jets and indeed constitutes the very basis of the *formation number* derivation. That such a velocity distribution is an unrealistic representation of the jet initiation process can be seen in Figure 1.3 ($t = 0\,\text{s}$). Due to an acceleration around the outlet edges, local maxima in the axial velocity component can be inferred, coinciding with a non-zero radial velocity component [113, 121]. From an analytical standpoint, any such radial/transverse velocity in turn can only exist in the presence of over-pressure inside the jet exit plane [122], reflecting the requirement to accelerate volumes of entrained fluid, added fluid as well as ejected fluid [123], all of which sharing the momentum supplied by the actuator. Looking at the effect of

over-pressure from a different perspective, it can be viewed as an additional source contributing to the total circulation, kinetic energy and momentum supplied to the flow [124, 122, 125]. In this regard, a larger relative importance can be ascribed to the generation of large-scale vortex rings compared to the trailing jet where no such over-pressure effect occurs [126, 127].

The introduction given above supports the argument that vortex structures may have particularly beneficial effects in active separation control. Not only do they lead to an additional momentum input at a given mass flux; an *energisation* of the near-wall flow can also be expected thanks to their entrainment characteristics [128, 129]. Given that typical outlet geometries of actuators employed in active separation control are rectangular, a few additional remarks are in order. Compared to circular outlets, vortex rings generated with elongated outlets undergo self-induced deformations [130], which may lead to even larger entrainment rates [131, 132]. Furthermore, a prolonged residence time near such outlets has been found during the jet initiation before vortex rings start to propagate with a self-induced velocity [133]. It is also important to note that a *pinch-off* (i.e., the spatial separation between vortex ring and trailing jet) has not been observed for vortices generated with such outlet geometries. As a result, there is an ongoing transfer of vorticity which has so far precluded the application of the *formation number* concept [133–135].

1.2.2 Influence of a cross-flow

Although findings inferred from pulsed jets ejected into still surroundings can be viewed as being relevant to vortical flows in general, including those produced by separation control actuators, one may argue that an important boundary condition is missing. Specifically, the presence of a cross-flow may impose an influence that needs to be taken into account when an effective flow manipulation by means of pulsed jets is desired.

As far as circular outlets are concerned, the concept of a *formation number* introduced above has been generalised for non-zero cross-flow conditions by Sau & Mahesh (2008) [136]. Starting from a jet to cross-flow velocity ratio $r = u_{\text{jet}}/U_\infty \to \infty$ (quiescent environment), a systematic reduction of the characteristic stroke ratio leading to a maximum-circulation vortex ring was noted for smaller velocity ratios. In other words, the vorticity accumulated inside the vortex ring is reduced. Furthermore, they note that hairpin vortices instead of vortex rings are generated at $r \leq 2$ due to the interaction with the incoming boundary-layer. Other investigations of transverse pulsed jets, where the axial jet velocity inside the exit plane is directed normal to the wall, suggest that the jet trajectory depends on the time delay between successive ejection cycles (in addition to the velocity ratio) [137–139]. In short, an enhanced penetration into the cross-flow is noted in the case of discrete vortex rings, where the delay is large compared to the convective time. To effectively prevent flow separation, however, a steep jet trajectory is not necessarily desired as the momentum flux needs to be supplied to the near-wall region. As mentioned above, this is usually achieved by introducing the pulsed jets with a certain inclination angle φ [140]. Hecklau & Nitsche (2010) conducted an investigation of flow structures subject to a variation of this parameter and concluded that pulsed jets indeed only attach to the downstream surface at angles of $\varphi = (30, 60)°$ but not for $\varphi = 90°$ [141]. Nonetheless, a beneficial influence was also attested for the latter case inasmuch as low-momentum fluid is transferred away from the wall before high-momentum

fluid is shifted in the other direction. Velocity field measurements, conducted in a flat-plate water tunnel setup, however, suggest that a $\varphi = 90°$ emission angle may lead to a detrimental blocking effect, impairing the benefit of larger entrainment rates associated with an observed wall-attached leading vortex [88].

In summary, pulsed jets, both injected into quiescent ambience and in a cross-flow, have been the subject of investigations for many decades. However, unresolved issues regarding their employment in active separation control remain. For instance, the roles of the leading vortex ring and the other flow structures of a pulsed jet are unclear in this context, as is their dependence on operating time scales, such as the pulse duration.

1.3 Objectives and limitations of this work

Although the introduction given above suggests that there is a large number of successful demonstrations of active separation control, no firm establishment of this method in the industry can be attested. In part, this may be due to an unclear picture of unsteady jets and their interaction with a boundary-layer. More than 60 years have passed, and there still appears to be some truth to the statement of Attinello (1961) as *the mixing phenomenon between the blowing jet sheet and the potential flow field is not fully understood.* Providing this understanding, however, and thereby enabling a more effective and efficient approach to separation control may help to lay the ground for a break-through of this intricate technology from a fluid mechanics perspective. Nothing short of this overarching objective is pursued in the current work.

The device chosen to generate unsteady jets in the present work is a PJA where a periodic flow interception is realised with a mechanical valve, see Figure 1.2 (c). This choice is mainly motivated by the perceived need to decouple forcing time scales and supply mass flow rate that is not met by sweeping jet actuators for a fixed geometry. In addition, investigations are necessary for a broad range of frequencies which precludes the employment of synthetic jet actuators for the reasons given in §1.1.2. Hence, results presented in the following should be viewed against the backdrop of the specific characteristics, and also shortcomings, associated with PJAs introduced above. Furthermore, I restrict myself to a fixed actuator geometry and do not consider the effects of scaling or different outlet shapes. Nonetheless, I assume that some of the major findings presented in the following can be transferred to other means of generating unsteady jets as will be discussed in chapter 5.

To achieve the overarching goal stated above, a subdivision into three major research questions appears to be appropriate. First, it is hypothesised that the leading vortex generated during the initiation of pulsed jets exhibits a superior contribution toward control authority compared to the trailing jet. Then, an efficiency enhancement is possible by adjusting the ejection time to exclusively generate the former flow structure. Oriented by the seminal article of Gharib et al. (1998) introduced in a previous paragraph, the first part of this work is therefore dedicated to the question:

Q1: Can the concept of a *formation number* be adapted to the flow found in pulsed-jet actuation?

Answering this question involves a clarification regarding the impact of a specific (non-circular) outlet geometry and an impulsive velocity program. This insight will then be transferred to a more application-relevant scenario characterised by a non-zero cross-flow, answering the following question:

Q2: What are the dominant flow structures and their respective contributions towards control authority in the case of PJA-generated jets?

Finally, the dynamical response of a boundary-layer susceptible to separation is considered, addressing the following issue:

Q3: (How) should the forcing signal of a PJA be adapted to flow characteristics in order to enhance the efficiency while retaining control authority?

I hope that finding answers to the questions stated above gives rise to a more informed choice of some of the parameters that govern the efficacy in active separation control, thereby also addressing an assertion made by Wygnanski (2004): *The need for a simple model that enables proper characterization of the various parameters involved is paramount in order to make AFC more efficient [...].*

2

Some methodological details

In this chapter, the actuation device under consideration will be introduced. Then, I will provide additional details on the velocity field measurement by means of particle image velocimetry (PIV) in order to make the specific approach to data acquisition and evaluation as transparent and reproducible as possible, noting that phase-locked PIV data are presented in all of the research articles inserted in the next chapter. For a more general explanation of this measurement technique, the interested reader is referred to introductory literature, for instance Ref. [142].

2.1 Method of generating pulsed jets

Before introducing the actuator design and function principle, let us briefly address the instrumentation employed to supply compressed air and electric signals to the PJA (Figure 2.1).
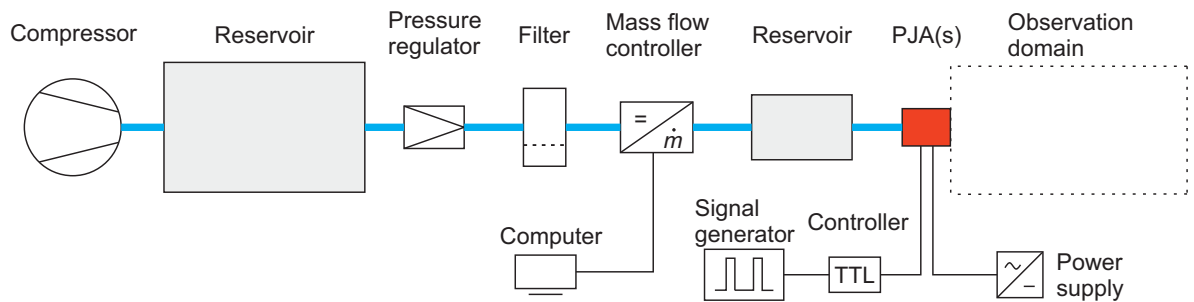
Figure 2.1: Compressed air supply chain - the figure illustrates the connection of instruments required to generate pulsed jets, compressed air tubing shown in blue

First, surrounding air is compressed and preserved in a large reservoir at a pressure of approximately 12 bar. Further downstream, the pressure is reduced to 8 bar, being the nominal operating pressure of the mass flow controller. After passing through an air filter and a precision hydraulic pipe inlet, the mass flow rate is adjusted by means of a device with a range of $\dot{m} = 1, \dots, 50\,\mathrm{l_s/min}$ where the subscript 's' refers to standard conditions of 20°C ambient temperature and 1013.25 mbar ambient pressure. The maximum uncertainty pertaining to this device is $\pm(0.5\%\,\mathrm{o.m.v.} + 0.1\%\,\mathrm{FS})$, which is the lowest for any mass flow

controller that the author of this thesis is aware of. Then, the compressed air again passes through a precision hydraulic pipe and into a 10 litre reservoir that compensates pressure fluctuations induced by the solenoid valve further downstream that is periodically opened by a transistor-transistor-logic controller supplied with a square-wave signal in the range $U_{\mathrm{sqw}} = 0, \dots, 5\,\mathrm{V}$. The valve is powered by the maximum approved direct current voltage of $U_{\mathrm{power}} = 53\,\mathrm{V}$ to ensure a reliable operation even for short pulse durations and large supply pressure. Eventually, pulsed jets are emitted into an observation domain, either being a volume of quiescent ambience (**Article 1**) or the test section of a wind tunnel (**Articles 2** through **5**).

The PJA, highlighted by a red box in Figure 2.1, is shown in more detail in Figure 2.2.
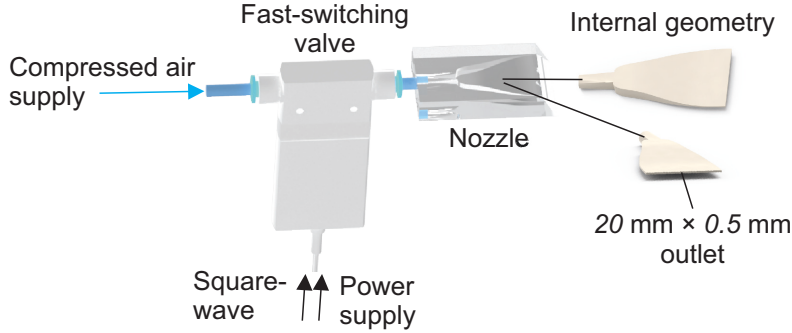

Figure 2.2: Pulsed-jet actuator consisting of a fast-switching valve and a 3D printed nozzle

The device consists of two components: an off-the-shelf fast-switching valve and a 3D printed nozzle. The mechanical valve function principle is illustrated in Figure 1.2 (c). The flow duct is only opened through a magnetic force when the solenoid carries current whereas no air passes through the valve in currentless mode. Hence, the actuation time scales can be readily set by generating a square-wave with a signal generator. The minimum opening and closure times are $t_{\mathrm{p,min}} = 0.6\,\mathrm{ms}$ and $t_{\mathrm{off,min}} = 0.4\,\mathrm{ms}$, respectively, yielding a maximum switching frequency of $f = 1,000\,\mathrm{Hz}$. The air is then led through a short tube with an internal diameter of $d_{\mathrm{in}} \approx 3.8\,\mathrm{mm}$ into the nozzle where the cross-section transitions into an elongated slit of $A_{\mathrm{out}} = (20 \times 0.5)\,\mathrm{mm}^2$. Homogeneity of outlet profiles to within 10% along the outlet span has been confirmed by means of pressure and hot-wire measurements for a variety of forcing signals.

Note that the same PJA is employed throughout this work, that is, magnetic valves with the specifications stated above and identical internal nozzle geometries are used. However, the 3D printed part containing the nozzle is adapted to allow for a flush installation of the PJA where applicable.

2.2 Acquisition of phase-locked velocity field data

Given that the flow fields under consideration are dominated by events associated with distinct frequencies, namely the pulsation frequencies, phase-averaging is a suitable tool to reduce stochastic noise. The actuation period, defined by an external trigger, can be divided into a finite number of phases or ensembles and instantaneous velocity fields belonging to a respective phase can be considered elements of the corresponding ensemble. In this section, it

is explained how measurements at defined phases are performed using a dual-pulsed laser and a complementary metal-oxide-semiconductor (CMOS) camera without mechanical shutter.

The analogue input to the transistor-transistor-logic controller of the mechanical valve is used as an external signal defining the actuation period. This signal equals a square-wave where the highs and lows coincide with an open or closed valve position, respectively. Although there is a marginal time delay (on the order of one millisecond) between the step change of these conditions and the beginning or end of the fluid emission, it is a reasonable representation of the periodic actuation process. Therefore, the rising edge of the square-wave that can be detected to within five nanoseconds in the current setup is defined as the start of the trigger sequence at time t_0. The beginning of the exposure sequence in turn is defined by a time delay $\Delta t_{\mathrm{delay}}$ with respect to the rising edge, which is set by sending a command to the time-synchronising unit of the PIV system via network connection. Then, at the beginning of the exposure sequence, all (2560×2160) pixels on the CMOS chip are reset before being read out as black images. Parallel to the storage of black images to the chip, the exposure of the first PIV image is initiated and stopped via global charge transfer after a duration Δt_{exp1} that equals the laser pumping time plus half the pulse delay. Then, the first image is saved to the memory where the black image is subtracted to reduce noise. Similarly, the second image is obtained, albeit with an exposure time by far exceeding the emission time of the second laser pulse. When defining the acquisition phase, it is important to take into account both the exposure time of the first image and the duration of the initial reset which depends on the number of sensor lines to be read out. The latter is on the order of $\Delta t_{\mathrm{reset}} \approx 9.91 \, \mathrm{ms}$ in the current setup when the complete sensor size is evaluated. Overall, the time of acquisition is defined as $t_{\mathrm{acq}} = t_0 + \Delta t_{\mathrm{delay}} + \Delta t_{\mathrm{reset}} + \Delta t_{\mathrm{exp1}}$. After taking a certain number of double images for a fixed phase (constant $\Delta t_{\mathrm{delay}}$) which is simply defined by the acquisition rate and the time interval where the PIV system remains in trigger mode, a command with a different $\Delta t_{\mathrm{delay}}$ is sent to the synchroniser unit, and measurements for the next phase begin.

To determine an appropriate number of snapshots taken per actuation phase, a compromise must be found between the amount of acquired data and an acceptable convergence of phase-averaged velocity field information. As an objective estimate, the root-mean-square deviation of relevant quantities can be computed as a function of the number of considered snapshots. This is exemplarily shown in Figure 2.3 where instantaneous spanwise vorticity fields ω_z of a pulsed wall jet in cross-flow are shown in the left. Increasing the number of snapshots leads to a convergence of the root-mean-square deviation of ω_z towards a limiting value of zero. As acceptable convergence is a matter of definition, it was routinely evaluated that the number of snapshots ensured a deviation that is very small compared to characteristic values of the quantity in question, typically much smaller than 1%.

It is worth noting that the phase-averaging procedure explained above results in filtered representations that, by design, hide the turbulent character of the studied unsteady flows. However, this is deemed necessary to shed some light on the generated flow structures as well as providing a data base for the computation of Lagrangian diagnostics as explained in the next section.
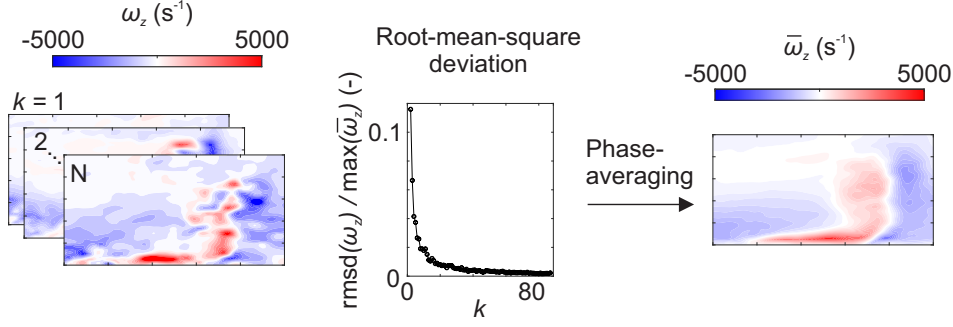
Figure 2.3: Phase-averaging of velocity fields - instantaneous vorticity fields (left), convergence of root-mean-square deviation (centre), phase-averaged vorticity field (right)

2.3 Computation of finite-time Lyapunov exponent fields

The computation of finite-time Lyapunov exponent (FTLE) fields has gained considerable prominence as a visual and quantitative diagnostic of dynamical systems. In fluid mechanics, it is used to reveal material lines or surfaces that govern the transport behaviour [143–146], loosely defined as Lagrangian coherent structures [147]. Such structures can be thought of as separatrices that divide regions of qualitatively different dynamics. Depending on them being stable or unstable manifolds, nearby fluid trajectories converge or separate at an exponential rate on a connected time interval. According to Ref. [148], unstable manifolds act as attractors and are responsible for folding patterns while stable manifolds act as repellors causing a stretching of particle sets normal to the manifold which is illustrated in Figure 2.4.
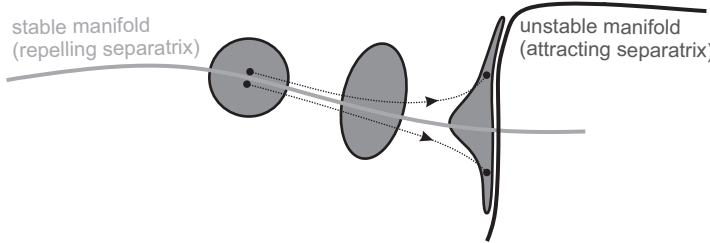

Figure 2.4: Deformation of particle blob due to stable and unstable manifold, based on depiction in Ref. [149]

The stretching of particle sets, and thus the presence of Lagrangian coherent structures, can be assessed by identifying ridges in the underlying FTLE fields. In the following, the procedure to compute such distributions based on the advection of virtual tracer particles as carried out in this work is explained.

Consider two-dimensional $m \times n$ vector fields $\mathbf{U}$ containing phase-averaged two-component velocity information for a finite number of coherent phases. In a **first step**, a temporal interpolation scheme is applied in order to increase the number of locations passed by a given tracer particle while travelling a certain distance. This step is optional but results in more realistic advection curves as the effect of small-scale flow structures is taken into account. The interpolation scheme must be chosen with care as to avoid overshoots in the velocity signals. This is illustrated in Figure 2.5 where a square-wave defined at the values highlighted by circles is interpolated with splines (red curves) and the method introduced in Ref. [150]. It is immediately apparent that spline interpolations may yield unreliable results in the investigated

pulsatile flow fields as they produce under- and overshoots which would heavily impact the computed advection of particles. The cubic Hermite interpolation (black curve) suggested by Akima (1970), on the other hand, is designed to avoid such behaviour by establishing piecewise functions.
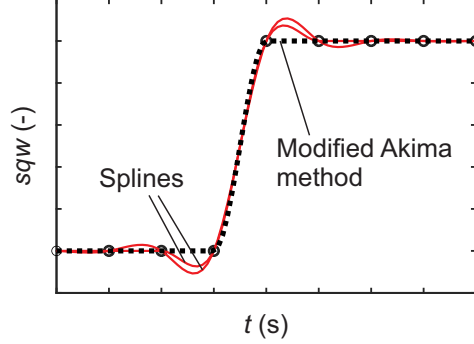

Figure 2.5: Interpolation of discrete square-wave - the figure shows that spline interpolations result in under- and overshoots whereas the modified Akima method does not

In a **second step**, tracer particles are initiated at time τ_0 and advected according to the (time-interpolated) velocity fields in order to compute a flow map. In the current study, a rudimentary algorithm without grid refinement is employed, hence the initial structured particle grid $\mathbf{x}_0 = (x_0, y_0)$ defines the spatial resolution of the FTLE field. Alternative procedures striving for a more efficient computation are provided in Refs. [151–155]. Note that the particle grid does not need to coincide with the measurement grid as a spatial interpolation provides the local velocity information at $m_\mathrm{q} \times n_\mathrm{q}$ query points initially defined by $\mathbf{x}_0$. The pathlines of individual particles are then determined by repeatedly (for multiple timesteps) evaluating the two velocity components at the query points that are updated after each timestep. Hence, for each tracer, one displacement vector $\Delta \mathbf{x}_{i,j} = \mathbf{U}_{i,j} \Delta t$ is computed per timestep where Δt corresponds to the temporal resolution. Then, the deformation of the particle grid that occurs between two timesteps can be written as $\mathbf{x}(t + \Delta t) = \mathbf{x}(t) + \Delta \mathbf{x}$. Since this approach is not very robust in non-linear problems, such as the velocity fields under consideration, a 4th order Runge Kutta scheme is implemented in the current work. Here, the displacement vector $\Delta \mathbf{x}$ is only considered as a predictor that is adjusted by combining it with three weighted correcting vectors. In this way, particle displacements are computed for a number of timesteps until the integration time Δt_int is reached, essentially defining the length of pathlines.

Following the numerical integration, the particle grid at time $t = \tau_0 + \Delta t_\mathrm{int}$ is compared with the initial state by computing the gradient of the flow map (**step 3**). In the two-dimensional case, for each location defined by the initial tracer grid, a 2×2 matrix is obtained by evaluating the deformation of an array that consists of the four neighbour particles using central differencing. For example, the gradient associated with the location $\mathbf{x}_{i,j}$ is

$$\frac{\mathrm{d}\Phi \mathbf{x}_{i,j}}{\mathrm{d}\mathbf{x}} = \begin{pmatrix} \dfrac{(x_{i+1,j} - x_{i-1,j})(\tau_0 + \Delta t_\mathrm{int})}{(x_{i+1,j} - x_{i-1,j})(\tau_0)} & \dfrac{(x_{i,j+1} - x_{i,j-1})(\tau_0 + \Delta t_\mathrm{int})}{(y_{i,j+1} - y_{i,j-1})(\tau_0)} \\ \dfrac{(y_{i+1,j} - y_{i-1,j})(\tau_0 + \Delta t_\mathrm{int})}{(x_{i+1,j} - x_{i-1,j})(\tau_0)} & \dfrac{(y_{i,j+1} - y_{i,j-1})(\tau_0 + \Delta t_\mathrm{int})}{(y_{i,j+1} - y_{i,j-1})(\tau_0)} \end{pmatrix} . \tag{2.1}$$

This matrix is then left-multiplied with its transpose, resulting in a Cauchy-Green deformation tensor that represents the linearisation of the flow map. The maximum stretching at $\mathbf{x}_{i,j}$ is

related to the maximum eigenvalue λ_{max} of this tensor, and the FTLE for this particular location is defined as

$$FTLE(\mathbf{x}_{i,j}) = \frac{1}{|\Delta t_{\text{int}}|} \ln \sqrt{\lambda_{\text{max}}(\mathbf{x}_{i,j})}. \tag{2.2}$$

To compute the entire $m_{\text{q}} \times n_{\text{q}}$ FTLE field, the procedure beginning with equation (2.1) is repeated for the remaining locations defined in $\mathbf{x}_0$. Time series of FTLE fields can be obtained by simply repeating the procedure explained above for initiation times other than τ_0.

As an example, Figure 2.6 contains an FTLE field for one timestep in a flow similar to the one presented in Figure 2.3. Here, an integration time of $\Delta t_{\text{int}} = -3\,\text{ms}$ was chosen, hence the particle advection was computed backward in time. As explained above, this is necessary to identify attracting material lines, in this case characterising the jet propagation front, a leading vortex and the upper boundary of the wall-attached jet.
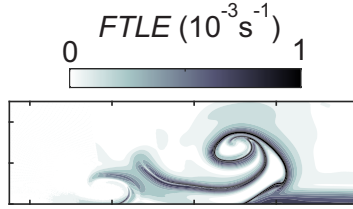

Figure 2.6: FTLE field for pulsed wall jet

It is important to note that the out-of-plane velocity component is neglected in the procedure introduced above. This may yield unrealistic results when highly three-dimensional flows are considered. However, it proves a justified assumption when the flow is dominated by spanwise vortical structures [156] as is the case in the current work. Nonetheless, FTLE fields based on three-dimensional three-component velocity domains will also be presented in the following papers for selected configurations. Extending the computations to accommodate such flow fields does not pose any conceptual difficulty. However, the computational cost as well as the effort to provide the required measurement data is increased. Specifically, phase-locked stereoscopic PIV must be performed for multiple parallel measurement planes. Then, a tomographic reconstruction of the flow field can be carried out by aggravating the phase-averaged data in a matrix with four dimensions spanning the three Cartesian coordinates and time before performing FTLE computations analogous to the procedure explained above.

3

Publications

Article 1

B. STEINFURTH AND J. WEISS. **Vortex rings produced by non-parallel planar starting jets.** *J. Fluid Mech.,* **903**, 2020.

Article 2

B. STEINFURTH AND J. WEISS. **Velocity ratio effect on flow structures of non-parallel planar starting jets in cross-flow.** *J. Fluid Mech.,* **915**, 2021.

Article 3

B. STEINFURTH AND J. WEISS. **Boundary-layer control by means of pulsed jets at different inclination angles.** *AIAA J.,* **59**(8), 2021.

Article 4

B. STEINFURTH AND J. WEISS. **Flow physics of pulsed-jet actuation: Efficiency enhancement in active separation control through optimization of the duty-cycle.** *AIAA J.,* 2022.

Article 5

B. STEINFURTH AND J. WEISS. **Modelling the decay of finite-span starting and stopping wall jets in an external stream.** *J. Fluid Mech.,* **951**, 2022.

Vortex rings produced by non-parallel planar starting jets

Ben Steinfurth[1]†, Julien Weiss[1]

[1]Institute of Aeronautics and Astronautics, Technische Universität Berlin, Marchstr. 12-14, 10587 Berlin, Germany

Experimental methods are employed to investigate vortex rings generated by impulsively emitting pressurised air through a rectangular outlet of high aspect ratio into quiescent surroundings. The flow is characterised by a rapid transverse expansion as thick-cored, almost spherical vortex rings with a diameter more than 40 times the outlet width and entrainment rates of $\eta > 0.9$ are generated. They continue to absorb vorticity far beyond the universal formation time of $t^* \approx 4$ applicable to axisymmetric parallel starting jets introduced by Gharib *et al.* (1998). Here, the maximum circulation and the corresponding formation time depend on the magnitude of over-pressure in the outlet plane. After momentarily reaching a non-dimensional energy close to or even below a value of $\alpha = 0.16$ associated with Hill's spherical vortex, vorticity is continuously shed into a trailing jet, and the vortex rings evolve into unsteady thinner-core states. No separation between the vortex ring and the trailing jet (pinch-off) is observed. The present study provides new insights into the flow physics of non-parallel planar starting jets that significantly differ from parallel starting flows investigated previously. The potential for active flow control applications is discussed.

1. Introduction

The capability to improve the efficiency of mixing processes by employing starting jets has been widely recognised. This can be ascribed to thus generated vortex rings that are associated with greater entrainment rates than those found in steady jets. Extensive reviews regarding the structure and motion of vortex rings for different boundary conditions are provided by Shariff & Leonard (1992) and Lim & Nickels (1995). Two mechanisms are responsible for their entrainment of ambient fluid. First, there is a continuous circulatory engulfment of large regions of surrounding fluid (convective entrainment) and second, shearing takes place at the interface between the vortex ring and the irrotational surrounding fluid, resulting in viscous diffusion (diffusive entrainment).

The characteristics of starting jets are reflected by the invariants of motion, i.e. the circulation Γ, the kinetic energy E and the impulse I. Among these quantities, the circulation is particularly important to the purpose of this study. As noted by Didden (1979), its rate of change is equal to the vorticity flux ejected through the jet exit plane, i.e.

$$\frac{\mathrm{d}\Gamma}{\mathrm{d}t} = \int\limits_{0}^{y_\infty} u\omega_z \mathrm{d}y \qquad (1.1)$$

when only convective transport is regarded, i.e. diffusive effects are neglected. Here,

† Email address for correspondence: ben.steinfurth@tu-berlin.de

a general two-dimensional starting jet is assumed where u is the axial jet velocity and y points along the lateral jet direction with the integration boundaries $y = 0$ on the centreline and $y = y_\infty$ in sufficient distance as to ensure a vanishing vorticity flux. The out-of-plane vorticity component is $\omega_z = \partial v/\partial x - \partial u/\partial y$ where the second term only depends on the centreline velocity u_0, hence can be determined without knowledge of the specific axial velocity profile (see Didden (1979), Rosenfeld et $al.$ (1998)). As a result, equation 1.1 is transformed to

$$\frac{\mathrm{d}\Gamma}{\mathrm{d}t} = \int\limits_0^{y_\infty} u\frac{\partial v}{\partial x}\mathrm{d}y + \frac{1}{2}u_0^2. \tag{1.2}$$

Assuming a uniform axial velocity at the outlet and parallel flow in the exit plane, i.e. a zero transverse velocity component v for all times, the first term on the right hand side can be neglected. This amounts to the slug model that is commonly used for the prediction of circulation development (Shariff & Leonard (1992), Glezer (1998)).

Based on this model for parallel starting jets, Gharib et $al.$ (1998) explain the existence of a time scale that governs the efficient formation of vortex rings. Essentially quantifying the amount of emitted fluid, they show that a specific ratio of stroke length and outlet diameter $L/d \approx 4$, which is dubbed formation number by the authors, separates two regimes of vortex ring appearance: at low stroke ratios, the majority of the vorticity generated by the starting jet occurs in a leading vortex ring whereas for higher stroke ratios, there is no further increase of the vortex ring circulation but it is now followed by a trailing jet. They argue that vortex rings of maximum circulation are characterised by a setup-specific dimensionless energy

$$\alpha_{\mathrm{lim}} = \frac{E}{\Gamma^{3/2}I^{1/2}} \tag{1.3}$$

that is linked with the vorticity distribution inside the vortex ring. This distribution in turn is dependent on the piston velocity signal, i.e. the history of the starting jet velocity in the exit plane. Readily extractable from particle image velocimetry (PIV) measurements, they find that the generated steady vortex rings exhibit nearly constant non-dimensional energies of $\alpha_{\mathrm{lim}} = 0.33 \pm 0.01$ once the formation number is exceeded. They compare this empirical quantity to the non-dimensional energy supplied by the apparatus α_{piston} and observe the following: as the stroke ratio is increased, α_{piston} decreases, which results in greater vortex ring dimensions. For stroke ratios greater than $L/d \approx 4$, α_{piston} falls below α_{lim} in their experiment, and "the apparatus is no longer able to deliver energy at a rate compatible with the requirement that a steadily translating vortex ring have maximum energy with respect to impulse-preserving iso-vortical perturbations." (Gharib et $al.$ (1998)) This implies that there is an upper threshold in the amount of fluid that can be converted into a single vortex structure. This conclusion and the universality of the formation number were shown to be applicable across a broad range of operating parameters for parallel starting jets, e.g. by Rosenfeld et $al.$ (1998), Dabiri & Gharib (2004), Krueger et $al.$ (2006), Pawlak et $al.$ (2007), Mohseni et $al.$ (2000) and Sau & Mahesh (2007). To avoid explicit measurements of α_{lim}, Mohseni & Gharib (1998) introduce an analytical model to predict the formation number based on the non-dimensional energy and circulation. This is accomplished by equating the invariants of motion for the family of steady vortex rings defined by Norbury (1973) and the corresponding quantities provided by the slug model.

Although the parallel flow assumption of the slug model may be applicable to many configurations where a fluid column is emitted into quiescent surroundings, it is also observed that the model can under-predict the vortex ring circulation substantially, e.g. by Didden (1979), Nitsche & Krasny (1994), James & Madnia (1996), Weigand & Gharib (1997) and Zhao *et al.* (2000). According to Krueger (2005), this under-prediction is linked with a peak in the circulation flux $\mathrm{d}\Gamma/\mathrm{d}t$ (equations 1.1 and 1.2) that can occur during the initial rapid acceleration of fluid. During this phase, a non-uniform axial velocity distribution is found in the outlet plane characterised by a maximum at the nozzle lip, coinciding with a peak in $\partial v/\partial x$ (Didden (1979)). In establishing a relationship between the non-zero transverse velocity component and over-pressure inside the jet exit plane, Krueger (2005) introduces a correction term for the slug model

$$\Gamma_p = \frac{1}{\varrho} \int\limits_0^{t_\mathrm{p}} (p_0 - p_\infty)\mathrm{d}t \qquad (1.4)$$

where p_0 denotes the centreline pressure inside the jet exit plane and p_∞ is the ambient pressure. Neglecting viscous effects, this correction term is equal to the temporal integral of the first term on the right hand side in equation 1.2 and can be viewed as a manifestation of non-parallel flow. Hence, over-pressure inside the outlet plane during the rapid jet initiation is responsible for two interrelated effects. First, it leads to an enhanced vorticity flux, thus larger overall circulation. Second, it imposes a curvature of streamlines close to the jet outlet, i.e. a transverse advection of fluid.

For the classical approach of generating vortex rings in the laboratory, a piston-cylinder arrangement is used to accelerate a defined amount of fluid and emit it into a water tank. However, more relevant to technical implementations in the field of active flow control (AFC) are pulsed jet actuators (PJAs) which periodically emit pressurised air in an impulsive fashion. The periodic flow manipulation is brought about either by a solenoid valve or a fluidic switching mechanism and among other devices, such as synthetic jet or plasma actuators, they may be used to control flow separation (Greenblatt & Wygnanski (2000)). For PJAs, the over-pressure is typically larger than for the piston-cylinder setup, resulting in a greater transverse flow acceleration. Furthermore, the jet outlets are typically not circular but slit-shaped as to efficiently affect greater flow regions. So far, the concept of a formation number was found to be not readily applicable to planar two-dimensional starting jets (Pedrizzetti *et al.* (2010)). This was generally explained by the observation made by Afanasyev (2006) and later by Das *et al.* (2013) that there is no clear separation between the produced vortex pair and the trailing jet (pinch-off) as the former does not acquire a sufficiently large translational speed. Hence, there is an ongoing interaction as the vortex dipole continues to entrain vorticity from the trailing jet even when the formation number of $L/d \approx 4$ is surpassed. It must be noted, however, that these investigations were also restricted to the generation of vortical structures by means of a piston-cylinder apparatus whereas the literature concerned with fundamental properties of vortex rings generated with PJAs or other flow control devices is sparse. For the specific case of synthetic jet actuators, Smith & Glezer (1998) show that the centreline velocity decay is greater while the spreading rate is lower in comparison to steady jets. The trajectories of vortex cores related to flow structures induced by planar synthetic jets are investigated by Béra *et al.* (2014). Focusing on purely alternating jets and mixed pulsed jets, they note that vortex structures develop farther from the jet orifice when the velocity is not decreased to zero between successive starting jets.

Choutapalli *et al.* (2009) study the properties of a pulsed axisymmetric jet at high Reynolds numbers that is generated by means of a rotating disk with drilled holes that allow the flow to enter the nozzle whereas the path is closed otherwise. As the duty cycle is defined by the ratio of open to closed area, a greater Strouhal number results in a closer distance between successive vortex rings in their experiment with a steady jet character assumed at a distance of five nozzle diameters. They also note distinct deviations when analysing characteristic turbulent quantities in separate regions of the pulsed jet as the vortex ring appears to boast greater shearing stresses than the trailing jet. A recent DNS study by Shin *et al.* (2017) is concerned with a suddenly stopped, hence decelerating axisymetric jet. The authors suggest that behind the deceleration wave, a statistically unsteady self-similar state can be noted, building on the experimental work by Witze (1983) who studied the velocity field of an impulsively started axisymmetrical jet and a simplified analytical approach by Musculus (2009) addressing the entrainment rate during the deceleration phase of a single-pulsed jet.

The main objective of this study is to reveal the properties of vortex rings associated with non-parallel planar starting jets that are generated with an AFC-typical device. In doing so, we also examine the hypothesis that the concept of a formation number proposed by Gharib *et al.* (1998) can be extended to this flow configuration. This is motivated by the fact that past studies have mainly been concerned with parallel starting jets of presumably similar limiting non-dimensional energies α_{lim}. However, the influence of highly non-parallel flow on this parameter, essentially defining the formation number, has not been studied to the best of our knowledge. Here, a PJA is employed, and driven by a solenoid valve, the flow periodically exits a $20\,\mathrm{mm} \times 0.5\,\mathrm{mm}$ rectangular outlet. The over-pressure required to provide relevant jet velocities of $u_{\mathrm{jet}} \approx 50\,\mathrm{m/s}$ is substantial due to the short valve opening durations. Hence, highly non-parallel flow is present close to the outlet of the starting jets.

The vortex rings generated with this setup are mainly studied on the basis of phase-locked PIV measurements while flow visualisations of starting jets ejected into a water tank are conducted as a reference case. A detailed description of the setup and procedure is provided in the following.

2. Methods

This section contains a description of the experimental approach. Two setups were used for this work: (1) A PJA system was employed to generate non-parallel planar starting jets of compressed air. (2) The classical piston-cylinder setup was utilised to produce vortex rings associated with parallel starting jets in a water tank. Thus, the influence of the non-parallel flow condition can be identified by comparing results from the two experiments.

2.1. *Non-parallel starting jets generated with PJA device*

2.1.1. *Experimental procedure*

The PJA device that was used to generate non-parallel starting jets was mainly composed of a mechanical valve and a nozzle with a rectangular slit-shaped outlet that was mounted flush in a wall. Pressurised air was fed through the solenoid valve with a minimum opening time of $t_{\mathrm{p,min}} = 0.6\,\mathrm{ms}$ that was operated at $f_{\mathrm{p}} = 50\,\mathrm{Hz}$. The accuracy with respect to the valve opening time was $\Delta t_{\mathrm{p}} = \pm 15\,\%$. As shown in figure 1, the inlet consists of a circular tube, connecting the nozzle and the solenoid valve. Then, a
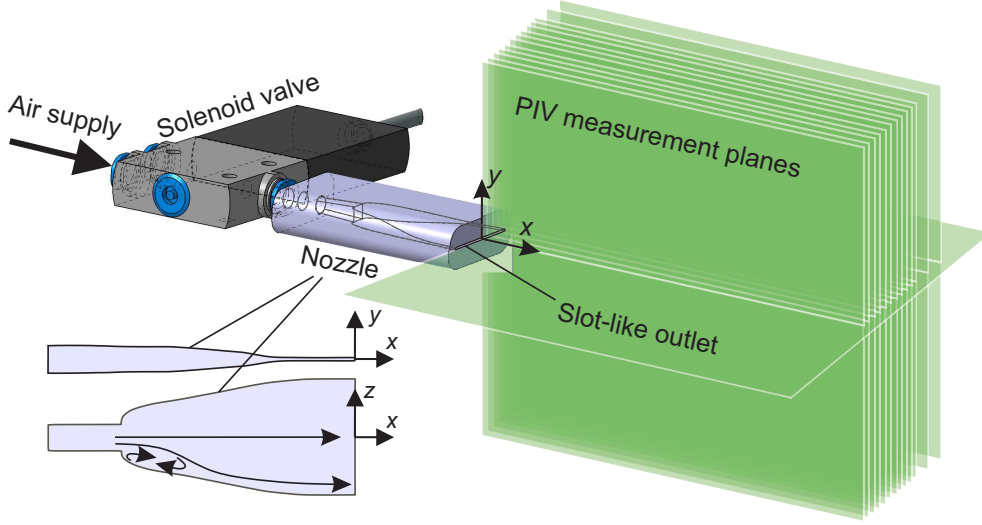
FIGURE 1. Arrangement of solenoid valve and nozzle with outlet aspect ratio of $l/d = 40$ for generation of non-parallel planar starting jets

transition from circular to rectangular cross-section ensues. This is accompanied by a sudden widening of the flow area in z direction which may result in a minor recirculation region associated with a bending separating streamline. The resulting velocity profiles close to the outlet will be analysed later on.

The slit-shaped outlet had a width of $d = 0.5\,\mathrm{mm}$ and a length of $l = 20\,\mathrm{mm}$. Based on a circle with the same area, this yields an equivalent diameter of $d_{\mathrm{eq}} \approx 3.57\,\mathrm{mm}$. Ensuring an equal volumetric flux, this quantity is used as the characteristic length scale in the current study. For other non-circular, namely elliptic, jets Hussain & Husain (1989) found that this definition yields an adequate length scale. Furthermore, it was used in the study of the pinch-off process of vortex rings generated with elliptic jets by O'Farrell & Dabiri (2014).

The nominal velocity of the jets u_{jet} was calculated based on mass conservation taking into account the outlet area, valve opening time and a constant supply mass flow. The latter was adjusted with a controller and fed into a tank upstream of the solenoid valve with a volume sufficiently large to compensate velocity fluctuations. The stroke ratio of the planar starting jets L/d_{eq} was varied by adjusting the pulse width and thus changing the length of a virtually emitted fluid column $L = u_{\mathrm{jet}}t_{\mathrm{p}}$. Three configurations encompassing relevant formation time scales for the specific starting jets studied here were narrowed down in preliminary experiments and will be discussed throughout the paper, see table 1. Specifically, equivalent stroke ratios of $L/d_{\mathrm{eq}} \approx [9, 15, 48]$ were investigated. Given the actuation frequency of $f_{\mathrm{p}} = 50\,\mathrm{Hz}$, these configurations are associated with duty cycles of DC $= [3, 5, 15]\%$. Operating the PJA device at such relatively low duty cycles means that fluid is almost completely at rest before the valve is opened. A substantial gradient force, driven by a supply pressure of roughly $p_{\mathrm{supply}} \approx 5\,\mathrm{bar}$, is necessary to ensure the required acceleration to reach AFC-relevant jet velocities listed in table 1. This rapid acceleration is the source for non-parallel flow effects that are specific to the method of generating vortex rings in the current study and will be addressed in more detail in the following. To assess the influence of these effects, two further configurations with a decreased supply pressure of $p_{\mathrm{supply}} \approx 4\,\mathrm{bar}$ and $p_{\mathrm{supply}} \approx 3.5\,\mathrm{bar}$ were investigated. The valve opening time for these configurations

TABLE 1. Main parameters of investigated non-parallel starting jet configurations

p_{supply} (bar)	u_{jet} (m/s)	t_{p} (ms)	L/d_{eq} (-)
5	51	0.6	9
5	54	1	15
5	57	3	48
4	42	1	11.8
3.5	38	1	10.6

was the same as for the medium stroke ratio, i.e. $t_{\text{p}} \approx 1\,\text{ms}$. This resulted in decreased jet velocities and stroke ratios that are also listed in table 1.

As indicated in figure 1, two-dimensional velocity fields were measured by means of stereoscopic PIV in 13 parallel planes at $z = 0, -2, \ldots, -20, -25, -30\,\text{mm}$. The gathered velocity information was then mirrored around the $z = 0\,\text{mm}$ plane as symmetry was verified by measuring additional planes at $z = 6\,\text{mm}$ and $z = 12\,\text{mm}$. The resulting PIV domain had dimensions of $X \approx 100\,\text{mm}$, $Y \approx 90\,\text{mm}$ and $Z \approx 60\,\text{mm}$. As indicated in figure 1, further measurements were also conducted inside the xz symmetry plane.

The measurement domain was filled with DEHS particles of $d_{\text{DEHS}} \approx 1\,\mu\text{m}$ diameter with an external seeding generator prior to measurements. However, particles were also added to the air supply of the PJA as to ensure a sufficient seeding density inside the starting jets in close outlet proximity. Particle slip due to dynamic forces induced by periodic oscillations present inside the flow field was expected to be negligible in accordance with considerations given by Mei (1996).

The cameras had an optical resolution of $2560\text{x}2160\,\text{px}^2$, and each measurement plane was divided into square overlapping interrogation areas with an edge length of 24 pixels, resulting in a spatial resolution of $\Delta x = \Delta y \approx 0.52\,\text{mm}$. With respect to the rising edge driving the solenoid valve, a dual-pulsed laser was triggered at 60 different time delays, equidistantly sampling the actuation process with a period of $T = 1/f_{\text{p}} = 20\,\text{ms}$. Thus, the temporal resolution of PIV measurements was $\mathrm{d}t \approx 0.33\,\text{ms}$. Further measurements with an increased temporal resolution of $\mathrm{d}t \approx 0.05\,\text{ms}$ during fluid emission were performed for an opening duration of $t_{\text{p}} = 1\,\text{ms}$ inside the xy symmetry plane to analyse the early vortex ring evolution process in more detail. The spatial resolution for those measurements was $\Delta x = \Delta y \approx 0.75\,\text{mm}$. For each configuration, about 70 double images of the illuminated particles were taken per phase, which resulted in an average standard deviation of $u_{\text{c,std}} \approx 0.11\,u_{\text{c}}$ on the jet centreline.

The moment when seeding particles first emerged from the nozzle was defined to be $t = 0\,\text{ms}$. Essentially quantifying the consumption of compressed air over time, the non-dimensional formation time $t^* = (tu_{\text{jet}})/d_{\text{eq}}$ is referred to in this article. Note that the time instance up to which fluid is nominally emitted is marked by $t^* = L/d_{\text{eq}}$.

2.1.2. Degree of non-parallel flow

Due to the substantial acceleration of fluid mentioned above, over-pressure effects can be expected to govern the flow configuration. These are associated with highly non-parallel flow as opposed to starting jets generated with a piston-cylinder apparatus. In this section, we qualify the specific flow scenario by focusing on relevant properties in
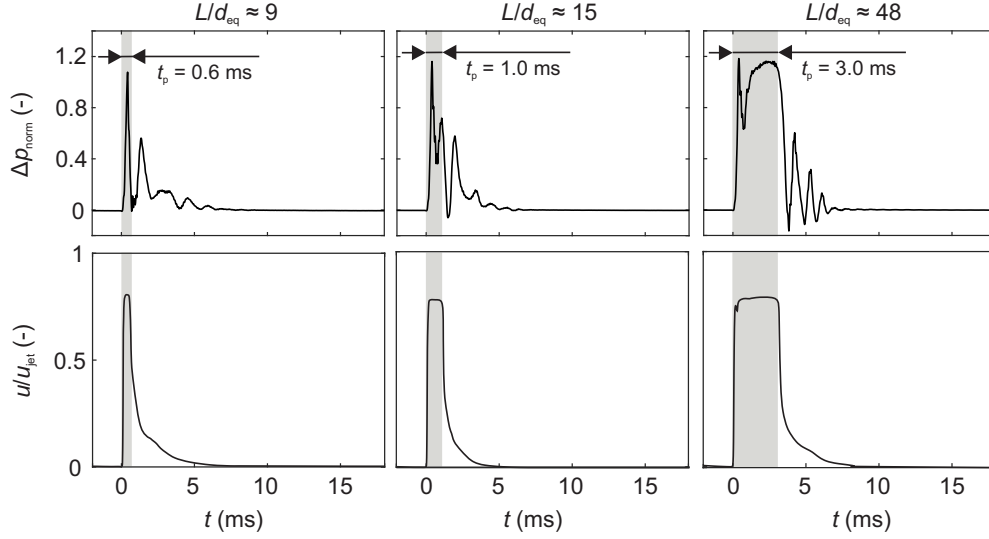
FIGURE 2. Pressure and velocity signals close to the centre of jet exit plane for three stroke ratios; pulse width t_p highlighted by shaded area for reference.

the near-outlet region.

The phase-averaged pressure and velocity signals close to the nozzle outlet are shown in figure 2 over the time of one actuation period where shaded regions indicate durations equal to the respective valve opening times.

The static pressure was measured using a piezo-resistive pressure transducer with a sensitivity of $S \approx 0.03\,\mathrm{mV/Pa}$ and a range of $p_\mathrm{max} = 0\ldots6.9\,\mathrm{kPa}$ mounted directly under the nozzle surface at $x = -2\,\mathrm{mm}$. The time-resolved signals are therefore deemed representative of the pressure in the jet exit plane. All of the investigated starting jets are characterised by distinct over-pressure of $\Delta p_\mathrm{norm} = (p - p_\infty)/(\varrho u_\mathrm{jet}^2) > 1$. An initial short-duration peak is observed for all configurations whereas a secondary pressure wave only follows for the two larger stroke ratios. A similar initial peak was also observed by Krieg & Mohseni (2015) who conducted force measurements on a water jet actuator. In their experiment, the peak in force was much more distinct when the fluid was accelerated in an impulsive fashion as opposed to sinusoidal velocity programs, indicating the significance of a rapid jet initiation. Compared to experiments with a piston-cylinder apparatus, however, the magnitude of over-pressure is much larger in the current study as for instance, Krieg & Mohseni (2013) report a non-dimensional over-pressure of only $\Delta p_\mathrm{norm} \approx 0.2$. Therefore, a larger contribution of the over-pressure term (equation 1.4) to the overall circulation can be expected.

Based on a point measurement with a hot wire anemometry (HWA) probe at $x \approx 2\,\mathrm{mm}$, an impulsive acceleration can be observed in the velocity signals. However, it is worth noting that this does not necessarily reflect the Lagrangian acceleration of fluid particles due to the large pressure gradient. The peak velocities are almost constant but smaller than the nominal jet velocities (table 1). This is mainly due to the calculation of the latter quantity which is based on a square-wave signal with a constant velocity high that is limited to the pulse width t_p. This is clearly not reflected in the velocity signal at $x \approx 2\,\mathrm{mm}$ where a deceleration wave can be observed to follow the starting jet. The actual duration of fluid ejection is therefore longer than t_p, hence a smaller peak velocity is found for the given mass flow rate.
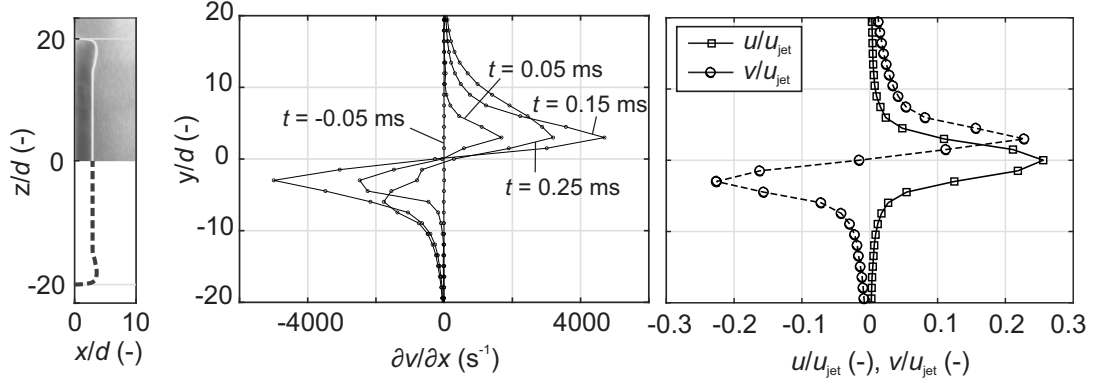
B. Steinfurth, J. Weiss

FIGURE 3. Velocity field information close to the outlet for $u_{\mathrm{jet}} \approx 54\,\mathrm{m/s}$: flow visualisation of axial velocity distribution in xz symmetry plane at $t = 0\,\mathrm{ms}$ (left), development of streamwise gradient of lateral velocity component at $x/d \approx 1.5$ (centre) and velocity profiles $u(y)$ and $v(y)$ during jet emission at $x/d \approx 1.5$ and $t = 0.25\,\mathrm{ms}$

In conclusion, the flow is dominated by large over-pressure in the jet exit plane which causes a rapid acceleration of fluid. In the following, we address the influence of these boundary conditions on quantities that can be directly related to the early formation process of vortex rings. Since the pressure and velocity signals are very similar at the onset of fluid emission for all stroke ratios, only information for one configuration ($L/d_{\mathrm{eq}} \approx 15$) is provided.

Figure 3 sheds light upon the velocity gradient distributions close to the jet exit plane.

An almost uniform axial velocity distribution is observed at $t = 0\,\mathrm{ms}$ inside the xz symmetry plane, i.e. along the larger dimension of the outlet (left in figure 3). The flow visualisation shown for $z/d > 0$ was achieved by illuminating this plane and recording roughly 100 images at $t = 0\,\mathrm{ms}$ that were averaged subsequently. Seeding particles were added to the quiescent ambient fluid but not to the PJA supply, enabling a distinct separation between the starting jet and surrounding fluid. In agreement with previous studies of impulsive starting jets, the velocity distribution is characterised by maxima close to the edges of the nozzle outlet, i.e. at $z/d = \pm 20$. Based on the work by Didden (1979), we expect that these peaks in axial velocity coincide with peaks in $\partial w / \partial x$, representing a main contributor towards vorticity flux that is related to over-pressure during jet initiation.

Very large peaks can also be observed in $\partial v / \partial x$, i.e. for the other lateral velocity component of the starting jets close to the outlet edges (centre in figure 3). They begin to develop when the fluid ejection starts at $t = 0\,\mathrm{ms}$, and extrema are reached around $t = 0.15\,\mathrm{ms}$. They decrease subsequently but are still very distinct at $t = 0.25\,\mathrm{ms}$ or $t^* \approx 4$. This roughly corresponds with the pressure rise shown in figure 2, and an increased circulation flux can be expected for this duration according to equation 1.2. Notably, this represents a time span that is relatively long compared to the formation process, equalling the formation number associated with maximum vortex ring circulation for circular parallel starting jets introduced by Gharib *et al.* (1998).

Velocity profiles for u and v are shown in the right of figure 3. It is worth noting that the extrema in transverse velocity v are of a similar magnitude as the axial velocity at $t = 0.25\,\mathrm{ms}$, pointing to a significant transverse advection of fluid due to the over-pressure effect causing a non-zero $\partial v / \partial x$ component.

Even though PIV measurements indicate very large velocity gradients close to the

outlet, it should be noted that these peaks are presumably still underestimated. This is explained by the size of interrogation areas that exceeds the very narrow potential core width and therefore contains particles advected with strongly varying velocities. This becomes apparent for the axial velocity component where a value close to $u/u_{\text{jet}} = 0.8$ can be expected on the centreline as measured with a HWA probe (figure 2) but PIV measurements only indicate $u/u_{\text{jet}} \approx 0.25$. The underestimated peak velocity invariably results in gradients of smaller magnitude close to the centreline. Thus, the vorticity component $\omega_z = \partial v/\partial x - \partial u/\partial y$ is underestimated in this flow region.

This experimental error is typical of PIV measurements in high-gradient flows. However, it is limited to the region close to the potential core in the current study, i.e. to nozzle distances of about $x \leqslant 6\,d$ or $x \leqslant 3\,\text{mm}$ where other PIV-related shortcomings due to strong laser light reflections or particle buoyancy cannot be eliminated completely. The vortex rings studied here are only located in this region for very small non-dimensional formation times of about $t^* < 5$. The main focus point of this article, however, is related to larger formation time scales as will be presented in the following.

Despite the mentioned insufficiencies concerning the experimental method, highly non-parallel flow can be attested. This is due to a rapid acceleration that ensues once the solenoid valve is opened. As a result, the circulation flux is increased and a strong transverse advection of fluid can be expected.

2.1.3. *Computation of finite-time Lyapunov exponent fields*

When referring to PIV data in the following, the phase-averaged velocity fields are regarded. No additional filter was applied to these. Using this database, time- and space-dependent 3D finite-time Lyapunov exponent (FTLE) fields were computed. This flow diagnostic has gained considerable prominence in the field of fluid mechanics, enabling an understanding of transport mechanisms in dynamical systems. Indicating Lagrangian coherent structures (Haller (2001)), it can help uncover regions with a dominant influence on the properties of a given flow field. In the current article, material surfaces of exponential convergence are deduced, pointing to interfaces between vortex rings and the surrounding fluid and providing a degree of comparability with flow visualisation experiments. This is based on the fact that certain flow structures attract a greater amount of dye particles.

To compute three-dimensional FTLE fields, the domain spanned by PIV measurement planes and their mirrored counterparts was seeded with virtual passive tracer particles that are advected according to local velocity vectors using a 4th order Runge-Kutta scheme. The initial distance between these tracers was $\Delta x = \Delta y = \Delta z = 0.3\,\text{mm}$, resulting in a structured grid of about 10^7 points for which the FTLE was obtained. The advection was computed backward in time and the regarded finite-time interval was $\tau = T/2 = 10\,\text{ms}$, ensuring particles interacted with a sufficient number of flow features as to reveal dominant material lines. However, the integration time was reduced for particles leaving the computation domain prematurely. Temporal interpolation based on a method introduced by Akima (1970) was applied, yielding time steps of $\Delta t \approx 0.06\,\text{ms}$ for the FTLE computation. To acquire information regarding local velocity vectors at respective tracer locations, tricubic interpolation was employed.
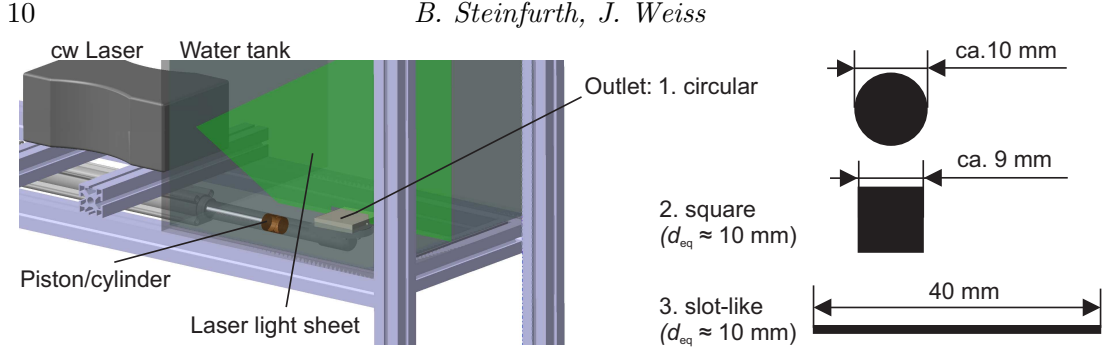
B. Steinfurth, J. Weiss

FIGURE 4. Experimental setup for flow visualisation

2.2. *Parallel starting jets generated with piston-cylinder arrangement*

Experiments were also conducted inside a water tank to reproduce the parallel flow condition found in most previous studies. During these flow visualisations, a slot-like outlet similar to the one of the PJA was used to compare vortex rings produced by parallel and non-parallel planar starting jets. Furthermore, a circular outlet was employed to qualify the setup by comparing the results to those previously obtained by Gharib *et al.* (1998) and others while a square outlet represented the intermediate case.

Figure 4 shows a schematic depiction of the test rig used for flow visualisations as well as the dimensions of the three mentioned outlet geometries. Water resting in a brazen tube was impulsively accelerated by a piston mounted to a PC-controlled electric cylinder. In order to visualise the respective vortex structures, diluted fluorescein was added to the fluid through a circumferential slit of $w = 0.3$ mm width roughly $\Delta s = 30$ mm upstream of the nozzle. The dye particles were illuminated inside the respective symmetry planes of the outlets by means of a continuous-wave laser, and pictures were taken at a sampling rate of $f = 400$ Hz, capturing the process of vortex ring formation and propagation. The amount of added dye was controlled by adjusting the mounting height of the fluorescein reservoir. Since a compact test rig design was desired, the flow was redirected by 90 degrees between cylinder axis and outlet direction. As the subsequent tube was sufficiently long compared to the outlet dimensions, this had no apparent effect on the generated vortex rings that were generally symmetric and followed a vertical trajectory. It should be noted that the camera was rotated so that the propagation direction is from left to right in the images and movies presented in the following section.

The Reynolds number was kept constant at $Re = (d_{\mathrm{h}} u_{\mathrm{jet}})/\nu = 1900$ for all of the outlet geometries. It was based on the hydraulic diameters of the outlets d_{h} and the nominal jet velocity u_{jet} deduced from the piston velocity and the ratio of tube to outlet area $A_{\mathrm{piston}}/A_{\mathrm{out}} \approx 6.4$. An impulsive velocity program with a piston acceleration of $|\mathrm{d}u/\mathrm{d}t| \approx 5$ m/s^2 was applied and a rotary encoder was used to monitor the accurate piston advance.

3. Results

This section is structured as follows: first, we address the structure and motion of vortex rings associated with non-parallel planar starting jets, comparing them to steady planar jets and vortex rings produced by parallel starting jets discussed in the literature. Then, we analyse the vorticity flux and entrainment characteristics to identify characteristic formation time scales associated with maximum vortex ring circulation. This quantity is then reassessed by reducing the supply pressure, hence decreasing the degree of non-
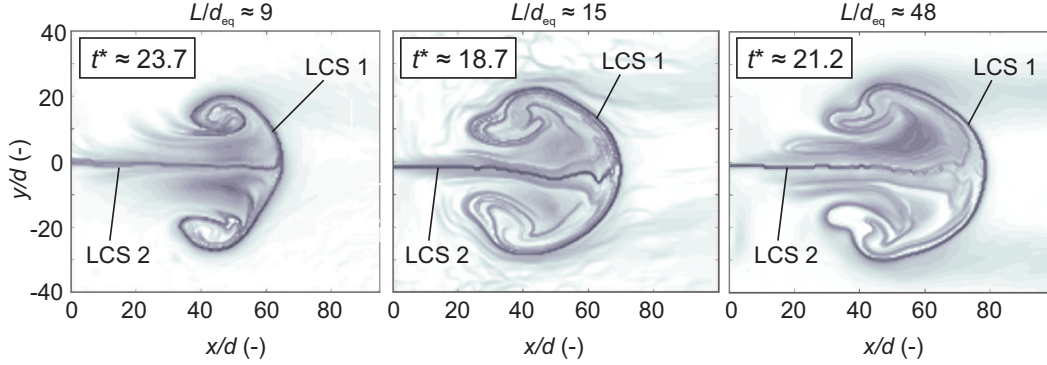
FIGURE 5. Dominant material lines revealed by FTLE fields in xy symmetry plane for different stroke ratios

parallel flow for two further configurations. Finally, we discuss flow visualisations of planar starting jets in a water tank where the effect of over-pressure is negligible.

3.1. *Appearance and propagation of vortex rings generated with PJA*

Figure 5 shows representative FTLE distributions associated with the vortex rings inside the symmetry plane at $z = 0\,\mathrm{mm}$. All three configurations are characterised by two dominant material surfaces, LCS 1 and 2. The first marks the propagation front of the jets and reflects the interface between the vortex ring and ambient fluid. It indicates the regions of locally maximum shear stresses due to high velocity gradients. The trailing sides of the vortex rings are not closed by this material surface, however. Instead, it extends inside the vortex ring, mapping the radial entrainment through the leeward side of the rings. This radial entrainment is enhanced by the second significant material surface - a horizontal layer on the centreline. The vortex ring generated with the smallest stroke ratio is clearly smaller in size from a Lagrangian perspective. In particular, the axial extent is significantly smaller than for the other pulse widths. Comparing the two larger stroke ratios, vortex rings of similar dimensions are created, indicating that the stroke ratio only influences the structure of the vortex ring as long as a certain threshold is not surpassed.

A further qualitative overview of the produced vortex rings is given in figure 6 where 3D iso-contours in the FTLE distribution are shown for the three stroke ratios at $t \approx 1.33\,\mathrm{ms}$. The respective non-dimensional formation times are indicated in the figure with the stroke ratio reflecting the nominal duration of jet emission. Hence, the jet emission has stopped for the small and medium stroke ratio whereas it is still ongoing for $L/d_{\mathrm{eq}} \approx 48$ at the depicted time instances.

Interestingly, all three vortex rings resemble spheroids characterised by a hole centred around the vortex core rotational axes. For the smallest stroke ratio $L/d_{\mathrm{eq}} \approx 9$, the vortex ring undergoes a rapid expansion in y direction whereas the other dimension appears to be slightly contracted. There is only a very minor trailing structure visible. Compared to the larger stroke ratios, the streamwise propagation appears to be small which will be addressed subsequently. When a stroke ratio of $L/d_{\mathrm{eq}} \approx 15$ is applied, the produced vortex ring is greater in size. The contraction close to the nozzle outlet is also less distinct, and a circular shape is apparent immediately as the vortex ring propagates with a greater mean velocity than for the lower stroke ratio. Even though a larger amount of fluid has been emitted for the greatest stroke ratio, there is no significant difference in terms of the vortex ring size compared to the medium stroke ratio. The
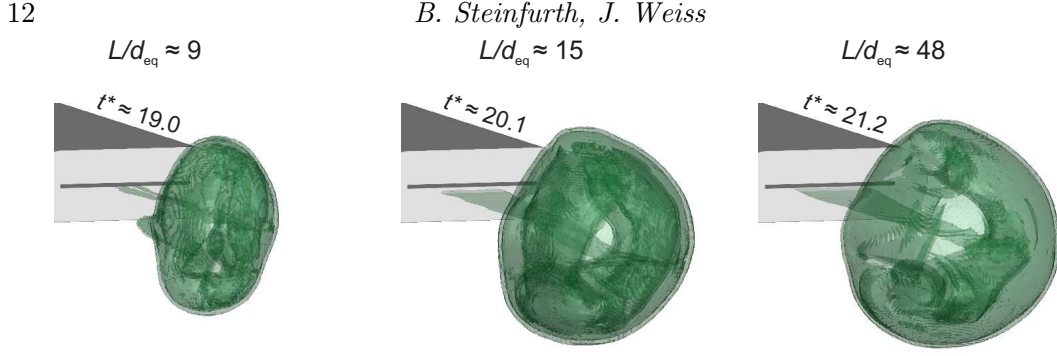
B. Steinfurth, J. Weiss

FIGURE 6. FTLE iso-contour of vortex rings associated with three investigated stroke ratios; slot-like jet outlet shown in the background for reference
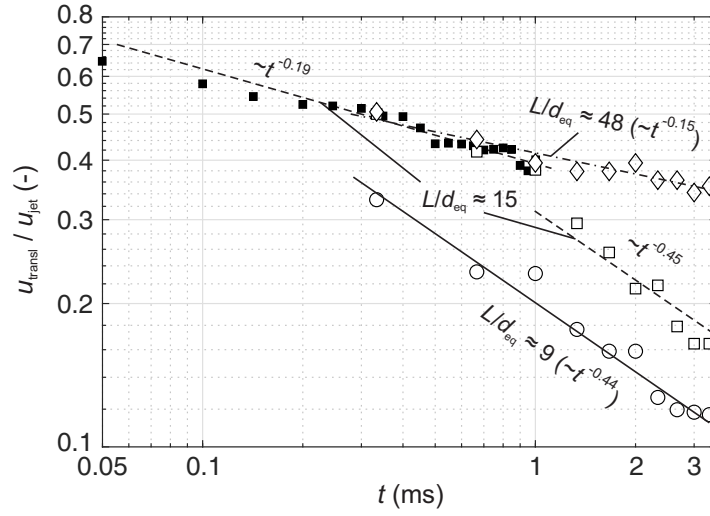

FIGURE 7. Translational velocity of vortex rings associated with different stroke ratios

distinct layer trailing the vortex ring corresponds to LCS 2 in figure 5 and points to a convergence of fluid towards the centreline of the jet.

In summary, the qualitative analysis has shown that the structure of all generated vortex rings is similar. However, the lowest stroke ratio yields a ring of significantly smaller dimensions while the diameter is almost equal for the other two configurations. We therefore assume that a characteristic formation time scale for vortex rings studied here lies in the range $L/d_{\mathrm{eq}} = 9\ldots15$. Before taking this hypothesis up in the next section, focus will be laid upon other characteristic properties of non-parallel planar starting jets.

In figure 7, the propagation speed of the vortex rings u_{transl} is shown with reference to the nominal jet velocity at the outlet. The translational velocity was deduced by evaluating the location of the jet propagation front on the centreline, marked by a ridge in the FTLE field, for successive time instances.

For all stroke ratios, a distinct deviation between jet outlet velocity and vortex ring propagation speed can be noticed with the latter amounting to roughly one third of the initial velocity for $L/d_{\mathrm{eq}} \approx 9$ and one half for $L/d_{\mathrm{eq}} \approx 15$ and $L/d_{\mathrm{eq}} \approx 48$ at $t \approx 0.33\,\mathrm{ms}$. For the medium stroke ratio, further measurements were conducted with a finer temporal resolution. Marked by filled symbols, they indicate that the translational velocity close

to the outlet is $u_{\text{transl}} \approx 0.65 u_{\text{jet}}$. Note that the axial velocity at $x \approx 2\,\text{mm}$ measured with HWA is $0.8 u_{\text{jet}}$ (figure 2).

Interestingly, the propagation speed of the vortex rings is clearly affected during the ongoing emission of fluid. Both the medium and the highest stroke ratio exhibit vortex rings whose translational velocities roughly follow a $-1/7$ power law decay initially. When the emission stops around $t = 1\,\text{ms}$ for $L/d_{\text{eq}} \approx 15$, the propagation speed drops abruptly and a $t^{-0.45}$ power law decay is observed thereafter. A decay of the same order of magnitude can be observed for the smallest stroke ratio even though the normalised velocity is much smaller. As for the greatest stroke ratio, no velocity data is available after the emission process has stopped since the vortex ring has already left the measurement domain by that time.

In the work of Maxworthy (1972), a -1 power law decay is predicted for vortex rings generated with circular outlets. However, this was not validated empirically by Dabiri & Gharib (2004) who reported an exponent of about $-1/3$. Compared to the latter value, the rate of velocity decay observed during the diffusive entrainment process in this study is larger. The discrepancy may be linked with the differences in the experiments, namely the outlet geometry and the significant over-pressure in the jet exit plane of the non-parallel jets studied here. It is conceivable that the initial transverse acceleration is accompanied by a smaller self-induced translational speed as noted by Afanasyev (2006). In his study of vortex dipoles generated with two-dimensional outlets, a very slow propagation is reported for small formation times. Once a characteristic *startup time* is reached, the vortex dipoles start translating with a larger, almost constant velocity of $u_{\text{transl}} \approx 0.5 u_{\text{jet}}$. A similar increase in velocity cannot be attested in our experiment as the propagation speed decreases monotonically. However, we also observed that the majority of jet expansion occurs at very small formation times as will be addressed in the following.

To estimate the spatial spreading rates of the non-parallel starting jets, the half width in both transverse directions was calculated, i. e. the transverse distance where the mean axial velocity $\bar{u}$ reaches half the mean centreline velocity. The mean value between positive and negative direction for $y_{1/2}$ is shown in figure 8 and the positive direction was chosen for $z_{1/2}$ - note that the velocity field was assumed symmetric in z direction.

Along the larger dimension of the slot-like outlet (z direction), the half widths do not exceed the extent of the jet orifice initially with values of $z_{1/2} \approx 10d$ found at an outlet distance of $x/d = 40$. For jets associated with the larger stroke ratios, an average expansion with a rate of roughly $s_z = (\text{d}z_{1/2})/(\text{d}x) = 0.12$ ensues. Interestingly, the smallest stroke ratio yields a significantly greater spatial expansion rate of $s_z \approx 0.18$ initially. Then, an abrupt reduction of the half width by $\Delta z_{1/2} \approx 4d$ follows before a decreased spreading rate appears for the remainder of the observation domain. This behaviour is largely in agreement with the vortex ring revealed by the FTLE field in figure 6 which appears to be contracted along the z direction at first.

As for the y direction, i. e. along the smaller dimension of the outlet, a rapid expansion can be observed up to an outlet distance of $x/d \approx 80$ with initial spreading rates of $s_y \approx 0.2$ for the two smaller stroke ratios and $s_y \approx 0.16$ for the largest stroke ratio respectively. Further downstream, a similar development of the half width can be observed. After reaching a value of about $20d$, only a minor expansion of the jet follows. Finally, spreading rates of $s_y \approx 0.11$ are found at $x/d > 140$.

To summarise, the non-parallel starting jets studied here differ from the conventional steady planar jet in that they do not spread linearly at a constant rate. Instead, a rapid increase of the half width along the smaller dimension of the outlet can be observed
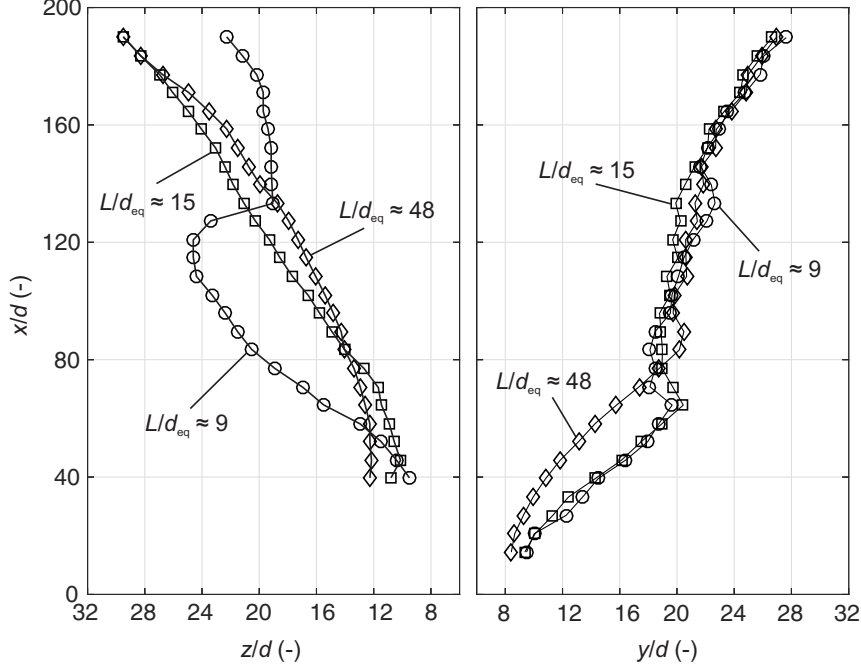
B. Steinfurth, J. Weiss

FIGURE 8. Jet half width of non-parallel starting jets for different stroke ratios evaluated in both transverse directions

which may be caused by the transverse advection of fluid due to over-pressure during jet initiation. Further downstream, i.e. at larger formation times, a moderate growth rate is assumed. During both phases, the spreading rate is greater than for steady planar jets which is reported to be of the order of $s_y \approx 0.1$, e. g. by Bradbury (1963), Knystautas (1964) or Gutmark & Wygnanski (1976). This deviation is explained by the high degree of non-parallel flow characterising the starting jets in the current study.

3.2. Entrainment characteristics and development of vorticity fields

To estimate the entrainment of surrounding fluid, the growth of the vortex rings is evaluated. Their boundaries are, however, not well defined. Therefore, the reference frame is changed by superimposing the velocity field with the axial velocity found at the locations of maximum vorticity. This method was previously used by Dabiri & Gharib (2004) and Sau & Mahesh (2007). The cross-sections of the resulting vortex bubbles inside both symmetry planes are displayed in figure 9.

At the first time step, the vortex rings exhibit a transverse extent 40 times the outlet width. This is consistent with the rapid initial jet spreading rate discussed previously. As a result, almost spherical vortex ring shapes characterised by thick cores are observed. Between the first and the second time step, a smaller increase in transversal growth can be noted in comparison. The smallest vortex ring ($L/d_{eq} \approx 9$) shows a significant contraction in longitudinal direction as the respective dimension is only about half the length of the virtual emitted fluid column.

As indicated in the figure, an ellipsoid fit is used to approximate the volumes of the three vortex bubbles Ω_B. This quantity is compared to the nominal volume of fluid Ω_N that has been emitted over time to derive the entrainment fraction

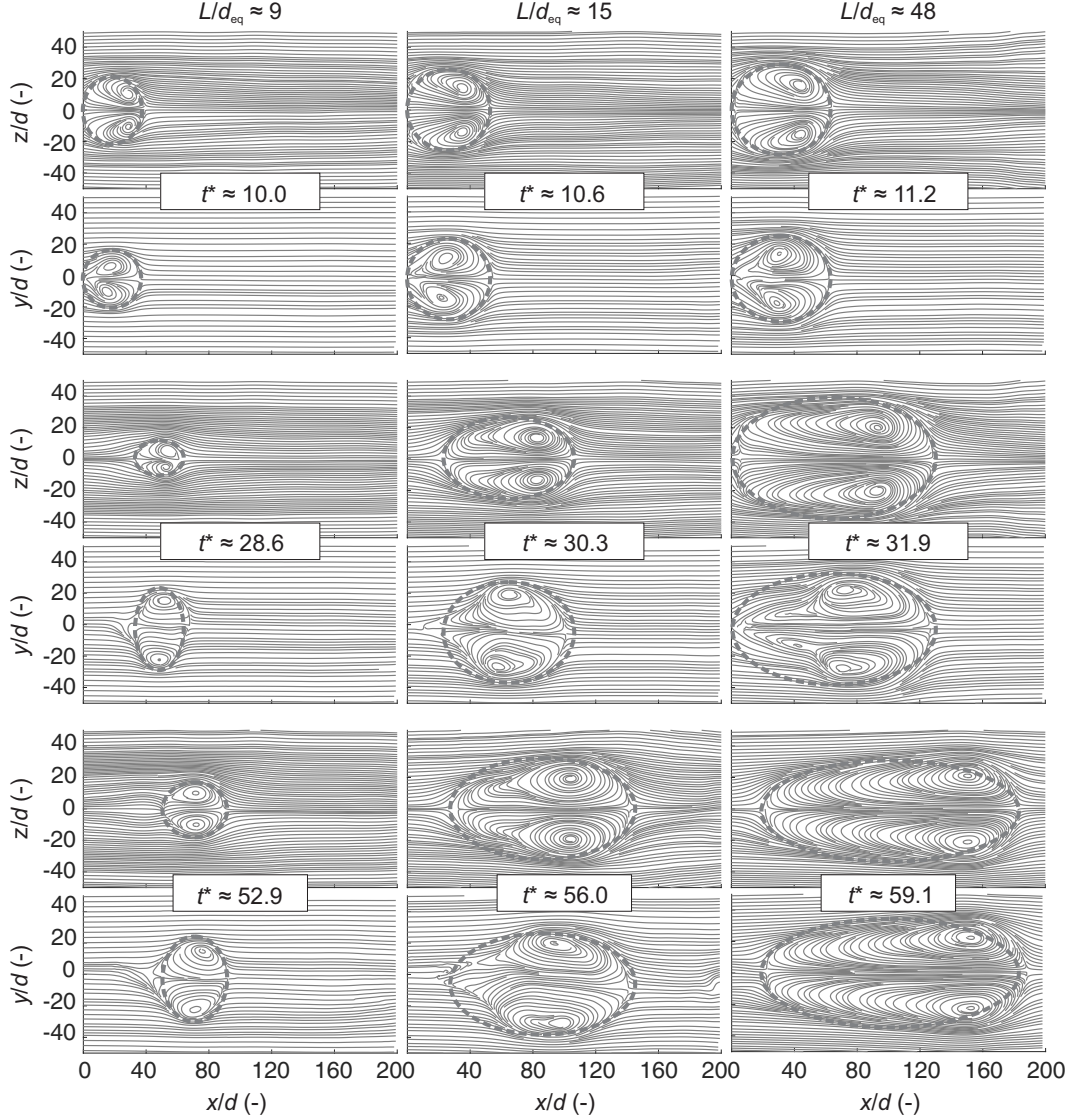$$\eta(t) = (\Omega_B - \Omega_N)/\Omega_B. \tag{3.1}$$

FIGURE 9. Streamlines of velocity field superimposed with constant velocity found at location of maximum vorticity revealing vortex bubbles associated with different stroke ratios; ellipsoid fit used for computation of vortex bubble volume highlighted by dashed lines

Compared to rings produced by parallel starting jets with typical entrainment fractions in the range of $\eta = 0.3 \ldots 0.4$ (Müller & Didden (2004); Dabiri & Gharib (2004)), the non-parallel starting jets appear to entrain significantly more ambient fluid (figure 10).

The calculated entrainment fractions are of the order of $\eta \approx 0.90 \ldots 0.91$ ($L/d_{\mathrm{eq}} \approx 9$) and $\eta \approx 0.96 \ldots 0.97$ ($L/d_{\mathrm{eq}} = 15, 48$). In other words, the non-parallel jets entrain an amount of fluid about 10 or more than 20 times their own volume respectively. This is about an order of magnitude greater than for parallel starting jets. Considering the outlet geometry, the most drastic expansion of the vortex bubbles takes place along the smaller dimension. As indicated in figure 8, the vortex rings are almost axisymmetric for the two greater stroke ratios. This is reflected by the dimensions of the vortex bubbles that are of similar order in both transverse directions. Therefore, an almost uniformly distributed radial entrainment can be expected. It is also apparent that the
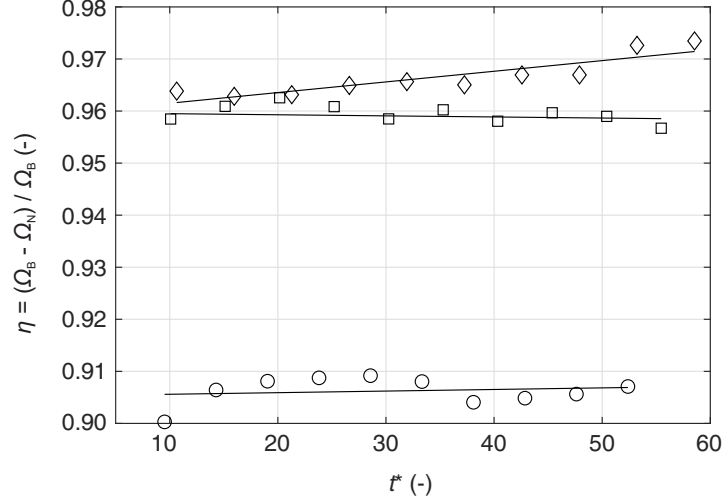
B. Steinfurth, J. Weiss

FIGURE 10. Entrainment fraction of vortex rings associated with different stroke ratios
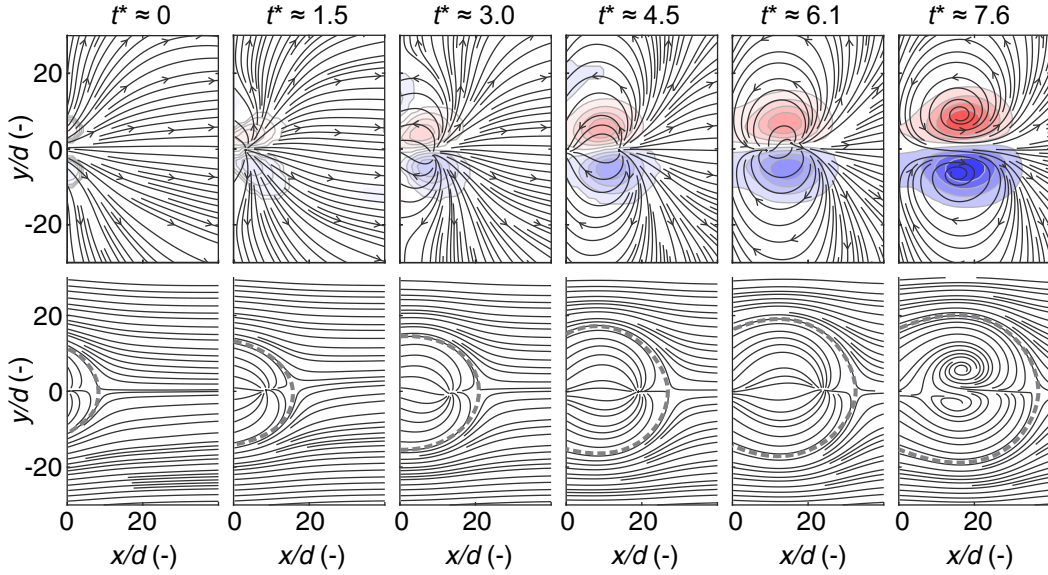

FIGURE 11. Vorticity fields and velocity field information during initiation of jet emission (top row) and vortex bubbles at the same time instances (bottom row)

early formation phase of the vortex rings is majorly responsible for this effect.

To investigate the early entrainment mechanisms in more detail, further measurements with a finer temporal resolution were conducted for the medium stroke ratio. Since the pressure and velocity information inside the nozzle exit plane were similar for the other stroke ratios during the initiation of fluid ejection, the results depicted in figure 11 are transferable to these configurations.

Directly following the onset of fluid ejection ($t^* \approx 0$), vorticity is advected in transverse direction and a vortex bubble extent of about $30\,d$ is found. For the next depicted time step ($t^* \approx 1.5$), the developing vortex ring cross-sections are aligned with the outward directed instantaneous streamlines as the transverse expansion continues. The vortex ring then continues to absorb vorticity but the growth of the vortex bubble in transverse direction is small in comparison to preceding time steps. Hence, the largest entrainment
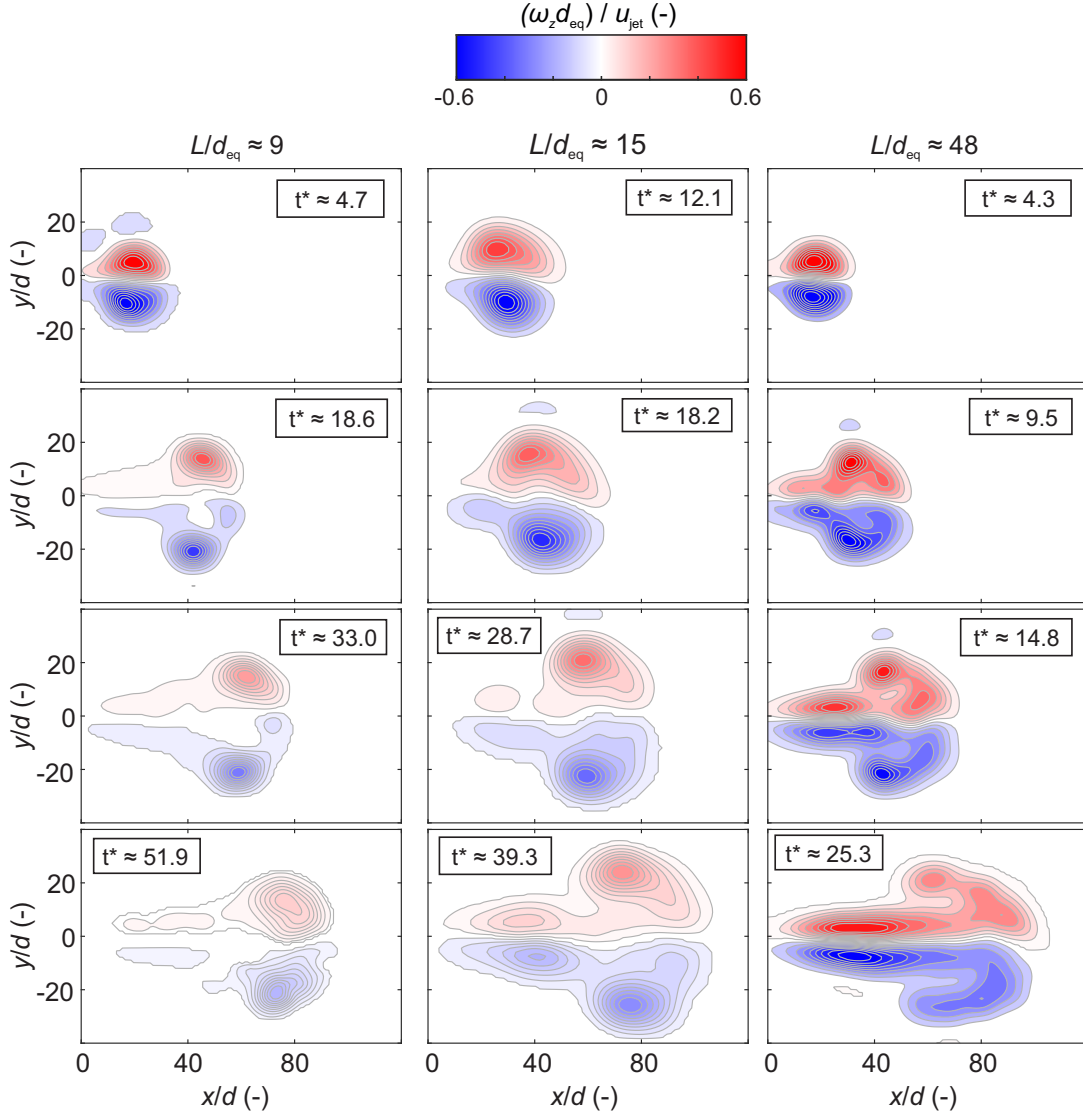
FIGURE 12. History of vorticity fields for non-parallel planar starting jets generated with different stroke ratios

rate can be expected at small formation times up to $t^* \approx 5$, i.e. during the early part of fluid emission. This corresponds well with the initial pressure rise and the resulting development of velocity gradients shown in figures 2 and 3. It is worth noting that the vortex rings are still in close proximity to the outlet for this time span due to their low translational velocity similar to the experiments performed by Afanasyev (2006).

This contrasts with investigations of compressible vortex rings reported by Arakeri *et al.* (2004) where the roll-up process is associated with much larger time scales than the initial pressure peak. It is therefore conceivable that the extent of non-parallel flow has a more distinct influence on the vortex ring formation in the current study.

Next, we evaluate the subsequent vorticity fields generated with the three stroke ratios (figure 12).

For the first displayed time step, the entire vorticity is located inside the vortex ring for all configurations. This is significant because the formation time scale introduced by

Gharib *et al.* (1998) is surpassed at that stage. Fluid is still emitted for all cases but no trailing jet structure is observed. During the second time step, the fluid ejection is only ongoing for the largest stroke ratio. It is interesting to note that small amounts of fluid are apparently detrained from the rear stagnation point for the smaller stroke ratios as minor trailing jets begin to develop. This process continues subsequently as the circulation of the vortex ring decreases. As for the largest stroke ratio, a trailing jet is formed already during jet emission and there is a distinct interaction between this flow feature and the vortex ring, causing the latter to become distinctly distorted by the last depicted time step.

Notably, once a trailing jet occurs, there is no clear separation between this jet and the vortex ring for any of the investigated stroke ratios, i.e. no pinch-off is observed as for circular or elliptic starting jets reported by Gharib *et al.* (1998) and O'Farrell & Dabiri (2014) respectively. This was ascertained previously by Pedrizzetti *et al.* (2010) and Afanasyev (2006), studying vortex dipoles generated by planar starting jets. However, the nature of the interaction between trailing jet and vortex ring appears to be fundamentally different in the current study as the entire vorticity is absorbed by vortex rings initially before being detrained into a trailing jet. In previous studies of rectangular starting flows, it is the trailing jet that feeds the vortex ring during their interaction. We discuss this interesting observation in more detail below.

3.3. *Development of circulation for $L/d_{eq} \approx 15$*

In the following, we focus on the time-resolved generation of circulation for the medium stroke ratio $L/d_{eq} \approx 15$ (figure 13). Similar characteristics can be expected for the smallest stroke ratio based on the vorticity contour fields shown in figure 12, whereas a strong distortion occurs for the largest stroke ratio, complicating a clear distinction between flow structures, namely the leading vortex ring and the trailing jet.

The circulation was obtained by integrating the vorticity field for the upper half plane where $y/d > 0$ and inside the boundaries of a reasonable contour level which was defined to be $\omega_{z,thresh} = 200\,\mathrm{s}^{-1}$. In the presence of a trailing jet structure, the vorticity associated with the vortex ring and the trailing jet were not readily separable. As an intuitive measure, the defining ridge in the FTLE distribution was therefore used and extended on the trailing side to define the integration domain. Thus, the total induced circulation can be compared to the circulation associated with the vortex ring. The slug model prediction for the total circulation $\Gamma_{sm} = \frac{1}{2}t_p u_{jet}^2$ is highlighted by a red dashed line in figure 13.

The measured circulation is proportional to the formation time t^*, and a maximum of $\Gamma/(u_{jet}d_{eq}) \approx 8.6$ is reached around $t^* \approx 20$, i.e. after the nominal end of the jet emission at $t^* = L/d_{eq} \approx 15$. This is consistent with velocity measurements shown in figure 2, indicating a decreasing axial velocity after this time instance. Note that the total circulation predicted by the slug model $\Gamma_{sm}/(u_{jet}d_{eq}) \approx 7.6$ is exceeded by about 13%. This is explained by the non-parallel flow condition enhancing the vorticity flux. However, a rapid increase in circulation can be expected for small formation times based on pressure measurements where an initial peak of large magnitude observed (figure 2). This is not reflected in PIV data that indicate a relatively small rate of change of circulation for $t^* < 3$. There are two explanations. First, the axial jet velocity determining the vorticity flux is zero for $t^* \approx 0$ and only reaches a maximum after an initial acceleration phase. Second, and perhaps more importantly, the measured vorticity is underestimated as explained in section 2.1.2 and also observed in the vorticity fields for small formation times shown in figure 11. The corresponding region characterised by a smaller circulation flux is highlighted by a shaded background in figure 13. This experimental limitation does
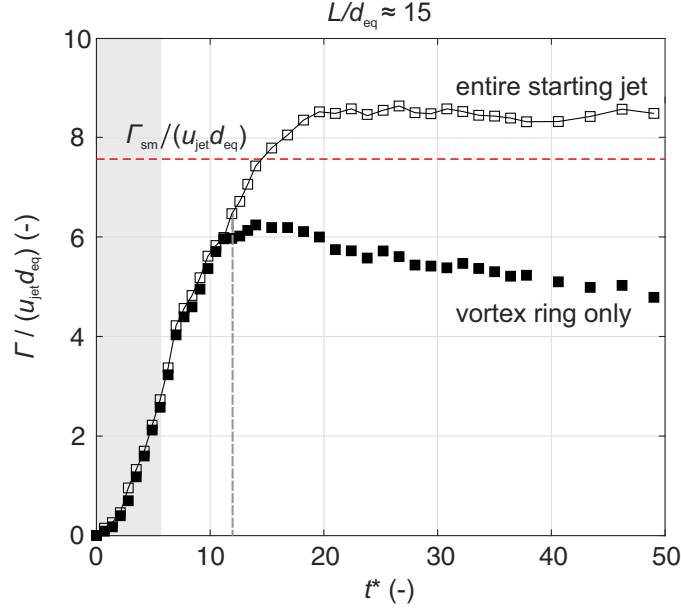
FIGURE 13. Circulation associated with entire starting jet (open symbols) and vortex ring (closed symbols) over time for $L/d_{eq} \approx 15$; total normalised circulation estimated by slug model highlighted by red horizontal; characteristic time scale associated with initiation of trailing jet highlighted by grey vertical

not affect our main conclusions found at larger formation times where the majority of vorticity is in greater distance to the outlet and the circulation predicted by the slug model is surpassed.

Initially, the entire vorticity is found inside the leading vortex ring indicated by almost equal values for the circulation of the entire starting jet (open symbols) and the vortex ring (closed symbols). This is in agreement with vorticity contour maps where no trailing jet is observed at that stage (figure 12). Around a non-dimensional formation time of $t^* \approx 12$ (grey vertical), no further increase of the vortex ring circulation can be noted although fluid is still emitted. Instead, the vortex ring circulation stagnates before decreasing for the remainder of the observation time. Contrarily, the entire circulation remains at an almost constant level. This suggests that vorticity of the vortex ring is indeed continuously fed into a trailing jet as indicated in figure 12. This is in strong contrast to steady vortex rings studied by Gharib *et al.* (1998) that exhibit almost constant circulation levels after pinch-off.

3.4. *Influence of over-pressure effects*

In the following, we examine the hypothesis that the specific behaviour discussed in the previous section is related to the degree of non-parallel flow driven by over-pressure in the nozzle exit plane. For this purpose, two further starting jet configurations were investigated where the supply pressure was varied at a fixed valve opening time of $t_p = 1\,\mathrm{ms}$, the same as for the medium stroke ratio of $L/d_{eq} \approx 15$. As a result, the jet velocity, stroke ratio and maxima in the pressure signal decreased (figure 14).

Recall that the normalised over-pressure maximum for the medium stroke ratio case so far was $\Delta p_{norm} \approx 1.2$ (see figure 2). In contrast, the initial peak for the further configurations is significantly decreased to $\Delta p_{norm} \approx 0.1$ and $\Delta p_{norm} \approx 0.06$ respectively. As a result, the over-pressure term contributing to the circulation generation (equation
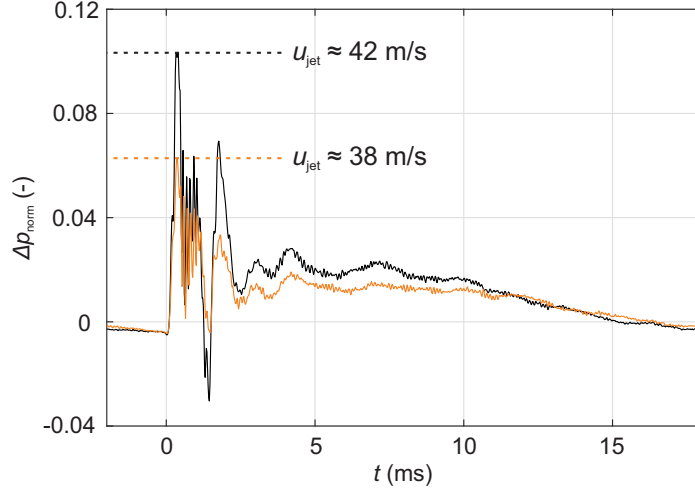
B. Steinfurth, J. Weiss

FIGURE 14. Pressure signals for two configurations with varied supply pressure at $(x, z) = (-2, 0)$ mm (compare with figure 2)
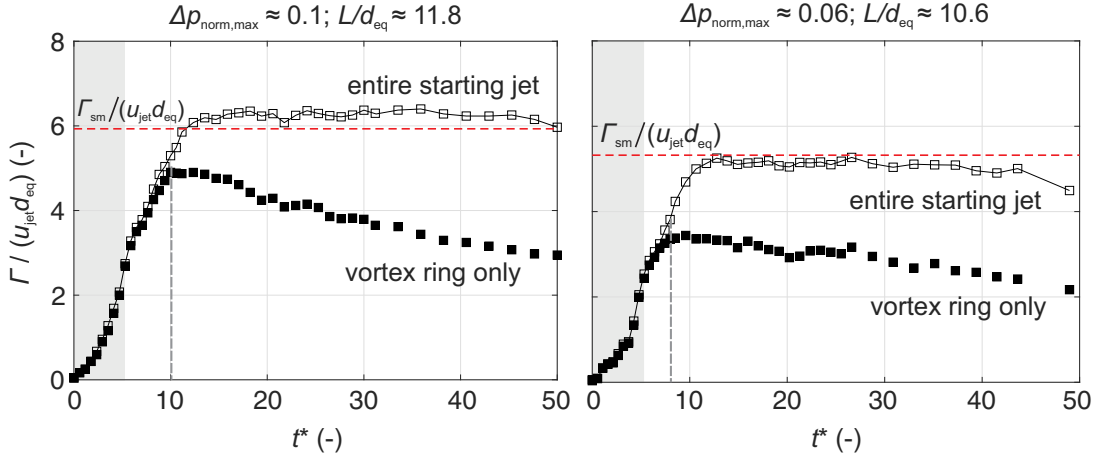

FIGURE 15. Produced circulation over time for cases of decreased over-pressure peak; distinction is made between vortex ring (closed symbols) and entire starting jet (open symbols)

1.4) decreases.

Analogous to the analysis in the previous section, the circulation was computed for these two configurations, see figure 15.

The qualitative behaviour is very similar to that of starting jets associated with larger over-pressure as the vortex ring incorporates the entire circulation initially and sheds a trailing jet by detraining excessive vorticity after a maximum is reached. Crucially, the measured circulation maximum is only 8% larger and on the order of the value predicted by the slug model for a reduced pressure peak of $\Delta p_{\mathrm{norm,max}} \approx 0.1$ and $\Delta p_{\mathrm{norm,max}} \approx 0.06$ respectively. Recall that the circulation for the largest supply pressure was under-predicted by 13%. This is in line with considerations given by Krueger (2005), arguing that an increased magnitude in over-pressure extends the underprediction by the slug model.

Furthermore, the formation time corresponding to the initiation of a trailing jet is systematically decreased as values of $t^* \approx 10$ and $t^* \approx 8$ are found for $\Delta p_{\mathrm{norm}} \approx 0.1$ and $\Delta p_{\mathrm{norm}} \approx 0.06$ respectively. As the characteristic formation time was of the order

Non-linear stability analysis
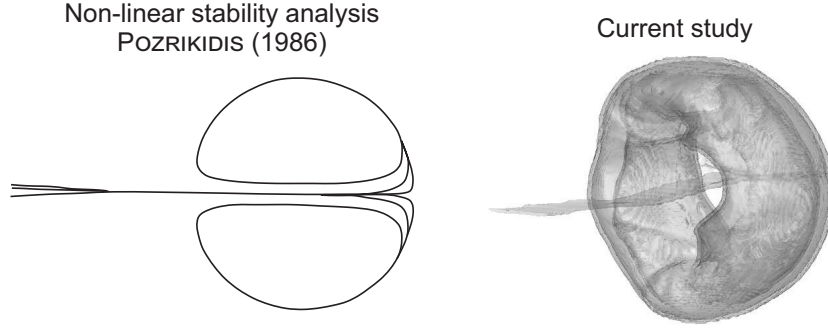Pozrikidis (1986)

Current study

Figure 16. Left: Vortex ring with small oblate perturbation (based on depiction by Pozrikidis (1986)); right: FTLE iso-surface of vortex ring generated with non-parallel planar starting jet at $L/d_{\mathrm{eq}} \approx 15$

of $t^* \approx 12$ for the case of the largest over-pressure peak, the degree of non-parallel flow appears to have a significant influence on the maximum circulation the vortex rings can absorb.

In establishing a formation number for circular parallel starting jets, Gharib *et al.* (1998) reference the stability analysis conducted by Pozrikidis (1986) supporting their finding that excessive vorticity is detrained from the rear stagnation point of the vortex ring. As a consequence, it remains axis-touching or returns to a steady axis-touching state. Clearly, this mechanism is not applicable to the vortex rings resulting from non-parallel starting jets studied here. They may be axis-touching during the initial formation stage but the vorticity peaks subsequently move apart due to a rapid transverse expansion and an ongoing interaction with a trailing jet (figure 12). The resulting vortex shape resembles a flatter spheroid with a hole, an appearance also observed by Pozrikidis (1986) - and also by Moffatt & Moore (1978) - when the vortex ring is subjected to axisymmetric oblate perturbations. For this case, excessive vorticity is also accumulated in a 'vortex tail'. This is in remarkable agreement with the vortex ring shapes observed in this study (figure 16). We therefore assume that the transverse acceleration of fluid, i.e. non-parallel flow, induces oblate perturbations whereas parallel or weakly non-parallel flow studied previously forces the vortex ring to become a prolate spheroid.

Given the larger diameter of the oblate vortex rings that is increased due to the lateral growth caused by over-pressure, the impulse $I = I(r^2)$ is larger than for prolate vortex rings. In addition, the circulation is increased compared to vortex rings generated with parallel starting jets as addressed previously. This suggests that the dimensionless energy α (equation 1.3) is smaller in comparison as the product of circulation and impulse $\Gamma^{3/2} I^{1/2}$ is increased to a greater extent than the kinetic energy $E = E(r)$. This estimation is supported by models for the invariants of motion for non-parallel starting jets supplied by Krieg & Mohseni (2013).

The non-dimensional energies of the studied vortex rings generated with varied supply pressure are shown in figure 17. The invariants of motion were obtained by area integration inside the xy symmetry plane based on phase-locked PIV measurements:
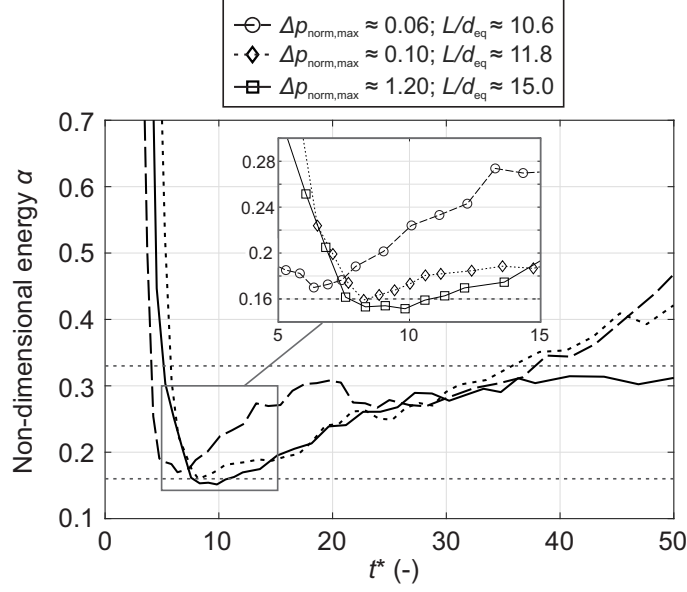
B. Steinfurth, J. Weiss

FIGURE 17. Dimensionless energies of vortex rings generated with different supply pressure; horizontals for limiting energy $\alpha_{\mathrm{lim}} = 0.33$ found by Gharib *et al.* (1998) as well as theoretical value for Hill's spherical vortex $\alpha = 0.16$ shown for reference

$$\Gamma = \int\limits_0^{x_\infty} \int\limits_0^{y_\infty} \omega\,\mathrm{d}y\mathrm{d}x;\ I = \varrho\pi \int\limits_0^{x_\infty} \int\limits_0^{y_\infty} \omega y^2\,\mathrm{d}y\mathrm{d}x;\ E = \varrho\pi \int\limits_0^{x_\infty} \int\limits_0^{y_\infty} (u^2 + v^2)\,\mathrm{d}y\mathrm{d}x. \qquad (3.2)$$

During the initial formation process, the non-dimensional energy drops as thicker vortex ring cores are rapidly generated. Slightly preceding the respective moments where maximum circulation is reached, the energy falls below the limiting value of $\alpha_{\mathrm{lim}} = 0.33$ reported by Gharib *et al.* (1998) around a formation time of $t^* \approx 5$. Subsequently, minima in vortex ring energy are reached. The configuration of largest over-pressure yields the smallest vortex ring energy of $\alpha \approx 0.15$, i.e. the thickest ring core. In comparison, slightly larger minimum energies of $\alpha \approx 0.16$ and $\alpha \approx 0.17$ are found for the other configurations. While these differences are relatively small, it is important to note that there is a clear tendency as vortex ring energies increase with reduced peaks in over-pressure. In other words, a larger over-pressure level yields a thicker vortex ring core. It should be noted that the limiting member of the Norbury-Fraenkel family of vortex rings is characterised by a non-dimensional energy of $\alpha \approx 0.16$. All configurations reach values of this order before starting to increase, indicating that this is in fact the limiting energy applicable to the current setup. However, no constant value is assumed afterwards as was observed for the steady vortex rings investigated by Gharib *et al.* (1998). This may be due to an ongoing interaction between the vortex ring and the trailing jet.

Overall, the degree of non-parallel flow associated with a varied magnitude in over-pressure has a systematic effect on vortex ring properties. First, the circulation flux is enhanced. Second, the moment when vortex rings start to shed vorticity is shifted to larger formation times which results in larger circulation maxima when the supply pressure is increased. And third, while vortex rings studied here have similar minimum non-dimensional energies, there is a trend in that greater over-pressure causes vortex
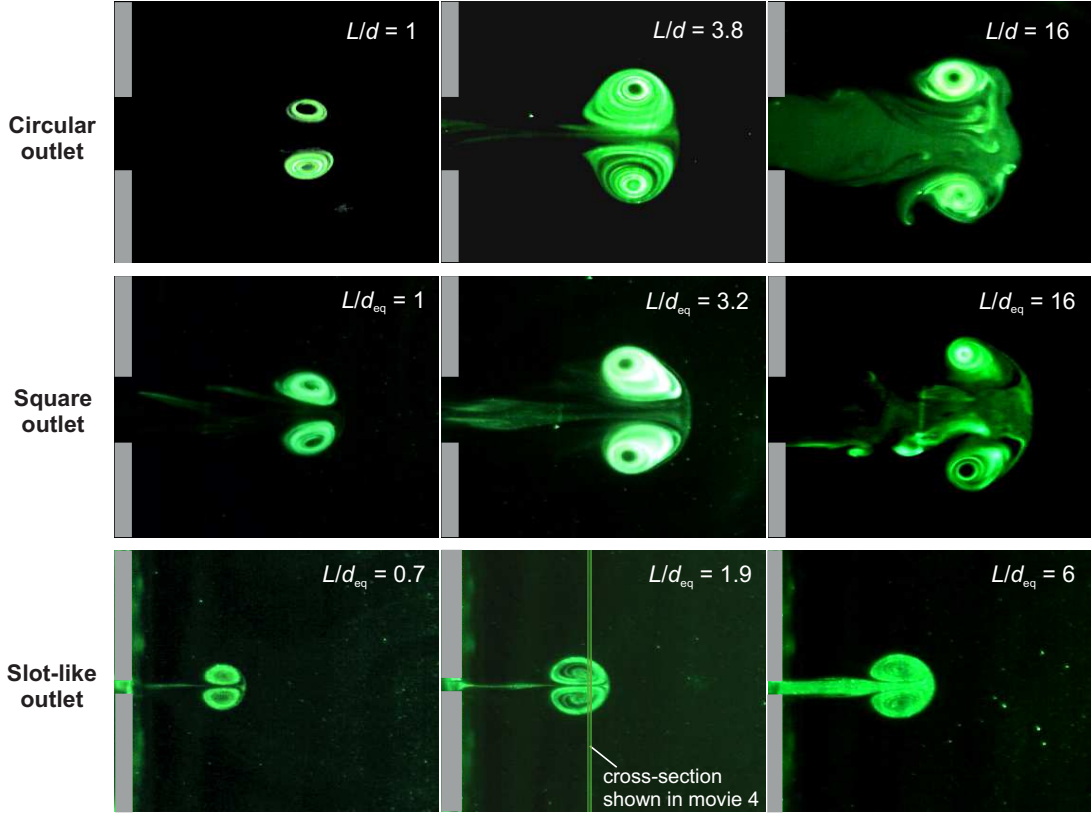
FIGURE 18. Flow visualisation of vortex rings generated with different outlet geometries; centre column shows vortex structures associated with characteristic formation time scale (Gharib *et al.* (1998)) yielding a vortex ring of maximum size without trailing jet whereas stroke ratio was set to lower and higher values for the pictures shown in left and right column respectively

rings with thicker cores.

3.5. *Parallel planar starting jets*

Finally, we shall validate that the effects discussed above are indeed caused by non-parallel flow and not by the specific outlet geometry that also differs from those usually studied in the literature. Using the experimental apparatus shown in figure 4, vortex rings were generated by emitting fluid columns in an impulsive fashion through outlets of different geometries into a water tank. Generating parallel starting jets, this setup was comparable to the ones used by Gharib *et al.* (1998) and others. The length of the fluid column was varied by changing the travel length of the cylinder, resulting in a large number of investigated stroke ratios. Figure 18 shows a selection of images that are relevant to the purpose of this discussion. Movies of the flow visualisations are provided with the supplementary material. Movie 1 contains recordings for the circular, movie 2 for the square and movie 3 for the slot-like outlet.

As for the circular starting jet, an individual vortex ring can be observed at small stroke ratios, e.g. $L/d = 1$. When increasing the stroke ratio, larger vortex rings are produced and the limiting case, i. e. the formation number, is in the region of $L/d = 3.8$ in our experiment. Hence, the results obtained with the current experiment are in good

agreement with the formation number for parallel circular starting jets $L/d \approx 3.6 \ldots 4.5$ established by Gharib *et al.* (1998).

Studying parallel starting jets emitted from a square orifice, small stroke ratios again result in individual vortex rings. The formation number for this scenario $L/d_{eq} \approx 3.2$ is slightly smaller than for the circular outlet. Furthermore, the vortex rings appear to be less stable and a sooner breakdown can be observed (movie 2).

The planar starting jets shown in the third row in figure 18 exhibit a comparable behaviour as the other parallel jets when the stroke ratio is varied. In contrast to the non-parallel starting jets addressed above, however, no circular vortex ring is produced. Instead, two parallel vortex tubes can be seen in movie 4 provided with the supplementary material showing the vortex dipoles generated with a stroke ratio of $L/d_{eq} \approx 1.9$ travel through the illuminated cross section at $x = 20\,\text{mm}$ highlighted in figure 18. This is in agreement with other studies of parallel planar starting jets, e.g. by Afanasyev (2006) or Das *et al.* (2013). Accordingly, the transverse dimension of vortex dipoles is only four to five times the outlet width whereas a diameter of $40\,d$ was observed for the vortex rings associated with non-parallel starting jets. The vortex tubes in our experiment reach a maximum diameter for $L/d_{eq} \approx 1.9$, i.e. half the value found for the circular outlet. This can be explained by the fact that the outlet width decreases for greater outlet aspect ratios at a given equivalent diameter d_{eq}. As the vortex dimension is proportional to the outlet width for parallel jets, this leads to a smaller formation number.

To summarise, the flow visualisations indicate that the specific behaviour observed for the vortex rings generated with pressurised air is indeed linked with the non-parallel flow condition and not with the slit-shaped outlet geometry.

4. Conclusions

The focus point of this study were starting jets generated with a device typically employed in AFC applications, ejecting defined amounts of compressed air as a mechanical valve is periodically opened for relatively small pulse durations. This specific flow configuration is characterised by two major differences compared to starting jets addressed in the majority of previous studies. First, the outlet geometry is not circular but slit-shaped and has an aspect ratio of $l/d = 40$. Second, the non-dimensional over-pressure during jet initiation is about an order of magnitude larger than for starting jets produced with a classical piston-cylinder setup reported by Krieg & Mohseni (2013) for instance. Therefore, the influence of over-pressure during the early vortex ring formation phase is much more distinct in the current study, initiating a strong transverse acceleration of fluid, i.e. highly non-parallel flow.

Two major objectives were addressed in investigating this flow: (1) reveal the properties relevant to AFC applications and compare them to previous studies of starting flows, (2) examine the hypothesis that the concept of a universal formation time scale applicable to parallel circular starting jets introduced by Gharib *et al.* (1998) can be extended to this particular flow configuration.

A significant transverse advection of fluid was observed close to the jet outlet. This was reflected in initial spreading rates up to $s_y \approx 0.2$ along the smaller dimension of the outlet, i.e. about twice the value for steady planar jets reported by Bradbury (1963) or Gutmark & Wygnanski (1976). Given these large spreading rates, almost spherical vortex rings with a diameter about 40 times the slot width were found despite the high-aspect ratio outlet geometry. This is explained by an enhanced vorticity flux previously

observed for impulsively initiated starting jets, e.g. by Didden (1979) or Krieg & Mohseni (2013) and is directly relatable to over-pressure inside the jet exit plane associated with the rapid acceleration of fluid as noted by Krueger (2005). In the current study, the over-pressure occurs for a long duration relative to the formation process of up to $t^* \approx 5$. The produced vortex rings are located close to the outlet for this duration, directly absorbing the enhanced vorticity flux which leads to a very large expansion of vortex rings for small formation times. This contrasts with experiments of compressible vortex rings generated with an open shock tube performed by Arakeri *et al.* (2004) where a similar over-pressure peak occurs but in that case, it is associated with much smaller time scales than the vortex sheet roll-up process. In the current study, the propagation during the initial pressure rise is smaller which may be ascribed to the outlet geometry as similar observations regarding the competing effects of expansion and translation were made by Afanasyev (2006), also studying two-dimensional starting jets. However, the over-pressure in his experiment was assumedly negligible. Hence, only a roll-up of parallel vortex tubes was observed, agreeing well with flow visualisations inside a water tank conducted in the current study where a transverse dimension of vortex dipoles less than 5 outlet widths is noted.

The rapid expansion is associated with very large entrainment rates up to $\eta \approx 0.97$, indicating that the starting jets are capable of entraining an amount of fluid about 20 times their own volume. Typical entrainment rates for parallel starting jets, on the other hand, are in the range $\eta = 0.3 \ldots 0.4$ (Dabiri & Gharib (2004)).

Considerable proof has also been presented that the applied over-pressure has a drastic effect on characteristic time scales applicable to the starting jets in the current article. Vortex rings were shown to gather circulation beyond the universal formation time $t^* \approx 4$ introduced by Gharib *et al.* (1998). Depending on the magnitude of over-pressure, circulation was accumulated inside the leading vortex ring up to $t^* \approx 8$ ($\Delta p_{\mathrm{norm,max}} \approx 0.06$) or even $t^* \approx 12$ ($\Delta p_{\mathrm{norm,max}} \approx 1.2$). Considering that the circulation flux was also increased by the extent of over-pressure, larger maxima in normalised vortex ring circulation were observed when the supply pressure was increased. Thus, the circulation predicted by the slug model was exceeded by as much as 13%.

In contrast to previous studies of circular or elliptic starting jets reported by Gharib *et al.* (1998) and O'Farrell & Dabiri (2014), no clear separation between the leading vortex ring and a trailing jet was observed. This is consistent with investigations of two-dimensional starting jets summarised by Pedrizzetti *et al.* (2010). Afanasyev (2006) observed that an ongoing interaction between the trailing jet and the vortex ring causes the latter to absorb vorticity beyond the characteristic formation time of $t^* \approx 4$. However, a fundamentally different mechanism was noted in the current study as a trailing jet only developed after a pressure-dependent maximum in vortex ring circulation was achieved. This is enabled by a persistent shedding of vorticity as the vortex ring reaches states of ever thinner cores. We attribute this to an overshoot in vortex ring energy, roughly coinciding with the time instance of maximum circulation. Here, an energy close to or even below the characteristic value of $\alpha \approx 0.16$ attributed to Hill's spherical vortex was measured. While the differences in non-dimensional energy were relatively small when the magnitude in over-pressure was varied, we still observed a tendency of larger over-pressure yielding a thicker vortex ring core. Following this overshoot in non-dimensional energy, vorticity is detrained. It is worth noting that this was also observed by Moffatt & Moore (1978) and Pozrikidis (1986), investigating perturbations applied to Hill's spherical vortex. The current work may therefore in some ways be seen as the experimental pendant to previous stability analyses. Furthermore, Gharib *et al.* (1998) reported a similar overshoot. However, this was not explicitly achieved by the magnitude in over-

B. Steinfurth, J. Weiss

pressure but by the merging of two vortex rings. Then, a larger vortex ring develops before shedding vorticity and reaching a stable state associated with a limiting non-dimensional energy of $\alpha_{\mathrm{lim}} \approx 0.33$ that was specific to their apparatus. Such a constant energy level was not observed in the current study as the vortex ring energy continuously increased inside the observation domain. This may be explained by the absence of a pinch-off and the unsteady character of interaction between vortex ring and trailing jet.

Therefore, the concept of a characteristic formation number introduced by Gharib *et al.* (1998) cannot be extended to the specific flow configuration investigated in the current article. No pinch-off between vortex ring and trailing jet is observed, and the formation time associated with maximum circulation can be changed by varied boundary conditions, namely the magnitude of over-pressure.

Nonetheless, our findings have some implications for AFC applications where vortex rings are generated with a method similar to the one used in this study.

First, the knowledge regarding the reported formation mechanisms enables an efficiency optimisation. Considering that the mixing effectivity is mainly determined by the leading vortex ring associated with a starting jet, the pulse width for a given outlet velocity can be adjusted so that this structure is exclusively generated. Beyond a certain pulse width, a trailing structure is not only indirectly formed by vorticity shed from the vortex ring but directly from ejected fluid not absorbed by the vortex ring. This was observed for the largest investigated stroke ratio of $L/d_{\mathrm{eq}} \approx 48$. The trailing jet is expected to have properties similar to steady jets with shear rates well below those inside the vortex ring (Choutapalli *et al.* (2009)). Thus, jet modulation with the pressure-dependent optimal pulse width can help to reduce the mass flow consumption.

Second, the degree of non-parallel flow was shown to correlate with the circulation of vortex rings. An enhancement of this quantity is typically desired in AFC applications. Hence, a pressure increase may be recommended. However, the supply pressure is usually limited in technical applications. Therefore, future studies must address the proportionality between over-pressure and entrainment of ambient fluid in more detail. In this regard, it is of particular interest if the increase in mixing rate is continuous or if it is suddenly enhanced when a vortex ring of different shape, i.e. with an oblate form, is produced beyond a certain magnitude of over-pressure.

Furthermore, it was shown that the early vortex ring formation phase of $t^* < 5$ is majorly responsible for the rapid jet expansion. This phase should be addressed in more detail in future numerical investigations as it was affected by experimental shortcomings in the current study due to the small outlet dimensions typical of AFC devices.

Acknowledgements

Declaration of interests

The authors report no conflict of interest.

REFERENCES

AFANASYEV, Y. D. 2006 Formation of vortex dipoles. *Phys. Fluids* **18**.

AKIMA, H. 1970 A new method of interpolation and smooth curve fitting based on local procedures. *J. ACM* **17** (4), 589–602.

ARAKERI, J. H., DAS, D., KROTHAPALLI, A. & LOURENCO, L. 2004 Vortex ring formation at the open end of a shock tube: A particle image velocimetry study . *Phys. Fluids* **16**.

BÉRA, J. C., MICHARD, M., GROSJEAN, N. & COMTE-BELLOT, G. 2014 Flow analysis of two-dimensional pulsed jets by particle image velocimetry. *Exp. Fluids* **31** (5), 519–532.

BRADBURY, L. J. S. 1963 An investigation into the structure of a turbulent plane jet. PhD thesis.

CHOUTAPALLI, I., KROTHAPALLI, A. & ARAKERI, J. H. 2009 An experimental study of an axisymmetric turbulent pulsed air jet. *J. Fluid Mech.* **631**, 23–63.

DABIRI, J. O. & GHARIB, M. 2004 Fluid entrainment by isolated vortex rings. *J. Fluid Mech.* **511**, 311–331.

DAS, P., GOVARDHAN, R. N. & ARAKERI, J. H. 2013 Effect of hinged leaflets on vortex pair generation. *J. Fluid Mech.* **730**, 626–658.

DIDDEN, N. 1979 On the formation of vortex rings: rolling-up and production of circulation. *Z. Angew. Math. Phys.* **30**, 101–116.

GHARIB, M., RAMBOD, E. & SHARIFF, K. 1998 A universal time scale for vortex ring formation. *J. Fluid Mech.* **360**, 121–140.

GLEZER, A. 1998 The formation of vortex rings. *Phys. Fluids* **31**, 3532–3542.

GREENBLATT, D. & WYGNANSKI, I. J. 2000 The control of flow separation by periodic excitation. *AIAA J.* **36**, 487–545.

GUTMARK, E. & WYGNANSKI, I. 1976 The turbulent planar jet. *J. Fluid Mech.* **73** (3), 465–495.

HALLER, G. 2001 Distinguished material surfaces and coherent structures in three-dimensional fluid flows. *Physica D* **149**, 248–277.

HUSSAIN, F. & HUSAIN, H. S. 1989 Elliptic jets. part 1. characteristics of unexcited and excited jets. *J. Fluid Mech.* **208**, 257–320.

JAMES, S. & MADNIA, C. K. 1996 Direct numerical simulation of a laminar vortex ring. *Phys. Fluids* **8** (2400–2414).

KNYSTAUTAS, R. 1964 The turbulent jet from a series of holes in line. *Aero. Quart.* **15** (1), 1–28.

KRIEG, M. & MOHSENI, K. 2013 Modelling circulation, impulse and kinetic energy of starting jets with non-zero radial velocity. *J. Fluid Mech.* **719**, 488–526.

KRIEG, M. & MOHSENI, K. 2015 Pressure and work analysis of unsteady, deformable, axisymmetric, jet producing cavity bodies. *J. Fluid Mech.* **769**, 337–368.

KRUEGER, P. S. 2005 An over-pressure correction to the slug model for vortex ring circulation. *J. Fluid Mech.* **545**, 427–443.

KRUEGER, P. S., DABIRI, J. O. & GHARIB, M. 2006 The formation number of vortex rings in uniform background coflow. *J. Fluid Mech.* **556**, 1271–1281.

LIM, T. T. & NICKELS, T. B. 1995 Vortex rings. In *Fluid Vortices. Fluid Mechanics and Its Applications*.

MAXWORTHY, T. 1972 The structure and stability of vortex rings. *J. Fluid Mech.* **51** (1), 15–32.

MEI, R. 1996 Velocity fidelity of flow tracer particles. *Exp. Fluids* **22** (1), 1–13.

MÜLLER, E. A. & DIDDEN, N. 2004 Zur Erzeugung der Zirkulation bei der Bildung eines Ringwirbels an einer Düsenmündung. *Stroj. Casop.* **31**, 363–372.

MOFFATT, H. K. & MOORE, D. W. 1978 The response of hill's spherical vortex to a small axisymmetric disturbance. *J. Fluid Mech.* **87**, 749–760.

MOHSENI, K. & GHARIB, M. 1998 A model for universal time scale of vortex ring formation. *Phys. Fluids* **10** (10).

MOHSENI, K., RAN, H. & COLONIUS, T. 2000 Numerical experiments on vortex ring formation. *J. Fluid Mech.* **430**, 267–282.

MUSCULUS, M. P. B. 2009 Entrainment wave in decelerating transient turbulent jets. *J. Fluid Mech.* **638**, 117–140.

NITSCHE, M. & KRASNY, R. 1994 A numerical study of vortex ring formation at the edge of a circular tube. *J. Fluid Mech.* **276**, 139–161.

NORBURY, J. 1973 A family of steady vortex rings. *J. Fluid Mech.* **57** (3), 417–431.

O'FARRELL, C. & DABIRI, J. O. 2014 Pinch-off of non-axisymmetric vortex rings. *J. Fluid Mech.* **740**, 61–96.

28   *B. Steinfurth, J. Weiss*

Pawlak, G., Cruz, C. M., Bazan, C. M. & Hrdyi, P. G. 2007 Experimental characterization of starting jet dynamics. *Fluid Dyn. Res.* **39**, 711–730.

Pedrizzetti, G., Domenichini, F. & Tonti, G. 2010 On the left ventricular vortex reversal after mitral valve replacement. *Ann Biomed Engng.* **38** (3), 769–773.

Pozrikidis, C. 1986 The nonlinear instability of hill's vortex. *J. Fluid Mech.* **168**, 337–367.

Rosenfeld, M., Rambod, E. & Gharib, M. 1998 Circulation and formation number of laminar vortex rings. *J. Fluid Mech.* **376**, 297 – 318.

Sau, R. & Mahesh, K. 2007 Passive scalar mixing in vortex rings. *J. Fluid Mech.* **582**, 449–461.

Shariff, K. & Leonard, A. 1992 Vortex rings. *Annu. Rev. Fluid Mech.* **24**, 235–279.

Shin, D., Aspden, A. J. & Richardson, E. S. 2017 Self-similar properties of decelerating turbulent jets. *J. Fluid Mech.* **833**.

Smith, B. L. & Glezer, A. 1998 The formation and evolution of synthetic jets. *Phys. Fluids* **10** (9).

Weigand, A. & Gharib, M. 1997 On the evolution of laminar vortex rings. *Exp. Fluids* **22**, 447–457.

Witze, P. O. 1983 Hot-film anemometer measurements in a starting turbulent jet. *AIAA J.* **21** (2), 308–309.

Zhao, W., Fraenkel, S. H. & Mongeau, L. G. 2000 Effects of trailing jet instability on vortex ring formation. *Phys. Fluids* **12**, 589–596.

Velocity ratio effect on flow structures of non-parallel planar starting jets in crossflow

Ben Steinfurth[1]†, Julien Weiss[1]

[1]Institute of Aeronautics and Astronautics, Technische Universität Berlin, Marchstr. 12-14, 10587 Berlin, Germany

The interaction between starting jets and a steady crossflow with a zero-pressure-gradient, turbulent boundary layer is studied based on phase-locked particle image velocimetry measurements. A device typically used in flow control applications is employed as jets of compressed air are periodically emitted through a rectangular high-aspect ratio outlet. In the absence of a crossflow, this particular flow is characterised by thick-cored vortex rings. Investigating different velocity ratios between starting jets and crossflow within the interval $r = u_{\text{jet}}/U_\infty = 2.4 \ldots 11$, we identify two regimes of different flow structure appearance, transferring the classification map applicable to parallel circular starting jets in crossflow established by Sau & Mahesh (2008). At $r < 4$, the vorticity associated with the upstream part of the starting jet is cancelled by the crossflow boundary layer. Hairpin vortices are observed. At $r > 4$, the starting jets penetrate through the boundary layer, and vortex rings are generated. They are asymmetric in shape as the windward vortex ring core is thinner due to the interaction with the crossflow. As the limiting case of zero crossflow ($r \to \infty$) is approached, the asymmetry decreases, and the formation time correspondent to maximum vortex ring circulation converges to the characteristic value of $t^* \approx 12$ recently determined for this type of non-parallel planar starting jets when emitted into quiescent surroundings (Steinfurth & Weiss (2020b)). The findings presented in the current article can promote the sophisticated selection of actuation parameters in active mixing and separation control.

1. Introduction

The jet in crossflow (JICF), or transverse jet, is a canonical flow configuration relevant to different branches of science. A short, and incomplete, list includes meteorology (volcanic eruptions), biology (locomotion of aquatic animals) and medicine (vein catheters). Largely thanks to the seminal work of Fric & Roshko (1994), the topology of this flow in its steady, incompressible configuration is well known, and extensive reviews for various boundary conditions are provided by Mahesh (2013) and Karagozian (2014).

Enabling the mixing of fluids within short temporal and spatial scales, JsICF are also employed in technical applications. In contrast to steady JsICF, imposing a time-dependent jet velocity is typically the more effective and efficient approach to produce a pronounced turbulent mixing layer associated with an enhanced momentum transfer. Hence, unsteady JsICF were found to have beneficial effects in the fields of active separation control as summarised by Greenblatt & Wygnanski (2000), combustion (Vermeulen *et al.* (1987)) and film cooling (Ekkad *et al.* (2006), Coulthard *et al.* (2006)). The advantage over their steady counterparts can be attributed to two effects: (1) an enhanced mixing with the crossflow, i.e. increased diffusive and convective entrainment

† Email address for correspondence: ben.steinfurth@tu-berlin.de

2   *B. Steinfurth, J. Weiss*

rates, (2) a larger affected flow region due to greater spreading rates.

The specific vorticity distribution associated with such unsteady jets is governed by the applied velocity program. While jet characteristics can be altered effectively through sinusoidal forcing as reported by Paschereit *et al.* (1995), Muldoon & Acharya (2010) or Coussement *et al.* (2012), the velocity signal is often characterised by a rapid acceleration of finite amounts of fluid that are at rest initially. The transient motion of these starting, or fully pulsed, jets leads to the generation of large-scale primary vortex rings that are mainly responsible for the desired effects mentioned above. Among others, this is noted by Chang & Vakili (1995) who also report that both mixing and spreading associated with vortex rings in a uniform crossflow strongly depend on the pulsation frequency as discrete vortex rings produced with low frequencies penetrate much deeper into the crossflow than vortex rings generated with higher frequencies or steady JsICF. This notion is taken up by Hermanson *et al.* (1998) and Johari *et al.* (1999), adding the pulse width as the second relevant parameter determining the effectivity of starting JsICF. For a given jet velocity, this quantity is directly correlated with the amount of ejected fluid. Hence, compact individual vortex rings are generated for small pulse widths whereas trailing puffs similar to those observed in steady JsICF are created when this parameter is increased. In terms of the penetration depth, the latter scenario is only accompanied by a moderate enhancement compared to steady jets whereas an increase by a factor of five is observed by Johari *et al.* (1999) for smaller pulse durations. These conclusions are verified by Eroglu & Breidenthal (2001) and M'Closkey *et al.* (2002) while also shedding further light on the interaction between successively generated vortex structures.

Quite remarkably, similar observations regarding the influence of the amount of ejected fluid on the appearance of vortex rings were made around the same time for starting jets emitted into quiescent surroundings, i.e. in the absence of a crossflow as Gharib *et al.* (1998) introduced the well-known concept of a universal formation time. Using a generic experimental setup where fluid is accelerated by means of a piston-cylinder apparatus, they noted that the starting jet structure is related to the stroke ratio L/d, i.e. the ratio between travel length of the piston L and the diameter of the circular pipe outlet d. Being a measure for the mass flow consumption per starting jet, they report that a characteristic value of $L/d \approx 4$, the formation number, divides two regimes of vortex ring appearance. For amounts of ejected fluid corresponding to stroke ratios smaller than the formation number, individual vortex rings are generated with their size, and circulation, proportional to the stroke ratio. The maximum vortex ring circulation is reached around the formation number, and a trailing jet of fluid not accumulated by the vortex ring is formed beyond that value. It has later been shown that this formation time scale is indeed universal across different experimental conditions, for instance by Rosenfeld *et al.* (1998), Dabiri & Gharib (2004), Krueger *et al.* (2006), Sau & Mahesh (2007) and O'Farrell & Dabiri (2014).

In an attempt to extend the concept of a formation number to starting JsICF, Johari (2006) introduces a classification map that is spanned by the stroke ratio L/d and the duty cycle λ, i.e. the pulse width relative to the pulsation period. Based on the experimental studies regarding starting JsICF mentioned above, he postulates that distinct vortex rings are observed for $L/d \leqslant 4$. At larger stroke ratios of $L/d \approx 4 \ldots 20$, a vortex ring or puff followed by a trailing jet structure is noted while multiple turbulent puffs are generated at even larger stroke ratios. In addition to the stroke ratio, the structure of vortices is also influenced by the duty cycle since this quantity defines the

separation time between successive pulses, and strong interactions are observed for large λ, leading to a quasi-steady jet character.

Considering individual vortex rings, i.e. assuming duty cycles sufficiently small to preclude an interaction between successively generated flow structures, Sau & Mahesh (2008) perform direct numerical simulations of starting JsICF. They note that the stroke ratio marking the transition between an individual vortex ring and a maximum-size vortex ring followed by a trailing jet is in fact dependent on the velocity ratio between jet and crossflow $r = u_{\text{jet}}/U_\infty$, justifying the addition of a further dimension to the classification map introduced by Johari (2006). The velocity ratio of starting jets emitted into still ambience is considered $r \rightarrow \infty$ with a formation number corresponding to $L/d \approx 4$. For decreasing velocity ratios, ever smaller characteristic formation time scales are noted. In other words, the amount of fluid accumulated inside the vortex ring decreases, and a trailing jet of excessive vorticity emerges. In the presence of this jet, the vortex ring tilts downstream whereas an upstream tilt is found for solitary vortex rings in agreement with experiments conducted by Chang & Vakili (1995) and Bidan & Nikitopoulos (2013). According to Sau & Mahesh (2008), the tilt mechanism is due to Kutta lift, or the Magnus effect, which is subsequently called into question by Lim *et al.* (2008) suggesting an alteration of the vortex core vorticity distribution as an alternative explanation.

From a flow control perspective, the knowledge regarding a time scale yielding maximum vortex ring circulation is of major interest. Assuming that the control authority is mainly determined by the primary vortex ring, starting jets may be modulated to exclusively generate this flow structure, thereby enhancing the efficiency. Investigating starting jets ejected into still surroundings by means of a pulsed jet actuator (PJA), recent experiments by Steinfurth & Weiss (2020*b*) show that conclusions drawn from previous fundamental studies cannot be directly transferred to PJA-generated starting jets often used in active flow control (AFC). Specifically, their expansion and entrainment rates are much larger as vortex rings with extremely thick cores are generated. This not only contrasts with starting jets investigated in generic experiments but also with other AFC methods such as synthetic JsICF addressed by Gordon *et al.* (2004) or Milanovic & Zaman (2005). Two major differences are responsible for the specific properties of PJA-generated starting jets. First, the velocity program exhibits a more rapid acceleration that is associated with a distinct over-pressure peak inside the jet exit plane. As previously noted by Krueger (2005), this over-pressure is relatable to axial gradients of the transverse velocity component $\partial v/\partial x$ in the outlet plane. As a consequence, the vorticity flux ejected through this plane

$$\Omega = \frac{1}{2}u_0^2 + \int\limits_0^\infty u\frac{\partial v}{\partial x}\mathrm{d}y \qquad (1.1)$$

is increased. Note that u and v are the axial and the lateral jet velocity components along the x and y direction respectively; the subscript 0 denotes the centreline velocity. Neglecting vorticity diffusion across the outlet plane, Ω is equal to the rate of change of circulation associated with the starting jet according to Didden (1979). For non-parallel starting jets characterised by a non-zero transverse velocity component during jet initiation, a short-term offset occurs, and the total circulation is larger than for starting jets usually studied in generic experiments. In the latter cases, a parallel flow assumption is justified and the second term on the right-hand side in equation 1.1 vanishes which

amounts to the so-called slug model commonly used to predict the circulation associated with parallel starting jets. Although a slight degree of non-parallel flow has been observed in previous experiments, e.g. by Didden (1979) or Krieg & Mohseni (2013), the peak in normalised over-pressure is about an order of magnitude larger in the case of the PJA device. As a result, the transverse advection close to the outlet is much more distinct, and thick-cored vortex rings associated with non-dimensional energies similar to that of Hill's spherical vortex, the limiting member of the family of steady vortex rings introduced by Norbury (1973), are generated. The extreme vortex ring core thickness coincides with high circulation levels that are reached as the vortex rings continue to absorb circulation well beyond the characteristic formation time scale established by Gharib *et al.* (1998). This is assumedly enabled by the second major difference compared to generic studies. In the case of PJAs, jets are emitted through rectangular, large-ascpect ratio orifices. For such flows, it was previously observed by Afanasyev (2006) that the initial propagation speed is much smaller than for commonly investigated circular starting jets. Hence, vortex rings are located in close outlet proximity where they accumulate the ejected vorticity for a longer duration (Steinfurth & Weiss (2020b)).

Our recent article enables a deeper understanding regarding the flow physics of non-parallel starting jets commonly employed in AFC applications. However, it is limited to the scenario where jets are ejected into still ambience. The motivation of the present effort stems from the fact that in many cases, these jets interact with a crossflow, especially in the fields of active mixing and separation control. The main objective is therefore to identify the influence of a crossflow on the vorticity production with particular focus on the characteristic development of flow structures subject to a varied velocity ratio. The analysis is mainly based on phase-locked particle image velocimetry (PIV) measurements that are also employed to shed some light on the three-dimensional evolution of flow structures as a volumetric reconstruction based on multiple measurement planes is performed.

2. Specific flow configuration of non-parallel planar starting jets

As touched upon above, pulsed jet actuators (PJAs) can be employed as a means of vortex ring generation, rendering them attractive for active flow control (AFC) applications. The device used in this study consists of a fast-switching solenoid valve and a downstream nozzle (figure 1).

The solenoid valve allows for an adjustable periodic interception of the supplied compressed air that is then fed through the nozzle where the initially circular cross section is converted into an elongated slit with a length of $l = 20\,\text{mm}$ and a width of $d = 0.5\,\text{mm}$. The nozzle area ratio between inlet and outlet is $A_{\text{in}}/A_{\text{out}} \approx 1.1$. Its internal geometry is characterised by backward facing steps that are required to force a strong deflection of streamlines. Further downstream, the geometry expands with two merging cubic polynomials along the larger slit dimension and contracts according to a fifth-order polynomial in the other direction. The final part upstream of the exit plane has a constant cross section. A detailed documentation of the flow characteristics in the near-outlet region is provided by Steinfurth & Weiss (2020b). Most notably, we measured distinct peaks both in the axial velocity component and in $\partial v/\partial x$ close to the outlet lips, the latter of which represents a manifestation of non-parallel flow, contributing to an enhanced vorticity flux (equation 1.1). This is in accordance with experiments conducted by Didden (1979) and can be related to over-pressure inside the jet exit plane associated with a rapid acceleration during the initiation of fluid emission
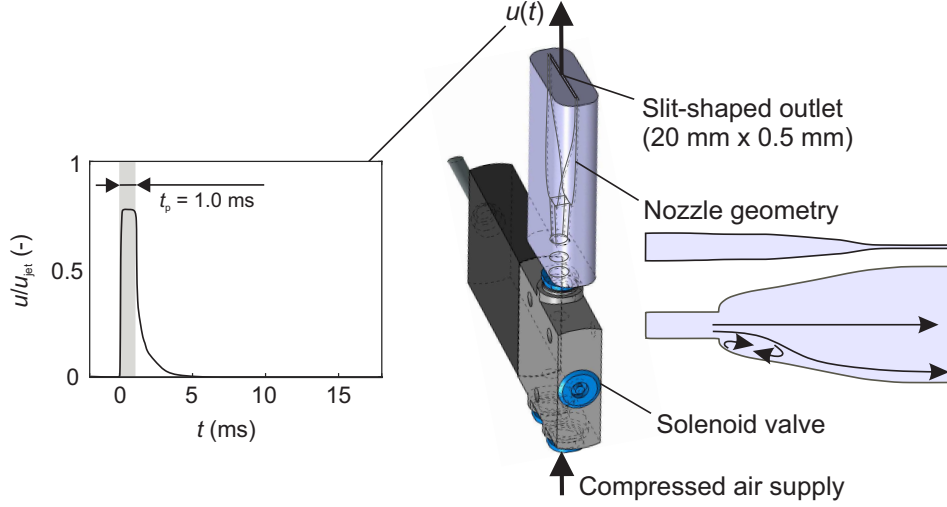
FIGURE 1. Pulsed jet actuator for generation of non-parallel planar starting jets; velocity signal close to the outlet shown in the left where shaded area represents valve opening time

TABLE 1. Main parameters of investigated non-parallel starting jets

u_{jet} (m/s)	t_p (ms)	L/d_{eq} (-)	f_p (Hz)	λ (-)
54	1	15	50	0.05

according to Krueger (2005). In the case of the PJA, the acceleration of fluid particles ensues once the mechanical valve opens, and its magnitude depends on the gradient force that is linked with the supply pressure. Crucially, the supply pressure required to achieve a given jet velocity in turn depends on various actuation parameters, especially on the nozzle geometry, the duty cycle and the pulse width. Changing these parameters therefore has an effect on the initial acceleration of fluid, resulting in a different degree of non-parallel flow. As the specific influence of these parameters is yet unknown, only one starting jet configuration with fixed parameters is addressed here (table 1). The jet with a velocity of $u_{jet} \approx 54$ m/s is emitted for a nominal pulse duration of $t_p = 1$ ms which yields a virtually emitted fluid column of length $L = u_{jet} t_p = 54$ mm. In the absence of a circular outlet, we use the equivalent diameter $d_{eq} \approx 3.57$ mm as the characteristic length scale. This value represents the diameter of a circle with the same area as the PJA outlet, a definition found to be adequate in previous studies of non-circular starting jets by Hussain & Husain (1989) and O'Farrell & Dabiri (2014). The resulting equivalent stroke ratio was $L/d_{eq} \approx 15$. The separation time between successive pulses was chosen so that no interaction occurs as flow structures associated with the preceding starting jet are convected sufficiently far downstream. For practical reasons, namely the use of phase-averaging, starting jets were still generated in a periodic manner at a pulse frequency of $f_p = 50$ Hz. The resulting duty cycle was $\lambda = t_p / f_p^{-1} = 0.05$.

Figure 2 shows the pressure signal inside the jet exit plane for the investigated parameter combination. A short-duration peak with a normalised over-pressure of $\Delta p_{norm} = (p - p_\infty)/(\varrho u_{jet}^2) \approx 1.2$ occurs around $t \approx 0.3$ ms where $t = 0$ ms marks the beginning of fluid ejection. Here, p is the pressure measured with a piezo-resistive transducer approximately 1 mm upstream of the outlet, p_∞ is the stagnation pressure in sufficient distance to the outlet, and ϱ is the jet mass density. Note that secondary peaks subsequent
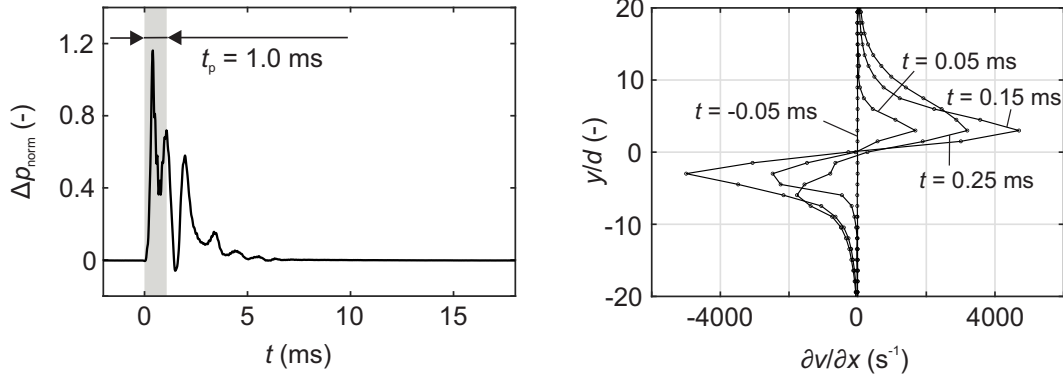
FIGURE 2. Left: time-dependent pressure signal inside the jet exit plane; right: evolution of velocity gradients corresponding to increase of vorticity flux due to over-pressure; based on depictions by Steinfurth & Weiss (2020b)

to the jet emission phase are assumedly due to an oscillation of the cavity volume above the pressure transducer. During the pressure rise, distinct velocity gradients occur close to the outlet edges (right in figure 2). Here, y is oriented along the smaller outlet dimension with $y/d = 0$ located on the centreline.

These initial conditions cause a drastic transverse advection of fluid close to the outlet, resulting in thick-cored vortex rings. For an analysis of these vortex rings generated in still surroundings, the reader is referred to our recent article (Steinfurth & Weiss (2020b)).

3. Experimental procedure

To shed some light on the interaction between the non-parallel starting jets introduced above and a steady crossflow, experiments were conducted inside the closed test section of a closed-loop low-speed wind tunnel. Shielded from the free stream, one PJA was installed beneath a splitter plate. As indicated in figure 3, the jet outlet was mounted flush in the splitter plate surface with the PJA axis at $x = 0$ mm oriented perpendicular to the free stream. The outlet was $\Delta x = 300$ mm downstream of the splitter plate leading edge and interacted with a turbulent boundary layer as a transition fixation was installed at $x = -200$ mm. A trailing flap on the downstream end of the splitter plate was adjusted to ensure a zero-pressure-gradient boundary layer.

Particle image velocimetry (PIV) measurements were conducted inside the symmetry plane at $z = 0$ mm, and further data in parallel planes at $z = (-2, -4, \ldots, -20, -25)$ mm was obtained for two selected configurations (table 2). For the latter, a stereoscopic arrangement was used and three-dimensional velocity fields were reconstructed, enabling a more detailed analysis of flow structures. The dimensions of measurement planes were approximately $(X, Y) \approx (100, 70)$ mm. Seeding particles introduced both through the free stream and the starting jets were illuminated using a double-pulsed Nd:YAG laser, and particular attention was paid to generating a thin light sheet with a width of $\Delta z \approx 1$ mm. CMOS cameras with 5 MP resolution were used, yielding a spatial distance between computed neighbouring vectors of $\Delta x = \Delta y \approx 0.74$ mm. Since the dimensions of PIV interrogation areas were large compared to the slit width $d = 0.5$ mm, velocity gradients close to the outlet caused highly non-uniform particle displacement fields. Specifically, the displacement variation inside interrogation areas exceeded the mean particle image diameter and therefore resulted in substantial measurement uncertainty as explained by Westerweel (2008). Here, no window deformation schemes were employed, and cyclic FFT algorithms were used for cross-correlation which results in a bias towards zero
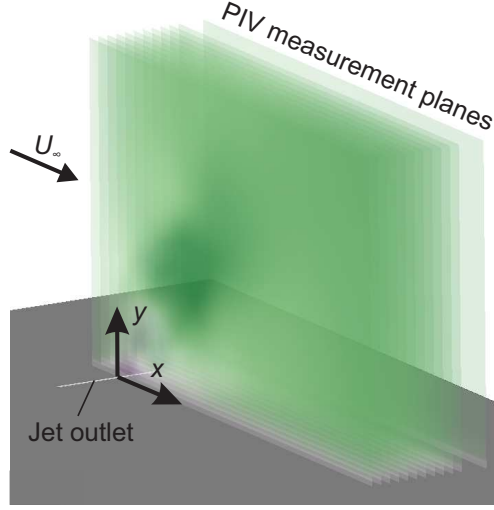
FIGURE 3. Test section setup

displacement. The magnitude of velocity gradients close to the jet outlet is therefore underestimated substantially. However, the measurement uncertainty decreases quickly in wall normal direction due to diffusing velocity gradients. Hence, the maximum uncertainty at $y = 5\,\text{mm}$ during jet emission is $\pm 6\%$ for instantaneous in-plane velocity components.

The PIV system was triggered at delay times defined with reference to the opening of the solenoid valve. Thus, phase-locked data were acquired, spanning the entire pulsation period. A larger temporal resolution ($\Delta t = 0.05\,\text{ms}$) was applied during the jet emission phase whereas the separation between phases was as large as $\Delta t = 2\,\text{ms}$ for periods where the rate of change of observables was marginal. The number of snapshots for these phases was also lowered ($N = 50$) while more information was required to ensure sufficient mean data convergence otherwise ($N = 90$). The time instance corresponding to the initial emergence of seeding particles from the PJA was defined as $t = 0\,\text{ms}$. Note that we refer to the non-dimensional formation time $t^* = tu_{\text{jet}}/d_{\text{eq}}$ throughout the article, quantifying the amount of fluid that has been ejected at respective time instances until the non-dimensional formation time equals the stroke ratio, i.e. $t^* = L/d_{\text{eq}}$, being the time when the jet emission nominally ends.

A major focus point of this study is the development of non-parallel starting jets subject to a varied velocity ratio between jet and crossflow $r = u_{\text{jet}}/U_\infty = 2.4\ldots 11.0$. This variation is achieved by adjusting the crossflow velocity while keeping the jet velocity constant. This strategy is chosen as a varied jet velocity would significantly affect the jet characteristics as explained above. However, an adjustment of the free stream speed results in altered boundary layer properties that we address in the following. The normalised boundary layer profiles for the investigated free stream velocities at $x = 0\,\text{mm}$ are shown in figure 4 (in the absence of starting jets). The velocity displayed at $y/d \approx 0$ was not directly measured but assumed to be zero as the respective near-wall region in PIV snapshots was masked. Note that the free stream velocity is here defined as the mean streamwise velocity in the range $y/d = 20\ldots 120$ inside the symmetry plane at $x/d = 0$. As shown in figure 4, this value is exceeded by approximately 10% in a wall distance of $y/d \approx 6\ldots 16$ for the case of the smallest inflow velocity ($r \approx 11$), which we explain as a
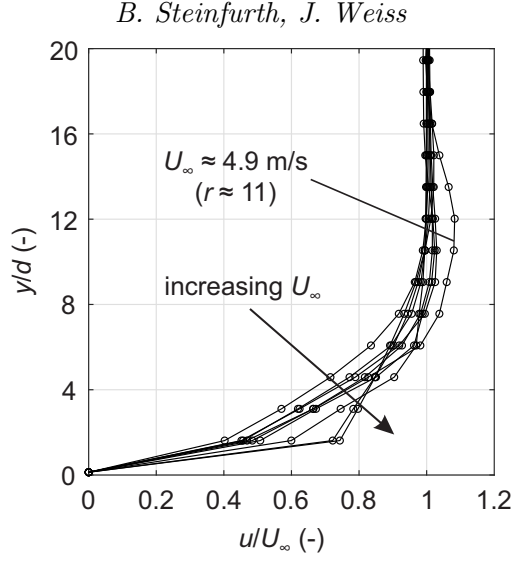
FIGURE 4. Boundary layer profiles for different free stream velocities

TABLE 2. Flow conditions and information regarding recorded data for investigated velocity ratios

$r = u_{\mathrm{jet}}/U_\infty$ (-)	u_{jet} (m/s)	U_∞ (m/s)	Velocity field information
2.4	54	22.9	2D2C & 3D3C
2.9	54	18.9	2D2C
3.8	54	14.1	2D2C
4.7	54	11.4	2D2C & 3D3C
5.6	54	9.6	2D2C
6.6	54	8.2	2D2C
7.6	54	7.1	2D2C
8.4	54	6.5	2D2C
11.0	54	4.9	2D2C

wind tunnel characteristic. This band of increased velocity is consistently present for all experiments of the largest velocity ratio.

Due to the short distance between the splitter plate leading edge and the PJA outlet, relatively thin boundary layers with $\delta_{99} \approx 10\,d$ are found for all configurations, i.e. $0.99U_\infty$ is reached at $y/d \approx 10$ or $y \approx 5\,\mathrm{mm}$. Turbulent states are observed for all free stream velocities due to the application of a transition fixation. However, the transverse velocity gradient $\partial u/\partial y$ close to the wall increases for larger U_∞. Hence, the normalised streamwise velocity for the largest free stream velocity is almost twice as large as for the smallest U_∞ at $y/d \approx 1.5$ ($y \approx 0.75\,\mathrm{mm}$). Near the wall, this coincides with an even larger crossflow momentum relative to the starting jet for small velocity ratios which we expect to result in two effects. First, the transverse advection of fluid inside the upstream part of the jet is diminished to a greater extent. Second, the jet trajectory is bent disproportionately and may not be scalable.

The investigated parameter combinations are summarised in table 2.

4. Results

In the following, we address the major experimental results regarding the interaction between non-parallel planar starting jets generated with a PJA and a steady crossflow

of varied velocity. The section is structured as follows. First, we focus on the evolution of two-dimensional vorticity fields inside the symmetry plane of the JsICF. In doing so, particular focus is laid upon the jet initiation phase that is essential for the understanding of three-dimensional flow structures associated with different velocity ratios analysed subsequently. Then, we turn our attention to the circulation induced by non-parallel planar starting JsICF before assessing the influence of the velocity ratio on jet trajectories.

4.1. *Development of vorticity fields*

Phase-averaged streamlines and the normalised out-of-plane vorticity component ω_z are shown in figure 5 for selected time steps inside the symmetry plane ($z = 0\,\mathrm{mm}$). Furthermore, footprints of spanwise vortex structures on that plane are visualised by means of the Q criterion introduced by Hunt *et al.* (1988) as iso-lines at $Q_z = 0\,\mathrm{s}^{-2}$ are displayed. Recall that the start and end of the jet emission phase nominally correspond with non-dimensional formation times of $t^* = 0$ and $t^* \approx 15.1$, separated by the investigated pulse width of $t_\mathrm{p} = 1\,\mathrm{ms}$.

It is immediately apparent that the velocity ratio has a significant influence on generated flow structures. Only a minor deflection of the boundary layer is observed for $r \approx 2.4$ as a small-scale recirculation zone forms on the leeward side of the JICF. Vortices identified by using the Q criterion are only associated with negative vorticity whereas regions of positive vorticity are merely found inside the boundary layer of the recirculation zone and contain a much smaller magnitude in comparison. Flow structures for this case are in good agreement with those observed by Hecklau *et al.* (2010) who investigated PJA-generated starting jets emitted into a crossflow with an adverse pressure gradient at $r \approx 2.5$.

For $r \approx 3.8$, the cross section of a vortex tube is found close to the outlet at the first time step. Then, a minor region of positive vorticity is observed associated with a small area of $Q_z > 0\,\mathrm{s}^{-2}$. As expected, the jet trajectory is steeper than for $r \approx 2.4$, and the recirculation zone is enlarged compared to the smallest velocity ratio. However, it is interesting to note that vorticity peaks at latter time steps $t^* \approx 30.0$ and $t^* \approx 46.9$ have a smaller magnitude of vorticity.

From a qualitative perspective, the generated flow structures for the larger velocity ratios $r \approx (4.7, 7.6, 11.0)$ are very similar to those observed for $r \approx 3.8$. However, the generation of positive vorticity is distinctly enhanced as a respective region is already found during jet initiation at $t^* \approx 3.0$ for these cases. Also based on the Q criterion, we therefore assume that (asymmetric) vortex rings are only produced for velocity ratios of $r > 4$ with a vortex core thickness of the upstream part (positive vorticity) that is proportional to the velocity ratio.

It is clear that the interaction between the crossflow boundary layer and the starting jet at early formation times, i.e. at the onset of fluid emission, plays a significant role in terms of the eventually developing flow structures. Before analysing this phase in detail, we would like to recall that non-parallel starting jets emitted into quiescent surroundings produce symmetric vortex rings with regions of positive and negative vorticity that are identical in terms of their size and vorticity distribution. When a crossflow is applied, the upstream part of the jet that contains positive vorticity interacts with the opposite-sign vorticity of the crossflow boundary layer. Hence, a cancellation of vorticity occurs, and for the case of starting jets ejected through a circular outlet, this cancellation precludes the generation of vortex rings at velocity ratios of $r < 2$ according to Sau & Mahesh (2008). However, the outlet dimension in main flow direction $d = 0.5\,\mathrm{mm}$ is much smaller for the PJA investigated here. Thus, the ejected boundary layer and the initial shear

B. Steinfurth, J. Weiss
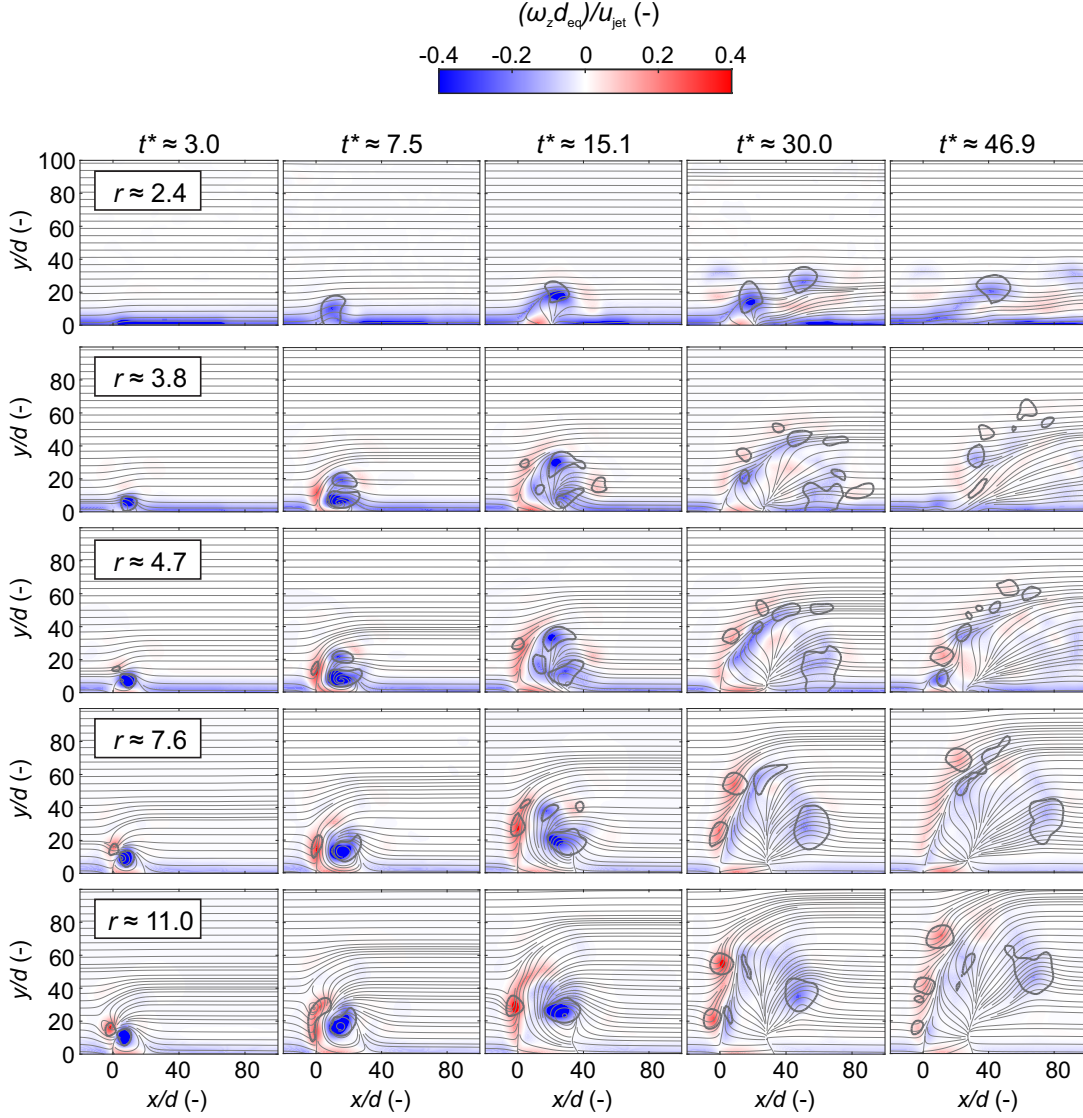
$(\omega_z d_{eq})/u_{jet}$ (-)

FIGURE 5. Temporal evolution of phase-averaged streamlines and normalised vorticity fields associated with non-parallel planar starting JsICF at different velocity ratios; vortex structures detected by employing Q criterion encircled by grey curves

layer are much thinner compared to the incoming boundary layer. In the following, we focus on the evolution of vorticity fields during the early formation phase subject to these specific boundary conditions.

Phase-averaged vorticity and velocity fields in the near-outlet region are shown in figure 6. Note that only every other velocity vector measured with PIV is shown in both x and y direction for reasons of clarity.

The upstream part of the thin initial shear layer is completely diminished at $r \approx 2.4$. For a velocity ratio of $r \approx 3.8$, the emergence of positive vorticity is distinctly delayed and only occurs at $t^* \approx 4.5$, i.e. after approximately one third of the jet emission phase. For larger velocity ratios, the relative magnitude of vorticity associated with the crossflow boundary layer decreases. Hence, the cancellation mechanism is less pronounced, and positive vorticity is produced at earlier formation time steps. This eventually results in a larger magnitude of positive vorticity as discussed in relation to figure 5, and ever more
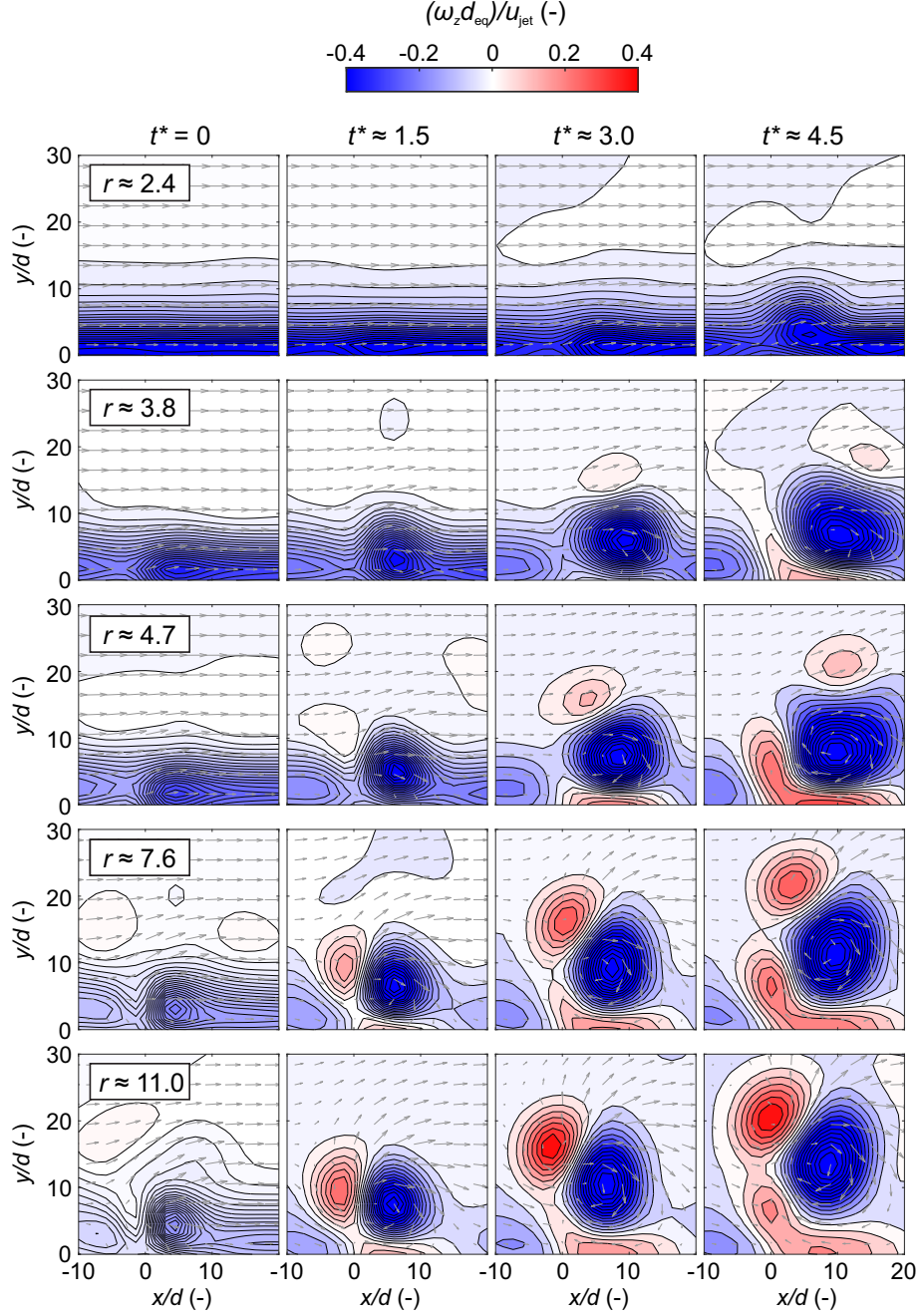
FIGURE 6. Phase-averaged velocity and vorticity fields in near-outlet region during jet initiation

distinct vortex rings are generated when the velocity ratio is increased as a result.

We conclude that the minimum velocity ratio required to produce vortex rings is larger than for starting jets generated with circular outlets documented by Sau & Mahesh (2008) who report a value of $r = 2$. Noting that the assignment of a specific value for this characteristic velocity ratio is an inherently difficult task, we estimate that a transition in the appearance of generated flow structures takes place around $r \approx 4$ for the given

B. Steinfurth, J. Weiss
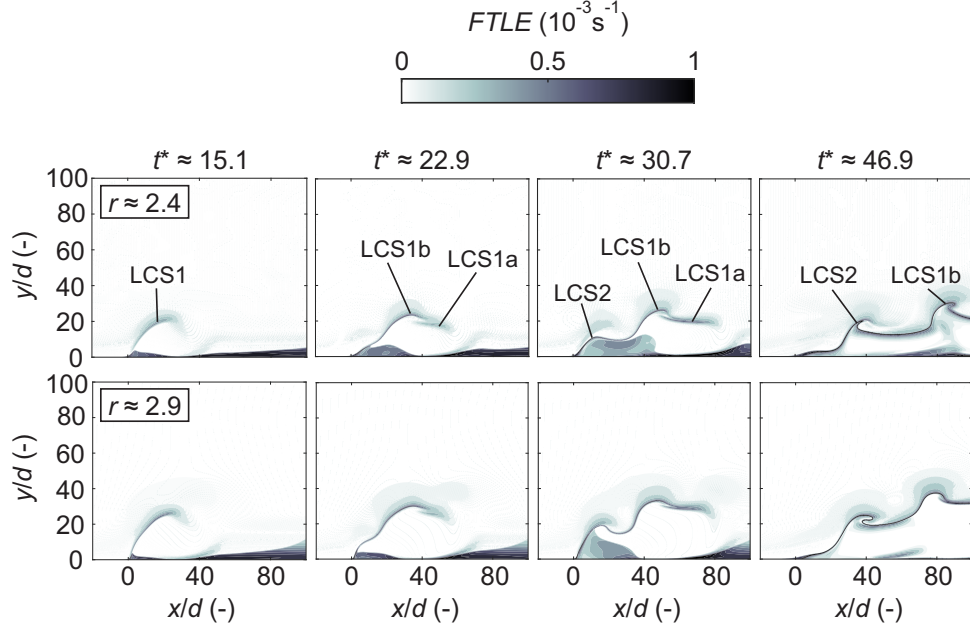
FIGURE 7. Development of FTLE fields inside the symmetry plane for velocity ratios $r < 4$

boundary conditions. In the remainder of this article, we address configurations divided by this value in a separate manner.

4.2. *Influence of crossflow on two- and three-dimensional vortex structures*

In this subsection, we analyse the flow structures induced by non-parallel planar starting JsICF in more detail. To this end, different flow diagnostics are employed. Among others, we study the dynamical behaviour inside the measurement domains by evaluating finite-time Lyapunov exponent (FTLE) fields. Since the calculation was based on backward-time integration, ridges in these fields correspond to attracting material lines to which fluid particles converge at an exponential rate. They are either computed based on phase-averaged velocity fields in the symmetry plane where the out-of-plane component is neglected or on 3D3C velocity fields that are available for $r \approx 2.4$ and $r \approx 4.7$. As suggested by Rockwood *et al.* (2019), neglecting the out-of-plane velocity component is justified when the flow field is dominated by spanwise vortex structures, which is the case in the JICF symmetry plane. A detailed documentation of the computation methodology is provided in our recent article (Steinfurth & Weiss (2020b)). The same approach is taken here.

4.2.1. *Velocity ratio $r < 4$*

The two-dimensional FTLE fields inside the symmetry plane for $r \approx 2.4$ and $r \approx 2.9$ are shown in figure 7.

For both cases, a weak separating material line (LCS1) is observed initially, representing the interface between the crossflow and the emerging starting jet. This flow structure then splits into a horizontal leading part (LCS1a) and a material line mapping the roll-up of the primary region of negative vorticity shown in figure 5 (LCS1b). Around $t^* \approx 30.7$, a trailing region of negative vorticity emerges as represented by LCS2. The material lines both for the primary and secondary vortex structures (LCS1b and LCS2) roll up subsequently as they are advected downstream. Flow structures observed for
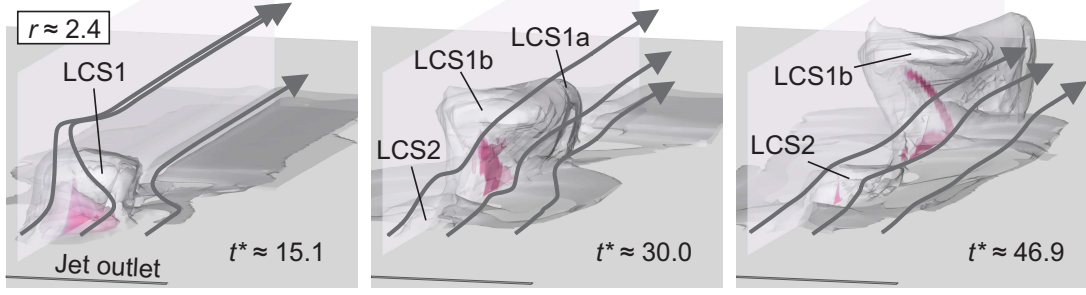
FIGURE 8. Development of three-dimensional FTLE iso-surface ($FTLE = 0.48 \cdot 10^{-3}\,\mathrm{s}^{-1}$) for velocity ratios $r \approx 2.4$; grey: related to crossflow fluid particles, purple: starting jet
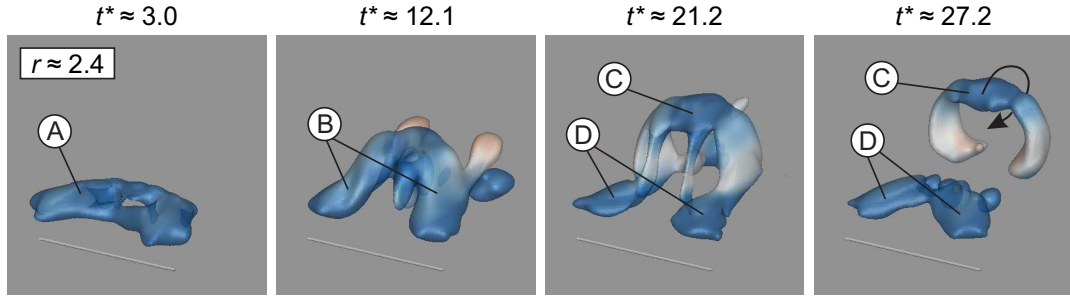

FIGURE 9. Temporal evolution of three-dimensional flow structures detected by employing Q criterion for $r \approx 2.4$, iso-surfaces coloured by transverse vorticity component ω_z within the range $(\omega_z d_{\mathrm{eq}})/u_{\mathrm{jet}} = -0.3 \ldots 0.3$; annotations referred to in the text

both cases are very similar. However, the jet trajectory is slightly steeper for $r \approx 2.9$.

Three-dimensional FTLE fields for $r \approx 2.4$ are shown in figure 8. Note that a distinction is made between fluid particles emerging from the outlet and those originating in the crossflow. They are shown in purple (jet) and grey (crossflow) respectively. In addition, three phase-averaged streamlines, seeded at $z = (0, 5, 10)\,\mathrm{mm}$ and a wall distance of $y = 5\,\mathrm{mm}$, are shown.

A hump-like structure mapping the deflection of the crossflow boundary layer is seen at $t^* \approx 15.1$ (LCS1). Interestingly, the spanwise extent is only about one half the outlet length as this flow structure is mitigated on the spanwise boundaries due to the crossflow influence. While all three streamlines are bent towards the symmetry plane, only particles initiated at $z = 0\,\mathrm{mm}$ and $z = 5\,\mathrm{mm}$ are shifted away from the wall. For the subsequent time steps, no such displacement can be noted as the jet emission phase has already stopped and the vertical velocity component is negligible. However, the vortical structure revealed by the FTLE iso-surface slightly expands in spanwise direction as it propagates downstream. It is also apparent that the trailing vortex (LCS2) is less dominant in this three-dimensional representation compared to the leading material surfaces LCS1a and LCS1b. The meaning of these flow structures in terms of the transport behaviour is addressed in more detail in the following.

The evolution of iso-surfaces of the three-dimensional Q criterion coloured by the transverse vorticity component ω_z is shown in figure 9.

In agreement with previous observations, a vortex tube (A) develops only on the leeward side of the jet during jet initiation ($t^* \approx 3.0$). It is trailed by two streamwise vortices (B) emerging from the outlet lips ($t^* \approx 7.5$). At $t^* \approx 21.2$, the typical structure of a hairpin vortex is observed, consisting of a curved leading structure (C) and two

B. Steinfurth, J. Weiss
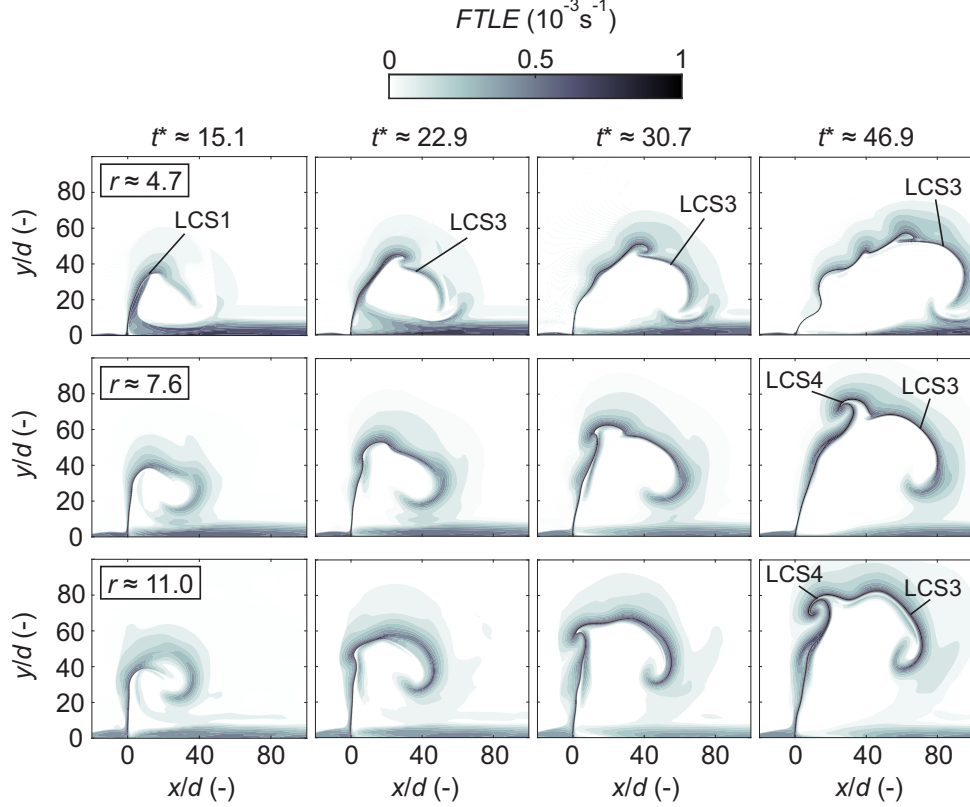
FIGURE 10. Development of FTLE fields inside the symmetry plane for velocity ratios $r > 4$

longitudinally oriented 'hairpin legs' (D). The same flow structure was reported by Sau & Mahesh (2008) for circular JsICF at small velocity ratios. Eventually, the hairpin vortex begins to break down as the leading part (C) pinches off from the 'hairpin legs' (D) at $t^* \approx 27.2$.

It is worth pointing out that the transport behaviour associated with hairpin vortices is different to that of vortex rings. In the case of the former, only the vortex tube associated with negative vorticity rolls up since the upstream part of the starting jet is suppressed. As a result, a ring-like vortex develops where fluid particles are transported inward. The closed vortex rings generated at larger velocity ratios, on the other hand, exhibit an opposite sense of rotation as jet fluid is shifted outward.

In summary, the crossflow causes a complete suppression of the upstream part of the shear layer due to vorticity cancellation. Hence, no vortex rings are generated but hairpin vortices are observed close to the wall at small velocity ratios ($r < 4$).

4.2.2. *Velocity ratio $r > 4$*

Analogous to the analysis above, flow structures observed at larger velocity ratios are discussed in the following sub-section. Figure 10 contains two-dimensional FTLE fields at different time instances.

A separating material line (LCS1) is again observed initially for $r \approx 4.7$. It is worth noting that it indicates an almost vertical jet trajectory at small formation times. Subsequently, a large-scale roll-up of negative vorticity takes place on the leeward side of the jet (LCS3). As the upstream part of the vortex ring only exhibits a small magnitude of vorticity and no roll-up is indicated by the streamlines shown in figure 5, it is not
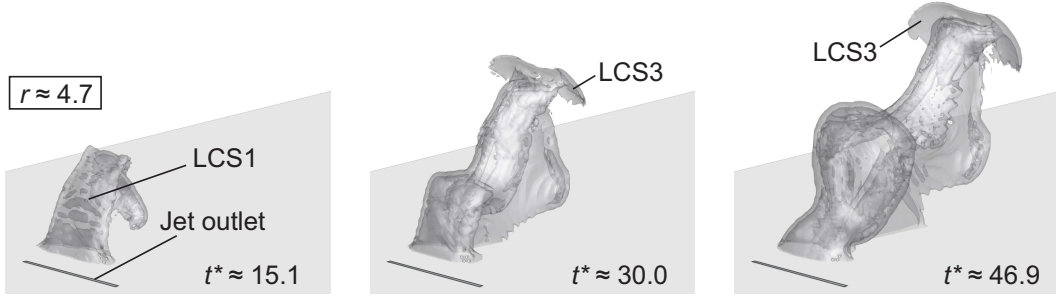
FIGURE 11. Development of three-dimensional FTLE iso-surface ($FTLE = 0.48 \cdot 10^{-3}\,\mathrm{s}^{-1}$) for velocity ratio $r \approx 4.7$; annotations referred to in the text
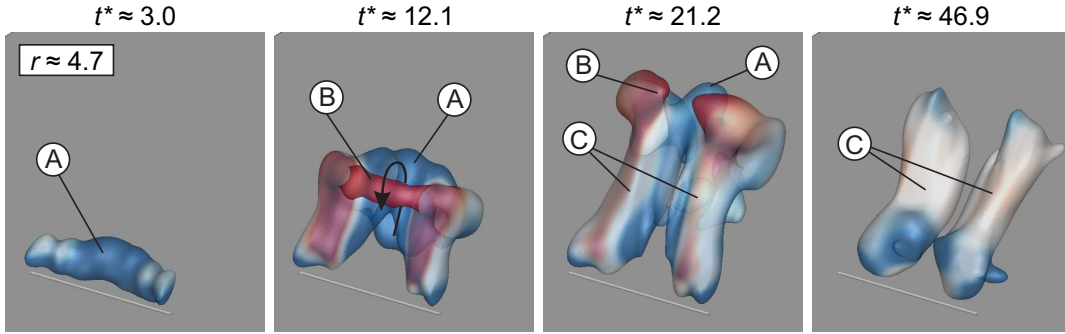

FIGURE 12. Temporal evolution of three-dimensional flow structures detected by employing Q criterion for $r \approx 4.7$; iso-surfaces coloured by transverse vorticity component ω_z within the range $(\omega_z d_{\mathrm{eq}})/u_{\mathrm{jet}} = -0.3 \ldots 0.3$; annotations referred to in the text

captured by the FTLE computation for $r \approx 4.7$. This upstream part of the vortex ring (LCS4) is, however, seen for the two larger velocity ratios $r \approx (7.6, 11.0)$ where the corresponding region of positive vorticity is more dominant.

Three-dimensional FTLE fields for $r \approx 4.7$ are shown in figure 11.

At $t^* \approx 15.1$, fluid particles from the incoming crossflow boundary layer are shifted almost vertically by a distance of about $40\,d$. The responsible material surface is the three-dimensional representation of LCS1 shown in figure 10 and covers the entire outlet length, contrasting with the smaller velocity ratio of $r \approx 2.4$. Even though no fluid is nominally emitted at $t^* > 15$, the transport barrier LCS1 is still apparent at $t^* \approx 30$. This can be ascribed to the presence of a recirculation zone on the leeward side of the starting jet, blocking the oncoming flow, that only gradually breaks down once no more fluid is ejected. Furthermore, the propagation front of the leading vortex ring (LCS3) associated with negative vorticity is clearly visible at $t^* \approx 15.1$ and $t^* \approx 30.0$.

In figure 12, iso-surfaces of the three-dimensional Q criterion are shown.

For the initial time-step, only a vortex tube of negative vorticity (A) is extracted ($t^* \approx 3.0$). Then, a strand of positive vorticity (B) emerges and is visible at $t^* \approx 12.1$. This confirms the conclusion that closed vortex rings are indeed generated at velocity ratios of $r > 4$. However, the ring at $r \approx 4.7$ only persists for a relatively short time as the small-scale region of positive vorticity is quickly diminished. Interestingly, the most dominant flow structure at larger formation times is a counter-rotating vortex pair (C) that is known to govern the far-field structure of steady JsICF as shown by Fric & Roshko (1994). In the current study, the vortex pair remains in close outlet proximity for

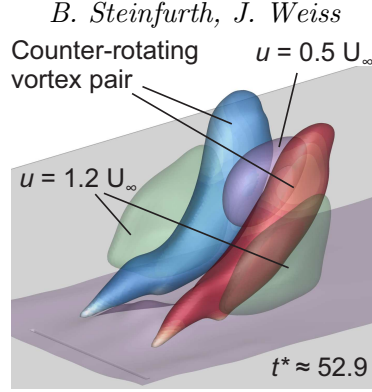16   *B. Steinfurth, J. Weiss*

FIGURE 13. Counter-rotating vortex pair detected by employing Q criterion for $r \approx 4.7$ and its influence on streamwise velocity component; iso-surfaces related to vortex pair coloured by streamwise normalised vorticity component within the range $(\omega_x d_{\mathrm{eq}})/u_{\mathrm{jet}} = -0.1 \ldots 0.1$

a duration that is long relative to the jet emission time (figure 13). This is linked with the gradual breakdown of the region characterised by a deficit in streamwise velocity downstream of the outlet (purple iso-surface in figure 13). In the outer region, on the other hand, fluid is accelerated (green iso-surface).

Contrasting with the smaller velocity ratios, vortex rings are generated at $r > 4$. This is due to the smaller relative vorticity associated with the crossflow boundary layer. However, we still note a mitigation of the upstream part of vortex rings that are asymmetrical in shape.

4.3. *Development of circulation associated with non-parallel planar starting JsICF*

Among the other invariants of motion, the circulation associated with a starting jet is a representation of its dynamical behaviour. It is also an appropriate parameter to estimate the mixing capability of such flows in AFC applications. The generation of this quantity over time is addressed in the following. Note that we define the circulation as the area-integrated magnitude of vorticity inside the symmetry plane. For the total jet circulation, the integration area is the entire measurement plane. Since the generated flow structures are highly asymmetrical due to the influence of the crossflow, the circulation associated with regions of positive and negative vorticity are assessed separately.

4.3.1. *Velocity ratio $r < 4$*

At first, we focus on small velocity ratios of $r < 4$ where the crossflow has a dominant influence as it causes a distinct cancellation of positive vorticity associated with the windward side of the starting jet. The development of circulation for these configurations is displayed as a function of the non-dimensional formation time in figure 14. It is shown above that starting JsICF operated at smaller velocity ratios of $r \approx (2.4, 2.9)$ lead to the generation of hairpin vortices whereas $r \approx 3.8$ marks the beginning of a transitional regime, leading over to the generation of vortex rings at larger velocity ratios.

For all cases, the circulation associated with negative vorticity found inside the leeward side of the jet is consistently larger than for the upstream part. This is in agreement with previous discussions of the vorticity development and reflects the cancellation of positive vorticity as the circulation only starts to increase around $t^* \approx 10$ ($r \approx 2.4$) and $t^* \approx 8$ ($r \approx 2.9$). The subsequent rise in circulation, however, is not caused by the upstream part of the starting jet where no vorticity is generated during the entire jet emission phase. Instead, it can be attributed to the boundary layer in the reverse-flow region that develops
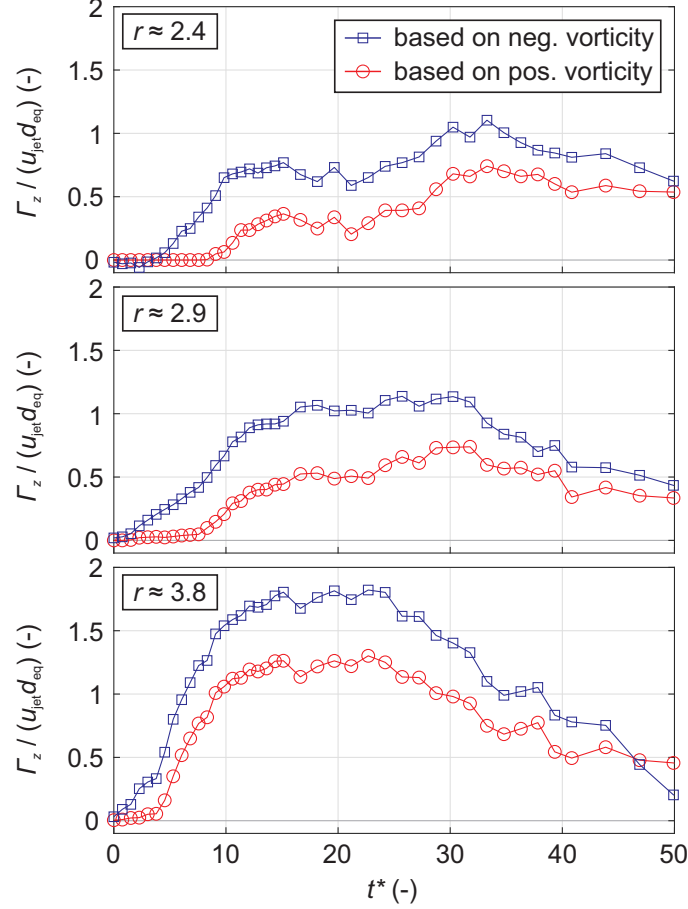
FIGURE 14. Temporal evolution of circulation associated with non-parallel planar starting JsICF at velocity ratios $r < 4$

beneath the dominant roll-up of negative vorticity shown in figure 5. This contrasts with the larger velocity ratio $r \approx 3.8$ where the rate of change of circulation is lifted around $t^* \approx 5$. In that case, the emergence of a thin region of positive vorticity is only delayed by the crossflow boundary layer but not completely suppressed as for the smaller velocity ratios. Hence, the rate of change of circulation both for the positive and negative vorticity regions is larger, and maxima of $\Gamma_z/(u_{\mathrm{jet}}d_{\mathrm{eq}}) \approx 1.25$ and $\Gamma_z/(u_{\mathrm{jet}}d_{\mathrm{eq}}) \approx 1.8$ are reached around $t^* \approx 15$, i.e. at the end of the jet emission phase. Smaller peaks in circulation coincide with the same time instance for the lower velocity ratios, and it is interesting to note that a high level of circulation is maintained for a longer duration in those cases. The circulation even increases beyond $t^* = 15$ for $r \approx 2.4$ as an overall maximum is reached around $t^* \approx 30$. This is assumedly linked with the breakdown of the hairpin vortex (figure 8) and the subsequent advection of the 'hairpin legs' towards the symmetry plane that is evaluated here.

4.3.2. *Velocity ratio $r > 4$*

Flow structures generated at larger velocity ratios of $r > 4$ differ from those discussed in the previous sub-section in that starting jets penetrate through the crossflow boundary layer and vortex rings are generated. The circulation associated with these vortex rings relative to the total induced circulation is discussed in the following. To extract vortex rings from measured vorticity fields and define the respective integration domains for the

circulation computation, we pursued an approach similar to that employed by Fernández & Sesterhenn (2017). The vortex ring core is defined as the location of maximum vorticity subject to two secondary conditions. First, the value of the Q criterion must be positive. Second, the ring core must be located near the jet propagation front indicated by LCS3 or LCS4 shown in figure 10. This avoids false detections of the core when the vortex ring begins to dissipate at large formation times, especially for $r \approx 4.7$. Once the vortex ring core is identified, an appropriate iso-line enclosing its location is used as the boundary for vorticity integration. Here, a value of $0.1\,\omega_{z,\mathrm{vc}}$, i.e. 10% of the vorticity found inside the vortex ring core was used as a threshold.

The development of circulation both for the entire starting jet (open symbols) and for the vortex rings (filled symbols) is shown in figure 15 for $r \approx (4.7, 7.6, 11.0)$. Again, a distinction is made between regions of positive and negative vorticity. As a relevant time scale, we also extract non-dimensional formation times associated with maximum vortex ring circulation τ. They represent the time instance up to which vorticity is entirely absorbed by the vortex ring. When fluid is ejected beyond this value, a trailing jet strucure forms as suggested by Sau & Mahesh (2008). However, it should be noted that their identification of characteristic time scales was based on direct numerical simulations regarding starting jets of different stroke ratios whereas this parameter is fixed in the current study.

First, we focus on the curves for the entire starting jet circulation. In agreement with the detailed measurements of the near-outlet region shown in figure 6, the generation of positive circulation is slightly delayed for the two smaller velocity ratios. Intuitively, this delay is inversely proportional to the velocity ratio. It is also worth noting that the rate of change of circulation is similar for all cases but significantly exceeds the rise observed for velocity ratios of $r < 4$. Maxima of the entire circulation are again reached at the end of the jet emission phase around $t^* \approx 15$ with the circulation based on regions of negative vorticity again being larger than for the upstream part of the jet. However, the influence of the velocity ratio on the respective maxima in circulation $\Gamma_z/(u_{\mathrm{jet}}d_{\mathrm{eq}}) \approx (2.2, 2.5, 2.7)$ is relatively small compared to the smaller velocity ratios of $r < 4$. Furthermore, the relative difference between both circulation curves is much smaller and decreases when the velocity ratio is lifted. This is explained by the starting jet approaching the limiting case of $r \to \infty$ where it is ejected into quiescent surroundings and symmetrical vortex rings are generated. In that particular case, the curves for the produced circulation in both half planes are identical.

Now, we turn our attention to the circulation associated with the vortex rings. Initially, they absorb the entire vorticity as the circulation of starting jets and vortex rings are almost equal for all configurations at small formation times. For $r \approx 4.7$, a maximum of vortex ring circulation is reached around $\tau \approx 8$, i.e. during the ongoing emission of fluid. This time instance is marked by a grey vertical in figure 15. Subsequently, secondary regions of negative vorticity develop inside the recirculation zone downstream of the outlet, and the thin upstream shear layer becomes stretched so that outer areas fall below the vorticity threshold and are not considered part of the vortex ring. Qualitatively, the same behaviour is found for the two larger velocity ratios. However, the maxima in vortex ring circulation associated with negative vorticity are gradually increased as the characteristic formation time is enlarged to $\tau \approx 12$ ($r \approx 7.6$) and $\tau \approx 13$ ($r \approx 11.0$).

To summarise the discussion of the circulation generation, the following points can be noted. Given the influence of the velocity ratio on generated flow structures, the two regimes identified above exhibit different characteristics in terms of the circulation
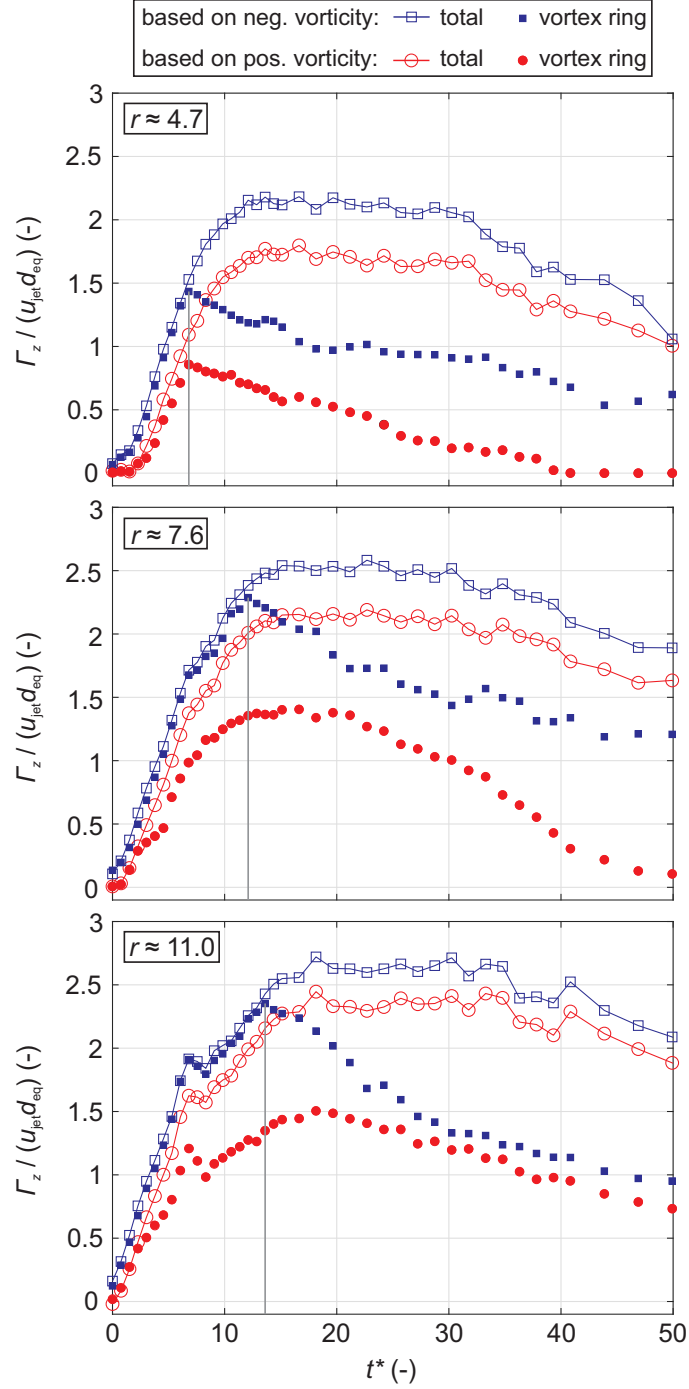
FIGURE 15. Temporal evolution of circulation associated with non-parallel planar starting JsICF at velocity ratios $r > 4$; vertical grey lines mark the characteristic formation times associated with maximum vortex ring circulation τ

development. At $r < 4$, the relative deviation in circulation associated with positive and negative vorticity is much larger, and the maximum achievable circulation is also distinctly influenced by the velocity ratio. At larger velocity ratios ($r > 4$) on the other hand, the jet is capable of penetrating through the crossflow boundary layer, and vortex rings are generated. The maximum normalised circulation associated with negative
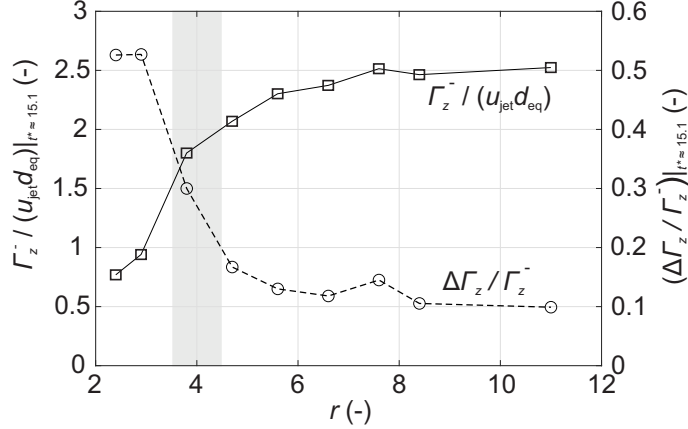
B. Steinfurth, J. Weiss

FIGURE 16. Influence of velocity ratio on circulation at the end of the jet emission phase $\Gamma_z^-(t^* \approx 15.1)$ and relative deviation between circulation associated with windward and leeward part of starting jets $\Delta\Gamma_z/\Gamma_z^-$

vorticity converges to a value of $\Gamma_z/(u_{\text{jet}}d_{\text{eq}}) = 2.5$ at the end of the jet emission phase, i.e. at $t^* \approx 15.1$, and the relative deviation in circulation between the two parts of the jet approaches a value of 10 %.

This is illustrated in figure 16 where Γ_z^- is the total circulation associated with negative vorticity and $\Delta\Gamma_z = (\Gamma_z^- - \Gamma_z^+)$ is the deviation in circulation between both parts of the starting jet. The transitional regime where neither hairpin vortices nor distinct vortex rings are generated is highlighted by a shaded region in the figure.

4.4. Jet trajectories

Finally, we briefly discuss the jet trajectories subject to a varied velocity ratio where the two regimes of starting jet appearance will again be addressed separately. As summarised by Mahesh (2013), different definitions of JICF trajectories exist. Here, we follow the method introduced by Ostermann *et al.* (2019) and consider virtual seeding particles emitted through the PJA outlet that are advected according to the measured time-resolved velocity data. We then define the trajectory as the connecting line between particle locations with the largest wall distance y_{max} for all streamwise positions. The obtained trajectories can therefore be regarded as envelopes of the flow regions affected by the starting JsICF. Using the common scaling with the product of velocity ratio and characteristic length scale suggested by Smith & Mungal (1998)

$$\frac{y_{\text{max}}}{rd} = A\left(\frac{x}{rd}\right)^B, \tag{4.1}$$

the jet trajectories for selected velocity ratios are shown in figure 17. The shaded region indicates the ranges for the constants $A = 1.2\ldots2.6$ and $B = 0.28\ldots0.34$ based on steady JICF experiments with various boundary conditions compiled by Margason (1993).

As for the smaller velocity ratios of $r < 4$, the measured trajectories are located around the lower boundary applicable to steady JsICF. Furthermore, the applied scaling appears to be inappropriate as the jet envelopes become steeper when the velocity ratio is raised. This is linked with the effect of vorticity cancellation that affects the smaller velocity ratios in a disproportionate fashion. The scaling leads to almost collapsing curves for the larger velocity ratios of $r > 4$. However, large deviations occur in the near-field region where the trajectories are almost vertical for the largest velocity ratios.
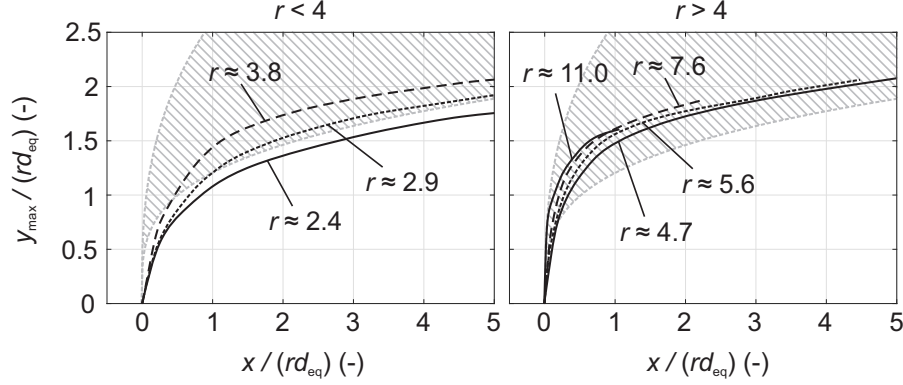
FIGURE 17. Scaled jet envelopes inside the symmetry plane for different velocity ratios; shaded region represents parameter ranges applicable to steady JsICF

Here, the jet envelopes are well within the parameter ranges established by Margason (1993).

To sum up, in none of the configurations studied here, the range of trajectories established for steady JsICF is exceeded. This may come as a surprise since Johari *et al.* (1999) attest a substantial enhancement of the trajectory steepness when starting jets with small pulse durations are emitted. We provide two explanations. First, the potential core of the starting jets in the current study is extremely small due to the slit-shaped outlet geometry. Hence, the velocity decay for a given shear layer growth rate is enhanced compared to larger, circular outlets, and the penetration depth is not as deep. Second, the pulse duration applied in the current study is relatively small, and we recently noted that steeper jet trajectories may in fact be observed when the stroke ratio is slightly increased (Steinfurth & Weiss (2020a)).

5. Concluding remarks

In this article, we addressed the interaction between a steady crossflow and starting jets generated with a device typically used in AFC applications, emitting compressed air for relatively small pulse durations through a $20\,\text{mm} \times 0.5\,\text{mm}$ rectangular outlet. It was recently shown by Steinfurth & Weiss (2020b) that this flow significantly differs from starting jets usually studied in the academic environment. The major difference is a distinct over-pressure peak during jet initiation that causes a rapid transverse vorticity flux as high-circulation, thick-cored vortex rings are generated when emitted into still ambience. The objective in the current effort was to identify the influence of a crossflow on the generation of these vortex rings. One starting jet configuration with a fixed degree of over-pressure was investigated, and the velocity ratio between jet and crossflow was varied in the range $r = 2.4 \ldots 11$ by adjusting the crossflow velocity.

The experimental investigation showed that flow structures generated with the PJA are distinctly influenced by the velocity ratio as we identified two regimes of different characteristics. The classification map for non-parallel planar starting JsICF shown in figure 18 can be viewed as the pendant to the classification established by Sau & Mahesh (2008) who investigated JsICF with fundamentally different boundary conditions. Firstly, they modelled a laminar boundary layer with a much smaller thickness compared to the outlet dimension $\delta_{99}/D \approx 0.1$. Second, the starting jets investigated in their numerical
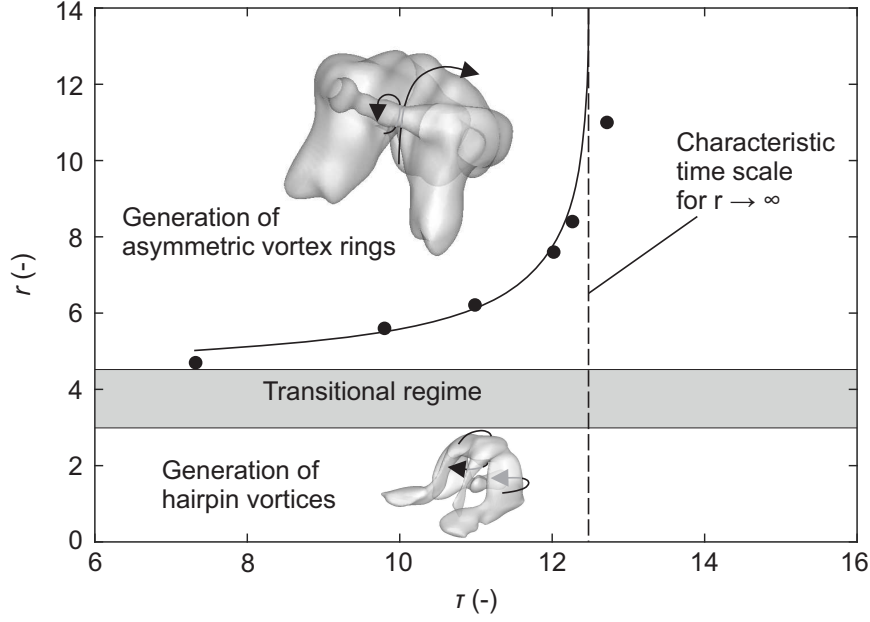
FIGURE 18. Classification map for non-parallel planar starting jets in crossflow

simulations were emitted through a circular outlet with an assumedly negligible degree of non-parallel flow. In our study, boundary conditions representative of typical AFC applications were chosen. To this end, a slit-shaped outlet geometry was studied where the rapid initial acceleration of fluid leads to significantly altered jet properties as explained above. Furthermore, the boundary layer was turbulent, and the relative thickness at small velocity ratios was approximately two orders of magnitude larger ($\delta_{99}/d \approx 10$), given the relatively small outlet width of $d = 0.5\,\text{mm}$. Considering these drastic differences, it may come as a surprise that similar flow structures are observed as the classification map can be transferred with some adjustments that are discussed in the following.

At small velocity ratios of $r < 3$, a complete cancellation of vorticity between the turbulent crossflow boundary layer and the upstream part of the starting jet shear layer takes place. As a result, no positive vorticity is generated as the windward side of the jet is diminished during the entire emission phase. The same mechanism was observed by Sau & Mahesh (2008). However, in their direct numerical simulation of circular starting jets, the suppression of positive vorticity occured at smaller velocity ratios of $r < 2$. This deviation is explained by the difference in crossflow boundary layer thicknesses stated above as a thinner initial shear layer may be diminished at larger velocity ratios. Despite the deviations regarding the limiting velocity ratio and the outlet geometry, the generated flow structures at these small velocity ratios are very similar as hairpin vortices were identified by performing a tomographic reconstruction of the three-dimensional velocity field in the current study.

Time-resolved measurements showed that the delay between the onset of jet emission and the roll-up of fluid upstream of the outlet shortens when the velocity ratio is increased. At slightly larger velocity ratios of $r \approx 4$, the topology of the produced flow structures transitions as the jets are capable of penetrating through the crossflow boundary layer. At $r \approx 4.7$, asymmetric vortex rings occur for a short duration before the thinner vortex core on the windward side is dissolved by the crossflow. Naturally, the asymmetry decreases for larger velocity ratios and the relative deviation between the circulation associated with the windward and leeward sides of the vortex ring converges

to approximately 10%. Furthermore, the maximum circulation only marginally increases when the velotiy ratio is raised. This is in agreement with observations regarding the characteristic time scale corresponding to maximum vortex ring circulation τ. The smallest value of $\tau \approx 8$ is noted for $r \approx 4.7$. For larger velocity ratios, τ increases as the vortex rings absorb vorticity for an increasing amount of time. It converges towards a value of $\tau \approx 13$ as the starting jet approaches the limiting case of $r \to \infty$, i.e. zero crossflow. A similar behaviour was also documented by Sau & Mahesh (2008) for parallel circular starting jets where the characteristic time scale converges to the universal formation number established by Gharib *et al.* (1998) ($\tau \approx 4$) when the influence of the crossflow is decreased.

In terms of the penetration into the crossflow, we expectedly found steeper jet trajectories when the velocity ratio was increased. However, no collapse in these curves is noted for small velocity ratios ($r < 4$) when scaled with the product of velocity ratio and equivalent diameter whereas the far field behaviour is mapped reasonably well for $r > 4$. Furthermore, the jet trajectories did not exceed the range in penetration depths for steady JsICF established by Margason (1993). This is mainly explained by the small potential core width due to the high-aspect ratio PJA-outlet, resulting in an increased velocity decay as was shown by Mi *et al.* (2005) for the case of zero-crossflow. This results in a decreased distance between the wall and generated vortex structures from which certain separation control applications where a momentum transfer towards the wall is desired may even benefit.

In general, the results presented in this study are relevant to AFC applications. First, the knowledge regarding a minimum velocity ratio required to produce vortex rings may prove useful as this flow structure is often associated with the desired control authority. However, we expect that this characteristic velocity ratio may be affected when boundary conditions are altered. In particular, the influence of an adverse pressure gradient and the jet emission angle relative to the free stream must be addressed in the future. Second, the efficiency of AFC efforts may be enhanced based on the identified characteristic time scales as the amount of fluid can be adjusted to exclusively generate leading vortex rings without the occurence of a trailing jet structure that is only produced at larger pulse durations. This is based on the assumption that the control effectivity of non-parallel planar starting JsICF is indeed governed by the leading vortex ring - a hypothesis that must be reassessed in the future.

Declaration of interests

The authors report no conflict of interest.

Acknowledgements

REFERENCES

AFANASYEV, Y. D. 2006 Formation of vortex dipoles. *Phys. Fluids* **18**.
BIDAN, G. & NIKITOPOULOS, D. E. 2013 On steady and pulsed low-blowing-ratio transverse jets. *J. Fluid Mech.* **714**, 393–433.

24   *B. Steinfurth, J. Weiss*

Chang, Y. K. & Vakili, A. D. 1995 Dynamics of vortex rings in crossflow. *Phys. Fluids* **7** (7), 1583–1597.

Coulthard, S. M., Volino, R. J. & Flack, K. A. 2006 Effect of jet pulsing on film cooling - Part I: Effectiveness and flow-field temperature results. *J. Turbomach.* **129** (2), 232–246.

Coussement, A., Gicquel, O. & Degrez, G. 2012 Large eddy simulation of a pulsed jet in cross-flow. *J. Fluid Mech.* **695**, 1–34.

Dabiri, J. O. & Gharib, M. 2004 Fluid entrainment by isolated vortex rings. *J. Fluid Mech.* **511**, 311–331.

Didden, N. 1979 On the formation of vortex rings: rolling-up and production of circulation. *Z. Angew. Math. Phys.* **30**, 101–116.

Ekkad, S. V., Ou, S. & Rivir, R. B. 2006 Effect of jet pulsation and duty cycle on film cooling from a single jet on a leading edge model. *J. Turbomach.* **128** (3), 564–571.

Eroglu, A. & Breidenthal, R. E. 2001 Structure, penetration, and mixing of pulsed jets in crossflow. *AIAA J.* **39** (3), 842–850.

Fernández, J. J. P. & Sesterhenn, J. 2017 Compressible starting jet: pinch-off and vortex ring–trailing jet interaction. *J. Fluid Mech.* **817**, 560–589.

Fric, T. F. & Roshko, A. 1994 Vortical structure in the wake of a transverse jet. *J. Fluid Mech.* **279**, 1–47.

Gharib, M., Rambod, E. & Shariff, K. 1998 A universal time scale for vortex ring formation. *J. Fluid Mech.* **360**, 121–140.

Gordon, M., Cater, J. E. & Soria, J. 2004 Investigation of the mean passive scalar field in zero-net-mass-flux jets in cross-flow using planar-laser-induced fluorescence. *Phys. Fluids* **16**.

Greenblatt, D. & Wygnanski, I. J. 2000 The control of flow separation by periodic excitation. *AIAA J.* **36**, 487–545.

Hecklau, M., Salazar, D. P. & Nitsche, W. 2010 *Influence of the Actuator Jet Angle on the Reattachment Process with Pulsed Excitation*. Berlin, Heidelberg: Springer.

Hermanson, J. C., Wahba, A. & Johari, H. 1998 Duty-cycle effects on penetration of fully modulated, turbulent jets in crossflow. *AIAA J.* **36** (10), 1935–1937.

Hunt, J. C. R., Wray, A. A. & Moin, P. 1988 Eddies, stream, and convergence zones in turbulent flows. In *Center for Turbulence Research Report CTR-S88*.

Hussain, F. & Husain, H. S. 1989 Elliptic jets. Part 1. characteristics of unexcited and excited jets. *J. Fluid Mech.* **208**, 257–320.

Johari, H. 2006 Scaling of fully pulsed jets in crossflow. *AIAA J.* **44** (11), 842–850.

Johari, H., Pacheco-Tougas, M. & Hermanson, J. C. 1999 Penetration and mixing of fully modulated turbulent jets in crossflow. *AIAA J.* **37** (7), 2719–2725.

Karagozian, A. R. 2014 The jet in crossflow. *Phys. Fluids* **26**.

Krieg, M. & Mohseni, K. 2013 Modelling circulation, impulse and kinetic energy of starting jets with non-zero radial velocity. *J. Fluid Mech.* **719**, 488–526.

Krueger, P. S. 2005 An over-pressure correction to the slug model for vortex ring circulation. *J. Fluid Mech.* **545**, 427–443.

Krueger, P. S., Dabiri, J. O. & Gharib, M. 2006 The formation number of vortex rings in uniform background coflow. *J. Fluid Mech.* **556**, 1271–1281.

Lim, T. T., Lua, K. B. & Thet, K. 2008 Does Kutta lift exist on a vortex ring in a uniform cross flow? *Phys. Fluids* **20**.

Mahesh, K. 2013 The interaction of jets with crossflow. *Annu. Rev. Fluid Mech.* **45**, 379–407.

Margason, R. J. 1993 Fifty years of jet in cross flow research. *AGARD Conference* **538**, 15–32.

M'Closkey, R. T., King, J. M., Cortelezzi, L. & Karagozian, A. R. 2002 The actively controlled jet in crossflow. *J. Fluid Mech.* **452**, 325–335.

Mi, J., Deo, R. C. & Nathan, G. J. 2005 Characterization of turbulent jets from high-aspect-ratio rectangular nozzles. *Phys. Fluids* **17** (6).

Milanovic, I. M. & Zaman, K. B. M. Q. 2005 Synthetic jets in crossflow. *AIAA J.* **43** (5), 929–940.

Muldoon, F. & Acharya, S. 2010 Direct numerical simulation of pulsed jets-in-crossflow. *Comput. Fluids* **39**, 1745–1773.

Norbury, J. 1973 A family of steady vortex rings. *J. Fluid Mech.* **57** (3), 417–431.

O'FARRELL, C. & DABIRI, J. O. 2014 Pinch-off of non-axisymmetric vortex rings. *J. Fluid Mech.* **740**, 61–96.

OSTERMANN, F., WOSZIDLO, R., NAYERI, C. N. & PASCHEREIT, C. O. 2019 The interaction between a spatially oscillating jet emitted by a fluidic oscillator and a cross-flow. *J. Fluid Mech.* **863**, 215–241.

PASCHEREIT, C. O., WYGNANSKI, I. & FIEDLER, H. E. 1995 Experimental investigation of subharmonic resonance in an axisymmetric jet. *J. Fluid Mech.* **283**, 365–407.

ROCKWOOD, M. P., LOISELLE, T. & GREEN, M. A. 2019 Practical concerns of implementing a finite-time lyapunov exponent analysis with under-resolved data. *Exp. Fluids* **60**.

ROSENFELD, M., RAMBOD, E. & GHARIB, M. 1998 Circulation and formation number of laminar vortex rings. *J. Fluid Mech.* **376**, 297 – 318.

SAU, R. & MAHESH, K. 2007 Passive scalar mixing in vortex rings. *J. Fluid Mech.* **582**, 449–461.

SAU, R. & MAHESH, K. 2008 Dynamics and mixing of vortex rings in crossflow. *J. Fluid Mech.* **604**, 389–409.

SMITH, S. H. & MUNGAL, M. G. 1998 Mixing, structure and scaling of the jet in cross-flow. *J. Fluid Mech.* **357**, 83–122.

STEINFURTH, B. & WEISS, J. 2020*a* Efficient vortex ring generation with non-parallel planar starting jets in crossflow. In *AIAA Scitech 2020 Forum*.

STEINFURTH, B. & WEISS, J. 2020*b* Vortex rings produced by non-parallel planar starting jets. *J. Fluid Mech.* **903**.

VERMEULEN, P. J., ODGERS, J. & RAMESH, V. 1987 "full-load" operation of a gas turbine combustor with acoustically controlled dilution-air mixingl. *Int. J. Turbo Jet Eng.* **4** (1–2), 139–148.

WESTERWEEL, J. 2008 On velocity gradients in PIV interrogation. *Exp. Fluids* **44**, 831–842.

Boundary-Layer Control by Means of Pulsed Jets at Different Inclination Angles

Ben Steinfurth[*] and Julien Weiss[†]
Technical University of Berlin, 10587 Berlin, Germany

https://doi.org/10.2514/1.J060474

Finite amounts of compressed air are impulsively emitted through a rectangular 20×0.5 mm outlet at an axial velocity of $u_{jet} \approx 54$ m/s. Their interaction with a steady crossflow with a zero-pressure-gradient turbulent boundary layer is studied on the basis of phase-locked particle image velocimetry measurements for a parameter space that is spanned by the jet inclination angle defined with respect to the surface tangent downstream of the outlet $\alpha = (60, 30)$ deg and the ratio between the axial jet velocity and the crossflow velocity $r = 2.4 \ldots 11$. Two types of vortex structures are observed. For $\alpha = 60$ deg, $r > 6.5$, jets penetrate into the crossflow, and distinct, asymmetrical vortex rings are produced. For $\alpha = 60$ deg, $r < 3$ as well as for $\alpha = 30$ deg, $r = 2.4 \ldots 11$, starting jets attach to the wall as leading vortex half-rings are formed. The latter type is better suited to energize the boundary layer as low-momentum fluid is shifted away from the surface and high-momentum fluid from the freestream is entrained into the jet wake. In terms of the overall gain in streamwise momentum, the impulse provided due to overpressure during the rapid jet initiation is of major importance in the present study, and its exploitation may enable a significant enhancement in future flow control applications.

Nomenclature

A_{jet}	=	jet outlet area, m^2
c_μ	=	momentum flux coefficient
d	=	outlet width, m
d_{eq}	=	equivalent outlet diameter, m
d_{99}	=	boundary-layer thickness, m
f_p	=	pulsation frequency, s^{-1}
I	=	total impulse applied to flowfield, (kg · m)/s
I_p	=	impulse due to overpressure, (kg · m)/s
$I_{U.jet}$	=	impulse due to momentum flux, kg/m/s
L	=	length of virtually emitted fluid column, m
l	=	outlet length, m
N	=	number of snapshots
p	=	pressure in outlet plane, kg/(m · s^2)
p_∞	=	stagnation pressure, kg/(m · s^2)
r	=	velocity ratio between jet and crossflow
T	=	pulsation period, s
t	=	time, s
t_p	=	pulse duration, s
t^*	=	nondimensional formation time
U_∞	=	crossflow velocity, m/s
u, v, w	=	Cartesian velocity components, m/s
u_c	=	convective velocity, m/s
u_{jet}	=	axial jet velocity, m/s
x, y, z	=	Cartesian coordinates, m
α	=	jet inclination angle, deg
β	=	jet pitch angle, deg
Γ	=	circulation, m^2/s
Δt	=	time interval, s
$\Delta x, \Delta y, \Delta z$	=	spatial distances in Cartesian coordinates, m
ΔI_x	=	difference in streamwise momentum, (kg · m)/s
δ	=	boundary-layer momentum thickness, m
δ_{99}	=	99% boundary-layer thickness, m
ϱ	=	volumetric mass density, kg/m^3
λ	=	duty cycle
ν	=	kinematic viscosity, m^2/s
ω_z	=	Cartesian vorticity component, s^{-1}

I. Introduction

THE application of vortex generators is a well-established method in preventing or delaying boundary-layer separation. Passive vortex generators (PVGs) typically consist of small triangular vanes that are mounted on the surface close to the suspected separation line and have been successfully employed in various flow configurations [1–3]. Often not exceeding the logarithmic region of the boundary layer, they generate streamwise vortices, effectively shifting high-momentum fluid toward the wall, and thereby energizing the boundary layer. A lack of adaptability, however, may be viewed as their major shortcoming. Once designed, they usually cannot be adjusted to varying boundary conditions: for instance, a nonconstant pressure gradient. Furthermore, parasitic drag is generated in working conditions where the flow is naturally attached.

A priori, similar drawbacks are not present when measures of active flow control (AFC) are employed. Here, an external energy source is required to modify the boundary layer. Although many tools of AFC [or, more specifically, boundary-layer control (BLC)] are available [4], we here restrict ourselves to the injection of fluid into a crossflow through outlets in the surface. Such jets are commonly referred to as active vortex generators (AVGs) or vortex generator jets in the literature. The steady jet in crossflow that is introduced in the wall-normal direction can be seen as the canonical representation of an AVG. Its topology is well known, largely thanks to the work of Fric and Roshko [5], and it resembles that produced by PVGs because a counter-rotating vortex pair is observed to persist far downstream of the jet orifice.

Whereas a steep jet trajectory and substantial mixing achieved by wall-normal transverse jets are desired in certain scenarios, the jet is typically inclined with respect to the freestream in BLC applications. First, vortex structures responsible for the transport of high-momentum fluid are then located closer to the wall. Second, the kinetic energy associated with the boundary layer, both upstream and downstream of the outlet, may be enhanced directly by the ejected fluid.

The first implementation of an inclined AVG was arguably performed by Wallis [6], reporting beneficial effects in shock-induced separation control experiments when the circular outlet of his device was inclined in the crossflow direction compared to transverse jets. Since then, many experimental [7–12] and numerical [13,14] studies of steady AVGs have been aimed at identifying the influence of the

initial jet direction that can be defined by two angles. Here, we refer to the angle enclosed by the axial jet velocity and the surface tangent downstream of the orifice as the inclination angle α, whereas the pitch angle β reflects the lateral deviation from the freestream direction. In terms of the inclination angle, it has been shown that vortex structures are indeed located closer to the surface when α is decreased but also become weaker and decay faster compared to transverse jets in crossflow [15]. Increasing the pitch angle β, on the other hand, can enhance the jet spreading in spanwise direction [16]. A theoretical model for jet trajectories as a function of α and β is provided in Ref. [17], also taking into account the velocity ratio between the jet and crossflow: $r = u_{\text{jet}}/U_\infty$. The latter quantity not only affects the penetration depth but also the appearance of flow structures because hairpin vortices are observed at small velocity ratios, whereas a counter-rotating vortex pair is produced otherwise [18,19].

Even though steady AVGs have been employed successfully, applying a time-dependent jet velocity is usually the more effective and efficient method. Various demonstrations of this technique have been performed [20–22], and a comprehensive overview is provided by Greenblatt and Wygnanski [23]. In particular, pulsed excitation where fluid is accelerated rapidly and only ejected during confined time intervals may be used to great effect. Here, the normalized supplied momentum flux $c_\mu = c_\mu(u_{\text{jet}}^2)$ is larger than for steady AVGs at a given mean mass flow rate (hence increased jet velocity). In addition to that, two further aspects explain the superior control authority of pulsed AVGs compared to their steady counterparts. First, the actuation frequency can be set to exploit inherent flow instabilities and initiate an enhanced mixing layer [24,25]. Second, pulsed AVGs represent starting jets where fluid is forced from an initial state of rest. Thus, large-scale vortex rings are generated, typically yielding enhanced diffusive and convective entrainment rates compared to those found in steady jets [26].

Among other BLC devices, pulsed jet actuators (PJAs) represent a technical implementation of an unsteady AVG. Consisting of a fast-switching valve and a nozzle with a slit-shaped outlet, PJAs have been used in past separation control experiments [27–30]. Contrasting with synthetic jet actuators [31], plasma actuators [32,33], and fluidic devices [34,35] that also allow for a periodic flowfield manipulation, PJA-generated starting jets are characterized by a more rapid acceleration of fluid. Recent fundamental experiments have shown that this acceleration may cause major differences in terms of the generated vortex structures. When emitted into still ambience, the axial and transverse velocity components are of similar magnitude in the outlet plane; i.e., highly nonparallel flow is present. As a result, thick-cored almost spherical, vortex rings are generated despite the high-aspect-ratio outlet geometry typical of PJAs [36]. When these jets are emitted transversely into a steady crossflow (i.e., at $\alpha = 90$ deg), two regimes of vortex structures can be noted, depending on the velocity ratio. At $r < 4$, cancellation of vorticity between the boundary layer and the windward side of the starting jet dominates, and hairpin vortices are produced close to the wall. At $r > 4$, the starting jet penetrates through the boundary layer as asymmetrical vortex rings are observed [37].

The properties of such pulsed jets are strongly affected by a short-duration overpressure peak inside the outlet plane during jet initiation. This exit overpressure is a manifestation of the force required to produce the specific flow, namely, to accelerate a certain amount of fluid that is either entrained by the vortex sheet rollup (entrained mass) or accelerated radially along the starting jet propagation front and sucked in on the jet trailing side, respectively (added mass) [38,39]. The latter component can be viewed as an analog to the added mass associated with Lagrangian drift induced by a solid body in irrotational flow [40,41]. In general, overpressure leads to an enhanced circulation flux due to increased velocity gradients in the jet exit plane [42,43]. Second, and perhaps more importantly for BLC, the impulse provided by a PJA of $I = I_{U,\text{jet}} + I_p$ is enhanced because, in addition to the flux term

$$I_{U,\text{jet}} = \varrho \int_0^{t_p} \int_{A_{\text{jet}}} u_{\text{jet}}^2 \, dA \, dt \qquad (1)$$

associated with the ejected mass flow, a pressure impulse

$$I_p = \int_0^{t_p} \int_{A_{\text{jet}}} (p - p_\infty) \, dA \, dt \qquad (2)$$

occurs [38]. Here, ϱ is the fluid density, t_p is the pulse duration, A_{jet} is the outlet area, p is the pressure inside the exit plane, i.e., at $x = 0$ and p_∞ the stagnation pressure at $x \to \infty$. The additional impulse in Eq. (2) depends on the amount of added and entrained mass, and is therefore enhanced by the formation of leading vortical structures; whereas it is negligible for the trailing jet ejected subsequently [38]. Being on the order of the flux term or even larger [43,44], it may be used as a means of thrust augmentation for the propulsion of underwater vehicles [45,46], perhaps inspired by the locomotion of aquatic animals [47].

To advance the fundamental knowledge of pulsatile starting jets in an AFC context, two major objectives are pursued in the current paper. First, we transfer the recent results regarding fundamental jet properties to flow configurations that are more relevant to BLC applications. To this end, three-dimensional flow structures are analyzed for inclined starting jets at angles of $\alpha = (60, 30)$ deg and velocity ratios within the interval $r = 2.4 \ldots 11$. Then, we identify parameter combinations that are beneficial for BLC by analyzing the momentum gain inside the near-wall region. The parameter space was chosen to reflect conditions relevant to AFC applications. However, we limit ourselves to the investigation of single-pulse jets in this paper; i.e., the interaction between successively generated flow structures is not considered.

II. Methods

This section contains documentation of the measurement setup and procedure.

Starting jets were generated with the pulsed jet actuator are shown in Fig. 1. It mainly consists of a fast-switching solenoid valve, allowing for minimum pulse durations of $t_p = 0.6$ ms at a maximum inaccuracy of $\pm 15\%$ and a three-dimensionally (3-D) printed nozzle transforming the circular inlet cross section into a rectangular outlet with an aspect ratio of $l/d = 20 \text{ mm}/0.5 \text{ mm} = 40$. The surface roughness inside the nozzle was $Ra < 2.5$ μm. With respect to the longer slot dimension, a homogenous jet velocity is achieved by deflecting the flow inside the nozzle by means of two backward-facing steps, which may result in minor recirculation zones. A detailed analysis of the specific near-outlet flow is provided in Ref. [36]. In summary, we noted a large transverse advection of fluid (i.e., highly nonparallel flow) due to an overpressure peak inside the jet exit plane. This is assumedly linked with the PJA function principle where fluid is accelerated more rapidly compared to other means of generating starting jets. For a given nozzle geometry, the magnitude of overpressure, or the degree of nonparallel flow, can be altered by changing actuation parameters. It is particularly affected by the jet velocity and the duty cycle, i.e., the pulse width relative to the excitation period. Since the exact influence of such variations on generated vortex structures is yet unknown, a fixed starting jet configuration is investigated here. The nominal jet velocity of $u_{\text{jet}} \approx 54$ m/s was set with a maximum inaccuracy of ± 0.4 m/s using a mass flow controller, taking into account the jet outlet area, the pulse width of $t_p = 1$ ms, and the actuation frequency of $f_p = 50$ Hz. The resulting actuation period was $T = 20$ ms, and the duty cycle was $\lambda = t_p/T = 0.05$. No interaction between successively generated starting jets takes place due to this relatively small duty cycle and the convective velocities on hand.

Being a measure for the mass flow consumption per starting jet, the equivalent stroke ratio was $L/d_{\text{eq}} = (u_{\text{jet}} t_p)/d_{\text{eq}} \approx 15.1$, where $d_{\text{eq}} \approx 3.57$ mm is the equivalent diameter of a circle with the same area as the PJA outlet. The specific stroke ratio was chosen because it leads to the generation of maximum-circulation vortex rings as well as a trailing jet in quiescent ambience and for $\alpha = 90$ deg [37]. When discussing the temporal evolution of flowfields, the nondimensional formation time of $t^* = t u_{\text{jet}}/d_{\text{eq}}$ is referred to, where $t = 0$ s marks
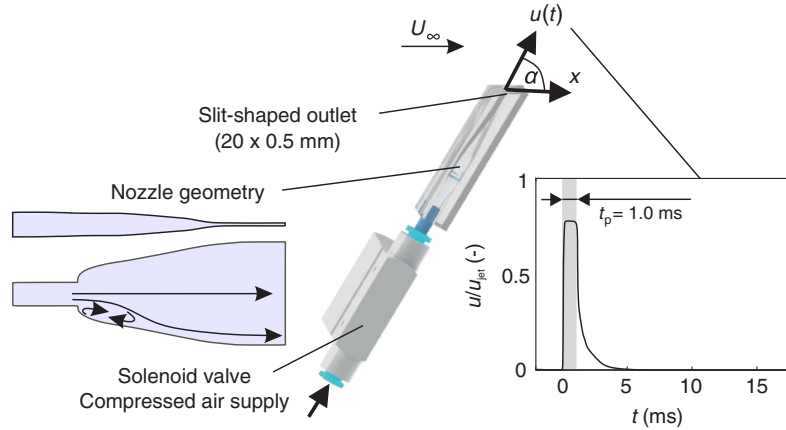
Fig. 1 Pulsed jet actuator and velocity signal; adapted with permission from Steinfurth and Weiss (Journal of Fluid Mechanics, 2021) [37].

the beginning of the jet emission phase; and the end of jet emission where $t = t_p$ is denoted by $t^* = L/d_{eq}$.

The PJA was mounted flush in the flat splitter plate inside the closed test section of a low-speed wind tunnel. This was possible due to the slanted front side shown in Fig. 1. Whereas the pitch angle β was zero during the entire study, two inclination angles of $\alpha = (30, 60)$ deg were investigated, which were enclosed by the axial jet velocity inside the outlet plane and the wall downstream of the orifice. In addition to the jet emission angle, the velocity ratio between the jet and crossflow of $r = u_{jet}/U_\infty$ was varied. Since the jet velocity was fixed, this was achieved by adjusting the freestream velocity to within $\pm 1\%$ uncertainty in the wind tunnel. The distance between the splitter plate and the test section ceiling was $\Delta y = 250$ mm, which exceeded the steepest studied jet trajectory at the location of the largest wall distance by a factor of five. No blockage correction was applied. A transition fixation upstream of the jet outlet was applied to ensure a turbulent-state boundary layer for all configurations. The boundary-layer thickness was found to be $\delta_{99} \approx 10d$ for all configurations. The momentum thickness at the jet outlet was on the order of $\delta \approx 0.5$ mm, and the resulting Reynolds numbers were in the range of $Re_\delta = (U_\infty \delta)/\nu \approx 250 \ldots 750$, depending on the crossflow velocity. The investigated configurations are listed in Table 1.

The experimental data were acquired by performing particle image velocimetry (PIV) measurements. In addition to two-dimensional two-component (2D2C) velocity fields measured for all starting jets, the three-dimensional domain was reconstructed based on three-dimensional three-component (3D3C) data for selected cases. Aerosol seeding particles were added both to the crossflow and to the PJA supply mass flow. These were successively illuminated in longitudinal measurement planes at $z = (0, -2, \ldots, -20, -25)$ mm with a dual-pulsed laser (Fig. 2). Two cameras with a resolution of [2560×2160] pixels^2 were employed to record images of the tracers. Multiple cross correlation via cyclic fast Fourier transform algorithms with an eventual interrogation window size of (32×32) pixels^2 was performed, yielding a velocity field resolution of $\Delta x = \Delta y \approx 0.58$ mm. No window deformation scheme was employed. To gain information on the dynamical behavior of generated vortex structures and adequately resolve the actuation period in time, phase-locked measurements were conducted. With respect to the rising edge

driving the solenoid valve, the PIV system was triggered at defined delay times. The phases, however, were not equidistantly distributed across the pulsation period but adjusted to the rate of change of relevant physical quantities inside the measurement domain. Thus, the temporal resolution was as high as $\Delta t = 0.05$ ms during the ejection of fluid while gradually being decreased to $\Delta t = 2$ ms for time intervals where flow structures of interest have been convected outside the measurement plane. Furthermore, the number of recordings per phase N was adjusted to ensure sufficient mean data convergence. This was achieved with $N = 90$ images during the ongoing jet emission and $N = 50$ for the remaining phases. The maximum uncertainty is $\pm 3\%$ for instantaneous in-plane velocity components, i.e., for u and v and $\pm 5\%$ for the derived out-of-plane component w.

To analyze the dynamical behavior inside the volumetric domain spanned by PIV measurement planes, finite-time Lyapunov exponent (FTLE) fields were deduced based on 3D3C velocity fields. To obtain this quantity, the advection of virtual tracer particles with an initial spacing of $\Delta x = \Delta y = \Delta_z = 0.3$ mm was computed backward in time using a fourth-order Runge–Kutta scheme across a duration of $\Delta t = -3$ ms based on the phase-averaged velocity fields obtained with PIV. The detailed procedure is explained in Ref. [36].

III. Results

The major findings regarding pulsed jets introduced into a crossflow under inclination angles of $\alpha = (60, 30)$ deg are presented in the following. The section is divided into two parts. First, we assess the flow structures generated for both inclination angles subject to a varied velocity ratio. Then, implications for separation control applications are addressed, primarily by focusing on the gain in streamwise momentum due to the starting jets.

Table 1 Investigated parameter configurations

α, deg	u_{jet}, m/s	U_∞, m/s	$r = u_{jet}/U_\infty$	Velocity field information
(60, 30)	54	22.9	2.4	2D2C, 3D3C
(60, 30)	54	18.9	2.9	2D2C
(60, 30)	54	11.4	4.7	2D2C, 3D3C
(60, 30)	54	8.2	6.6	2D2C
(60, 30)	54	4.9	11.0	2D2C, 3D3C
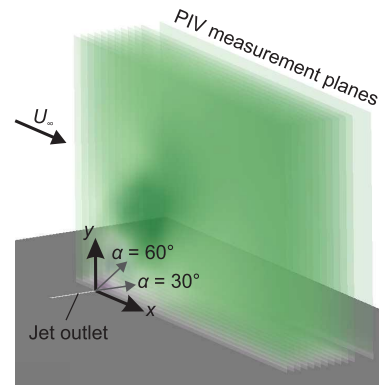
Fig. 2 Measurement setup; based on depiction in Ref. [37].

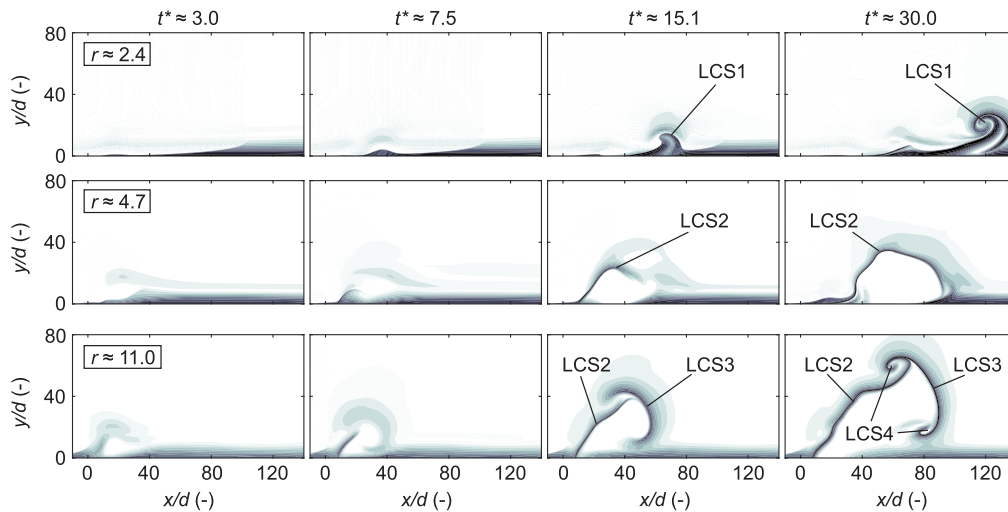**Fig. 3 Development of FTLE fields in symmetry plane for $\alpha = 60$ deg, color bar is within the range of FTLE $= 0 \ldots 1 \ \mathrm{m \cdot s^{-1}}$ (white to black).**

A. Generated Vortex Structures

Employing appropriate flow diagnostics, such as the finite-time Lyapunov exponent and the Q criterion [48], focus is laid upon the vortical structures induced by PJA-generated starting jets in the following. Note that results regarding the two investigated inclination angles are discussed in a separate manner. A movie, visualizing flow structures for the larger inclination angle, is provided in Ref. [49].

1. Jet Inclination Angle $\alpha = 60$ Degrees

The temporal evolution of FTLE fields for $\alpha = 60$ deg subject to different velocity ratios is shown in Fig. 3. This quantity enables an investigation of transport mechanisms inside the flowfield as dominant material lines are revealed as ridges. Here, they represent attractors to which fluid particles converge at an exponential rate while acting as transport barriers with negligible flux across them [50]. Recall that jet emission starts at $t^* \approx 0$ and stops at $t^* \approx 15.1$.

At the smallest velocity ratio of $r \approx 2.4$, the impact on the crossflow is minor at first. This may be attributed to a cancellation between vorticity associated with the starting jet and the crossflow boundary layer previously observed for small velocity ratio jets at $\alpha = 90$ deg [37]. However, at later time steps, the rollup of a vortex structure in the jet symmetry plane is indicated by a dominant Lagrangian coherent structure (LCS), highlighted as LCS1 in Fig. 3. Whereas the generation of hairpin vortices associated with negative vorticity was observed for $\alpha = 90$ deg, the spanwise vorticity component appears to be of the opposite sign here. This will be addressed in more detail later on.

Completely different transport characteristics can be noted for the medium velocity ratio of $r \approx 4.7$, where LCS2 marks the bent jet trajectory, representing the interface between the starting jet and the crossflow. At $t^* \approx 30$, this material line encloses a region on the leeward side of the jet, assumedly characterized by recirculating flow.

The trajectory approximately follows the jet emission direction defined by $\alpha = 60$ deg initially for the largest velocity ratio ($r \approx 11$). In this case, a propagation front (LCS3) is observed as a distinct vortex ring develops (LCS4). It is clearly asymmetric in shape because the leeward part is further away from the jet trajectory highlighted by LCS2.

In summary, the velocity ratio has a significant influence on flow structures generated at $\alpha = 60$ deg. The starting jet remains in the near-wall region for $r \approx 2.4$, whereas the jet trajectory becomes steeper for $r \approx 4.7$ but no major vortical structures are revealed through FTLE fields. In contrast, a distinct vortex ring is generated at the largest investigated velocity ratio of $r \approx 11$. A similar transitional behavior with regard to the appearance of flow structures was previously observed for transverse starting jets, i.e., at an inclination angle of $\alpha = 90$ deg. In that case, vorticity cancellation between the

jet and crossflow boundary layer prevented the generation of vortex rings for small velocity ratios [37]. However, there is a distinct difference, in that the leading vortex structure appears to have an opposite sense of rotation in the current scenario at $r \approx 2.4$.

We now address the three-dimensional flow structures for these jet configurations based on a volumetric reconstruction of the flowfield, using measurement data from multiple PIV planes. In Fig. 4, iso-surfaces of the 3-D Q criterion are shown in the left column for $t^* \approx 30$; whereas 3-D FTLE fields colored by the spanwise vorticity component are displayed in the right for the same time step.

At $r \approx 2.4$, the leading part of the starting jet is accompanied by a vortex tube that is responsible for the advection of fluid away from the wall as a positive vorticity is measured. It is worth noting that the region of maximum vorticity is limited to the area close to the jet symmetry plane because the overall jet spreading in lateral direction appears to be small. In addition to the leading vortex structure, a vortex tube with the same sense of rotation is observed at the trailing part of the jet. The generation of this secondary flow structure is a consequence of the initial radial displacement of fluid particles. Satisfying mass conservation, fluid particles are advected in the other direction, i.e., toward the wall on the trailing part of the jet.

As for the medium velocity ratio, the pulsed jet extends further from the wall but both methods reveal a distinctly mitigated vortex structure, which is inline with the reduced vorticity component ω_z discussed earlier in this paper.

Depictions shown in the bottom row ($r \approx 11$) confirm the afore-mentioned observations regarding FTLE fields inside the symmetry plane. A distinct vortex ring is generated because the vorticity associated with the windward part of the starting jet has a sufficient magnitude relative to the crossflow boundary layer and persists during their interaction. It is interesting to note that the vortex ring is not axisymmetric because the half-axis in the symmetry plane is approximately twice as long as the half-axis along the spanwise direction. This is in part explained by the general asymmetry of vortex rings when they interact with a crossflow as the downstream part is drawn toward the recirculation zone on the leeward side of the jet [37]. Second, a larger expansion along the smaller jet dimension was also noted for pulsed planar jets emitted into still surroundings [36] and may be caused by the specific outlet geometry. Here, both effects occur, and a distinctly elongated vortex ring is generated. Trailing this vortex ring, two counter-rotating vortex strands are produced, similar to those observed in steady jets in crossflow.

The results presented so far suggest the existence of two separate regimes: at small velocity ratios; the jet attaches to the wall, whereas distinct vortex rings are observed for larger velocity ratios. To narrow down the transitional range in the velocity ratio between these regimes, we now investigate phase-averaged vorticity and velocity
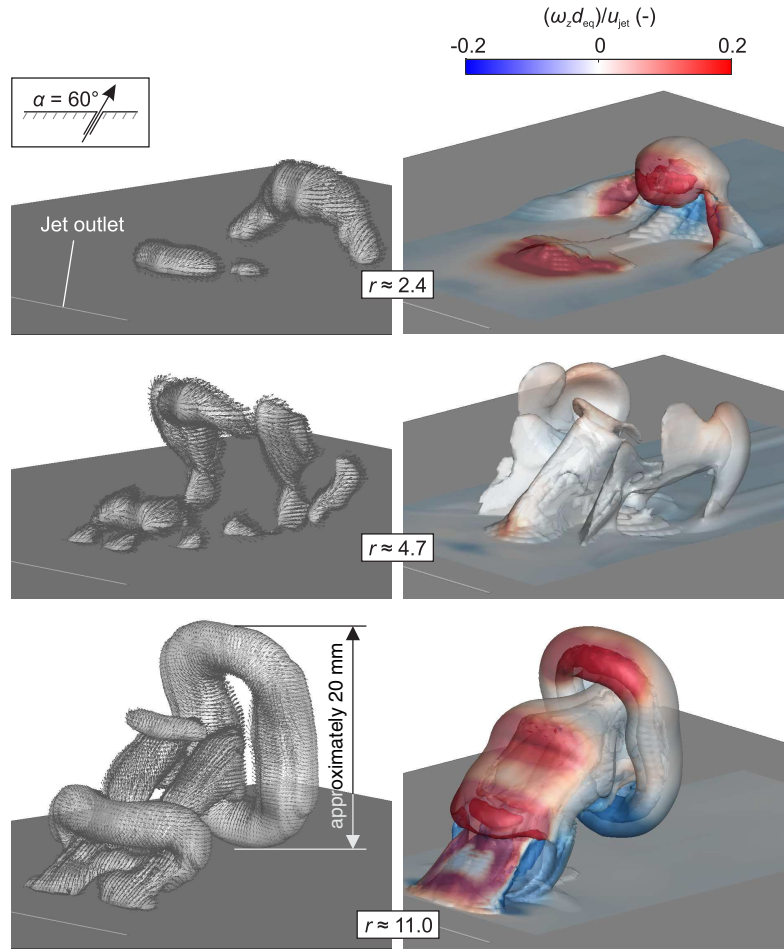
Fig. 4 3-D vortex structures for $\alpha = 60$ deg at $t^* \approx 30$: Q criterion isosurfaces with velocity vectors (left), and semitransparent FTLE isosurface colored by spanwise vorticity (right).

fields inside the symmetry plane. Note that results for two further configurations ($r \approx 2.9$ and $r \approx 6.6$) are also included in Fig. 5.

For $r \approx 2.4$, the emergence of the starting jet is indicated as the vorticity assumes a value of approximately zero close to the outlet initially ($t^* \approx 3$). Thus, the negative boundary-layer vorticity is cancelled during jet initiation before a region of positive vorticity develops during the subsequent time steps. It is worth noting that the jet appears to be attached to the wall, as indicated by almost horizontal instantaneous streamlines, despite the relatively large ejection angle of $\alpha = 60$ deg. This can be explained by a pressure difference across the jet propagation front that develops due to the presence of the wall, inhibiting the entrainment of fluid on the lower part of the jet, thereby limiting the compensation of the low-pressure region as opposed to the windward side. Commonly referred to as the Coandă effect, this mechanism is responsible for the jet deflection close to the outlet as a propagation direction along the wall is assumed. The streamwise velocity component of the resulting wall jet is larger than the velocity of the outer flow. Hence, transverse velocity gradients $\partial u / \partial y$ become negative and larger in magnitude, and the out-of-plane vorticity component $\omega_z = \partial v / \partial x - \partial u / \partial y$ increases. This is fundamentally different compared to an inclination angle of $\alpha = 90$ deg, where hairpin vortices are generated at $r \approx 2.4$ with the same setup, yielding an opposite-sign vorticity component inside the vortex tube [37]. In that case, the larger inclination angle prevents the generation of a wall jet due to the Coandă effect. Interestingly, the same phenomenon applies to larger velocity ratios in the current study where jets penetrate through the boundary layer beyond $r \approx 4.7$. No Coandă effect is observed due to the larger relative jet momentum and because

a low-pressure region develops as the upstream vortex sheet rolls up, drawing the jet away from the wall. In the case of the largest velocity ratio, the relative magnitude of vorticity associated with the boundary layer is even smaller, and a vortex ring is generated since the vorticity associated with the windward side of the jet is not suppressed to the same extent.

The additional velocity ratios that are only presented in Fig. 5 suggest that the transitional regime can be narrowed to $r = 3.0 \ldots 6.5$ because a wall jet similar to the one observed for $r \approx 2.4$ is also generated at $r \approx 2.9$, whereas a vortex ring is observed for $r \approx 6.6$, albeit with a decreased magnitude in vorticity compared to the $r \approx 11$ case.

Being a quantity that can be related to the control authority in AFC applications, we now turn our attention to the circulation induced by $\alpha = 60$ deg pulsed jets (Fig. 6). Here, it is defined as the area-integrated vorticity inside the symmetry plane. Whereas only the region of positive vorticity is considered for $r \approx 2.4$, a distinction is made between areas associated with positive and negative vorticities, respectively, for the larger velocity ratios. When a vortex ring is generated ($r \approx 11$), the circulation of that vortex is evaluated separately using the approach explained in Ref. [37]. In short, the vortex core was defined as the location of maximum vorticity magnitude, and the integration area was defined by an enclosing isoline with 10% of that vorticity magnitude. The region was then validated through the Q criterion and the distance to the jet propagation front to avoid false detections.

For $r \approx 2.4$, the circulation only starts to increase around a non-dimensional formation time of $t^* \approx 5$, i.e., after one-third of the pulse duration. In agreement with the preceding discussion regarding
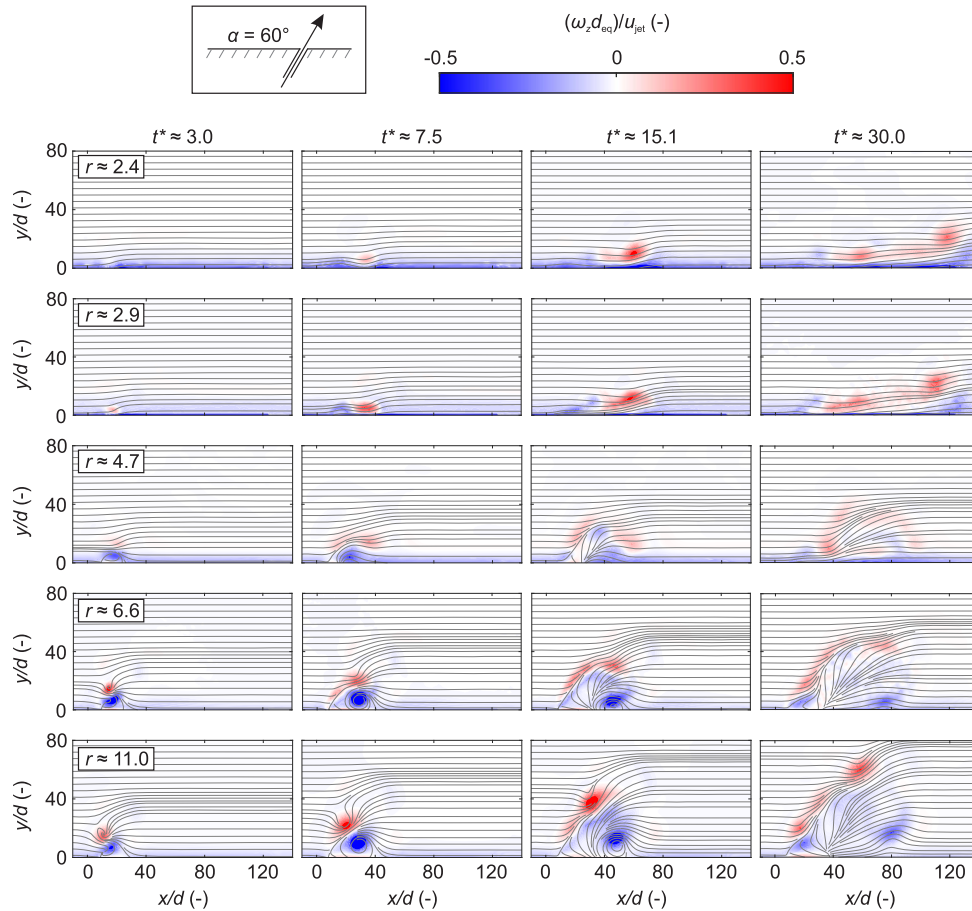
Fig. 5   Development of vorticity fields and phase-averaged streamlines for $\alpha = 60$ deg.

vorticity fields, positive vorticity is cancelled due to the interaction with the oncoming boundary layer before that instant. Once a wall jet emerges, a region of positive vorticity develops as a footprint of the 3-D vortex tube shown in Fig. 4 onto the symmetry plane. It is worth noting that the circulation keeps increasing well beyond the end of the jet emission phase, i.e., for $t^* > 15$. During this phase, no further circulation is ejected by the PJA but the rollup of the leading vortex structure is still ongoing. Furthermore, a secondary area of positive vorticity develops as fluid is entrained toward the wall on the trailing part of the wall jet (Fig. 4).

For $r \approx 4.7$, a region of negative vorticity develops immediately after the beginning of jet emission as a recirculation zone is generated on the leeward side of the jet. The circulation associated with this region remains at a relatively stable level even when no more fluid is emitted. Regions of positive vorticity are found inside the weakened upstream shear layer and downstream of the recirculation zone where fluid is redirected in the horizontal direction. However, the circulation magnitude associated with these regions is smaller than for the vortex structures generated at $r \approx 2.4$ despite an almost doubled velocity ratio, which is a direct consequence of the vorticity cancellation discussed above.

For the largest velocity ratio, maxima in overall circulation (open symbols in Fig. 6) are reached at the end of the jet emission phase at $t^* \approx 15$. The maximum associated with negative vorticity is larger because it is not negatively affected by the crossflow. Initially, the entire circulation is found inside the vortex ring (closed symbols). However, around a formation time of $t^* \approx 11$, a maximum in vortex ring circulation is reached, and decreasing values are observed subsequently. As the overall circulation remains at an almost constant level, it can be assumed that excessive vorticity from the vortex ring is detrained into the trailing jet. Similar observations have been made in

previous investigations of PJA-generated vortex rings ejected into still ambience or into a crossflow at $\alpha = 90$ deg, respectively [36,37].

2.   Jet Inclination Angle $\alpha = 30$ Degrees

In the following, we address the same aspects as earlier in this paper regarding pulsed jets emitted at a smaller inclination angle of $\alpha = 30$ deg, i.e., with a larger initial jet velocity component in the main flow direction.

The development of FTLE fields inside the symmetry plane for this setup is shown in Fig. 7.

From a qualitative perspective, flow structures appear to be independent of the velocity ratio because wall jets can be observed for all configurations. These jets are similar in their overall appearance to the one generated at $\alpha = 60$ deg using the smallest velocity ratio. Here as well, FTLE fields reveal dominant propagation fronts (LCS5) that shift low-momentum fluid of the boundary layer away from the wall. Furthermore, a rollup of the shear layer between the crossflow and the jet occurs (LCS6), shifting fluid away from the wall through LCS6 but not directly transporting high-momentum fluid from the crossflow inside the near-wall region due to the presence of a transport barrier in LCS7. Only on the trailing part of the jet, fluid is entrained owing to mass conservation; and the minor rollup of a vortex tube (LCS8) can be seen for the larger velocity ratios.

Three-dimensional flow structures generated by pulsed jets emitted at $\alpha = 30$ deg as revealed by the Q criterion and FTLE fields are shown in Fig. 8.

Wall jets are found for all three velocity ratios, characterized by a leading structure that resembles one-half of a vortex ring. It is interesting to note that the upper part of the vortex ring core is thinner compared to the vertically oriented parts. This can be explained by the difference in velocities between the jet and the crossflow that is larger
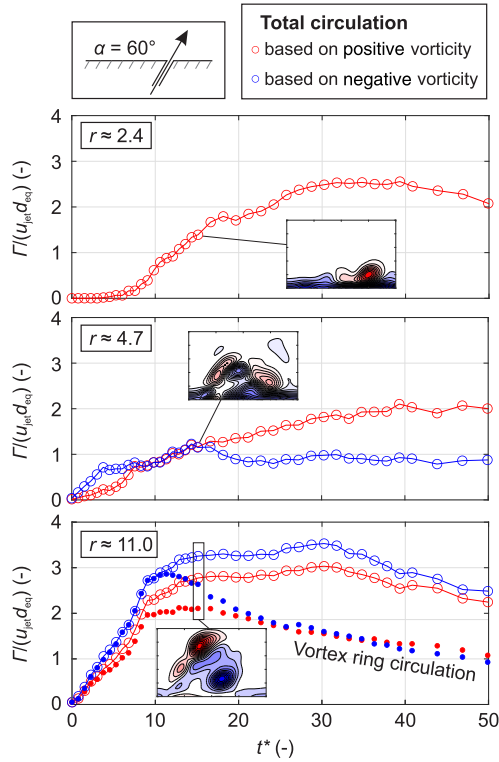
Fig. 6 Time-dependent circulation associated with vortex structures for $\alpha = 60$ deg.

with positive vorticity remains smaller for the $r \approx 2.4$ case subsequently. Due to the propagation front, a deformation of the boundary layer is particularly apparent at $t^* \approx 15$ and $t^* \approx 30$, where the corresponding regions of negative vorticity are moved away from the wall. Evaluating the time-dependent vortex core positions (marked by black crosses in Fig. 9) for several velocity ratios, we found a linear increase in normalized convective velocity of $u_c/U_\infty = 0.44r$. It is important to note that the convective velocity decreases for larger velocity ratios since the variation in r was achieved through adjusting the crossflow speed at a fixed jet velocity in this study. Even though the majority of spanwise vorticity is associated with the leading (point A) and trailing (point C) vortices, a weak shear layer (point B) is also noticeable between these flow structures. It emerges before the termination of jet emission ($t^* \approx 15$), suggesting that the leading vortex half-ring has reached saturation in terms of the maximum absorbable vorticity by that stage.

From a flow control perspective, the time scale corresponding with maximum circulation of the leading vortex half-ring is of some significance. We expect that this flow structure is the main contributor toward boundary-layer energization. Adjusting the pulse duration to exclusively generate a leading vortex may therefore represent an efficiency enhancement when a smaller mass flow consumption is required for the same control authority. In the following, we identify this characteristic formation time subject to a varied velocity ratio by comparing the overall circulation to that associated with the leading vortex (Fig. 10). Only regions of positive vorticity are evaluated here.

First, we focus on the total induced circulation that is highlighted by open symbols. Due to the initial cancellation of vorticity for $r \approx 2.4$, the circulation remains zero until $t^* \approx 3$. Then, a rate of change of circulation similar to those for the larger velocity ratios occurs initially. Both for the smallest velocity ratio and for the medium velocity ratio, it drops at around $t^* \approx 8$ as a gradually decreasing circulation flux is apparent. This can be explained by the interaction with the boundary layer upstream of the wall jet. As the vorticity in the boundary layer is smaller for larger velocity ratios, an enhanced circulation maximum is achieved. For all cases, a local maximum is reached at the end of the jet emission ($t^* \approx 15$). However, the overall circulation starts to increase further around $t^* \approx 20$ as the secondary vortex tube located at the trailing part of the jet begins to develop.

The circulation associated with the leading vortex half-ring (closed red symbols) equals the total jet circulation initially. In other words, the entire vorticity is accumulated inside this flow structure. However, the curves for entire jet and leading vortex circulation diverge before the end of the jet emission phase, marking the emergence of a trailing jet. Characteristic formation time steps are highlighted by verticals in Fig. 10, located in the intersections between entire jet circulation curves and horizontals representing maximum vortex circulation. This definition represents the minimum pulse duration yielding a maximum-circulation vortex under the assumption that the entire ejected vorticity is eventually accumulated by the leading vortex. Practically identical characteristic formation times of $t^* \approx 9$ can be noted for the medium and large velocity ratios. For $r \approx 2.4$, on the other hand, a larger value of $t^* \approx 12$ is extracted. Interestingly, this

inside the boundary layer, resulting in increased shearing. For the same reason, the vortex ring core becomes thicker when the velocity ratio is increased (left column in Fig. 8) and has a larger spanwise vorticity component (right column in Fig. 8).

Despite these minor differences, the overall appearance of vortex structures for $\alpha = 30$ deg is very similar inside a wide range of velocity ratios. Namely, wall jets characterized by a dominant leading vortex and a smaller-scale trailing vortex tube are generated. Whereas the leading vortex half-ring is responsible for transferring low-momentum fluid away from the wall, the trailing vortex maps the entrainment of fluid on the other end of the jet.

The development of spanwise vorticity fields is displayed in Fig. 9.

Based on distributions shown for the first time step ($t^* \approx 3$), a strong cancellation of vorticity can be attested only for the smallest velocity ratio. Nonetheless, the rollup of a leading vortex (point A in Fig. 9) is observed afterward since the wall jet has a streamwise velocity component that is larger than the freestream velocity. Compared to the larger velocity ratios where positive vorticity is ejected and not cancelled by the crossflow, however, the region associated
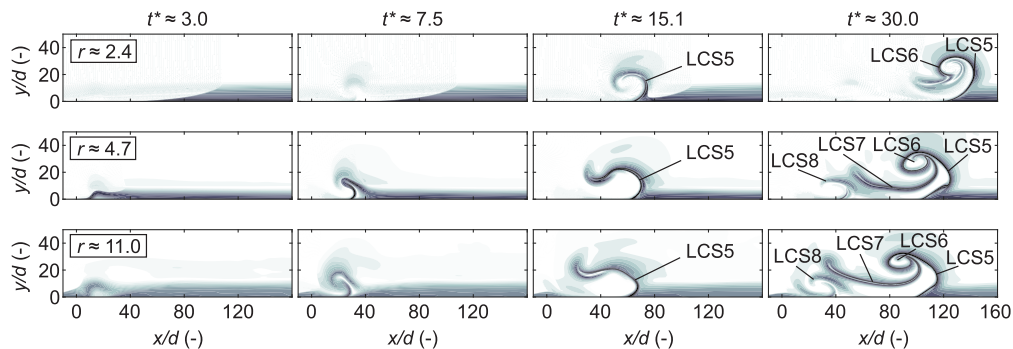

Fig. 7 Development of FTLE fields in symmetry plane for $\alpha = 30$ deg; color bar is within the range of FTLE $= 0 \ldots 1$ m $\cdot$ s^{-1} (white to black).
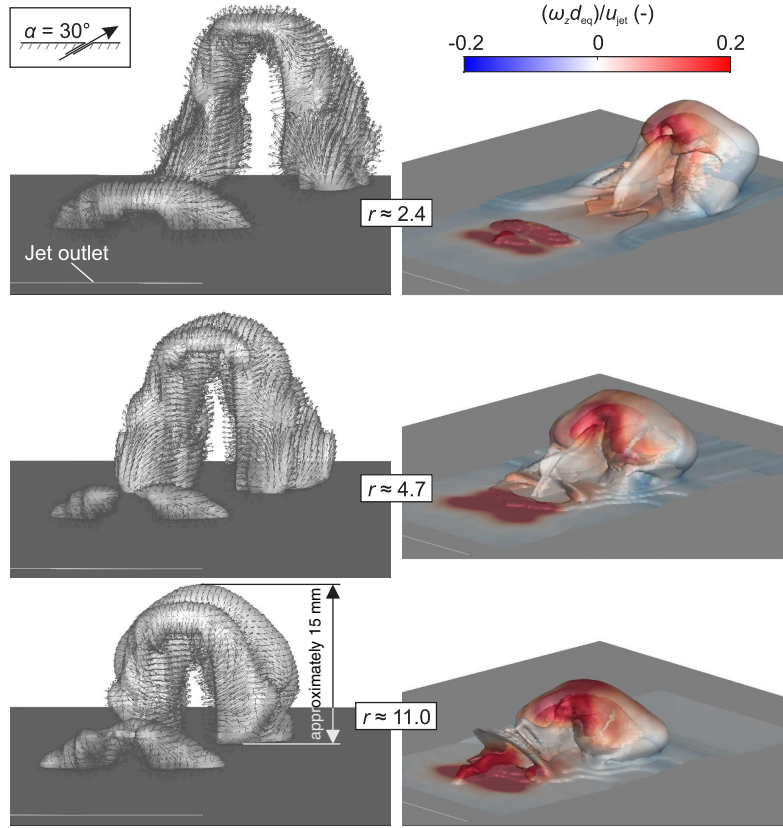
79

Fig. 8 3-D vortex structures for $\alpha = 30$ deg at $t^* \approx 30$: Q criterion with velocity vectors (left), and semitransparent FTLE isosurface colored by spanwise vorticity (right).

deviation is equal to the initial delay in vorticity production for the smallest velocity ratio. Therefore, the effective duration where positive vorticity associated with the leading vortex half-ring rolls up before it reaches a limiting value is very similar for all cases.

In summary, the results presented in this section suggest that flow structures generated with inclined pulsed jets at $\alpha = 60$ deg depend on the velocity ratio. At $r < 3$, vorticity cancellation occurs as jets attach to the wall due to the Coandă effect, and a leading vortex ring develops near the propagation front. At $r > 6.5$, on the other hand, the vorticity associated with the upstream part of the starting jet is sufficiently large, and jets penetrate through the crossflow boundary layer. This leads to the generation of distinct vortex rings. Inside the transitional regime, only weak vortex structures are produced. As for

the more inclined starting jets ($\alpha = 30$ deg), vorticity cancellation is observed for small velocity ratios as well. Nonetheless, wall-attached jets similar to the one produced at $\alpha = 60$ deg with $r < 3$ are noted inside the entire investigated parameter space.

As previously suggested in Ref. [51], the beneficial effect in boundary-layer control of these wall jets may depend on the leading vortex structure that was shown to resemble a vortex half-ring in this section. It incorporates the entire vorticity produced by the starting jet up to a nondimensional formation time of $t^* \approx 9$ both for $r \approx 11$ and $r \approx 4.7$. For the smaller velocity ratio of $r \approx 2.4$, the rollup of the half-ring is delayed due to vorticity cancellation with the crossflow boundary layer. However, the effective formation time of the leading vortex is equal to that found for the larger velocity ratios.
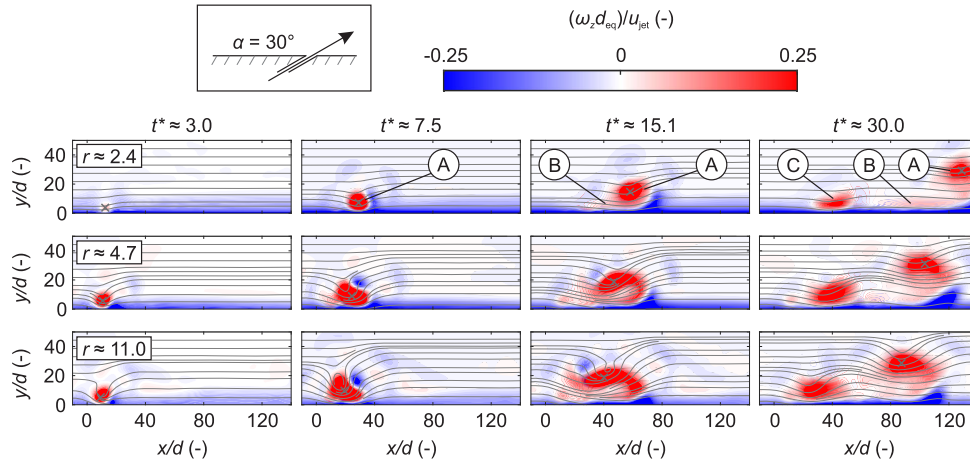

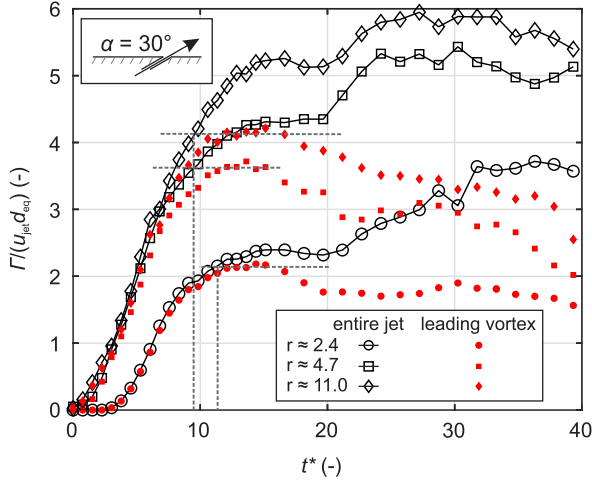**Fig. 9 Development of vorticity fields and phase-averaged streamlines for $\alpha = 30$ deg.**

Fig. 10 Time-dependent circulation associated with regions of positive vorticity for entire starting jet and vortex half-ring at $\alpha = 30$ deg.

B. Manipulation of Streamwise Flowfield Momentum

Let us now focus on the potential benefits of PJA-generated starting jets with respect to BLC. Specifically, we evaluate their influence in terms of the change in squared streamwise velocity

$$\Delta(u^2) = \mathrm{sgn}(u)u^2 - \mathrm{sgn}(u_0)u_0^2 \qquad (3)$$

where u_0 denotes the velocity field in the absence of actuation (i.e., at $t^* \to -\infty$), and the sign function accounts for recirculating flow. Here, we analyze the spatiotemporal evolution of $\Delta(u^2)/u_0^2$ as an estimate for the relative effect on the flowfield. Note that this quantity represents the integrand for the computation of the relative gain in streamwise momentum flux that was also used as an "assessment factor" in Ref. [52] but does not explicitly enable conclusions regarding the efficiency since the relative momentum input is not considered. We therefore also compare the change in streamwise momentum
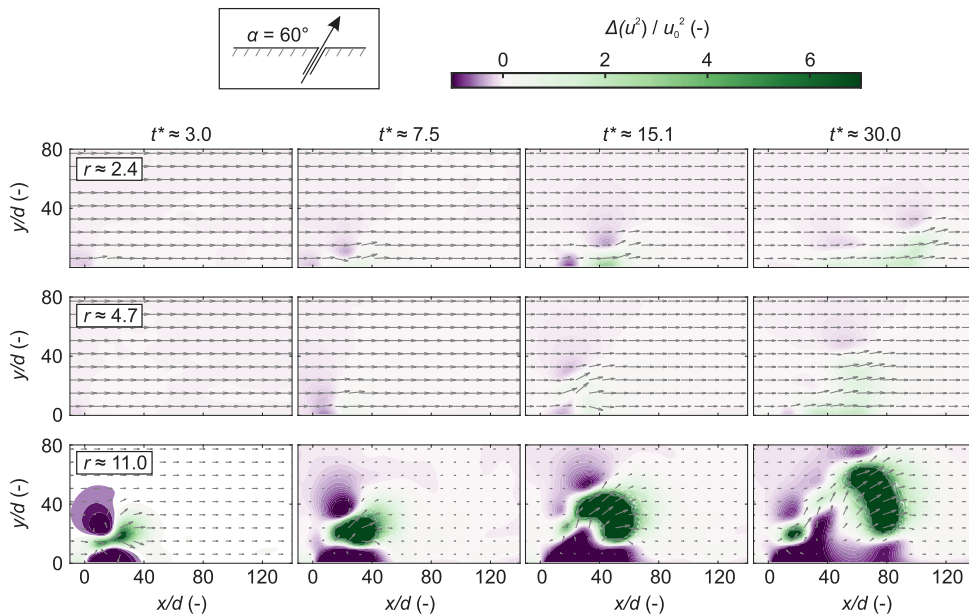
$$\Delta I_x = \varrho \int_0^T \int_A \Delta(u^2)\, \mathrm{d}A\, \mathrm{d}t \qquad (4)$$

with the impulse due to momentum flux provided by the PJA [Eq. (1)], where a square-wave pulse is assumed so that $I_{U,\mathrm{jet}} = \varrho u_{\mathrm{jet}}^2 t_p A_{\mathrm{jet}}$. This leads to a minor overestimation since the real ejection time is slightly longer than the valve opening time t_p, resulting in a decreased axial outlet velocity. Note that $I_{U,\mathrm{jet}}$ is constant for all configurations since the jet velocity was fixed. The ratio $\Delta I_x/I_{U,\mathrm{jet}}$ is evaluated for cross sections inside the near-wall region, where A is bounded by $|z/d| = 50$ and $y/d = 12d$, which is motivated by the fact that an increased boundary-layer momentum makes it less likely to undergo flow separation. Hence, we consider a momentum gain in this region as an enhanced control authority. It is important to note that we do not attempt to establish a momentum balance: in particular, because accurate information regarding viscous forces is not available and we are only interested in one momentum component, namely, the one in the streamwise direction. Nonetheless, the order of magnitude of the pressure impulse [Eq. (2)], being the second factor contributing toward a streamwise momentum increase, can be approximated by comparing the impulse due to momentum flux provided by the PJA and the momentum gain inside the measurement domain, i.e., $I_p \approx \Delta I_x - I_{U,\mathrm{jet}}$.

1. Jet Inclination Angle $\alpha = 60$ Degrees

Figure 11 sheds some light on the change in the squared streamwise velocity [Eq. (3)] relative to the base flow without actuation inside the symmetry plane.

Given the smallest relative momentum flux input at $r \approx 2.4$, the influence of starting jets on the flowfield is marginal. Nonetheless, a positive effect can be attested inside the near-wall region where the squared velocity is increased due to the wall jet discussed earlier in this paper. Both the primary and the secondary vortices, however, yield slight reductions in the streamwise momentum flux in greater wall distance. As for the medium velocity ratio, the pulsed jet penetrates through the boundary layer, and the resulting recirculation zone on its leeward side has an adverse effect in terms of the streamwise momentum flux. Once the recirculation zone breaks down, a region of increased squared velocity develops in the near-wall region ($t^* \approx 30$). It is interesting to note that the relative effect on the flowfield as quantified by positive or negative values of $\Delta(u^2)/u_0^2$ is not larger than for $r \approx 2.4$. This is in line with the mitigation of distinct flow structures because neither a wall jet nor a vortex ring is produced for the medium velocity ratio. The largest relative impulse is supplied at $r \approx 11$. Here, the streamwise momentum increase is almost

Fig. 11 Gain in streamwise momentum flux for $\alpha = 60$ deg inside the symmetry plane ($z/d = 0$).

exclusively associated with the propagation of the vortex ring, whereas a significant defect in near-wall momentum flux can be observed.

We now turn our attention to the instantaneous change in squared streamwise velocity at $t^* \approx 30$ for selected cross sections located in the leading and trailing parts of the starting jets (Fig. 12). Phase-averaged in-plane vector fields are also displayed, enabling an understanding of momentum transport.

Interestingly, the positive effect brought about by PJA-generated starting jets in the current study is limited to the jet outlet length, i.e., to the region of $|z/d| < 20$; whereas a deficit in streamwise momentum is present in a greater spanwise distance. At $\alpha = 60$ deg, this conclusion applies to all velocity ratios. However, only for $r \approx 2.4$ and $r \approx 4.7$, the momentum inside the near-wall region is increased while the generation of a distinct vortex ring with a dominant spanwise vorticity component at $r \approx 11$ comes at the expense of a decreased momentum flux closer to the wall. Based on the displayed velocity field information, the benefit of the wall jet generated at $r \approx 2.4$ can be ascribed to three interrelated mechanisms: 1) low-momentum fluid is shifted away from the wall as indicated by the positive vertical component at the larger x/d, 2) the near-wall region is energized by the wall jet, 3) further high-momentum fluid from the freestream is entrained on the trailing part of the jet as highlighted by the negative vertical component for smaller x/d (see also Fig. 18). As for the weak vortex structures observed for $r \approx 4.7$, the gain in squared streamwise velocity appears to be of similar order despite the larger relative momentum input, which is explained by the cancellation of flow structures discussed in the first part of this paper.

In summary, the capability of pulsed jets to penetrate through the boundary layer at larger velocity ratios is accompanied with a deficit in streamwise velocity, hence momentum flux, as recirculation zones are generated. On the contrary, the wall jet generated at the smallest velocity ratio may be better suited to enhance the boundary-layer impulse.

Taking up the latter hypothesis, the momentum gain inside the near-wall region [Eq. (4)] (i.e., at $y < 12d$ relative to the impulse due to momentum flux provided by the PJA [Eq. (1)]) is quantified in Fig. 13 as a function of x/d.

As for the region upstream of the jet outlet ($x/d < 0$), slight positive effects are observed for the two larger velocity ratios; whereas starting jets yield a deceleration associated with $\Delta I_x \approx -0.25 I_{U,\mathrm{jet}}$ for $r \approx 2.4$. Directly downstream of the outlet, the largest velocity ratio induces a minor momentum gain as the jet imposes a positive streamwise velocity when penetrating through the boundary layer. This only applies to the region of $x/d < 50$, whereas the momentum inside the near-wall region is only slightly affected or even decreased otherwise due to the recirculating flow shown in Figs. 12 and 11. For $r \approx 2.4$ and $r \approx 4.7$, on the other hand, an enhancement in momentum is achieved because an increase up to $x/d \approx 50$ is noted for both configurations. Crucially, the relative gain inside the near-wall region is approximately twice as large for the smallest velocity ratio. This can be explained by a more distinct diffusion of momentum in the wall-normal direction for $r \approx 4.7$, whereas regions of positive $\Delta(u^2)$ remain closer to the wall for $r \approx 2.4$.

Taking into account the entire height of measurement planes, the relative streamwise momentum gain reaches values between $2.5 I_{U,\mathrm{jet}}$ ($r \approx 2.4$) and $1.8 I_{U,\mathrm{jet}}$ ($r \approx 11$). The discrepancy between the measured momentum and the injected momentum flux over time is due to the pressure impulse that occurs during the rapid jet initiation [Eq. (2)], which will be discussed in more detail later on. However, for the case of the smallest velocity ratio, the gain in momentum clearly exceeds the flux term provided by the PJA in the near-wall region. It can therefore be regarded as the most efficient in terms of the distribution of momentum. This is linked with the generation of wall jets as discussed in the first part of the paper.

2. Jet Inclination Angle $\alpha = 30$ Degrees

In the following, the influence of pulsed jets emitted at an inclination angle of $\alpha = 30$ deg on the streamwise momentum flux is addressed. The first part of this paper showed that similar flow structures are generated within the studied range in velocity ratios, namely, wall jets led by a primary vortex. The influence of these jets on the squared streamwise velocity component inside the symmetry plane is displayed in Fig. 14.

The starting jets clearly yield an increased momentum flux inside the near-wall region for all configurations at $\alpha = 30$ deg, whereas a minor velocity deficit occurs just above the jets. This is due to the development of large-scale vortices inside the shear layer between the starting jets and the freestream characterized by a positive sense of rotation. Comparing the two investigated jet inclination angles, a larger gain in squared velocity is present for $\alpha = 30$ deg.

Selected cross sections representative of flow conditions inside the leading and trailing parts are shown in Fig. 15.
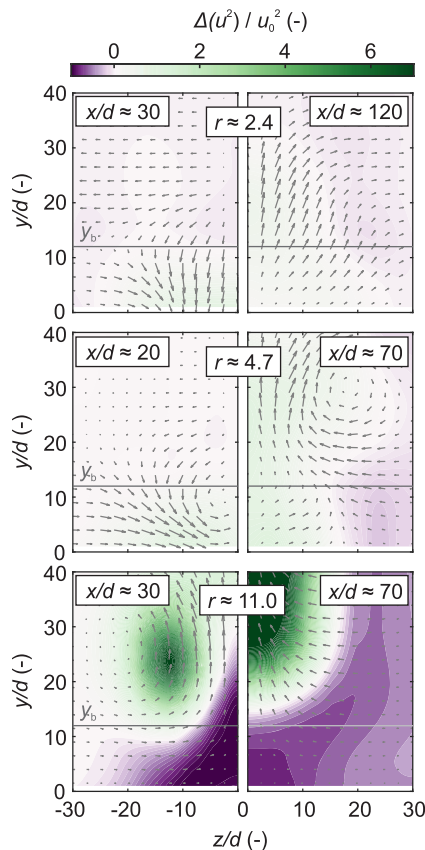

Fig. 12 Relative gain in momentum flux inside selected cross sections for $\alpha = 60$ deg and $t^* \approx 30$; horizontal line indicates boundary of near-wall region ($y/d = 12$).

Fig. 13 Relative momentum gain in near-wall ($y/d < 12$) region for $\alpha = 60$ deg; I_x calculated within the range of $z/d = \pm 50$.
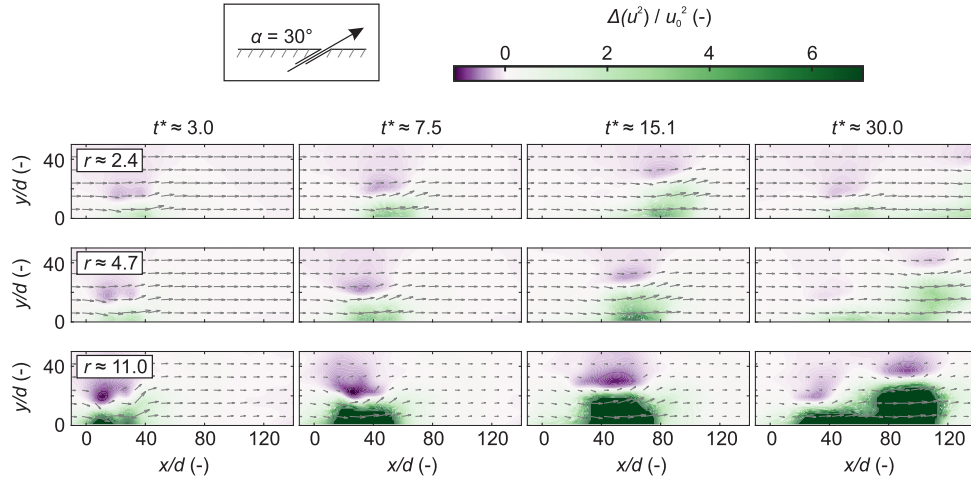
Fig. 14   Gain in streamwise momentum flux for $\alpha = 30$ deg inside the symmetry plane ($z/d = 0$).

As was the case for $\alpha = 60$ deg, the positive effect in terms of the momentum flux is restricted to the jet outlet in spanwise direction with the maximum in $\Delta(u^2)$ inside the symmetry plane and decreasing values for larger $|z/d|$. Whereas the dimension of the high-momentum wall jet in spanwise direction remains of a similar order along x/d, its extent in the wall-normal direction is distinctly reduced because a height of approximately one-third (compared to the leading part) can be noted inside the trailing part of the jet (left column in Fig. 15) for all velocity ratios. This is explained by
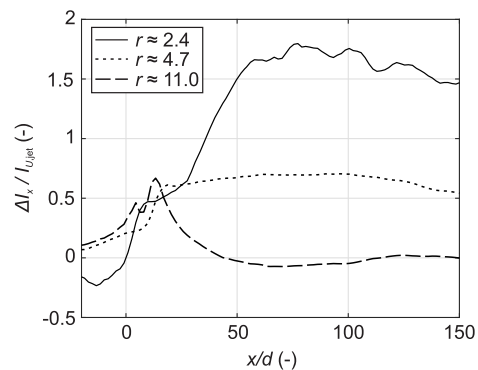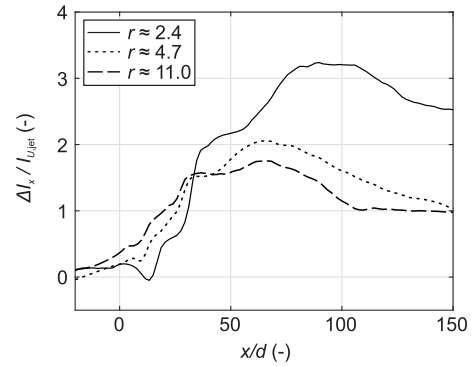

Fig. 16   Relative momentum gain in near-wall ($y/d < 12$) region for $\alpha = 30$ deg; I_x calculated within the range of $z/d = \pm 50$.

the influence of the primary vortex, shifting high-momentum fluid downward, and may be viewed as beneficial with respect to the BLC authority as the momentum gain inside the near-wall region is increased.

The ratio between momentum gain inside the near-wall region and the impulse due to momentum flux ejected by the PJA for $\alpha = 30$ deg is shown in Fig. 16.

Compared to $\alpha = 60$ deg, the ratio between supplied momentum flux over time and measured momentum is consistently larger for the more inclined jets, as could be expected based on previous analyses. A minor enhancement is found upstream of the outlet due to the accelerating effect of starting jets emitted at $\alpha = 30$ deg. Peaks in relative momentum gain are reached in the range of $x/d = 50 \ldots 100$ with continuously decreasing values in greater outlet distance due to the influence of viscous forces on both the wall and inside the shear layer. When the entire cross sections of the measurement volume are considered, maxima in relative momentum gain are of a similar order as for the $\alpha = 60$ deg configuration (i.e., $\Delta I_x / I_{U,\text{jet}} \approx 2.5 \ldots 3$) which confirms the important effect of the jet inclination angle in terms of distributing the momentum input.

Overall, a better suitability for BLC can be attested for the $\alpha = 30$ deg case where the momentum is distributed in a more efficient manner. It is also worth mentioning that the best efficiency, as defined here, is found for the smallest velocity ratios since the largest fraction of momentum flux is supplied to the near-wall region although the nominal momentum input was equal for all configurations. An overview of the control authority associated with the investigated emission angles and velocity ratios is given in Fig. 17, which will be discussed in the following section.
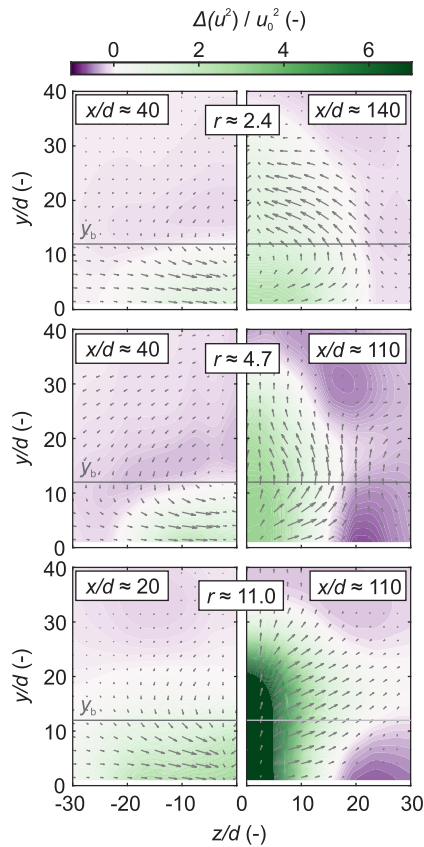

Fig. 15   Relative gain in momentum flux inside selected cross sections for $\alpha = 30$ deg and $t^* \approx 30$; horizontal line indicates boundary of near-wall region ($y/d = 12$).
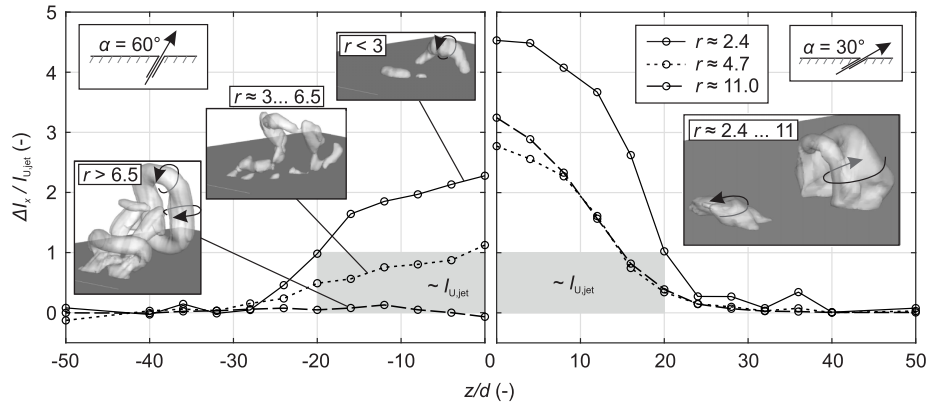
Fig. 17 **Vortex structures and associated momentum gain in near wall-region for different jet emission angles and velocity ratios.**

IV. Conclusions

Drawing on previous fundamental investigations of planar pulsed jets [36,37], their suitability for boundary-layer control was addressed in the current paper. Jets were generated by means of a pulsed jet actuator, ejecting defined amounts of fluid through a rectangular high-aspect-ratio outlet as a fast-switching solenoid valve is opened for relatively short time intervals. Here, starting jets were emitted into a steady crossflow with a turbulent zero-pressure-gradient boundary layer at inclination angles of $\alpha = (60, 30)$ deg, and the velocity ratio between the axial jet velocity and freestream velocity was varied in the range of $r = 2.4 \ldots 11$. Whereas the first part of the paper was dedicated to the general identification of resulting flow structures inside this parameter space, the gain in streamwise momentum due to actuation was subsequently assessed as a measure of control authority. The major results are summarized in Fig. 17, displaying generated flow structures for different parameter combinations and the resulting gain in streamwise momentum per unit width inside the near-wall region ($y/d < 12$) averaged over a streamwise range of $x/d = -20 \ldots 200$. Note that the jet outlet has a spanwise extent of $l/d = 40$, and the momentum flux supplied per starting jet is represented by the shaded area in the figure.

Two types of flow structures were observed: 1) flat jets that remain attached to the wall and are led by a vortex half-ring, and 2) closed vortex rings penetrating into the crossflow. The latter are only generated when starting jets are operated at $\alpha = 60$ deg and $r > 6.5$. The former are produced at $\alpha = 30$ deg (independent of the velocity ratio) and small velocity ratios for $\alpha = 60$ deg.

In general, the generation of a distinct vortex ring has a marginal, if not adverse, effect in terms of enhancing the boundary-layer momentum. Wall-attached jets with a leading half-ring, on the other hand, yield a substantial gain in streamwise momentum in the near-wall region. In this regard, three transport mechanisms were identified as major contributors (Fig. 18). First, the leading part of the wall jets is characterized by a material line, along which low-momentum fluid is accelerated away from the wall (annotation 1). The boundary-layer momentum is then directly increased by the passage of the wall jet (annotation 2); and only on its trailing part, high-momentum fluid from the freestream is entrained, i.e., shifted toward the wall as a consequence of mass conservation (annotation 3).

It is important to note that the vortex half-ring plays a major role in energizing the boundary layer by lowering the local static pressure
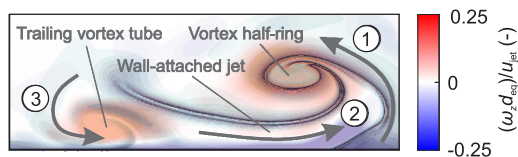

Fig. 18 **Illustration of different mechanisms contributing to boundary-layer energization.**

[51]. For all wall-attached jets generated at $\alpha = 30$ deg, the ring reaches its maximum circulation after a rollup duration of $\Delta t^* \approx 9$. Subsequently, the wall-attached jet becomes excessively long although the control authority associated with the leading vortex ring is not increased. Knowledge regarding the characteristic formation time of the vortex half-ring may therefore enable an efficiency enhancement in BLC applications as the pulse duration may be adjusted to exclusively generate dominant vortices.

To quantify the implications of the observed vortex structures, the gain in streamwise momentum ΔI_x inside the near-wall region was compared with the impulse due to momentum flux $I_{U,\text{jet}}$ provided by the PJA. Put simply, the entire momentum flux is supplied to the streamwise near-wall flow when a value of $\Delta I_x / I_{U,\text{jet}} = 1$ is found in the absence of other contributing impulse terms. Interestingly, the overall gain reaches values larger than can be expected based on the supplied momentum flux alone for all configurations where vortex half-rings are generated (Fig. 17). This is explained as due to overpressure inside the jet exit plane that occurs during the rapid jet initiation and was previously reported to have a significant influence on the properties of starting jets [36]. Exit overpressure is a result of the requirement to accelerate mass in addition to that associated with the ejected fluid (namely, entrained and added mass [40,41]) and provides a pressure impulse

$$I_p = \iint (p - p_\infty)\, dA\, dt$$

in addition to the impulse due to momentum flux. It is important to note that a similar degree in overpressure can be expected for all configurations studied here. However, it contributes to the generation of a thick-cored vortex ring and a large-scale recirculation zone for $\alpha = 60$ deg with $r \approx 11$ instead of enhancing the streamwise boundary-layer momentum, as for the cases where wall-attached jets are produced. From a BLC perspective, the generation of full vortex rings is therefore regarded as less efficient.

The deliberate exploitation of the exit overpressure effect in BLC applications has not been reported to the best of the authors' knowledge, even though the presented results indicate a substantial or, more boldly, the predominant contribution toward control authority in the current setup. However, it is important to note that benefits associated with the pressure impulse invariably come at the cost of an increased energy consumption [53], usually reflected in a larger supply pressure. When estimating the efficiency, surely a larger control volume needs to be applied that is not restricted to the flowfield in question, as was done here.

To enable a more sophisticated utilization of pulsed jets, a number of issues need to be addressed in the future. This includes the investigation of geometrical changes of BLC devices as well as the applied velocity program for which the influence on overpressure is yet unknown. Furthermore, it is clear that the generation of leading vortex structures is of great relative importance in terms of the

pressure impulse since the overpressure associated with the ejection of the trailing fluid column is the same as for a steady jet, i.e., negligible [38]. This raises the question regarding an optimal amount of ejected fluid per starting jet. Some insight regarding such a quantity has been gained recently for generic configurations of non-parallel starting jets ejected into still ambience or transversely into a crossflow [36,37]. In the current article this approach was extended to inclined pulsed jets commonly used in BLC applications, and a characteristic rollup duration of the leading vortex half-ring corresponding to a formation time interval of $\Delta t^* \approx 9$ was noted for different velocity ratios.

Based on the results presented in this paper, the effect of overpressure that is specific for the generation of such pulsed jets may contribute toward a substantial efficiency enhancement in flow control applications. At a fixed mass flow consumption, it can lead to an increase in momentum gain by a factor of two and more, as was shown in the current paper. Advancing the knowledge regarding this phenomenon therefore appears to be a worthwhile task.

Acknowledgements

References

[1] Pearcey, H. H., "Shock Induced Separation and its Prevention," *Boundary Layer and Flow Control*, Vol. 2, edited by G. V. Lachmann, Pergamon, New York, 1961, pp. 1170–1344.

[2] Smith, F. T., "Theoretical Prediction and Design for Vortex Generators in Turbulent Boundary Layers," *Journal of Fluid Mechanics*, Vol. 270, July 1994, pp. 91–132.
https://doi.org/10.1017/S0022112094004210

[3] Seshagiri, A., Cooper, E., and Traub, L. W., "Effects of Vortex Generators on an Airfoil at Low Reynolds Numbers," *Journal of Aircraft*, Vol. 46, No. 1, 2009, pp. 116–122.
https://doi.org/10.2514/1.36241

[4] Cattafesta, L. N., and Sheplak, M., "Actuators for Active Flow Control," *Annual Review of Fluid Mechanics*, Vol. 43, No. 1, 2011, pp. 247–272.
https://doi.org/10.1146/annurev-fluid-122109-160634

[5] Fric, T. F., and Roshko, A., "Vortical Structure in the Wake of a Transverse Jet," *Journal of Fluid Mechanics*, Vol. 279, Nov. 1994, pp. 1–47.
https://doi.org/10.1017/S0022112094003860

[6] Wallis, R. A., "A Preliminary Note on a Modified Type of Air Jet for Boundary Layer Control," Aeronautical Research Council TR 513, London, Great Britain, 1960.

[7] Ball, W. H., "Tests of Wall Blowing Concepts for Diffuser Boundary Layer Control," *20th Joint Propulsion Conference*, AIAA Paper 1984-1276, 1984.

[8] Johnston, J. P., and Nishi, M., "Vortex Generator Jets–Means for Flow Separation Control," *AIAA Journal*, Vol. 28, No. 6, 1990, pp. 989–994.
https://doi.org/10.2514/3.25155

[9] Selby, G. V., Lin, J. C., and Howard, F. G., "Control of Low-Speed Turbulent Separated Flow Using Jet Vortex Generators," *Experiments in Fluids*, Vol. 12, No. 6, 1992, pp. 394–400.
https://doi.org/10.1007/BF00193886

[10] Zhang, X., "An Inclined Rectangular Jet in a Turbulent Boundary Layer-Vortex Flow," *Experiments in Fluids*, Vol. 28, No. 4, 2000, pp. 344–354.
https://doi.org/10.1007/s003480050393

[11] Peterson, S. D., and Plesniakl, M. W., "Flow Structure and Skin Friction in the Vicinity of a Streamwise-Angled Injection Hole Fed by a Short Pipe," *Experiments in Fluids*, Vol. 43, No. 4, 2007, pp. 627–638.
https://doi.org/10.1007/s00348-007-0350-y

[12] Coletti, F., Benson, M. J., Ling, J., Elkins, C. J., and Eaton, J. K., "Turbulent Transport in an Inclined Jet in Crossflow," *International Journal of Head and Fluid Flow*, Vol. 43, Oct. 2013, pp. 149–160.
https://doi.org/10.1016/j.ijheatfluidflow.2013.06.001

[13] Henry, F. S., and Pearcey, H. H., "Numerical Model of Boundary-Layer Control Using Air-Jet Generated Vortices," *AIAA Journal*, Vol. 32, No. 12, 1994, pp. 2415–2425.
https://doi.org/10.2514/3.12308

[14] Küpper, C., and Henry, F. S., "Numerical Study of Air-Jet Vortex Generators in a Turbulent Boundary Layer," *Applied Mathematical Modelling*, Vol. 27, No. 5, 2003, pp. 359–377.
https://doi.org/10.1016/S0307-904X(02)00138-5

[15] Compton, D. A., and Johnston, J. P., "Pitched and Skewed Jets in a Turbulent Boundary Layer," *29th Aerospace Sciences Meeting*, AIAA Paper 1991-0038, 1991.

[16] Milanovic, I. M., and Zaman, K. B. M. Q., "Fluid Dynamics of Highly Pitched and Yawed Jets in Crossflow," *AIAA Journal*, Vol. 42, No. 5, 2004, pp. 874–882.
https://doi.org/10.2514/1.2924

[17] Feng, Y.-Y., Song, Y.-P., and Breitenthal, R. E., "Model of the Trajectory of an Inclined Jet in Incompressible Crossflow," *AIAA Journal*, Vol. 56, No. 2, 2018, pp. 458–464.
https://doi.org/10.2514/1.J056181

[18] Sakai, E., Takahashi, T., and Watanabe, H., "Large-Eddy Simulation of an Inclined Round Jet Issuing Into a Crossflow," *International Journal of Heat and Mass Transfer*, Vol. 69, Feb. 2014, pp. 300–311.
https://doi.org/10.1016/j.ijheatmasstransfer.2013.10.027

[19] Dai, C., Jia, L., Zhang, J., Shu, Z., and Mi, J., "On the Flow Structure of an Inclined Jet in Crossflow at Low Velocity Ratios," *International Journal of Heat and Fluid Flow*, Vol. 58, April 2016, pp. 11–18.
https://doi.org/10.1016/j.ijheatfluidflow.2015.12.001

[20] Seifert, A., Darabi, A., and Wygnanski, I., "Delay of Airfoil Stall by Periodic Excitation," *Journal of Aircraft*, Vol. 33, No. 4, 1996, pp. 691–698.
https://doi.org/10.2514/3.47003

[21] Nishri, B., and Wygnanski, I., "Effects of Periodic Excitation on Turbulent Flow Separation from a Flap," *AIAA Journal*, Vol. 36, No. 4, 1998, pp. 547–556.
https://doi.org/10.2514/2.428

[22] Barros, D., Borée, J., Noack, B. R., Spohn, A., and Ruiz, T., "Bluff Body Drag Manipulation Using Pulsed Jets and Coanda Effect," *Journal of Fluid Mechanics*, Vol. 805, Oct. 2016, pp. 422–459.
https://doi.org/10.1017/jfm.2016.508

[23] Greenblatt, D., and Wygnanski, I. J., "The Control of Flow Separation by Periodic Excitation," *AIAA Journal* Vol. 36, No. 7, 2000, pp. 487–545.
https://doi.org/10.1016/S0376-0421(00)00008-7

[24] Lasheras, J. C., and Choi, H., "Three-Dimensional Instability of a Plane Free Shear Layer: An Experimental Study of the Formation and Evolution of Streamwise Vortices," *Journal of Fluid Mechanics*, Vol. 189, April 1988, pp. 53–86.
https://doi.org/10.1017/S0022112088000916

[25] Li, Y., and Gaster, M., "Active Control of Boundary-Layer Instabilities," *Journal of Fluid Mechanics*, Vol. 550, March 2006, pp. 185–205.
https://doi.org/10.1017/S0022112005008219

[26] Dabiri, J. O., and Gharib, M., "Fluid Entrainment by Isolated Vortex Rings," *Journal of Fluid Mechanics*, Vol. 511, July 2004, pp. 311–331.
https://doi.org/10.1017/S0022112004009784

[27] Bons, J. P., Sondergaard, R., and Rivir, R. B., "The Fluid Dynamics of LPT Blade Separation Control Using Pulsed Jets," *Journal of Turbomachinery*, Vol. 124, No. 1, 2002, pp. 77–85.
https://doi.org/10.1115/1.1425392

[28] Petz, R., and Nitsche, W., "Active Separation Control on the Flap of a Two-Dimensional Generic High-Lift Configuration," *Journal of Aircraft*, Vol. 44, No. 3, 2007, pp. 865–874.
https://doi.org/10.2514/1.25425

[29] Hecklau, M., Wiederhold, O., Zander, V., King, R., Nitsche, W., Huppertz, A., and Swoboda, M., "Active Separation Control with Pulsed Jets in a Critically Loaded Compressor Cascade," *AIAA Journal*, Vol. 49, No. 8, 2011, pp. 1729–1739.
https://doi.org/10.2514/1.J050931

[30] Steinfurth, B., and Haucke, F., "Coherent Structures in the Actively Controlled Wake of a High-Lift Configuration," *AIAA Journal*, Vol. 56, No. 10, 2018, pp. 3848–3856.
https://doi.org/10.2514/1.J057094

[31] Milanovic, I. M., and Zaman, K. B. M. Q., "Synthetic Jets in Crossflow," *AIAA Journal*, Vol. 43, No. 5, 2005, pp. 929–940.
https://doi.org/10.2514/1.4714

[32] Greenblatt, D., Schneider, T., and Schule, C. Y., "Mechanism of Flow Separation Control Using Plasma Actuation," *Physics of Fluids*, Vol. 24, No. 7, 2012, Paper 077102.
https://doi.org/10.1063/1.4733399

[33] Jukes, T. N., and Choi, K.-S., "On the Formation of Streamwise Vortices by Plasma Vortex Generators," *Journal of Fluid Mechanics*, Vol. 733, Oct. 2013, pp. 370–393.
https://doi.org/10.1017/jfm.2013.418

[34] Bauer, M., Lohse, J., Haucke, F., and Nitsche, W., "High-Lift Performance Investigation of a Two Element Configuration with a Two-Stage Actuator System," *AIAA Journal*, Vol. 52, No. 6, 2014, pp. 1307–1313.
https://doi.org/10.2514/1.J052639

3. Publications

[35] Woszidlo, R., Ostermann, F., and Schmidt, H.-J., "Fundamental Properties of Fluidic Oscillators for Flow Control Applications," *AIAA Journal*, Vol. 57, No. 3, 2019, pp. 978–992.
https://doi.org/10.2514/1.J056775

[36] Steinfurth, B., and Weiss, J., "Vortex Rings Produced by Non-Parallel Planar Starting Jets," *Journal of Fluid Mechanics*, Vol. 903, Nov 2020, Paper A16.
https://doi.org/10.1017/jfm.2020.637

[37] Steinfurth, B., and Weiss, J., "Velocity Ratio Effect on Flow Structures of Non-Parallel Planar Starting Jets in Cross-Flow," *Journal of Fluid Mechanics*, Vol. 915, May 2021, Paper A11.
https://doi.org/10.1017/jfm.2021.40

[38] Krueger, P. S., and Gharib, M., "The Significance of Vortex Ring Formation to the Impulse and Thrust of a Starting Jet," *Physics of Fluids*, Vol. 15, No. 5, 2003, pp. 1271–1281.
https://doi.org/10.1063/1.1564600

[39] Olcay, A. B., and Krueger, P. S., "Momentum Evolution of Ejected and Entrained Fluid During Laminar Vortex Ring Formation," *Theoretical and Computational Fluid Dynamics*, Vol. 24, No. 5, 2010, pp. 465–482.
https://doi.org/10.1007/s00162-009-0173-y

[40] Darwin, C., "Note on Hydrodynamics," *Mathematical Proceedings of the Cambridge Philosophical Society*, Vol. 49, No. 2, 1953, pp. 342–354.
https://doi.org/10.1017/S0305004100028449

[41] Dabiri, J. O., "Note on the Induced Lagrangian Drift and Added-Mass of a Vortex," *Journal of Fluid Mechanics*, Vol. 547, Jan. 2006, pp. 105–113.
https://doi.org/10.1017/S0022112005007585

[42] Didden, N., "On the Formation of Vortex Rings: Rolling-Up and Production of Circulation," *Zeitschrift für Angewandte Mathematik und Physik*, Vol. 30, No. 1, 1979, pp. 101–116.
https://doi.org/10.1007/BF01597484

[43] Krueger, P. S., "An Over-Pressure Correction to the Slug Model for Vortex Ring Circulation," *Journal of Fluid Mechanics*, Vol. 545, Dec. 2005, pp. 427–443.
https://doi.org/10.1017/S0022112005006853

[44] Krieg, M., and Mohseni, K., "Modelling Circulation, Impulse and Kinetic Energy of Starting Jets with Non-Zero Radial Velocity," *Journal of Fluid Mechanics*, Vol. 719, March 2013, pp. 488–526.
https://doi.org/10.1017/jfm.2013.9

[45] Ruiz, L. A., Whittlesey, R. W., and Dabiri, J. O., "Vortex-Enhanced Propulsion," *Journal of Fluid Mechanics*, Vol. 668, Feb. 2011, pp. 5–32.
https://doi.org/10.1017/S0022112010004908

[46] Krieg, M., and Mohseni, K., "Pressure and Work Analysis of Unsteady, Deformable, Axisymmetric, Jet Producing Cavity Bodies," *Journal of Fluid Mechanics*, Vol. 769, April 2015, pp. 337–368.
https://doi.org/10.1017/jfm.2015.120

[47] Weihs, D., "Periodic Jet Propulsion of Aquatic Creatures," *Fortschritte der Zoologie*, Vol. 24, Nos. 2–3, 1977, pp. 171–175.

[48] Hunt, J. C. R., Wray, A. A., and Moin, P., "Eddies, Stream, and Convergence Zones in Turbulent Flows," Center for Turbulence Research Rept. CTR-S88, Stanford, CA, 1988.

[49] Steinfurth, B., and Weiss, J., "Inclined Non-Parallel Planar Starting Jets in Crossflow," *Gallery of Fluid Motion*, American Physical Soc., College Park, MD, 2020.
https://doi.org/10.1103/APS.DFD.2020.GFM.V0050

[50] Shadden, S. C., Lekien, F., and Marsden, J. E., "Definition and Properties of Lagrangian Coherent Structures from Finite-Time Lyapunov Exponents in Two-Dimensional Aperiodic Flows," *Physica D*, Vol. 212, Nos. 3–4, 2005, pp. 271–304.
https://doi.org/10.1016/j.physd.2005.10.007

[51] Darabi, A., and Wygnanski, I., "Active Management of Naturally Separated Flow over a Solid Surface. Part 1. The Forced Reattachment Process," *Journal of Fluid Mechanics*, Vol. 510, July 2004, pp. 105–129.
https://doi.org/10.1017/S0022112004009231

[52] Ortmanns, J., Bitter, M., and Kähler, C. J., "Dynamic Vortex Structures for Flow-Control Applications," *Experiments in Fluids*, Vol. 44, No. 3, 2008, pp. 397–408.
https://doi.org/10.1007/s00348-007-0442-8

[53] Choutapalli, I., Krothapalli, A., and Arakeri, J. H., "An Experimental Study of an Axisymmetric Turbulent Pulsed Air Jet," *Journal of Fluid Mechanics*, Vol. 631, July 2009, pp. 23–63.
https://doi.org/10.1017/S0022112009007009

J. Floryan
Associate Editor

Efficiency Enhancement in Active Separation Control Through Optimizing the Duty Cycle of Pulsed Jets

Ben Steinfurth* and Julien Weiss[†]
Technical University of Berlin, 10587 Berlin, Germany

https://doi.org/10.2514/1.J061667

This paper is concerned with active separation control in a one-sided diffuser test section using pulsed wall jets. Particular focus is laid on the two timescales defining the periodic forcing signal, which are the pulse duration t_p and the time delay between successive pulses t_{off}. The latter is addressed in a dedicated type of experiment where forcing is terminated abruptly as the flow is allowed to evolve into its natural, separated state. Lasting for a duration approximately 50 times the convective time t_c, this transient process is largely independent of initial forcing conditions. The onset of reverse flow near the diffuser foot is shown to occur after a characteristic separation time of only $t_s^* \approx 2.2 t_c$ for a variety of actuation signals when a mean momentum input of $c_{\mu,\text{thres}} = 1.5\%$ is exceeded. Setting the forcing signal according to these flow-inherent quantities is demonstrated to reliably prevent the recurrence of mean reverse flow throughout the actuation period. For such parameter combinations, a systematic reduction of the required mass flow is feasible by reducing the pulse duration t_p, and thereby the duty cycle. Thus, $DC \approx 0.1$ is associated with an equal or even superior control authority compared to the typically used $DC = 0.5$ case in the current setup, although only one-third of the mass flow is required. The results presented in this paper therefore promote significant efficiency gains in active boundary-layer control by optimizing the duty cycle of pulsed-jet actuators.

Nomenclature

A_{ref}	=	reference area, m²
c_n	=	normal force coefficient
c_p	=	pressure coefficient
c_Q	=	mass-flow coefficient, %
c_μ	=	momentum coefficient, %
$c_{\mu,\text{thres}}$	=	momentum coefficient threshold value, %
DC	=	duty cycle
d	=	outlet width, m
d_{eq}	=	equivalent outlet diameter, m
FM	=	figure of merit
F_{opt}^+	=	optimum reduced forcing frequency
F^+	=	reduced forcing frequency
f	=	forcing frequency, s⁻¹
f_s	=	sampling frequency, s⁻¹
$I_{u,\text{jet}}$	=	momentum flow rate per unit width, (kg · m)/s²
L	=	length of diffuser ramp, m
L_c	=	length of control domain, m
l	=	outlet span, m
$\dot{m}_{\text{jet}}$	=	mass-flow rate per unit width, kg/(ms)
p_{max}	=	range of pressure transducer, kg/(ms²)
q_∞	=	freestream dynamic pressure, kg/(ms²)
Ra	=	roughness parameter, m
r	=	jet velocity ratio
T	=	forcing period, s
t	=	time, s
t_c	=	convective time, s
t_{off}	=	time delay between successive pulses, s
$t_{\text{off,crit}}$	=	critical time delay between successive pulses, s
t_p	=	pulse duration, s
t_s^*	=	characteristic separation time, s
t^*	=	nondimensional time
U_∞	=	nominal freestream velocity, m/s
u, v	=	velocity components in x and y directions, m/s
u_{jet}	=	nominal jet velocity, m/s
$\tilde{u}, \tilde{v}$	=	velocity components in $\tilde{x}$ and $\tilde{y}$ directions, m/s
$\tilde{V}_m$	=	maximum wall-normal velocity, m/s
x, y, z	=	Cartesian coordinates, m
$\tilde{x}, \tilde{y}, \tilde{z}$	=	Cartesian coordinates, m
$\tilde{x}_{\text{ind}}$	=	indicator sensor location, m
α	=	diffuser opening angle, deg
γ	=	forward-flow fraction
γ_{min}	=	minimum forward-flow fraction
Δc_n	=	deviation in normal force coefficients with regard to unforced baseline
$\Delta c_{n,\text{inv}}$	=	deviation in normal force coefficients with regard to inviscid simulation
Δt	=	time delay, s
ΔU	=	deviation in wall-parallel velocity, m/s
ΔV_m	=	deviation in maximum wall-normal velocity, m/s
ΔV_{min}	=	deviation in minimum wall-normal velocity, m/s
$\Delta x, \Delta y, \Delta z$	=	spatial distances in (x, y, y) coordinate system, m
$\Delta \tau$	=	deviation in wall shear stress, kg/(ms²)
ϱ	=	mass density, kg/m³
τ	=	wall shear stress, kg/(ms²)
φ	=	jet emission angle, deg
ω_z	=	spanwise vorticity component, s⁻¹

I. Introduction

OVER the last decades, the field of active separation control (ASC) has given rise to various methods of countering boundary-layer separation. Typically relying on some kind of external energy source, different technical implementations exist, often introducing unsteady perturbations to energize the boundary layer in question and prevent or delay its separation from a solid surface [1]. Common devices are plasma [2–4], zero-net-mass-flux [5,6], sweeping-jet [7–9], and pulsed-jet actuators [10–14]. The latter type in particular represents the advancement of a steady-blowing approach and is considered to cause a more effective flow manipulation in comparison [15,16]. Here, defined amounts of fluid that are small relative to the affected flow domain are periodically injected into a crossflowing boundary layer, where they increase the momentum flux [17–20].

The considerable body of literature dedicated to ASC with pulsed-jet actuators (PJAs) involves many suggestions regarding adequate

operating conditions [16,21]. It appears to be commonly accepted that the jet origin needs to be located as close as possible to the natural separation line because the prevention of boundary-layer separation is much more efficient than the reattachment of a separated flow [22]. Furthermore, some consensus with regard to the outlet geometry and orientation can be noted because jets ejected through elongated slots and inclined toward the downstream surface have been employed to great effect [10,14,21]. Leaving such geometrical considerations aside, one needs to adjust a limited number of parameters to define the PJA forcing signal that can often be approximated by a square wave (Fig. 1).

Assuming two-dimensional flow, the time-dependent forcing intensity

$$c_\mu(t) = \frac{I_{u,\mathrm{jet}}(t)}{q_\infty L_c} \tag{1}$$

can be quantified by the supplied momentum flow rate per unit width $I_{u,\mathrm{jet}} = \dot{m}_{\mathrm{jet}} u_{\mathrm{jet}}$ relative to the product of freestream dynamic pressure q_∞ and the extent of the controlled flow region L_c [23]. Enabling a better comparison of forcing intensities applied in different setups, time-averaged values of the momentum coefficient $\bar{c}_\mu$ are usually stated, with the bar being dropped for convenience in the following.

The minimum c_μ required to prevent separation is highly sensitive toward the flow configuration [specifically, with regard to the magnitude of the adverse pressure gradient (APG) and the streamwise extent of the control region] but is also dependent on the remaining actuation parameters. This is reflected in the broad range of effective forcing intensities of $c_\mu = 0.01, \ldots, 3\%$ summarized by Greenblatt and Wygnanski for different airfoil configurations [16]. It is important to note that pulsed forcing can also have a detrimental effect (i.e., lead to a reduction of the near-wall momentum) when the velocity ratio $r = u_{\mathrm{jet}}/U_\infty$ is relatively small [15]. On the other hand, an excessive increase of the momentum input beyond the value that ensures an attached boundary layer has no significant effect in terms of the aerodynamic loads although the maximum lift can be slightly enhanced through circulation control in some flows [24].

There is perhaps even more debate over the choice of the actuation frequency f that is often communicated in its dimensionless form:

$$F^+ = fL_c/U_\infty \tag{2}$$

An order of magnitude approximation for the optimum of this parameter in many flow configurations is $\mathcal{O}(F^+_{\mathrm{opt}}) = 1$, which is based on two observations [16]. First, acoustic excitation experiments show a trend toward this value when the forcing intensity is increased [25], i.e., when perturbation levels approach values achieved with PJAs. Second, it was shown that the expansion rate of a turbulent free shear layer can be enhanced most effectively through excitation with a frequency on this order [26,27]. This is assumed and, on some occasions, indeed shown to cause a larger entrainment of high-momentum fluid into the near-wall region, thereby controlling separation [15,28]. Other investigations suggest that for the prevention of flow separation (i.e., in the absence of a separated shear layer), a larger reduced frequency of $F^+_{\mathrm{opt}} = 3, \ldots, 4$ [22] or even $\mathcal{O}(F^+) = 10$ [29] needs to be applied. We conclude this
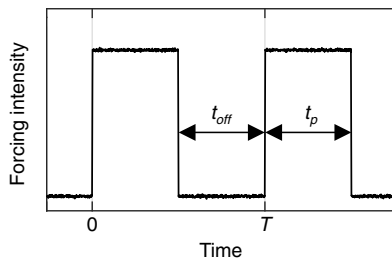
brief overview of the optimum reduced frequency by pointing out that its exact value is sensitive to changes of the forcing intensity [27,28]. For more information, the interested reader is once more referred to Ref. [16].

Perhaps surprisingly, the timescales shown in Fig. 1 (namely, the jet pulse width t_p and the time delay between successive pulses t_{off}) are not explicitly considered in any of the aforementioned studies where a duty cycle of 50% is preset ($t_p/T = 0.5$ and $t_p = t_{\mathrm{off}}$). This may be viewed as an attempt to tame the multidimensional parameter space because the actuation signal can be parametrized by the forcing intensity and the frequency only. Other explanations lie in the historical reference to acoustic harmonic forcing where the duty cycle is fixed or the use of devices that, by design, do not allow for such variations [30]. Nonetheless, there is reason to believe that an optimization of the duty cycle may significantly improve the effectivity and efficiency of PJAs because it is directly related to the momentum input (effectivity) and mass-flow consumption (efficiency). This was in fact proven to be the case by Bons et al. [31], reporting effective ASC on a low-pressure turbine blade at a duty cycle as low as 10%, which they attributed to the relatively large timescale at which the boundary layer resumes its separated state. They concluded that "some economy of jet flow may be possible by optimizing the pulse duty cycle", which has been confirmed in other experiments [32,33].

In the present study, the over-riding objective is to further the knowledge of flow physics governing the effectivity of pulsed jets in ASC, enabling an informed choice of timescales defining the forcing signal. Recent efforts by the authors were already dedicated to optimizing the pulse width t_p [14,20,34] based on the assumption that the control authority of pulsed jets is mainly governed by the leading vortex ring. Hence, we identified nondimensional pulse durations maximizing the circulation of this flow structure: an approach consistent with the concept of a formation number [35]. However, the control range of such pulsed jets associated with relatively small amounts of ejected mass appears to be limited [36]. In other words, the flow is only affected in the jet near field, whereas the influence in the greater outlet distance is negligible. The topic of the relative importance attributed to the individual flow structures of pulsed wall jets is therefore revisited in the present paper (Sec. III). Then, we address the relaxation process unfolding in between successive pulses, enabling an educated choice of the time delay t_{off} (Sec. IV) before presenting guidelines for the adjustment of the pulse duration t_p (Sec. V). Based on these guidelines, the timescales depicted in Fig. 1 can be set separately, and demonstrations of potential efficiency enhancements are provided.

II.   Experimental Setup and Approach

In the following, we will introduce the investigated flow configuration before addressing the ASC approach. Then, the measurement procedure will be documented.

A.   Unforced One-Sided Diffuser Flow

Experiments were conducted in a subsonic closed-loop wind tunnel where a one-sided diffuser test section was installed (left-side image in Fig. 2). The mean velocity inside the test section entrance was $U_\infty = 20$ m/s with further measurements conducted at $U_\infty = (15, 25)$ m/s to assess the Reynolds number dependence for selected cases. Although the upper boundary of the test section at $y = 400$ mm is a flat plate, the bottom part allows for a linear widening of the cross-sectional area because the angle of the diffuser ramp of length $L = 337$ mm is adjustable in the range $\alpha = 0, \ldots, 25$ deg. Two coordinate systems will be referred to in this paper: the (x, y) system is aligned with the horizontal freestream, whereas the $(\tilde{x}, \tilde{y})$ coordinate system is rotated by the diffuser angle so that $\tilde{x}$ is aligned with the ramp. While the (x, y) system has its origin in the connection between the horizontal test section inlet and the diffuser ramp where a rounded transition prevents geometry-induced flow separation at small and moderate diffuser angles, the $(\tilde{x}, \tilde{y})$ system is rooted at the jet outlet location.

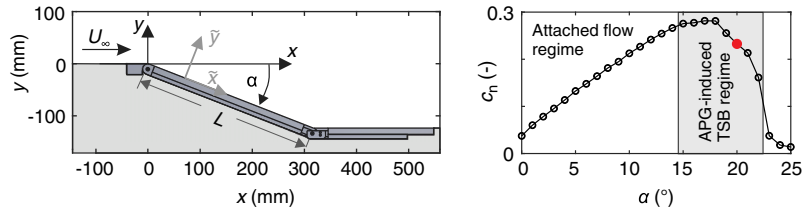**Fig. 1   Idealized actuation signal of a PJA.**

Fig. 2 One-sided diffuser test section (left), and normal force coefficient on the diffuser ramp as a function of opening angle (right): configuration $\alpha = 20$ deg, addressed in this paper, is highlighted in red.

The characteristic normal force development for increasing diffuser opening angles is shown in the right-side image of Fig. 2. This quantity was evaluated based on time-averaged pressure measurements throughout the diffuser ramp that are compared with the static pressure at $x = -0.2$ m. For a zero diffuser opening angle, the test section floor resembles a flat plate with a negligible pressure gradient; hence, only a very small normal force relative to the test section inflow is found. When the diffuser is opened, the normal force coefficient increases in a linear fashion initially as the flow decelerates and an APG develops. This gradient is then responsible for the onset of turbulent flow separation near the ramp foot at approximately $\alpha = 15$ deg. When the diffuser angle is further increased, the unsteady separation line is shifted upstream, and the region of recirculating flow grows in size. This first yields stagnating and then decreasing normal force coefficients. At $\alpha > 22$ deg, geometry-induced separation occurs because the flow is not capable of following the ramp deflection. Thus, boundary-layer separation induced by an APG is found in the range of $\alpha = 15, \ldots, 22$ deg for this specific setup, with a diffuser angle of $\alpha = 20$ deg investigated in the present study (highlighted in Fig. 2).

For this configuration, information on the natural (i.e., uncontrolled) flowfield is presented in Fig. 3. A drop in pressure coefficients can be noted at the diffuser entrance, which is explained by bending path lines and a local flow acceleration. Then, a distinct APG is generated on the upper part of the ramp ($x = 0, \ldots, 100$ mm), causing boundary-layer separation as indicated by the reduced pressure gradient.

These general observations are confirmed by particle image velocimetry (PIV) measurements presented in the bottom of the figure, where a large mean region of recirculating flow is indeed revealed, enclosed by the $\bar{u} = 0$ m/s isoline. To estimate the extent of this separation bubble, the forward-flow fraction γ is evaluated (Fig. 3, top), defined as the relative number of samples that indicate forward-directed near-wall flow. This quantity was extracted from instantaneous PIV measurements (solid black line) by evaluating velocity vectors closest to the surface for each streamwise location and compared to measurements with wall shear-stress sensors (red circles). For the latter, positive shear-stress values were interpreted as forward-directed flow. Both measurement methods are in good agreement, indicating a forward-flow fraction of $\gamma \approx 1$ is up to a

streamwise location of $x = 50$ mm. This confirms that flow separation is indeed APG-induced and not geometry-induced because there is no instantaneous reverse flow at the diffuser opening. Being a characteristic location inside a separating and reattaching flow [37], the point of incipient detachment (ID) where $\gamma = 0.99$ is highlighted by a vertical line in Fig. 3. Further downstream, the forward-flow fraction decreases continuously and a value of $\gamma = 0.5$ [transitory detachment (TD)] is found at $x = 210$ mm. Nonzero minima in γ are reached at the foot of the diffuser ramp, suggesting the intermittent presence of forward-directed flow. The transitory reattachment (TR) line at the downstream end of the recirculation region is located at $x = 390$ mm. Thus, a characteristic length of the separation bubble, enclosed by TD and TR, of $L_b \approx 180$ mm can be deduced. Further downstream, complete reattachment ensues, albeit not directly measured by means of PIV because it lies slightly outside the field of view for this method.

B. Method of Active Separation Control and Investigated Forcing Signals

Control of the flow configuration introduced previously in this paper was facilitated by emitting compressed air in a pulsatile fashion by means of an array of five identical pulsed-jet actuators: one of which is shown in Fig. 4. They feature fast-switching solenoid valves, allowing for minimum pulse durations of $t_p = 0.6$ ms at a maximum inaccuracy of 15%. Note that t_p was assumed to be of equal duration as the valve opening time, which was controlled by a square-wave signal. Following the opening of the valve, a slight time delay (on the order of 1 ms) occurs before fluid is ejected from the outlet. Downstream of the solenoid valve, a three-dimensionally (3-D)-printed nozzle transforms the circular inlet cross section into a rectangular outlet with an aspect ratio of $l/d = 20$ mm/0.5 mm = 40. Owing to the employed stereolithography technology and layer thicknesses of 25 μm for 3-D printing, the surface roughness inside the nozzle was $Ra < 2.5$ μm. With respect to the longer slot dimension, a homogeneous jet velocity is achieved by deflecting the flow inside the nozzle by means of two backward-facing steps, which may result in minor recirculation zones. A detailed analysis of the specific near-outlet flow was provided in a recent paper [38]. In summary, we noted a large transverse advection of fluid (i.e., highly nonparallel flow) due to an overpressure peak inside the jet exit plane. This is assumedly linked with the PJA function principle in which fluid is accelerated more rapidly as compared to other means of generating starting jets.
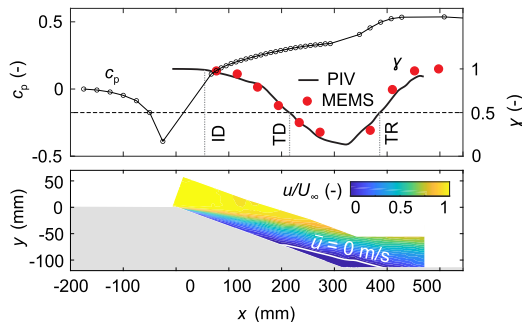

Fig. 3 Natural one-sided diffuser flow in absence of forcing for $\alpha = 20$ deg: mean pressure distribution in symmetry plane and forward-flow fractions measured with PIV and MEMS wall shear-stress sensors (top); and mean velocity field (bottom).
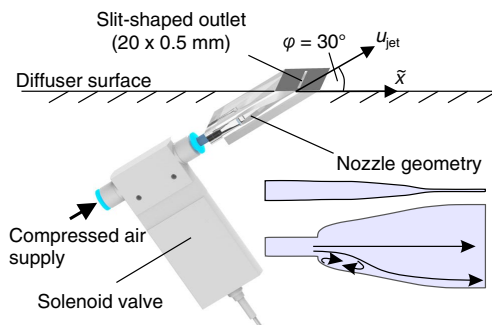

Fig. 4 Pulsed-jet actuator operated at emission angle of $\varphi = 30$ deg.

The PJAs were mounted flush in the diffuser wall with outlets located at $x \approx 65$ mm for $\alpha = 0$ deg ($\tilde{x} = 0$ mm) and a spanwise distance between neighboring slots of $\Delta z = 2$ mm. The longer slot dimension was oriented in the spanwise direction, and the pitch angle was zero during the entire study; hence, jets were introduced in the main flow direction without a nominal transverse component. The jet inclination angle, on the other hand, was set to $\varphi = 30$ deg, representing an effective operating condition as vortex half-rings trailed by wall-attached jets are generated [20].

Indicated in Fig. 1, the major actuation parameters addressed in this study were the forcing intensity, represented by the jet velocity ratio $r = u_{jet}/U_\infty$; the pulse duration t_p; and the time delay t_{off}. For fixed t_p and t_{off}, the forcing intensity was varied by adjusting the nominal jet velocity that could be set with a maximum uncertainty of ± 0.4 m/s using a mass-flow controller, taking into account the jet outlet area, the pulse width, and the actuation period. The timescales t_p and t_{off}, on the other hand, were assumed to correspond to durations where the magnetic valve of the PJA was open and closed, respectively, which was controlled with a signal generator. The separate variation of these three quantities leads to a large number of parameter combinations, with different subspaces addressed individually as explained in the following.

1. Investigation of Single-Pulse Jets

First, we will consider the scenario where the interaction between successively generated jets is limited. For practical reasons, fluid was still emitted periodically but the time delay t_{off} was kept constant at relatively large values. To study the interaction of the jet array with an APG boundary layer, a tomographic reconstruction of the flow-field was performed based on phase-locked three-dimensional three-component (3C) PIV measurements in 35 planes. Here, only one parameter combination was considered. Furthermore, two-dimensional (2-D) two-component (2C) PIV as well as wall shear-stress data were obtained for the parameter ranges given in the second row of Table 1.

2. Influence of the Pulse Delay

Then, the time delay between successive pulses was varied with three values $t_{off} = (4.8, 11, 20.3)$ ms addressed in detail at a velocity ratio of $r = 4$ and a pulse duration of $t_p = 3$ ms. Here, two types of experiments were conducted. During *terminated-forcing* experiments, actuation with the parameter combinations stated in Table 2 was only applied initially before forcing was stopped and the flow was allowed to settle into its natural, unforced configuration. This enabled conclusions regarding the impact of initial forcing conditions on the onset of flow separation. A representation of the investigated forcing signal is shown in Fig. 5 (left). Note that steady blowing was used as a reference case. To allow for phase averaging of measurement data, the intervals of forcing and no fluid emission were repeated periodically with each phase lasting for 1 s, which was verified to be sufficiently long to ensure converged flow states.

In a second set of experiments, *continuous forcing* was addressed where the flow was not allowed to return to its natural state (Fig. 5, right). This represents the typical scenario found in ASC so that conclusions regarding the applicability of an optimized t_{off} can be drawn.

3. Influence of Pulse Duration

Finally, a combination of parameter spaces introduced in the two previous sub-sections is considered to determine the effect of a varied pulse duration (Table 3). Furthermore, the control authority as well as the efficiency associated with the resulting forcing signals are assessed.

C. Applied Measurement Techniques

The results presented in this paper are mainly based on three experimental methods that are briefly introduced in the following:

Synchronized bidirectional wall shear-stress measurements were conducted with calorimetric microelectromechanical system (MEMS) sensors of the same type as introduced by Weiss et al. [39,40]. Here, a microbeam suspended over a micrometer-scale cavity is heated by an electric current, and the thermal wake is measured with two additional lateral detector beams acting as resistance thermometers. Following a calibration up to $\tau = 7$ Pa in a dedicated wind tunnel, the detector signals can be related to the direction and magnitude of the local wall shear stress with a maximum uncertainty of approximately 5% [40]. Ten of these sensors were mounted flush inside the symmetry plane, with six of them located on the diffuser

Table 1   Parameter space addressed in Sec. III

	t_{off}, ms	t_p, ms	DC	F^+	r	c_μ, %
3-D 3C	20.3	3	0.13	0.58	2.5	0.35
2-D 2C/wall shear stress	50	$3, \ldots, 20$	$0.06, \ldots, 0.29$	$0.19, \ldots, 0.25$	3, 7	$0.22, \ldots, 6.17$

Table 2   Parameter space addressed in Sec. IV

	t_{off}, ms	t_p, ms	DC, %	F^+	r	c_μ, %
Pulsed blowing	$3, \ldots, 40$	3	$7, \ldots, 50$	$0.3, \ldots, 2.3$	$1.5, \ldots, 10$	$0.2, \ldots, 6.2$
Steady blowing	0	$\to \infty$	100	——	$1, \ldots, 10$	$0.4, \ldots, 44.1$
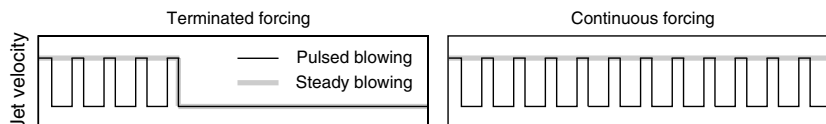
Fig. 5   Exemplary actuation signals for the two types of experiments presented in Sec. IV.

Table 3   Parameter space addressed in Sec. V

	t_{off}, ms	t_p, ms	DC, %	F^+	r	c_μ, %
Pulsed blowing	6, 11	1, 3, 5, 6, 7, 11	$0.1, \ldots, 0.5$	$0.52, \ldots, 1$	$1, \ldots, 10$	$0.05, \ldots, 4.5$
Steady blowing	0	$\to \infty$	100	–	$0.5, \ldots, 3.2$	$0.1, \ldots, 4.5$

Fig. 6 Overview of employed measurement techniques.

ramp and the remaining sensors on the plate downstream (Fig. 6, left). Samples were taken at a frequency of $f_s = 5$ kHz over durations that corresponded to at least 150 forcing periods for each parameter combination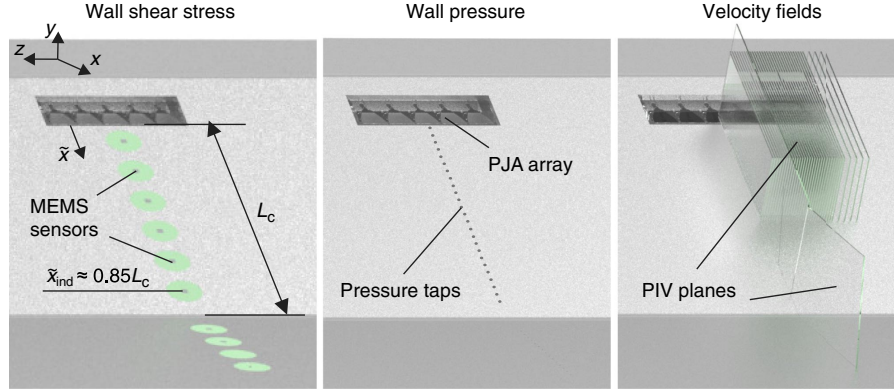. Note that $\tau > 0$ Pa indicates flow in the positive $\tilde{x}$ or x direction by design. Although we are aware that vanishing wall shear stress does not necessarily indicate the detachment of a turbulent flow [37,41], zero crossings will be used as an approximate indicator for the onset of reverse flow in the following. Because the region near the diffuser foot is most prone to flow separation, the sensor located at $\tilde{x} \approx 0.85L_c$ ($x \approx 230$ mm in Fig. 3) will be evaluated as an indicator. The distance between jet outlets and the downstream end of the diffuser ramp is defined as the control length $L_c = 0.27$ m.

Pressure measurements were conducted at 25 equidistantly spaced locations on the diffuser ramp. Differential pressure sensors with a maximum inaccuracy of 2.5 Pa were used to attain mean pressure distributions. In addition, piezoresistive pressure transducers were employed to acquire time-resolved signals. Three sensors with a range of $p_{max} \approx 6.9$ kPa and a maximum inaccuracy of approximately 0.6% full-scale output were successively operated at the same sampling parameters as the wall shear-stress sensors.

Velocity field information was obtained by performing PIV. A double-pulse laser was employed to illuminate aerosol particles, and images of the reflections were taken with a complementary metal-oxide-semiconductor camera with a resolution of (2560×2150) square pixels and a pixel size of (6.5×6.5) μm^2. A coating was applied to the surface to reduce reflections so that velocities could be measured up to a wall distance of $\Delta y \approx 2$ mm. Measurements were conducted in multiple areas of the one-sided diffuser flow. First, phase-locked two-component velocity fields were determined through measurements in two overlapping planes in the symmetry plane. This was achieved by triggering the PIV system at different time instances with respect to the square-wave signal controlling the solenoid valves. The number of snapshots per phase was chosen to ensure sufficient mean data convergence. Then, detailed stereoscopic measurements were conducted in the near-outlet region for one selected configuration ($r = 2.5$, $t_p = 3$ ms, and $t_{off} = 20.3$ ms). Phase-averaged data from 35 measurement planes (Fig. 6, right) were used to perform a tomographic reconstruction of the time-resolved flow domain.

III. Flow Structures Contributing to Separation Control Authority

In the following section, we will address the threefold mechanism leading to an increased near-wall momentum flux through pulsed-jet actuation. The results are mainly presented for velocity ratios of $r = (3, 7)$. However, no explicit comparison in terms of the control effectivity is implied at this stage. Instead, focus is laid on the generation of flow structures with different jet velocities, thereby setting the stage for the following sections of this paper.

The authors recently suggested that the effectivity of pulsed wall jets is driven by three flow structures (Fig. 7) [20]. First, a leading
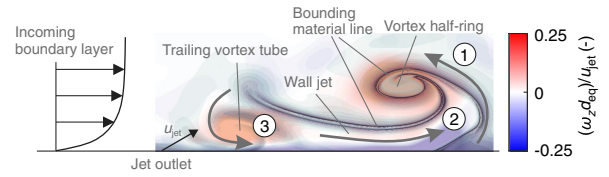

Fig. 7 Major flow structures associated with a PJA-generated wall jet; figure, in part, reproduced with permission from Steinfurth and Weiss [20].

vortex (LV) develops during the initiation of momentum addition, i.e., for small t. It has the shape of a vortex half-ring that extends from the wall and attains its maximum circulation around a nondimensional formation time of approximately $t^* = 9$ in a zero-pressure-gradient boundary layer. The LV is enclosed by the jet propagation front, along which low-momentum boundary-layer fluid is pushed aside [42]. Second, the wall-attached jet replaces the low-momentum fluid with high-momentum fluid injected through the outlet. The entrainment into this wall jet, however, is negligible, as indicated by the bounding separating material line in Fig. 7. And third, a tubelike stopping vortex develops immediately following the end of the jet emission phase. Associated with positive spanwise vorticity of the same order as the LV, it causes radial entrainment of fluid from the outer flow into the near-wall region.

Although the mechanisms introduced above have been revealed recently, their interaction and dependence on actuation parameters remain unclear. We will tackle these issues by assessing the flow structures separately in the following.

A. Leading Vortex Half-Ring

Figure 8 contains a times series shedding some light on the impact of the LV when interacting with a low-momentum boundary layer.

The configuration is characterized by a velocity ratio of $r = 2.5$, a pulse duration of $t_p = 3$ ms, and a time delay of $t_{off} = 23.3$ ms. Similar findings are expected for other cases of pulsed blowing because previous studies have shown that the overall jet structure is insensitive to changes of these parameters [20,36]. Based on phase-locked measurements in several streamwise PIV planes, the following flow properties are visualized: vortex structures are revealed by a gray isosurface of the three-dimensional finite-time Lyapunov exponent, indicating an attracting material surface. The wall-normal velocity component $\tilde{v}$ is shown inside the symmetry plane. And, the momentum deficit of the near-wall flow is shown in a cross section at $\tilde{x} = 100$ mm. To the interested reader, a visualization video for this configuration is available [42]. By investigating a periodically forced turbulent separation bubble, similar flow structures were found in a different study [43].

Note that the fluid emission begins at $t = 0$ s per definition. With fluid still being emitted at the first displayed time step ($t \approx 2.4$ ms),
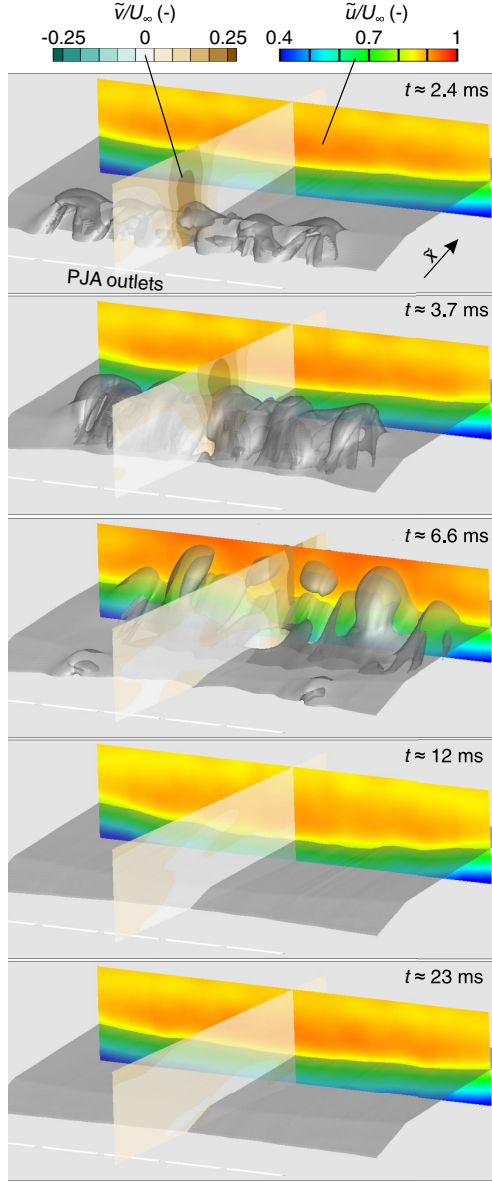
Fig. 8 Three-dimensional flowfield manipulation over the course of one actuation period.

the emergence of pulsed jets from the array of PJAs is observed. The jet propagation front (gray isosurface) contains the growing LVs as the jets roll up during the interaction with the boundary layer. A region of substantial wall-normal velocity can be observed with maxima on the order of $\tilde{v} = 0.25U_\infty$ in the center plane. This is linked to the advection of boundary-layer fluid away from the wall touched upon earlier in this paper. The subsequent time steps indicate that the jets grow slightly in the wall-normal direction while propagating downstream. Once they arrive at the highlighted cross section, an increase of $\tilde{u}$ can be observed before the boundary layer again grows in thickness, following the jet passage, which can be seen in the two last time steps.

We will now assess the development of the LV and the induced wall-normal velocity for two different velocity ratios during the jet starting process, i.e., during the ongoing fluid emission phase. The velocity ratio of $r = 3$ shown in the first column of Fig. 9 is only slightly larger than the one presented in Fig. 8, whereas $r = 7$ (second column) represents a significantly larger momentum addition.

The first time step at $t = 1$ ms corresponds to formation times of $t^* \approx (16, 39)$ for the two configurations, both exceeding the non-dimensional time that yields a maximum-circulation LV. Accordingly, a trailing jet can be observed in both cases, containing the excessive vorticity. As can be expected, an LV of larger dimensions and higher vorticity (i.e., greater circulation) is noted at $r = 7$.

Let us now consider the maxima in $\tilde{v}$ at different streamwise locations and compare them with the maximum velocities in the absence of forcing: $\Delta V_m = \tilde{V}_m(x, t) - \tilde{V}_m(x, t < 0 \text{ s})$. Clearly, the induced wall-normal velocity at $r = 7$ of up to $\Delta V_m = 0.8U_\infty$ is larger than the smaller value found for the smaller velocity ratio of $\Delta V_m = 0.6U_\infty$. Furthermore, the streamwise extent of the region where $\tilde{v}$ is enhanced is substantially larger. Therefore, a superior transport of boundary-layer fluid can be expected for $r = 7$. Although the deviation is relatively small at $t = 1$ ms, a different picture is subsequently revealed: LVs can still be identified in the vorticity fields for $r = 7$, but no such flow structure is apparent for the smaller velocity ratio. This leads us to conclude that a certain excess in streamwise momentum flux is required at the downstream end of the jet to maintain the LV. Importantly, the absence of an LV at $t = 4$ ms and $t = 8$ ms coincides with negligible induced wall-normal velocities, whereas a maintained contribution can be attested for the $r = 7$ configuration.

These results confirm that the major effect of the leading vortex half-ring is the displacement of low-momentum fluid initially located downstream of the PJA-generated jet.

B. Wall Jet

Attention is now turned to the second flow structure displayed in Fig. 7, i.e., the wall-attached jet.

The gain in streamwise velocity with regard to the unforced flowfield $\Delta U = \tilde{u}(x, t) - \tilde{u}(x, t < 0 \text{ s})$ is presented in Fig. 10 for the
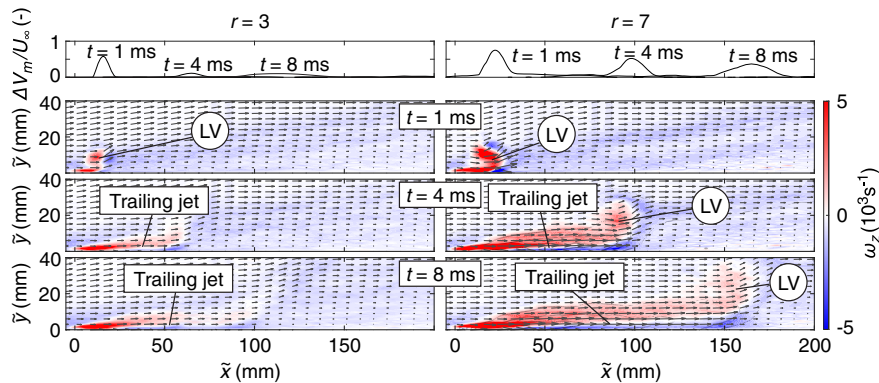

Fig. 9 Time series of vorticity fields for velocity ratios $r = 3$ and $r = 7$ overlaid with velocity vector fields; induced wall-normal velocity presented in top row.
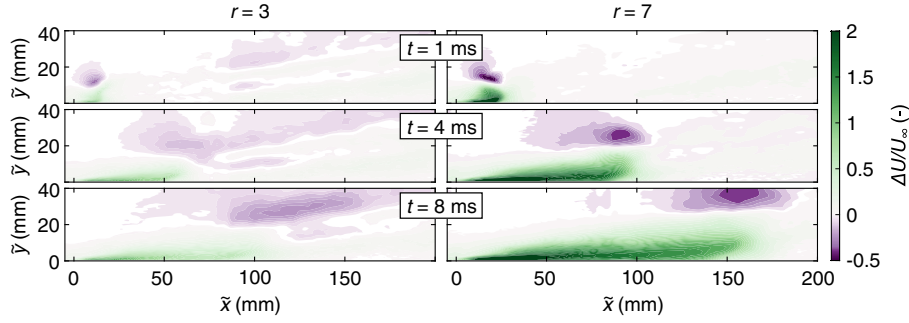
Fig. 10 Time series of gain in streamwise velocity for $r = 3$ and $r = 7$.

same phase-averaged flowfields assessed in Fig. 9. Note that $\tilde{u}$ is the velocity component directed along $\tilde{x}$. It can be confirmed that the jets attach to the wall immediately downstream of the outlet, which is attributed to the Coandă effect. Further downstream, momentum flux is only enhanced in the near-wall region at $\tilde{y} < 20$ mm, which may be argued to be an efficient distribution of momentum as opposed to that found for larger jet emission angles [20]. However, the gain in velocity becomes negligible in a greater outlet distance for $r = 3$, explaining the absence of an LV that is manifested in regions of decreased velocity (purple) above the jet propagation front otherwise.

Considering only the time step of $t = 8$ ms, velocity profiles are shown for different streamwise locations in Fig. 11, taking into account both velocity ratios as well as the unforced flow ($r = 0$). Note that the location of $\tilde{x} = 200$ mm is reached by neither wall jet at the evaluated time instant. Hence, identical velocity profiles as for the unforced flow are measured. Further upstream, typical wall jet profiles can be noted for $r = 7$ as the freestream velocity is exceeded in the near-wall region [44]. Even though this does not happen for the smaller velocity ratio, the streamwise velocity in the near-wall region is still increased at the locations spanned by the jet [$x = (50, 100)$ mm]. Because the observed peaks measured close to the diffuser surface are associated with larger velocity gradients $\partial \tilde{u}/\partial \tilde{y}$ as compared to the unforced flow, an increased wall shear stress can be expected; whereas a vanishing wall shear stress appears to be at hand in the jet far field that coincides with the

location of the transitory detachment line shown in Fig. 3. As an estimate for the likelihood of separation, we therefore consider the local wall shear stress in the following.

The phase-averaged time signals $\tau(t)$ measured at three sensor locations downstream of the jet outlets are displayed in Fig. 12. Before the arrival of pulsed jets, the wall shear stress is indeed close to zero at all sensor locations. Then, a slight increase up to $\tau \approx 1$ Pa is observed for the smaller velocity ratio at $\tilde{x} = 99$ mm. Here, an initial plateau initiated around $t \approx 7$ ms is measured, which is related to velocity gradients induced by the jet leading part that are smaller than those inside the trailing jet, cf. Fig. 9. Further downstream, the maximum jet velocity decays and only a very minor impact is noted at $\tilde{x} = 183$ mm. As for the larger velocity ratio of $r = 7$, LV footprints can be clearly identified in the time signals, represented by initial peaks in wall shear stress. It is also worth mentioning that an increased convective velocity can be inferred as compared to the $r = 3$ case, given that τ already begins to increase around $t \approx 4$ ms at the first sensor location. Following the LV passage, much larger levels of wall shear stress are induced by the wall jets, mainly because the peak jet velocity is reached closer to the wall than inside the LV. As the jet velocity decays in $\tilde{x}$, decreasing values of τ are noted going downstream. Nonetheless, a distinct enhancement up to $\Delta\tau \approx 3$ Pa is found at $\tilde{x} = 183$ mm.

In summary, two major effects of the wall jet can be attested. First, it directly increases the momentum flux and the wall shear stress by supplying the ejected fluid to the near-wall region. And second, it maintains the LV that in turn pushes aside low-momentum boundary-layer fluid.

C. Trailing Vortex Tube

Finally, we will briefly address the trailing vortex tube shown in Fig. 7. Due to the temporal resolution of PIV measurements ($\Delta t = 0.5$–1 ms), the evolution of the trailing vortex is not adequately resolved. In fact, it is only captured in one phase for each jet configuration, suggesting a relatively quick diffusion. The beneficial effect of this vortex structure in terms of an enhancement of the near-wall momentum flux may therefore be limited. In addition, the induced negative wall-normal velocity shown in the upper diagram of
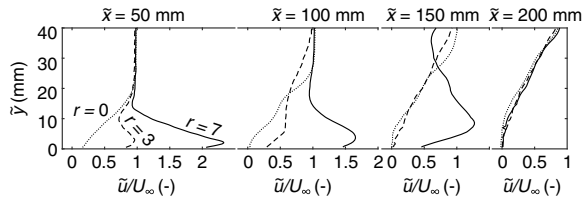

Fig. 11 Streamwise velocity profiles at different outlet distances for unforced flow ($r = 0$) and pulsed jets associated with different velocity ratios.
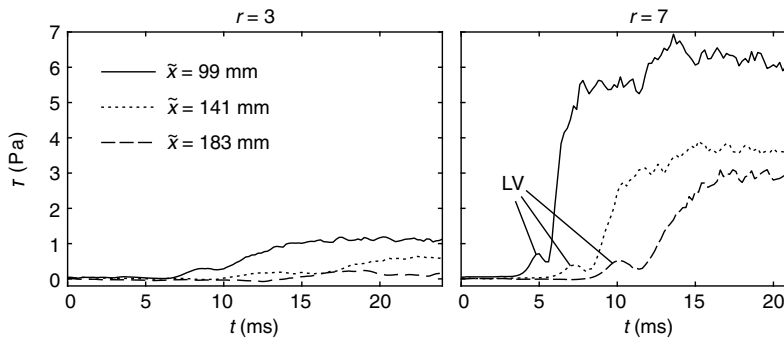

Fig. 12 Wall shear-stress signals at different outlet distances for velocity ratios $r = 3$ and $r = 7$.
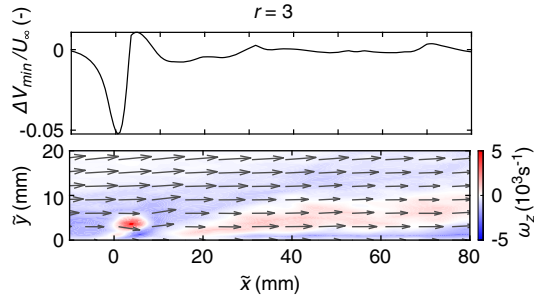
Fig. 13 Minimum wall-normal velocity component at $t = 7$ ms for $r = 3$, $t_p = 5$ ms pulsed jet (top); and vorticity field for the same jet containing trailing vortex tube, overlaid with velocity vector field (bottom).

Fig. 13 is small as compared to the magnitude of the same velocity component near the jet leading part. Therefore, the entrainment of high-momentum fluid from the outer flow due to the trailing vortex tube may be of minor relative importance to the overall control authority in the present setup.

Summarizing the results presented in this section, it can be confirmed that the control authority of PJAs is mainly linked to three flow structures: the LV, the wall jet, and a trailing vortex. Contrasting with other means of separation control where large-scale vortex structures also lead to an entrainment of the outer flow [45,46], the predominant effect of PJA-generated jets lies in the displacement of low-momentum fluid away from the near-wall region by the LV and its replacement by high-momentum wall jet flow. We therefore conclude that the pulse duration should be set to values that ensure the generation of a wall jet, i.e., it should be larger than the nondimensional timescale that leads to the exclusive generation of a maximum-circulation LV [20]. Before returning to the optimization of the pulse duration, attention is now turned to the transient dynamics unfolding between successive pulses.

IV.   Adjusting the Time Delay Between Pulses t_{off}

A reduced mass-flow consumption may be seen as a reasonable definition of an enhanced efficiency in ASC as long as the control authority is maintained. It therefore appears to be a worthwhile task to optimize the duration t_{off} where the ejected mass flow is zero (Fig. 1).

When pulsed actuation is applied to control boundary-layer separation, there is a periodic cessation of momentum addition, namely, at the end of each emission phase. Subsequently, the manipulated flow begins to evolve into its natural state. We will now investigate the dynamics governing this process when it is not interrupted by the addition of further momentum. The type of forcing signal first addressed in this section is shown in the left-side image of Fig. 5. Note that a similar experiment was conducted by Darabi and Wygnanski for the case of a deflected flap [47].

Phase-averaged signals based on unsteady pressure measurements are shown in Fig. 14 for selected locations downstream of the jet outlets ($\tilde{x} \approx 10, \ldots, 250$ mm). Here, initial forcing conditions are characterized by a velocity ratio of $r = 4$ and a pulse delay of $t_{off} = 11$ ms with the normalized form $t_{off} \approx 0.8 L_c/U_\infty$ referred to in the following. Note that, in this section, the fluid emission was terminated at $t = 0$ ms by definition. The spacing between the pressure taps evaluated in this figure is constant so that information regarding the pressure gradient can be readily extracted by visual inspection. The converged pressure distribution for $t \to \infty$ is displayed in Fig. 3.

Directly following each jet emission cycle, the footprint of the wall-attached jet manifests itself in a short-time increase directly followed by a drop in static pressure, which is caused by the propagation front and the trailing part of the jet, respectively. The dashed vertical line in Fig. 14 marks the time $t = L_c/U_\infty$ which approximately coincides with the presence of the jet at the most downstream pressure tap located at $\tilde{x} \approx 0.92 L_c$. Therefore, U_∞ appears to be a reasonable approximate for the jet convective
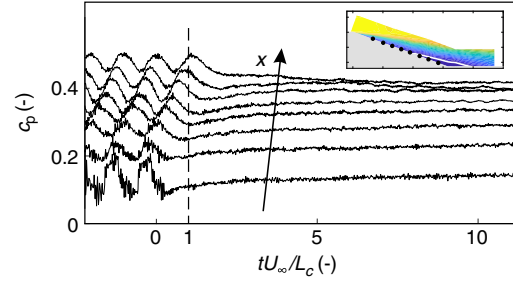

Fig. 14 Phase-averaged development of pressure coefficients at different locations on the diffuser ramp; sensor locations highlighted by black markers.

velocity, and $t_c = L_c/U_\infty$ will be regarded as the convective timescale of the flow. Subsequent to the passage of the final pulsed jet, converged pressure coefficients cannot be attested immediately. Instead, a decreased pressure gradient gradually develops as the difference in pressure coefficients for neighboring locations becomes smaller as compared to the initial state of active forcing. Even at $t > 5 L_c/U_\infty$, small but nonzero rates of change are observed as the pressure appears to increase in upstream locations and decrease in downstream locations. This gradual change is attributed to the slow recovery of the flow toward its initial uncontrolled state, previously noted in Ref. [47].

Enabling more integral insight into this dynamical process, the development of the normal force coefficient for the same configuration is shown in Fig. 15. Now, only pressure taps inside the eventual region of reverse flow on the diffuser ramp, denoted "I", are evaluated. This allows us to make some comparisons with Ref. [47], where evolving normal force coefficients associated with a completely separated flap were addressed.

It is immediately apparent that substantial dynamical loads act on the diffuser ramp during the periodic fluid emission at $t < 0$ ms, which will not be addressed in much detail in this paper. The major characteristics of the flow response toward a sudden termination of forcing are in good agreement with the results presented by Darabi and Wygnanski; see their figure 1 [47]. Namely, the separation process is initiated by the convection of a dominant flow structure, which is the pulsed wall jet in the current study. Then, an ongoing reduction in normal force is measured, which is followed by a slight undershoot as $c_{n,I}$ reaches values smaller than those found in the unforced flow around $t \approx 10 L_c/U_\infty$. Interestingly, the entire development lasts for a duration that is a multiple of the convective timescale because the eventual flow state is arguably not reached before $t \approx 50 L_c/U_\infty$ or $t \approx 0.7$ s. Although this observation may shed some light on the fundamental response of the diffuser flow evolving at large timescales, the insight regarding the initiation of flow separation is limited. Therefore, a detail diagram for the time range of $t = -1, \ldots, 5 L_c/U_\infty$ is also presented in Fig. 15. Here, the footprint of the final pulsed jet can be seen after approximately one convective
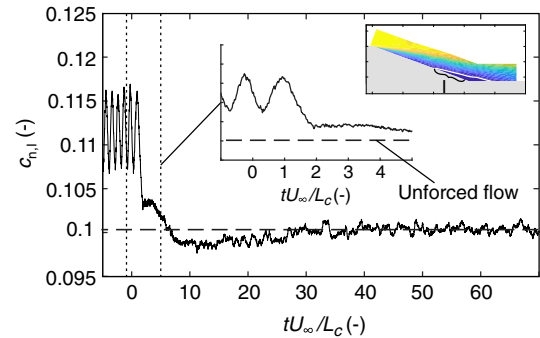

Fig. 15 Phase-averaged development of normal force coefficient inside the highlighted flow region.

timescale before a rapid decrease in normal force is observed as the coefficient falls below the average value achieved during forcing at approximately $t \approx 1.5L_c/U_\infty$. Thereafter, c_n continues to decrease before a smaller rate of change is measured after $t = 2L_c/U_\infty$.

In an attempt to relate the normal force signal to the local flow state, specifically to the potential occurrence of flow separation, we now consider wall shear-stress signals allowing for time-resolved information on the local flow direction. First, information on the development of wall shear stress τ and the forward-flow fraction γ near the diffuser foot will be provided for the configuration discussed above along with two further time delays (Fig. 16).

It is worth noting that before the termination of forcing at $t = 0$ s, the mean wall shear stress is the largest for the shortest time delay of $t_{off} = 0.4L_c/U_\infty$, which can be explained by the larger mean momentum supplied to the flow in this case. Once fluid emission is stopped, a behavior similar to the one associated with the time-resolved normal force is seen. Immediately subsequent to the end of the forcing phase, τ begins to rise, which can be ascribed to the delayed arrival of the final pulsed jet(s) at the sensor location $\tilde{x} = 225$ mm. Only around L_c/U_∞ does the local wall shear stress begin to drop abruptly for all three configurations. A slightly larger convective velocity appears to be at hand for the shortest pulse duration as τ starts to decrease slightly sooner than for the other configurations. Nonetheless, the quickest zero crossing (i.e., the first occurrence of reverse flow from a phase-averaged perspective) is observed for the $t_{off} = 1.5L_c/U_\infty$ case around $t \approx 1.7L_c/U_\infty$.

These findings are confirmed by the forward-flow fraction signals shown in the bottom image of Fig. 16. Up to $t \approx L_c/U_\infty$, positive wall shear stress is measured at almost all times in the case of the shortest time delay ($\gamma \approx 0.95$). Then, the final pulsed jet passes the diffuser ramp, a region of reverse flow occurs, and the location of transitory detachment where $\gamma = 0.5$ propagates upstream, passing the sensor location around $t \approx 2.2L_c/U_\infty$. This time instant will be referred to as separation time t_s in the following. As for the larger time delays, values of $\gamma < 0.5$ are already found after $t_s \approx 2L_c/U_\infty$ and $t_s \approx 1.7L_c/U_\infty$, respectively (highlighted by dashed vertical lines in the figure). Interestingly, the separation time measured for the medium t_{off} coincides with the time instant where the rapid drop in normal force comes to a halt (Fig. 15). It is therefore reasonable to assume that the initial phase directly following the termination of forcing is linked to the passage of the deceleration wave, whereas the subsequent development associated with smaller rates of change is related to the expansion of the separated flow region. Assuming that knowledge regarding the separation time t_s, marking the transition between these two phases, enables an optimization of the pulse delay t_{off}, the question is raised of whether the occurrence of phase-mean reverse flow ($\gamma < 0.5$) depends on forcing conditions. In an attempt to answer this question, we now vary the velocity ratio in the range of $r = 2.5, \ldots, 10$ for a fixed pulse duration of $t_p = 3$ ms and the same pulse delays discussed above. The separation times t_s, again obtained
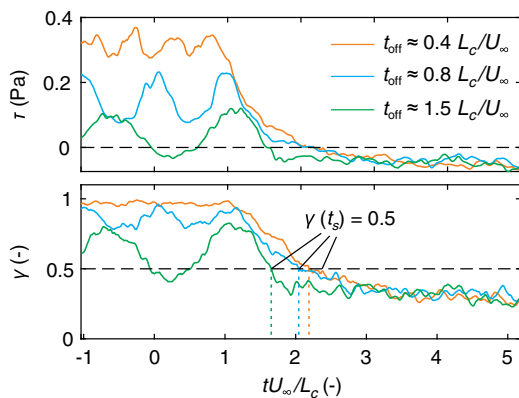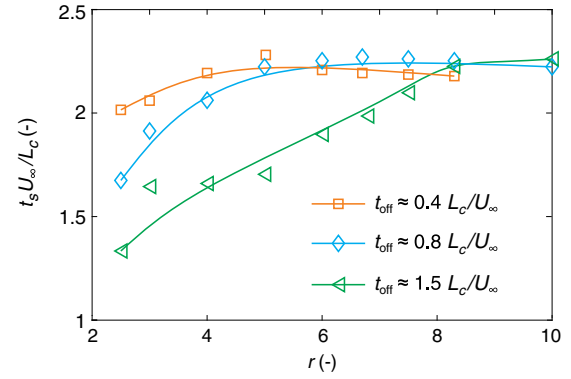

Fig. 17 Separation time as a function of the velocity ratio.

from the indicator sensor located at $\tilde{x}_{ind}/L \approx 0.85$, are shown as a function of the velocity ratio in Fig. 17.

For relatively small velocity ratios (up to $r = 4$), there appears to be a strong dependence on the pulse delay, inasmuch as there is a much quicker occurrence of reverse flow for the largest pulse delay ($t_s \leq 1.7L_c/U_\infty$). However, the separation time converges to a value of $t_s = 2.2L_c/U_\infty$ for velocity ratios of $r \geq 5$ in the case of the two shorter time delays, whereas similar values are only measured at $r = (8.3, 10)$ for the largest time delay. This suggests two important conclusions. First, there appears to be a limiting value for the separation time. And second, a certain mean momentum input is required to ensure that this specific separation time is reached.

Following up on these statements, the separation times for different types of forcing signals belonging to the parameter space introduced in Table 2 are shown in Fig. 18 as a function of the respective mean momentum coefficients c_μ.

Indicated by the dashed vertical line, two categories defining the dependence on c_μ can be ascertained. For small momentum coefficients, the separation time t_s is proportional to the forcing intensity, which can also be noted in Fig. 17, where the momentum coefficient is varied through an adjustment of the velocity ratio. For larger momentum coefficients, on the other hand, there is no further increase of the separation time. Due to the procedure of computing this quantity, which relies on the measurement of vanishing wall shear stress, some scatter in results can be expected; note the difference between the two sets of measurements of the steady-blowing case highlighted by stars in Fig. 18. Nonetheless, it is clear that the separation time becomes independent of the forcing intensity once c_μ is sufficiently large, and a characteristic value of approximately $t_s^* = 2.2L_c/U_\infty$ is determined. This separation timescale may be viewed as an inherent flow characteristic that is linked with the boundary-layer relaxation following the periodic flow manipulation. As for

Fig. 16 Phase-averaged signals measured with wall shear-stress sensor near the diffuser foot ($\tilde{x}_{ind}/L_c \approx 0.85$); separation times highlighted by dashed vertical lines.


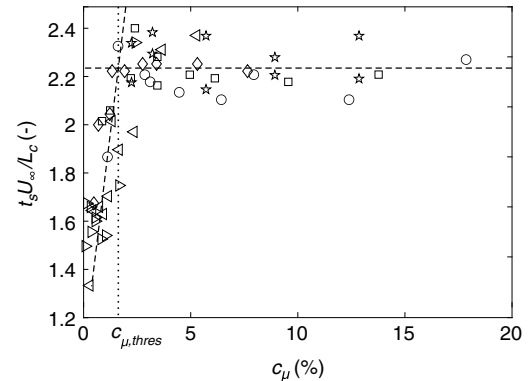**Fig. 18 Separation time depending on mean momentum input: $t_{off} \approx 0.2L_c/U_\infty$ (circles), $t_{off} \approx 0.4L_c/U_\infty$ (squares), $t_{off} \approx 0.8L_c/U_\infty$ (diamonds), $t_{off} \approx 1.5L_c/U_\infty$ (left-pointing arrows), $t_{off} \approx 3.0L_c/U_\infty$ (right-pointing arrows), and steady blowing (stars).**

smaller momentum coefficients, we assume that the region of reverse flow is not completely suppressed. Instead, the location of transitory detachment ($\gamma = 0.5$) is merely shifted downstream of the evaluated sensor location, which indeed will be shown later on. As a result, the process of separation recurrence is at a more advanced state when forcing is terminated and a smaller separation time is measured. The threshold momentum coefficient required to achieve a fully suppressed separation bubble of $c_{\mu,\text{thres}} \approx 1.5\%$ (marked by a dashed vertical in Fig. 18) can be viewed as the second flow-inherent value.

Before elaborating on the potential of an inherent (hence constant) separation time, we briefly address the influence of two important flow parameters on this quantity. In Fig. 19, separation times are presented for different Reynolds numbers associated with inflow velocities of $U_\infty = (15, 25)$ m/s and for two further diffuser angles of $\alpha = (19, 21)°$.

When scaled with the reference velocity U_∞, identical general characteristics can be noted for the Reynolds number variation. Again, small momentum coefficients lead to a sooner recurrence of reverse flow, whereas a characteristic value similar to the $U_\infty = 20$ m/s case can be determined for sufficiently large forcing intensities. The variation of the diffuser angle α, essentially resulting in a different APG magnitude, has a more pronounced effect in comparison. For $\alpha = 19$ deg, the increase at small c_μ appears to follow a larger slope than for the $\alpha = 20$ deg case indicated by the dashed line. In other words, a smaller momentum coefficient is required to yield a specific separation time, which may be expected, given that the APG is reduced. Accordingly, a larger momentum input is necessary to overcome the stronger APG at $\alpha = 21$ deg (open symbols). Given the relative sparsity of measurements conducted for momentum coefficients of $c_\mu > 1.5\%$, we do not attempt to define characteristic separation times for these cases, although they appear to be of a similar order as in the $\alpha = 20$ deg configuration (Fig. 18).
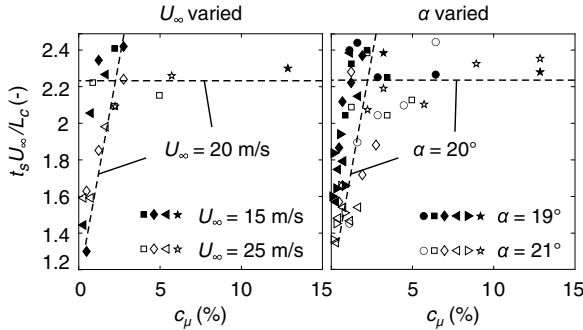
Summarizing the terminated-forcing experiments, two timescales were found to govern the development of the diffuser flow into its unforced state once forcing is terminated. The evolution of the pressure field is characterized by a rapid drop of normal force acting on the diffuser ramp before ever smaller rates of change are noted. In agreement with experiments on a deflected flap [47], the entire flow development was shown to last for a duration many times the convective time of the flow: here, approximately $50L_c/U_\infty$. Interestingly, the duration after which the transitory detachment line ($\gamma = 0.5$) reaches the indicator location near the diffuser foot of $\tilde{x} \approx 0.85L_c$ is much smaller and independent of the initial forcing conditions when the mean momentum input is sufficient to ensure complete separation suppression. This duration, dubbed the characteristic separation time t_s^*, may therefore be viewed as an inherent flow property. Leading over to the following assessment of the effectivity and efficiency of continuous forcing, we hypothesize that knowledge of t_s^* may be useful in adjusting the time delay between successive pulses. Specifically, the phase-mean reverse flow at $\tilde{x} = 0.85L_c$ and upstream thereof may not occur when

$$t_{\text{off}} < t_s^* - t_c \tag{3}$$

because the succeeding jet reaches the downstream end of the control domain before the separation time is exceeded, i.e., before reverse flow occurs. We will now assess the validity of this criterion, which yields a critical value of $t_{\text{off,crit}} = t_s^* - t_c = 1.2L_c/U_\infty$.

The mean streamwise velocity fields in the symmetry plane, obtained from phase-locked measurements at equidistant phases during the emission cycle, are shown in the top row of Fig. 20 along with time-averaged in-plane velocity vector fields. Note that these measurements were carried out while applying continuous forcing (Fig. 5, right).

Compared to the flowfield in the absence of forcing (Fig. 3), the velocity deficit in the near-wall region is clearly reduced for all configurations. Small regions of time-averaged flow recirculation are only found for the two larger time delays, which confirms the conclusion made earlier in this paper that a momentum input of $c_{\mu,\text{thres}} \approx 1.5\%$ is required to suppress flow separation completely. However, the regions of mean reverse flow do not enclose the adjacent wall shear-stress sensor locations highlighted in the figure, for which the output signals are used to reveal the evolution of forward-flow fractions (bottom row in Fig. 20). Note that the red curve was measured with the sensor used to determine the separation time above. For the shortest pulse delay of $t_{\text{off}} \approx 0.4L_c/U_\infty$, values of $\gamma > 0.9$ are measured throughout the actuation period, indicating that the flow is directed forward at almost all times. This is in agreement with the criteria defined earlier in this paper. First, the momentum coefficient is sufficiently large; and second, the criterion stated in Eq. (3) is fulfilled because the pulse delay is substantially smaller than the critical value of $t_{\text{off,crit}} = 1.2L_c/U_\infty$. This is also true for the medium pulse delay of $t_{\text{off}} \approx 0.8L_c/U_\infty$. However, the mean momentum input is significantly smaller, leading to a more frequent occurrence of reverse flow at $\tilde{x} \approx 0.85L_c$ ($\gamma \approx 0.8$) and the presence of

Fig. 19 Separation time depending on mean momentum input, Reynolds number, and diffuser angle: $t_{\text{off}} \approx 0.2L_c/U_\infty$ (circles), $t_{\text{off}} \approx 0.4L_c/U_\infty$ (squares), $t_{\text{off}} \approx 0.7L_c/U_\infty$ (diamonds), $t_{\text{off}} \approx 1.5L_c/U_\infty$ (left-pointing arrows), $t_{\text{off}} \approx 3.0L_c/U_\infty$ (right-pointing arrows), and steady-blowing (stars).
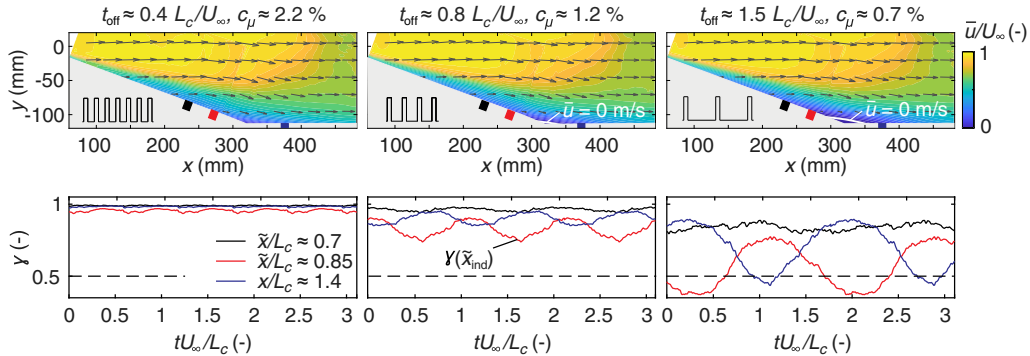

Fig. 20 Mean velocity fields (top) and forward-flow fraction signals at three sensor locations (bottom) for pulsed blowing with different time delays.

a very small mean separation bubble further downstream. Only the largest displayed pulse delay of $t_{off} \approx 1.5 L_c/U_\infty$ exceeds the critical value for t_{off}, which leads to the periodic passage of the transitory detachment line (red curve in Fig. 20). However, a propagation further upstream is inhibited by the arrival of the following pulsed jet (black curve). It is also interesting to note that the two signals measured near the diffuser foot are phase shifted, suggesting that pulsed jets push the separation bubble downstream before it travels back upstream following the jet passage. Overall, the criterion for the t_{off} adjustment [Eq. (3)] is fully confirmed by these observations. Reverse flow from a phase-averaged perspective is indeed only found for the case where $t_{off} > t_{off,crit}$.

We now offer an overview regarding the reliability of this criterion by taking into account many more parameter combinations. The contour map in Fig. 21 shows the minimum forward-flow fractions measured during the actuation period near the diffuser foot (red curves in Fig. 20). This quantity is shown as a function of the momentum coefficient and the time delay between pulses for various parameter combinations and may be interpreted as a probability of reverse-flow occurrence. A value of $\gamma_{min} = 1$, for instance, indicates that forcing leads to forward-directed flow throughout the actuation period, whereas there is an occurrence of reverse flow from a phase-averaged perspective when $\gamma_{min} < 0.5$. The choice of γ_{min}, instead of a mean value, allows for the detection of temporary reverse flow that may be overlooked otherwise.

Perhaps unsurprisingly, the least frequent occurrence of reverse flow is observed for large c_μ and small t_{off}, i.e., when the jets are associated with high momentum and the duration between subsequent pulses is short enough to prevent the recurrence of reverse flow. Values of $\gamma_{min} > 0.5$ can also be noted when the momentum input is smaller than $c_{\mu,thres} = 1.5\%$, which was found to be required to ensure a maximum separation time. However, this is only true when the time delay between pulses is reduced below $t_{off,crit}$ accordingly. In other words, reducing c_μ comes at the expense of a shorter pulse delay. When a larger c_μ can be facilitated, on the other hand, t_{off} may be increased up to the critical value fulfilling the criterion in Eq. (3) that is marked by the dashed vertical line in Fig. 21. Once the pulse delay is larger than this value, however, even an excessive mean momentum input cannot prevent reverse flow that invariably occurs after the characteristic separation time of $t_s^* \approx 2.2 L_c/U_\infty$.

We conclude that flow separation can be prevented effectively by applying knowledge regarding the recurrence of reverse flow subsequent to the termination of forcing. This allows us to establish some guidelines for the adjustment of two parameters defining the actuation signal. Specifically, the time delay between pulses must not exceed $t_{off,crit} = 1.2 L_c/U_\infty$ in the present setup. And second, the mean momentum input must be larger than $c_{\mu,thres} = 1.5\%$.

V. Adjusting the Pulse Duration t_p

Although the guidelines proposed in the previous section enable an informed choice of forcing parameters, no explicit consideration is given to the adjustment of the pulse duration so far. It is also unclear whether the criteria regarding t_{off} and c_μ (established based on wall shear stress measurements) are suited to adequately control the normal force, i.e., the quantity that is typically associated with control authority. We will therefore, once more, consider pressure measurements that enable an estimation of the effectivity by assessing the figure of merit introduced by Otto et al. [46] for different forcing signals. In doing so, emphasis is put on the influence of a varied pulse duration t_p.

Static pressure distributions for selected forcing signals are shown in Fig. 22. A reference distribution is provided by an inviscid simulation solving Poisson's equation for the diffuser flow, with boundary conditions matching those of the experiment. Comparison with the unforced flow (baseline) shows almost identical pressure coefficients for $x < 120$ mm. Further downstream, a different flow geometry is at hand in the experiment due to the presence of a separation bubble, and smaller pressure coefficients are measured as compared to the inviscid solution. The figure also contains distributions of three ASC cases: each for momentum coefficients of $c_\mu \approx (0.5, 3.5)\%$. Those are a steady-blowing configuration, a case where the time delay was chosen according to the characteristic separation time (i.e., $t_{off} = 11$ ms $\approx 0.7 t_{off,crit}$), and a forcing signal with a 50% duty cycle ($t_p = t_{off} = 6$ ms). Because the latter case also corresponds to a reduced forcing frequency of $F^+ \approx 1$, it can be considered a typical parameter combination chosen in ASC applications that has also been employed in the same experimental setup previously [19].

Already at $c_\mu \approx 0.5\%$, all three forcing cases impose a distinct effect because increased pressure coefficients are measured on the downstream part of the diffuser ramp as compared to the baseline. However, neither of them reaches the inviscid solution, which can be explained by the insufficient momentum input $c_\mu < c_{\mu,thres}$ and the resulting occurrence of flow separation. It is also worth mentioning that the difference between the two pulsed-blowing cases is negligible, whereas slightly smaller pressure coefficients are observed for the steady forcing case near the diffuser foot. This may be explained by a reduced jet velocity (given that c_μ is constant). When the forcing intensity is increased to $c_\mu \approx 3.5\%$, the deviation between resulting pressure distributions and the numerical simulation becomes smaller. In fact, the inviscid limit is exceeded by the $t_p = 3$ ms case directly downstream of the outlet as well as at the location closest to the diffuser foot.
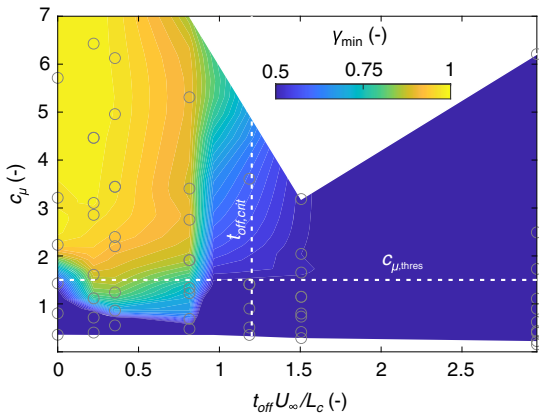

Fig. 21 Minimum forward-flow fraction near the diffuser foot during actuation period as a function of the momentum coefficient and the time delay between pulses; studied parameter combinations highlighted by circles.
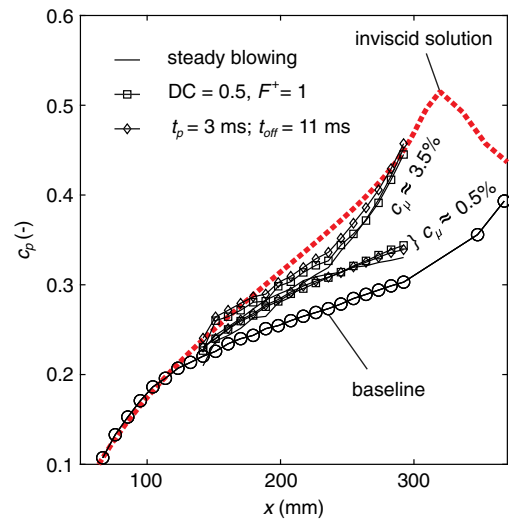

Fig. 22 Pressure distributions on the diffuser ramp for selected forcing signals along with distributions for unforced flow (baseline) and inviscid solution.

Based on pressure distributions, such as those shown in Fig. 22, normal force coefficients c_n can be computed by integration along $\tilde{x}$. Note that only pressure taps in the range of $\tilde{x} = 86, \ldots, 246$ mm are considered. The main effect becomes apparent by subtracting the normal force coefficient associated with the baseline, i.e., by inspecting Δc_n. As was recently suggested in Ref. [46], we relate this quantity to the difference between the inviscid solution and the baseline $\Delta c_{n,\mathrm{inv}}$, yielding a figure of merit:

$$\mathrm{FM} = \Delta c_n / \Delta c_{n,\mathrm{inv}} \tag{4}$$

that can be viewed as a measure for the control authority. Values of $\mathrm{FM} = (0, 1)$ mean that the forced flow is identical to the baseline or the inviscid solution, whereas $\mathrm{FM} > 1$ simply indicates normal force coefficients exceeding that of the numerical simulation.

The figures of merit for the same forcing timescales discussed earlier in this paper are shown for various momentum coefficients in Fig. 23. Interestingly, $\mathrm{FM} < 0$ is found for two cases associated with the smallest momentum input, confirming that pulsed blowing may indeed have an adverse effect [15]. Apart from that, two regimes characterized by different slopes can be clearly seen in the diagram. For relatively small momentum coefficients (say, $c_\mu < 1\%$), increasing the forcing intensity has a significant effect as the figure of merit is increased from zero to $\mathrm{FM} \approx 0.8$. For even larger c_μ, the rate of increase is significantly reduced. In other words, the benefit that comes with a momentum input increased beyond this value is limited. These observations are consistent with the usual classification into separation (or boundary layer) control and circulation control [23,48]. Even though, the concept of circulation does not directly apply to our half-diffuser flow. An alternative explanation may therefore lie in a reduced benefit associated with a complete suppression of flow reversal at all times ($\gamma_{\min} \to 1$; see Fig. 21).

It is worth mentioning that the momentum coefficient separating these regimes is close to, but slightly smaller than, the threshold value of $c_{\mu,\mathrm{thres}} \approx 1.5\%$ determined in the previous section. It was shown that forcing intensities on this order ensure that reverse flow only occurs after a duration equal to the characteristic separation time once the momentum addition is terminated. However, the time delay considered here is shorter than the critical value proposed earlier in this paper ($t_{\mathrm{off}} \approx 0.7 t_{\mathrm{off,crit}}$), compensating for momentum coefficients that do not reach the threshold value. We therefore conclude that the ASC effectivity indicated by pressure measurements is consistent with findings regarding the occurrence of reverse flow based on wall shear-stress measurements (Fig. 21).

Whereas differences are negligible for relatively small momentum coefficients, deviating figures of merit are mostly found for $c_\mu > 1\%$. This may be explained by the larger jet velocity for $t_p = 3$ ms delaying the dissipation of wall jets. Here, the figure of merit even exceeds $\mathrm{FM} = 1$, which indicates that the measured normal force coefficient is larger than that of the inviscid solution. Although $F^+ = 1$ and $\mathrm{DC} = 0.5$ can be considered best-practice parameters, they do not yield the same effect in the current study. As for the
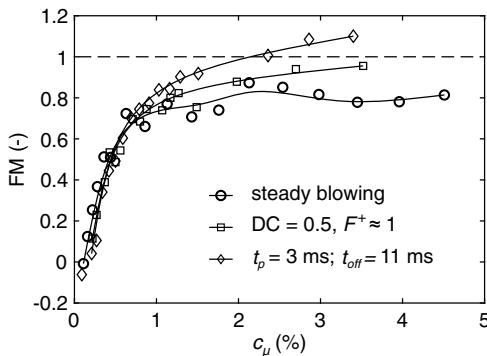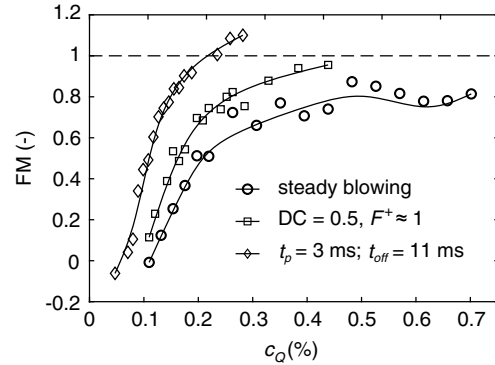

Fig. 24   Figures of merit depending on the mass-flow coefficient for selected forcing signals.

steady-blowing case, the smallest gain in normal force coefficients can be attested, which we attribute to the smaller jet velocities in the absence of an LV that is only generated with pulsed jets.

We now consider the efficiency of forcing signals by defining a 2-D mass-flow coefficient

$$c_Q = \frac{\dot{m}_{\mathrm{jet}}}{\varrho U_\infty L_c} \tag{5}$$

where, again, $\dot{m}_{\mathrm{jet}}$ refers to the mass-flow rate per unit width.

In Fig. 24, the figures of merit discussed earlier in this paper are now plotted over c_Q. It is immediately apparent that forcing signals yielding certain values of the FM are achieved with strongly different mass-flow coefficients. For instance, $\mathrm{FM} = 0.8$ is reached at around $c_Q \approx 0.13\%$ for $t_p = 3$ ms and $c_Q \approx 0.26\%$ for $\mathrm{DC} = 0.5$. In other words, the mass-flow consumption is approximately twice as large for the latter configuration or, the other way round, a much larger normal force is generated at a given mass-flow rate using a time delay according to the criterion proposed in the previous section. Both statements suggest a significant efficiency enhancement is feasible through an optimization of the duty cycle.

We now focus on the influence of this parameter (the duty cycle) in more detail by assessing forcing signals with constant $t_{\mathrm{off}} = 11$ ms and different pulse durations of $t_p = (1, 3, 5, 7, 11)$ ms, resulting in duty cycles in the range of $\mathrm{DC} \approx 0.1, \ldots, 0.5$ and reduced frequencies of $F^+ \approx 0.6, \ldots, 1$.

By first focusing on the influence of the momentum input (Fig. 25, left), the existence of two regimes characterized by different dependencies on c_μ can be confirmed, again separated by $c_\mu \approx 1\%$. For smaller momentum coefficients, the deviation between cases of different pulse durations is negligible. One notable exception is found for $t_p = 1$ ms. Here, negative figures of merit are measured for $c_\mu < 0.5\%$, where the equivalent stroke ratio is $t_p u_{\mathrm{jet}}/d_{\mathrm{eq}} < 20$, indicating that only a weak wall jet is generated [20]. It was shown in Sec. III that this flow structure governs the effectivity in pulsed-blowing ASC by maintaining the LV and energizing the near-wall flow, explaining the lack of control authority in its absence. It is worth noting that negative figures of merit are also obtained for the larger pulse durations when they correspond to equivalent stroke ratios of $t_p u_{\mathrm{jet}}/d_{\mathrm{eq}} < 20$ (detailed diagram on the left side in Fig. 25). In contrast, a beneficial effect of pulsed-jet actuation is noted for larger amounts of ejected fluid per pulse. Here, the shortest pulse duration ($t_p = 1$ ms) leads to the highest figures of merit, which is in line with the effect of the jet velocity discussed in relation to Fig. 24. Along these lines, the smallest gains are found for the largest pulse duration of $t_p = 11$ ms, yielding a duty cycle of $\mathrm{DC} = 0.5$. Despite the observed slight deviations, the curves for all pulse durations collapse reasonably well, which underlines the importance of the momentum coefficient in estimating the control authority. The reduced frequency, which is also varied by the adjustment of t_p, plays a minor role in comparison.

In the right-side image of Fig. 25, the measured figures of merit are shown as functions of the mass-flow coefficient. A clear trend can be
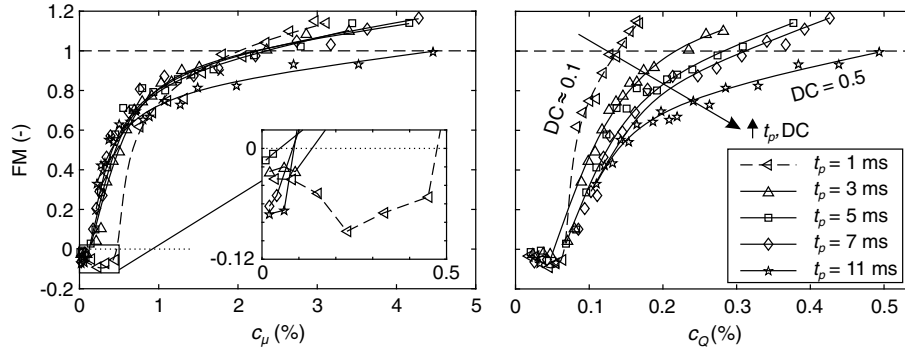

Fig. 23   Figures of merit depending on the momentum coefficient for selected forcing signals.

Fig. 25 **Figures of merit depending on the momentum coefficient (left) and mass-flow coefficient (right) for forcing signals with fixed $t_{\text{off}} = 11$ ms and different t_p and DC.**

observed inasmuch as increasing the duty cycle (larger t_p) leads to a reduced efficiency because larger amounts of mass flow are required to achieve the same control authority. Thus, FM = 1 is reached at $c_Q = 0.14\%$ for the smallest duty cycle and $c_Q = 0.50\%$ for the largest duty cycle, representing a deviation in mass-flow consumption by more than a factor of three. It is also interesting to note that the distribution for DC = 0.5 is similar to the one presented in Fig. 24 (DC = 0.5, $F^+ = 1$), although the forcing timescales are now increased to $t_p = t_{\text{off}} = 11$ ms ($F^+ \approx 0.6$). This suggests that the efficiency cannot be enhanced significantly through explicit changes of the actuation frequency in the current setup. Instead, major effects are only seen for an adjustment of the duty cycle.

An explanation for the efficiency gain presented above is offered in Fig. 26, where the mass-flow coefficient c_Q and the velocity ratio of $r = u_{\text{jet}}/U_\infty$ are shown as functions of the duty cycle for a constant c_μ. Both quantities are normalized with values found for DC = 1 (steady blowing). For decreasing duty cycles, the mass flow required to ensure a certain momentum input is reduced according to a square-root function because the momentum coefficient scales with the ratio of the squared mean jet velocity and the duty cycle: $c_\mu \sim \overline{u_{\text{jet}}}^2/\text{DC}$. At the same time, the jet velocity of $u_{\text{jet}} = \overline{u_{\text{jet}}}/\text{DC}$, and hence the velocity ratio, increases significantly.

In summary, the results presented in this section confirm the applicability of the criterion defining a critical time delay $t_{\text{off,crit}}$ [Eq. (3)]. Large gains in normal force were achieved by choosing $t_{\text{off}} \approx 0.7 t_{\text{off,crit}}$ and setting the momentum coefficient according to the threshold value proposed in the previous section of $c_{\mu,\text{thres}} = 1.5\%$. Increasing the forcing intensity beyond this value only had a small impact in comparison, indicating that flow separation was already suppressed. Furthermore, the importance of the wall jet could be confirmed because a negligible control authority was observed for cases where the amount of ejected fluid was not sufficient to generate this flow structure. Within the regime of effective separation control, however, the control authority predominantly depends on c_μ. This means that significant efficiency gains are possible by reducing

the pulse duration because a decreased mass flow is required to ensure a given momentum coefficient for smaller t_p.

VI. Conclusions and Outlook

In this paper, the unsteady dynamics associated with periodically ejected pulsed jets that are used to control boundary-layer separation were addressed. The overriding objective was to determine whether the timescales defining the forcing signal can be optimized to increase the efficiency of an ASC system, i.e., reduce the mass-flow consumption while retaining a certain control authority. To this end, experiments were conducted in a one-sided diffuser where the boundary layer separated from the surface due to an APG in the absence of forcing. This was countered by adding momentum to the near-wall flow through an array of five PJAs with slotlike outlets on the upper part of the diffuser ramp. In addition to the jet velocity, the focus point was the influence of the pulse duration t_p and the time delay between pulses t_{off}, essentially defining the duty cycle as DC = $t_p/(t_p + t_{\text{off}})$.

First, the flow structures generated when inclined pulsed jets are emitted into a crossflowing boundary layer were addressed. The results presented in a recent paper could be confirmed inasmuch as the flow control authority of pulsed wall jets is mainly governed by a leading vortex ring, a wall-attached jet, and (to a lesser extent) a stopping vortex [20]. It was shown that the major effect of the LV lies in the displacement of low-momentum fluid during its interaction with the boundary layer. It is trailed by the wall jet characterized by a near-wall peak in streamwise velocity, thus inducing substantial wall shear stress. A large relative importance is attributed to this flow structure because it maintains the LV in addition to directly increasing the near-wall momentum flux. Indeed, a negligible control authority was noted when no wall-attached jet was generated due to insufficient amounts of ejected fluid.

Then, the time delay between pulses t_{off} was addressed in a set of terminated-forcing experiments in which actuation with different time delays was stopped abruptly. The main finding of these experiments was that the evolution from the forced state into the natural, separated configuration is of a duration many times the convective timescale, which was approximated by $t_c \approx L_c/U_\infty$. Once fluid emission is stopped, this process is characterized by a drop in normal and shear force acting on the diffuser surface before ever smaller rates of change are noted. Interestingly, the timescale associated with the onset of reverse flow is independent of initial forcing conditions (specifically, the mean momentum input), and may thus be declared a flow-inherent property. Wall shear-stress measurements of a large number of parameter combinations suggest a characteristic separation timescale of $t_s^* \approx 2.2 t_c$ in the present setup, which was defined as the time instant when the transitory detachment location indicated by a forward-flow fraction of $\gamma = 0.5$ reaches a specific location near the diffuser foot. However, this timescale is only reached when the momentum coefficient is larger than a threshold value: here, $c_{\mu,\text{thres}} \approx 1.5\%$. For smaller forcing intensities, there is a quicker recurrence of flow separation that is attributed to the incomplete suppression of reverse flow.
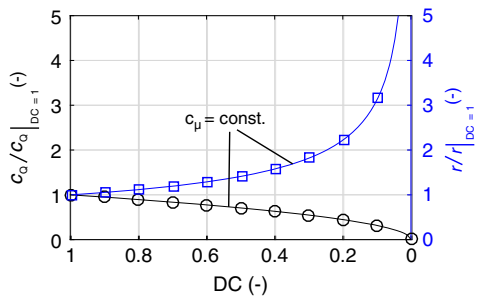

Fig. 26 **Normalized mass-flow coefficient and velocity ratio for constant (const.) momentum coefficient as functions of the duty cycle.**

These findings allow us to establish a criterion to define the forcing signal in ASC applications, enabling an optimization of the time delay between successive pulses with the help of a critical value $t_{\text{off,crit}} = t_s^* - t_c$.

For $t_{\text{off}} > t_{\text{off,crit}}$, phase-mean reverse flow invariably occurs at some point during the actuation period and cannot be prevented, e.g., by increasing the momentum input. When the pulse delay is set to $t_{\text{off}} < t_{\text{off,crit}}$, on the other hand, the forward-flow fraction does not drop below a value of $\gamma = 0.5$ because the upstream propagation of the separation line is prevented by the following pulsed jet arriving after t_c. However, this can only be ensured when $c_\mu > c_{\mu,\text{thres}}$, so as to yield a complete suppression of reverse flow. Otherwise, the separation time does not reach its limiting value t_s^*, which may be offset by applying a shorter pulse delay.

It was then examined whether the guidelines based on the local wall shear stress are suited to control the normal force. And, indeed, large gains were observed for a time delay of $t_{\text{off}} \approx 0.7 t_{\text{off,crit}}$. The momentum coefficient c_μ could be confirmed as the major parameter governing the control authority, whereas the influence of the forcing frequency was negligible. Importantly, for a given c_μ, shorter pulse durations are associated with a reduced mass-flow consumption. Thus, a forcing signal with a duty cycle as low as DC ≈ 0.1 was shown to equal the normal force provided by an inviscid solution while being associated with only one-third of the mass-flow consumption required for the often employed DC $= 0.5$ configuration. This shows that substantial efficiency enhancements are feasible by applying knowledge regarding a characteristic separation time and a threshold momentum coefficient. However, it is worth mentioning that reducing the duty cycle is associated with larger jet velocities to ensure a certain momentum input, which usually requires an increased supply pressure. This type of energy consumption was not considered in the current study.

Clarifying the relevance of the criterion proposed in this paper to other ASC applications, some remarks are in order. Its main advantage lies in the relative independence of the characteristic separation time as a flow-inherent property. However, there is no reason to believe that the specific value of $t_s^* = 2.2 L_c / U_\infty$ determined in the current study is universally applicable to different flow configurations, although previous ASC studies suggest a similar behavior in the recurrence of flow separation on low-pressure turbine blades and a laminar airfoil [31,33]. Therefore, the specific value of t_s^* needs to be determined with a time-resolved single-point measurement to adapt the criterion stated in Eq. (3). Here, the sensor location $\tilde{x}_{\text{ind}}$ plays a crucial role because it needs to be placed inside the region where flow separation initially occurs: for instance, near the trailing edge of a deflected flap. It is also worth mentioning that the definition of the separation time may be open to debate. In the current study, the objective was to indicate the initial occurrence of phase-averaged flow reversal, accompanied by a forward-flow fraction of $\gamma = 0.5$. However, a more restrictive formulation (i.e., a larger forward-flow fraction) may be chosen to prevent undesired effects of occasional flow separation, such as unsteady loads. Furthermore, it was assumed that the convective timescale $t_c = L_c / U_\infty$ after which pulsed jets reach the downstream end of the control domain is not significantly affected by forcing parameters. Although this proved to be an acceptable approximate in the present study, it is easy to envisage a refinement in the future.

Acknowledgments

References

[1] Cattafesta, L. N., and Sheplak, M., "Actuators for Active Flow Control," *Annual Review of Fluid Mechanics*, Vol. 43, No. 1, 2011, pp. 247–272.
https://doi.org/10.1146/annurev-fluid-122109-160634

[2] Font, G. I., "Boundary-Layer Control with Atmospheric Plasma Discharges," *AIAA Journal*, Vol. 44, No. 7, 2006, pp. 1572–1578.
https://doi.org/10.2514/1.18542

[3] Abe, P., Takizawa, Y., Sato, S., and Kimura, N., "Experimental Study for Momentum Transfer in a Dielectric Barrier Discharge Plasma Actuator," *AIAA Journal*, Vol. 46, No. 9, 2008, pp. 2248–2256.
https://doi.org/10.2514/1.30985

[4] Corke, T. C., Enloe, C. L., and Wilkinson, S. P., "Dielectric Barrier Discharge Plasma Actuators for Flow Control," *Annual Review of Fluid Mechanics*, Vol. 42, Jan. 2010, pp. 505–529.
https://doi.org/10.1146/annurev-fluid-121108-145550

[5] Smith, B. L., and Glezer, A., "The Formation and Evolution of Synthetic Jets," *Physics of Fluids*, Vol. 10, No. 9, 1998, pp. 2281–2297.
https://doi.org/10.1063/1.869828

[6] Glezer, A., and Amitay, M., "Synthetic Jets," *Annual Review of Fluid Mechanics*, Vol. 34, No. 1, 2002, pp. 503–529.
https://doi.org/10.1146/annurev.fluid.34.090501.094913

[7] Raghu, S., "Fluidic Oscillators for Flow Control," *Experiments in Fluids*, Vol. 54, No. 2, 2013, pp. 1–11.
https://doi.org/10.1007/s00348-012-1455-5

[8] Gregory, J. W., and Tomac, M. N., "A Review of Fluidic Oscillator Development and Application for Flow Control," *43rd Fluid Dynamics Conference*, AIAA Paper 2013-2474, 2013.
https://doi.org/10.2514/6.2013-2474

[9] Ostermann, F., Woszidlo, R., Nayeri, C. N., and Paschereit, C. O., "The Interaction Between a Spatially Oscillating Jet Emitted by a Fluidic Oscillator and a Cross-Flow," *Journal of Fluid Mechanics*, Vol. 863, March 2019, pp. 215–241.
https://doi.org/10.1017/jfm.2018.981

[10] Petz, R., and Nitsche, W., "Active Separation Control on the Flap of a Two-Dimensional Generic High-Lift Configuration," *Journal of Aircraft*, Vol. 44, No. 3, 2007, pp. 865–874.
https://doi.org/10.2514/1.25425

[11] Warsop, C., Hucker, M., Press, A. J., and Dawson, P., "Pulsed Air-Jet Actuators for Flow Separation Control," *Flow, Turbulence and Combustion*, Vol. 78, No. 3, 2007, pp. 255–281.
https://doi.org/10.1007/s10494-006-9060-4

[12] Arwatz, G., Fono, I., and Seifert, A., "Suction and Oscillatory Blowing Actuator Modeling and Validation," *AIAA Journal*, Vol. 46, No. 5, 2008, pp. 1107–1118.
https://doi.org/10.2514/1.30468

[13] Barros, D., Borée, J., Noack, B. R., Spohn, A., and Ruiz, T., "Bluff Body Drag Manipulation Using Pulsed Jets and Coanda Effect," *Journal of Fluid Mechanics*, Vol. 805, Oct. 2016, pp. 422–459.
https://doi.org/10.1017/jfm.2016.508

[14] Steinfurth, B., and Weiss, J., "Vortex Rings Produced by Non-Parallel Planar Starting Jets," *Journal of Fluid Mechanics*, Vol. 903, Nov. 2020, Paper A16.
https://doi.org/10.1017/jfm.2020.637

[15] Seifert, A., Darabi, A., and Wygnanski, I., "Delay of Airfoil Stall by Periodic Excitation," *Journal of Aircraft*, Vol. 33, No. 4, 1996, pp. 691–698.
https://doi.org/10.2514/3.47003

[16] Greenblatt, D., and Wygnanski, I. J., "The Control of Flow Separation by Periodic Excitation," *Progress in Aerospace Sciences*, Vol. 36, No. 7, 2000, pp. 487–545.
https://doi.org/10.1016/S0376-0421(00)00008-7

[17] Hansen, L., and Bons, J., "Flow Measurements of Vortex Generator Jets in Separating Boundary Layer," *Journal of Propulsion and Power*, Vol. 22, No. 3, 2006, pp. 558–566.
https://doi.org/10.2514/1.13820

[18] Ortmanns, J., Bitter, M., and Kähler, C. J., "Dynamic Vortex Structures for Flow-Control Applications," *Experiments in Fluids*, Vol. 44, No. 3, 2008, pp. 397–408.
https://doi.org/10.1007/s00348-007-0442-8

[19] Hecklau, M., Salazar, D. P., and Nitsche, W., "Influence of the Actuator Jet Angle on the Reattachment Process with Pulsed Excitation," *New Results in Numerical and Experimental Fluid Mechanics VIII*, Vol. 121, edited by A. Dillmann, G. Heller, H. P. Kreplin, W. Nitsche, and I. Peltzer, Springer, New York, 2013, pp. 143–150.
https://doi.org/10.1007/978-3-642-35680-3_18

[20] Steinfurth, B., and Weiss, J., "Boundary-Layer Control by Means of Pulsed Jets at Different Inclination Angles," *AIAA Journal*, Vol. 59,

No. 8, 2021, pp. 3946–3959.
https://doi.org/10.2514/1.J060474

[21] Wygnanski, I., "The Variables Affecting the Control of Separation by Periodic Excitation," *2nd AIAA Flow Control Conference*, AIAA Paper 2004-2505, 2004.
https://doi.org/10.2514/6.2004-2505

[22] Nishri, B., and Wygnanski, I., "Effects of Periodic Excitation on Turbulent Flow Separation from a Flap," *AIAA Journal*, Vol. 36, No. 4, 1998, pp. 547–556.
https://doi.org/10.2514/2.428

[23] Poisson-Quinton, P., and Lepage, L., "Survey of French Research on the Control of Boundary Layer and Circulation," *Boundary Layer and Flow Control*, Vol. 1, edited by G. V. Lachmann, Pergamon Press, Oxford, England, U.K., 1961, pp. 21–73.

[24] Wygnanski, I., and Newman, B. G., "The Effect of Jet Entrainment on Lift and Moment for a Thin Aerofoil with Blowing," *Aeronautical Quarterly*, Vol. 15, No. 2, 1964, pp. 122–150.
https://doi.org/10.1017/S0001925900003085

[25] Zaman, K. B. M. Q., "Effect of Acoustic Excitation on Stalled Flows over an Airfoil," *AIAA Journal*, Vol. 30, No. 6, 1992, pp. 1492–1499.
https://doi.org/10.2514/6.1990-4009

[26] Oster, D., Wygnanski, I., Dziomba, B., and Fiedler, H., "The Effect of Initial Conditions on the Two-Dimensional Turbulent Mixing Layer," *Structure and Mechanics of Turbulence*, edited by H. Fiedler, Springer, New York, 1978, pp. 48–64.

[27] Wygnanski, I., and Peterson, R. A., "Coherent Motion in Excited Free Shear Flows," *AIAA Journal*, Vol. 25, No. 2, 1987, pp. 201–213.
https://doi.org/10.2514/3.9610

[28] Chang, R. C., "Forcing Level Effects of Internal Acoustic Excitation on the Improvement of Airfoil Performance," *Journal of Aircraft*, Vol. 29, No. 5, 1992, pp. 823–829.
https://doi.org/10.2514/3.46252

[29] Amitay, M., and Glezer, A., "Role of Actuation Frequency in Controlled Flow Reattachment over a Stalled Airfoil," *AIAA Journal*, Vol. 40, No. 2, 2002, pp. 209–216.
https://doi.org/10.2514/2.1662

[30] Löffler, S., Ebert, C., and Weiss, J., "Fluidic-Oscillator-Based Pulsed Jet Actuators for Flow Separation Control," *Fluids*, Vol. 6, No. 4, 2021, Paper 166.
https://doi.org/10.3390/fluids6040166

[31] Bons, J. P., Sondergaard, R., and Rivir, R. B., "The Fluid Dynamics of LPT Blade Separation Control Using Pulsed Jets," *Journal of Turbomachinery*, Vol. 124, No. 1, 2002, pp. 77–85.
https://doi.org/10.1115/1.1425392

[32] Haucke, F., and Nitsche, W., "Active Separation Control on a 2D High-Lift Wing Section Towards High Reynolds Number Application," AIAA Paper 2013-2514, 2013.

[33] Hipp, K. D., Walker, M. M., Benton, S. I., and Bons, J. P., "Control of Poststall Airfoil Using Leading-Edge Pulsed Jets," *AIAA Journal*, Vol. 55, No. 2, 2017, pp. 365–376.
https://doi.org/10.2514/6.2016-1822

[34] Steinfurth, B., and Weiss, J., "Velocity Ratio Effect on Flow Structures of Non-Parallel Planar Starting Jets in Cross-Flow," *Journal of Fluid Mechanics*, Vol. 915, May 2021, Paper A11.
https://doi.org/jfm.2021.40

[35] Gharib, M., Rambod, E., and Shariff, K., "A Universal Time Scale for Vortex Ring Formation," *Journal of Fluid Mechanics*, Vol. 360, April 1998, pp. 121–140.
https://doi.org/10.1017/S0022112097008410

[36] Steinfurth, B., and Weiss, J., "Development of Inclined Pulsed Jets in an Adverse-Pressure-Gradient Crossflow," *AIAA Aviation 2021 Forum*, Vol. 59, AIAA Paper 2021-2837, 2021.
https://doi.org/10.2514/6.2021-2837

[37] Simpson, R. L., "Turbulent Boundary-Layer Separation," *Annual Review of Fluid Mechanics*, Vol. 21, No. 1, 1989, pp. 205–232.
https://doi.org/10.1146/annurev.fl.21.010189.001225

[38] Steinfurth, B., and Weiss, J., "Efficient Vortex Ring Generation with Non-Parallel Planar Starting Jets in Crossflow," *AIAA SciTech 2020*, AIAA Paper 2020-0814, 2020.
https://doi.org/10.2514/6.2020-0814

[39] Weiss, J., Schwaab, Q., Boucetta, Y., Giani, A., Guigue, C., Combette, P., and Charlot, B., "Simulation and Testing of a MEMS Calorimetric Shear-Stress Sensor," *Sensor Actuators A: Physics*, Vol. 253, Jan. 2017, pp. 210–217.
https://doi.org/10.1016/j.sna.2016.11.018

[40] Weiss, J., Jondeau, E., Giani, A., Charlot, B., and Combette, P., "Static and Dynamic Calibration of a MEMS Calorimetric Shear-Stress Sensor," *Sensor Actuators A: Physics*, Vol. 265, Oct. 2017, pp. 211–216.
https://doi.org/10.1016/j.sna.2017.08.048

[41] Sears, W. R., and Telionis, D. P., "Boundary-Layer Separation in Unsteady Flow," *SIAM Journal on Applied Mathematics*, Vol. 28, No. 1, 1975, pp. 215–235.
https://doi.org/10.1137/0128018

[42] Steinfurth, B., and Weiss, J., "Flow Visualization of Pulsed Wall Jets Used for Active Separation Control," *AIAA Aviation 2021 Forum*, AIAA Paper 2021-2218, 2021, https://tinyurl.com/5n93m54k.
https://doi.org/10.13140/RG.2.2.19160.62722

[43] Mohammed-Taifour, A., and Weiss, J., "Periodic Forcing of a Large Turbulent Separation Bubble," *Journal of Fluid Mechanics*, Vol. 915, May 2021, p. A24.
https://doi.org/10.1017/jfm.2021.77

[44] Launder, B. E., and Rodi, W., "The Turbulent Wall Jet—Measurements and Modeling," *Annual Review of Fluid Mechanics*, Vol. 15, No. 1, 1983, pp. 429–459.
https://doi.org/10.1146/annurev.fl.15.010183.002241

[45] Lin, J. C., "Review of Research on Low-Profile Vortex Generators to Control Boundary-Layer Separation," *Progress in Aerospace Sciences*, Vol. 38, Nos. 4–5, 2002, pp. 389–420.
https://doi.org/10.1016/S0376-0421(02)00010-6

[46] Otto, C., Tewes, P., Little, J. C., and Woszidlo, R., "Comparison Between Fluidic Oscillators and Steady Jets for Separation Control," *AIAA Journal*, Vol. 57, No. 12, 2019, pp. 5220–5228.
https://doi.org/10.2514/1.J058081

[47] Darabi, A., and Wygnanski, I., "Active Management of Naturally Separated Flow over a Solid Surface. Part 2. The Separation Process," *Journal of Fluid Mechanics*, Vol. 510, July 2004, pp. 131–144.
https://doi.org/10.1017/S0022112004009243

[48] Radespiel, R., Burnazzi, M., Casper, M., and Scholz, P., "Active Flow Control for High Lift with Steady Blowing," *Aeronautical Journal*, Vol. 120, No. 1223, 2016, pp. 171–200.
https://doi.org/doi:10.1017/aer.2015.7

Y. Zhou
Associate Editor

101

Modelling the decay of finite-span starting and stopping wall jets in cross-flow

Ben Steinfurth[1]†**, Julien Weiss**[1]

[1]Institute of Aeronautics and Astronautics, Technische Universität Berlin, Marchstr. 12-14, 10587 Berlin, Germany

The flow under consideration is a wall jet emitted into a zero-pressure-gradient turbulent boundary-layer from a slot-like outlet of width $b = 0.5\,\mathrm{mm}$ and span $L = 20\,\mathrm{mm}$. Despite the finite jet span, the velocity decay and wall-normal spreading rate in the symmetry plane can be described with power laws almost identical to those for the two-dimensional flow determined by Zhou & Wygnanski (1993). This is explained by the lack of significant lateral spreading found in the present configuration due to a self-amplifying inward-directed fluid motion, fundamentally differing from conditions found in the absence of a cross-flow. Regions with 'approximately self-similar' properties also exist in the case of unsteady velocity programs where the fluid is ejected in a pulsatile fashion. Here, the wall jet is enclosed by a leading vortex structure and a deceleration wave, for which the time-dependent locations can be predicted by means of empirical constants. This yields models for the major properties inside the advancing and diffusing wall jet that only require knowledge regarding the velocity ratio, the ejected momentum flux and the kinematic viscosity, representing an extension to scaling laws suggested by Narasimha *et al.* (1973).

1. Introduction

Wall jets can be regarded as boundary-layer flows where the free stream velocity U_∞ is exceeded at some near-wall location separating two regions with characteristics closely resembling those in a boundary-layer and a free shear-layer respectively. Initiated by the introduction of momentum flux (eventually) directed along a solid surface, such flows are encountered in a variety of engineering applications, perhaps most prominently in those related to heat transfer. To cite only one example, the thermal load acting on gas turbine blades is typically reduced by external wall jets providing a shielding air film as well as radial wall jets caused by the impingement of air onto the internal blade surface. Extensive review articles addressing various wall jet configurations are provided by Launder & Rodi (1979, 1983).

The major characteristics of turbulent wall jets were arguably first addressed by Förthmann (1934), extending the work of Tollmien (1926) regarding a free shear-layer to the wall-bounded configuration. Later, Glauert (1956) showed that the spreading rate of turbulent wall jets can be described satisfactorily by introducing the concept of an eddy viscosity. However, a complete similarity is not attainable as this eddy viscosity evolves non-synchronously in the inner and outer layer of the wall jet. Nonetheless, 'approximate self-similarity', i.e. similar velocity profiles, when scaled with the maximum velocity U_m at respective streamwise locations and the jet outlet width b, was reported soon afterwards by Bakke (1957) and Sigalla (1958). They also show that U_m decays with a power law

† Email address for correspondence: ben.steinfurth@tu-berlin.de

in the form $U_m \propto x^a$ where $a = -1/2$ for the case of a two-dimensional wall jet. Similar values of the power law exponent have been stated by Bradshaw & Gee (1962) and Myers *et al.* (1963) whereas a significant deviation was found, for instance, by Schwarz & Cosart (1961) where $a = -0.62$, suggesting an inadequecy of the conventional scaling quantities. Against this backdrop, Narasimha *et al.* (1973) evaluated experimental data sets of plane wall jets ejected in still air available at the time and showed that near-outlet parameters, namely the jet velocity U_j and the nozzle geometry, become irrelevant in the region of a 'fully-developed flow', say at $x/b > 30$. Instead, they argue that the ejected momentum flux J and the kinematic viscosity ν shall be used to determine the jet development. Specifically, these gross properties were shown to be suited to describe the decay of U_m and wall shear-stress τ as well as the expansion rate, which was later confirmed by Wygnanski *et al.* (1992) and George *et al.* (2000).

Notably, the scaling approach suggested by Narasimha *et al.* (1973) is not limited to the case of wall jets emitted into still ambience but also applies when there is a steady, uniform crossflow as long as the excess in kinematic momentum flux is sufficiently large. Zhou & Wygnanski (1993), from here on referred to as ZW93, show that this only requires the addition of a velocity ratio parameter $R = (U_j - U_\infty)/(U_j + U_\infty)$. Then, similar power law expressions were determined in their experiment as in those of other wall jets in cross-flow conducted by Seban & Back (1961), Patel (1962) and Kruka & Eskinazi (1964).

Importantly, two-dimensional flow is regarded as a requirement for the 'approximate self-similarity' characteristics introduced above. For the case of short lateral outlet dimensions, on the other hand, a behaviour referred to as anomalous by Narasimha *et al.* (1973) is noted, i.e. power law expressions substantially differing from those of wall jets emitted from slots of sufficiently long span. Indeed, a much larger expansion in spanwise than in wall-normal direction was reported for such finite-span wall jets by Sforza & Herbst (1970), Newman *et al.* (1972) and Abrahamsson *et al.* (1996). As the primary explanation for this enhanced lateral spreading, a secondary mean fluid motion manifested in strong streamwise vorticity, essentially arising from the no-slip condition at the wall, is stated by Launder & Rodi (1983) and Craft & Launder (2001). However, this effect appears to be much more pronounced in the absence of an external stream as the 'directing influence' of a cross-flow is acknowledged by Narasimha *et al.* (1973). In fact, negligible lateral spreading was recently observed for the case of finite-span pulsed jets in a cross-flow addressed by the authors of the present paper (Steinfurth & Weiss 2021*a*).

Knowledge regarding the parameters affecting the decay of wall jets injected into a cross-flow are of great interest in technical applications as it enables, for instance, the prediction of heat transfer coefficients (Pai & Whitelaw 1971) or the estimation of authority in circulation or separation control (Thomas 1963; Gartshore & Newman 1969). However, three-dimensional flow may limit the universal character in such configurations where outlet dimensions of finite span are usually employed. Furthermore, fluid is often not ejected steadily but during confined time intervals, leading to the (periodic) generation of starting and stopping wall jets that are known to be effective in countering boundary layer separation (Greenblatt & Wygnanski 2000). The objective of this study is therefore to determine the influence of these boundary conditions, namely finite outlet span und pulse width, on the applicability of scaling laws introduced by Narasimha *et al.* (1973). To this end, phase-locked particle image velocimetry (PIV) and wall shear-stress measurements are conducted for different jet velocity programs governing the generation of pulsed planar wall jets in an external stream, a flow recently addressed by Steinfurth & Weiss (2021*c,a*). First, steady jets are considered to identify potential three-dimensional
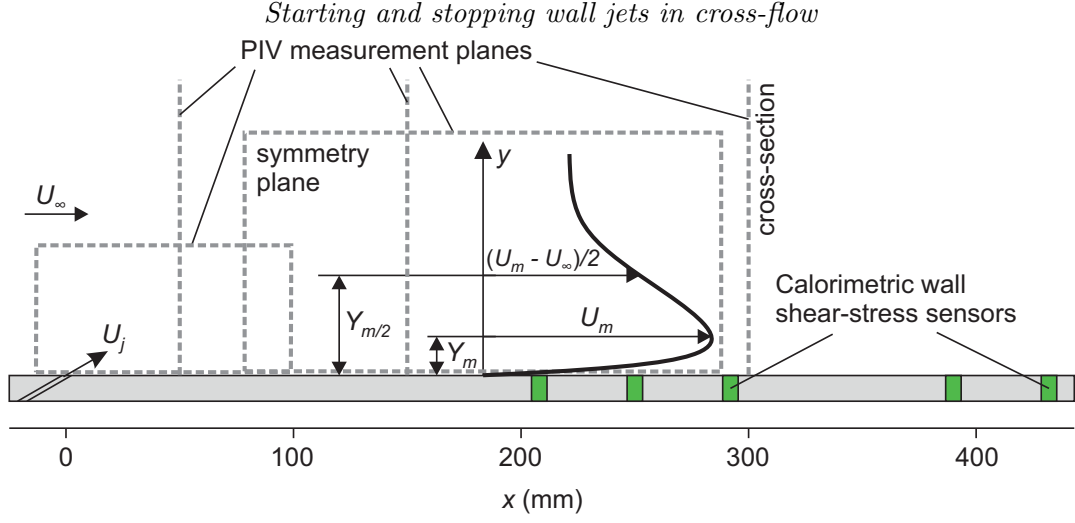
FIGURE 1. Experimental setup and sketch of wall jet velocity profile

flow effects. Then, the starting and stopping processes of fluid emission are addressed individually before a model for the case of finite pulse durations is provided.

2. Methods

The experiments were conducted in a temperature-regulated closed-loop wind tunnel with wall jets injected into a free stream with a velocity of $U_\infty = 20\,\mathrm{m/s}$ and negligible pressure gradient. The turbulent boundary layer had a momentum thickness of $\theta \approx 1.3\,\mathrm{mm}$ at the location of fluid injection $x = 0\,\mathrm{mm}$ (figure 1). A pulsed-jet actuator was employed to generate the wall jets, containing a fast-switching valve caapable of either providing a constant mass flow supply or intercepting the momentum addition for certain velocity programs introduced later on. Downstream of the valve, the flow passes through a nozzle where the circular inlet cross-section is transformed into a slot-like outlet with a width of $b = 0.5\,\mathrm{mm}$ and a spanwise dimension of $L = 20\,\mathrm{mm}$. The flow field of starting wall jets generated with this device was shown to be characterised by a three-dimensional leading vortex half ring (Steinfurth & Weiss 2020, 2021 *c,a*), which is due to the limited lateral outlet extent that is much smaller than in the studies of quasi-two-dimensional wall jets stated in the previous section. ZW93, for example, used a nozzle with $L = 600\,\mathrm{mm}$ while Sforza & Herbst (1970) reported three-dimensional effects even for $L \approx 250\,\mathrm{mm}$ in the absence of a cross-flow.

The jet emission angle, enclosed by the nozzle axis and the wall downstream of the outlet, was $\alpha = 30°$, representing a typical configuration in active separation control. Despite this non-tangential introduction of momentum flux, the jet immediately attaches to the wall due to the so-called Coandă effect addressed, among others, by Wille & Fernholz (1965). It is worth mentioning that Lai & Lu (1996) noted a stronger velocity decay and larger spreading rate for a similar configuration, i.e. when the jet is not injected parallel to the surface.

Figure 1 also contains the sketch of a representative velocity profile (not drawn to scale) with quantities relevant to the purpose of this article. The maximum velocity U_m is reached at a wall-normal distance Y_m while $Y_{m/2}$ indicates the jet half-width. The main objective of this study is to shed some light on the time- and space-dependent development of these quantities along with the wall-shear stress τ inside the jet symmetry plane.
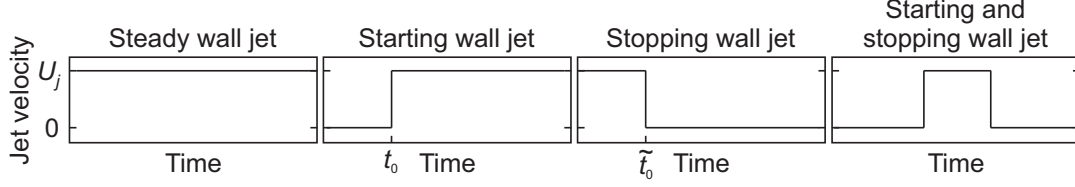
FIGURE 2. Idealised velocity programs for investigated wall jet configurations

The nominal jet velocity inside the exit plane was set to $U_j = (3, 5, 7)U_\infty$ using a mass flow controller, corresponding to velocity ratios $R = (U_j - U_\infty)/(U_j + U_\infty) \approx (0.5, 0.67, 0.75)$. For each jet velocity, different velocity programs were assessed (figure 2). The first case involves a continuous momentum addition with a constant jet velocity (steady wall jets). Then, wall jets generated subsequent to the rapid initiation of fluid ejection are considered, facilitated by opening the fast-switching valve at time $t = 0\,\text{s}$ (starting wall jets). A further configuration involves stopping wall jets where the fluid emission is terminated at $\tilde{t} = 0\,\text{s}$. Finally, finite pulse durations usually employed in active flow control are assessed, i.e. wall jets that are affected both by the starting and the stopping process.

Two experimental techniques were employed. To determine U_m as well as Y_m and $Y_{m/2}$, monoscopic PIV was performed in the jet symmetry plane. Two cameras with different lenses were used to synchronously obtain velocity field information in the regions indicated in figure 1. A larger spatial resolution, i.e. smaller distances between neighbouring velocity vectors ($\Delta x \approx 0.65\,\text{mm}$, $\Delta y \approx 0.16\,\text{mm}$) was provided in the near-outlet region where we expected larger velocity gradients, especially in wall-normal direction. Here, velocities were measured up to a wall distance of $y \approx 0.50\,\text{mm}$. In the second measurement plane, located further downstream, the spatial resolution corresponds to $\Delta x \approx 1.32\,\text{mm}$, $\Delta y \approx 0.33\,\text{mm}$, and measurements were conducted at $y \geqslant 1.17\,\text{mm}$. The setup allowed to resolve the near-wall velocity maximum for all configurations at $x/b > 50$, which is required to determine U_m and Y_m. The results presented in the next section are based on merged instantaneous snapshots recorded at the same time instants. To reveal the dynamical development of wall jets associated with unsteady velocity programs, phase-locked measurements were conducted. Here, the PIV system was triggered at selected time delays following the opening/closing of the fast-switching valve. Furthermore, stereoscopic PIV measurements were performed at cross-sections located at $x = (50, 150, 300)\,\text{mm}$ to investigate the jet spreading in wall-normal and spanwise direction. Here, only steady jets with a velocity of $U_j = 100\,\text{m/s}$ were considered both for $U_\infty = 20\,\text{m/s}$ and $U_\infty = 0\,\text{m/s}$ to determine the influence of the cross-flow.

In addition to velocity fields, the unsteady wall shear-stress $\tau(t)$ was measured with five calorimetric sensors at the locations highlighted in figure 1. The function principle of these sensors is linked to the deformation of the thermal wake of a heated micro-beam due to shear-stress. Specifically, the asymmetry of this wake is detected by two further beams, one on each side of the heater. After calibrating the sensors in a dedicated wind tunnel where a maximum wall-shear stress of $\tau \approx 6.8\,\text{Pa}$ is reached, the sensor output can be related to the magnitude and direction of τ with a maximum uncertainty of $\pm 5\%$. For further information on the function pricinple and calibration procedure of the sensors, the interested reader is referred to the articles by Weiss *et al.* (2017*b*,*a*, 2022).

To conclude this section, it is worth mentioning that the normalised outlet distances up to which measurement data are obtained in the present study ($x/b \approx 570$ for PIV, $x/b \approx 860$ for wall shear-stress measurements) substantially exceed the boundaries of experimental and computational domains investigated in most previous studies. For
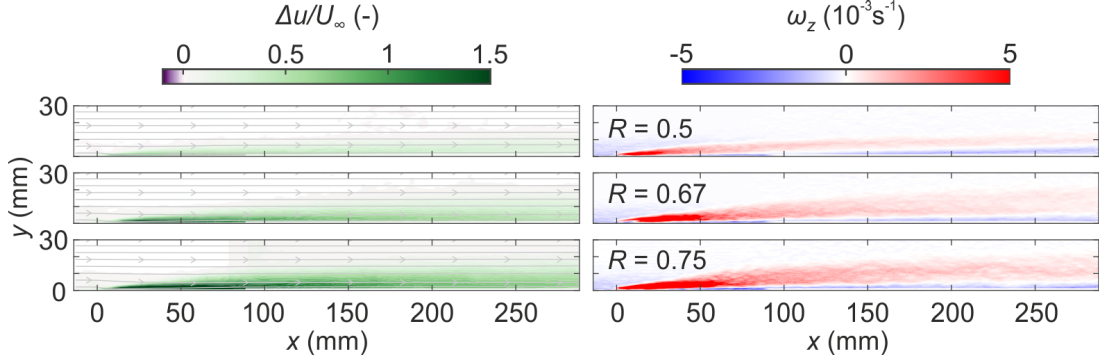
FIGURE 3. Gain in streamwise velocity due to steady wall jets of different velocity ratios (left) and mean spanwise vorticity fields (right)

instance, ZW93 consider a streamwise length of approximately $160b$ whereas the domain is limited to 40 slot heights in a recent direct numerical simulation conducted by Naqavi *et al.* (2018). The relatively large streamwise extent appears to be particularly important in light of comments made by Craft & Launder (2001), suggesting that a fully-developed flow may only be observed several hundred slot heights downstream of the outlet in the case of three-dimensional wall jets.

3. Results

In the following, the streamwise development of wall jet properties will be addressed. The section is structured as follows. First, steady wall jets are assessed to identify the potential influence of a finite outlet span. Then, unsteady velocity programs will be considered, namely those that involve the sudden initiation or termination of fluid emission. Finally, observations regarding these configurations will be used to establish a model for pulsed wall jets.

3.1. *Steady finite-span wall jet*

First, let us assess the velocity fields of steady wall jets for different velocity ratios. The mean excess in momentum flux inside the jet centre plane is illustrated in the left column of figure 3. The deviation $\Delta u = \overline{u} - \overline{u_0}$ is obtained by subtracting the velocity field in the absence of wall jets $\overline{u_0}$ from the mean wall jet velocity field $\overline{u}$.

As can be expected, the maximum gain in velocity is observed in the near-wall region close to the outlet located at $x = 0\,\mathrm{mm}$. It can also be confirmed that the jets immediately attach to the wall despite the non-tangential fluid injection, and no reverse-flow directly downstream of the outlet is measured. Hence, the alteration of the velocity field, compared to the unforced boundary-layer flow, is restricted to small wall distances of approximately $y < 15\,\mathrm{mm}$, which is also true for relatively large outlet distances considered in this study. Compared to the other velocity ratios, the gain in streamwise momentum flux is almost negligible for $R = 0.5$ where the maxima barely exceed $\Delta u/U_\infty = 1$ in the near-outlet region. This may affect local similarity characteristics considering that ZW93 suggested a threshold of $U_m/U_\infty = 2$ needs to be exceeded. As for the other velocity ratios, local velocities over this threshold are only reached at $x/b < 30$ ($R = 0.67$) and $x/b < 120$ ($R = 0.75$). We will address the importance of local velocity maxima with regards to 'approximate self-similarity' in due course. The velocity fields shown in the left of figure 3 also contain time-averaged streamlines. Except for a slight bending towards the jet outlet, these are directed horizontally. A significant negative wall-normal velocity component in
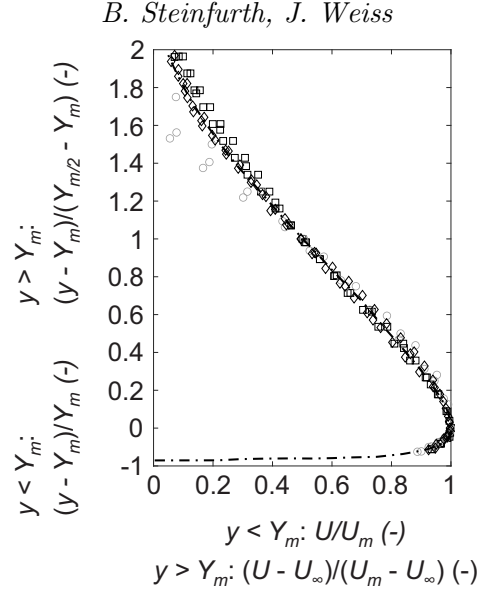
FIGURE 4. Steady wall jet velocity profiles with scaling suggested by Zhou & Wygnanski (1993), ∘ $R = 0.5$, ☐ $R = 0.67$, ◇ $R = 0.75$, $- \cdot -$ data by Zhou & Wygnanski (1993)

the fully-developed wall jet, as assumed to be at hand for three-dimensional wall jets in the absence of a cross-flow by Launder & Rodi (1983), cannot be attested.

The mean spanwise vorticity component is presented in the right column of figure 3. Overall values are mainly driven by wall-normal velocity gradients $\partial u/\partial y$ that contribute more than 90% to the total spanwise vorticity throughout the measurement plane, which can therefore be expected to change sign at the location of maximum velocity Y_m, suggesting an asymptotical jet spreading to be addressed later on. It is also worth mentioning that the outer wall jet layer (positive vorticity) is much thinner for the smallest velocity ratio due to the negligible excess in momentum flux discussed above.

From the data presented in figure 3, some of the major wall jet quantities (U_m, Y_m, $Y_{m/2}$) can be readily extracted. We will now use these parameters to assess wall-normal velocity profiles that are scaled as suggested by ZW93 who argue that two velocity scales need to be applied. While the shape of the inner layer is governed by U_m, the local velocity scale in the outer layer is $U_m - U_\infty$. Accordingly, Y_m and $Y_{m/2} - Y_m$ are chosen as characteristic length scales for the inner and outer layer (figure 4).

Evaluating the flow region $x/b = 100, \ldots, 300$, a reasonable collapse is noted for the two larger jet velocities. For $R = 0.5$, a differing gradient is noted in the outer layer which was also observed by ZW93 for a similar velocity ratio ($R = 0.59$) and attributed to the insufficient excess in momentum flux that we touched upon above. Otherwise, the scaled velocity profiles are practically identical to those measured by ZW93 whose data are represented by the dash-dotted line. This may come as a surprise given the significant differences in the wall jet configuration. Specifically, the finite-span outlets employed in the current study appear to have no effect on similarity characteristics inside the centre plane provided the velocity ratio is sufficiently large ($R \geqslant 0.67$).

Encouraged by this finding, we will now assess the development of steady wall jet properties by applying the scalings introduced by Narasimha *et al.* (1973) who argued that the sole parameter determining the velocity profiles in the absence of an external stream is the kinematic momentum flux J in the jet exit plane. ZW93 extended this approach by showing that J needs to be defined as the excess in momentum flux when a co-flowing cross-flow is present. Neglecting the momentum deficit in the upstream
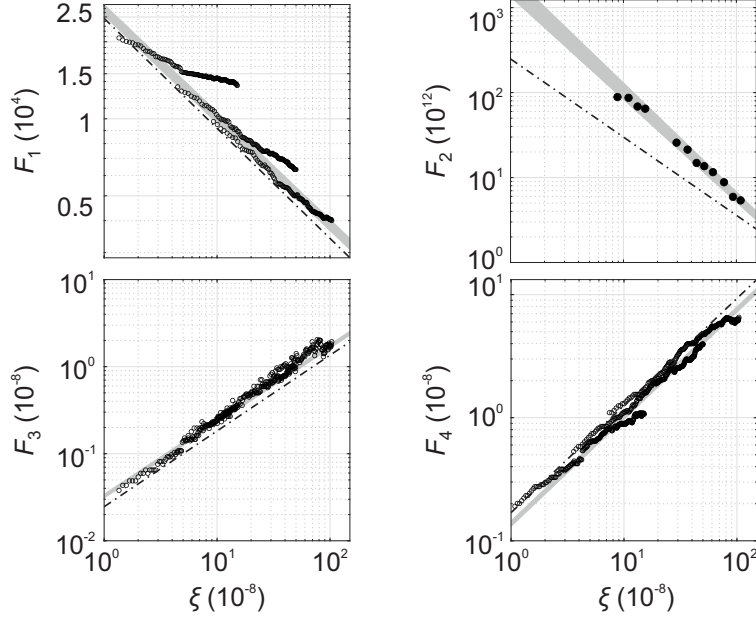
FIGURE 5. Scaled steady wall jet properties for the range $x/b = 50, \ldots, 570$, $\pm5\%$ interval of power law fit highlighted by shaded area, for scaled wall shear-stress data (F_2), the shaded area presents estimations based on correlation by Bradshaw & Gee (1962), $- \cdot -$ data by Zhou & Wygnanski (1993)

boundary-layer and assuming that ejected fluid is directed along the wall immediately, this quantity can be approximated by

$$J = b(U_j - U_\infty)U_j. \tag{3.1}$$

Then, a non-dimensional streamwise coordinate is defined as

$$\xi = \frac{xJ}{\nu^2} = \frac{xb(U_j - U_\infty)U_j}{\nu^2}. \tag{3.2}$$

The dependencies of wall jet properties on ξ, adapted from ZW93, are

$$F_1(\xi) = \frac{U_m \nu R}{J}, \; F_2(\xi) = \frac{\tau R}{\varrho}\left(\frac{\nu}{J}\right)^2, \; F_3(\xi) = \frac{Y_m J}{\nu^2}, \; F_4(\xi) = \frac{Y_{m/2} J}{R\nu^2}. \tag{3.3}$$

Note that we did not subtract an offset in F_3 and F_4 since the nozzle width is relatively small in the current study. The scaled wall jet quantities are plotted in figure 5 (black circles) along with shaded areas representing $\pm5\%$ intervals enclosing the respective power law fits

$$F_1(\xi) = 0.61\xi^{-0.42}, \; F_2(\xi) = 1.62\xi^{-1.14}, \; F_3(\xi) = 0.43\xi^{0.86}, \; F_4(\xi) = 1.51\xi^{0.87}, \tag{3.4}$$

The corresponding constants determined by ZW93 are indicated by dash-dotted lines, and a good agreement can be attested to those computed in the present study. In fact, the exponent is identical for the case of the scaled wall jet half-width $Y_{m/2}$ (F_4) and only differs by 0.01 for U_m (F_1) and Y_m (F_3). However, a substantial deviation, almost by a factor of three, is found for the scaled wall shear-stress (F_2). We assume that the data provided by ZW93 are based on measurements of the velocity gradient by means of hot-wire anemometry because they reference the experimental procedure introduced

B. Steinfurth, J. Weiss

by Wygnanski *et al.* (1992) in their article. Here, the authors themselves note that the accuracy of this approach may be affected by the traversing system, the quality of the hot-wire probe and the number of acquired data points. Previously, Launder & Rodi (1979) stated that this type of experimental approach has produced wall shear-stress values significantly below those measured with impact tube probes. For the sensors employed in the present study, on the other hand, the maximum deviation compared to Preston tube measurements is $\pm 5\%$ in a turbulent boundary layer up to $\tau \approx 7\,\mathrm{Pa}$. We also compared our data to the wall shear-stress correlation established by Bradshaw & Gee (1962) for wall jets without a cross-flow

$$\tau = \frac{0.0315 \varrho U_\mathrm{m}^2}{2} \left(\frac{U_\mathrm{m} Y_\mathrm{m}}{\nu} \right)^{-0.182} , \tag{3.5}$$

which is represented by a shaded area in figure 5 (upper right) containing wall shear-stress values estimated with the available PIV data. The measurement data are clearly consistent with the correlation, hence we are confident that our measurements are reliable.

As for the scaled maximum velocity U_m (F_1), a slower decay can be noted for the smallest velocity ratio that is represented by the array of symbols in the upper left. The same is also true for the far-field of the medium velocity ratio. This behaviour can be explained by the insufficient local excess in momentum flux discussed above, here associated with peak jet velocities of $U_m/U_\infty < 0.5$. Notably, this is a much less restrictive criterion than the threshold value of $U_m/U_\infty = 2$ stated by ZW93. For the largest investigated jet velocity ($R = 0.75$), on the other hand, the scaled velocities fall into the $\pm 5\%$ interval while values measured at $\xi < 30 \cdot 10^8$ practically collapse with the data provided by ZW93. The relatively small excess in local momentum flux found for $R = 0.5$ and $R = 0.67$ appears to have a less significant effect on the 'approximate self-similar' behaviour of the remaining jet quantities. Here, the applied scalings are suited to collapse the data onto single curves throughout the measurement domain with scatter that is on a similar order as that observed by ZW93.

Overall, the similarity of velocity profiles discussed above is reflected in the streamwise development of major wall jet properties. Specifically, power law expressions very similar to those determined by ZW93 were shown to describe the velocity decay and the spreading rate for the case of steady fluid emission.

The good agreement between the nominally two-dimensional flow addressed by ZW93 and three-dimensional wall jets under consideration in the current study may come as a surprise since substantial lateral spreading has been argued to preclude the applicability of 'approximate self-similarity' to the latter type of wall jet (Narasimha *et al.* 1973). However, this assertion has only been made in the absence of an external stream. We will therefore briefly address the influence of a cross-flow on the jet expansion in the following. The mean velocity fields in cross-sections located at $x = (50, 150, 300)\,\mathrm{mm}$ are presented in figure 6 where the cross-flow configuration ($U_\infty = 20\,\mathrm{m/s}$) and the case of quiescent ambience ($U_\infty = 0\,\mathrm{m/s}$) are shown in the left and right column respectively. Black arrows indicate the in-plane vector field defined by the velocity components v and w.

The major effect of an external stream becomes apparent when assessing the regions enclosed by white lines where the excess in streamwise velocity is larger than half the maximum, a definition analogous to the half-width discussed above. Much larger spreading rates, both in wall-normal and lateral dimension, can be attested for the $U_\infty = 0\,\mathrm{m/s}$ case. Based on measurements at $x = 150\,\mathrm{mm}$ and $x = 300\,\mathrm{mm}$, rates
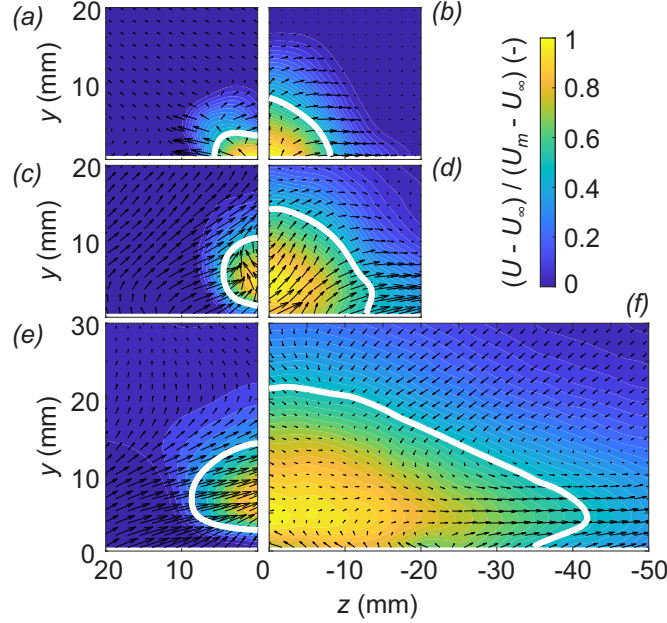
FIGURE 6. Mean velocity fields in cross-sections at $x = 50\,\mathrm{mm}$ (a,b), $x = 150\,\mathrm{mm}$ (c,d) and $x = 300\,\mathrm{mm}$ (e,f); left column: cross-flow with mean inflow velocity $U_\infty = 20\,\mathrm{m/s}$, right column: no cross-flow ($U_\infty = 0\,\mathrm{m/s}$); jet half-width indicated by white line

of $\mathrm{d}Y_{\mathrm{m}/2}/\mathrm{d}x \approx 0.047$ and $\mathrm{d}Z_{\mathrm{m}/2}/\mathrm{d}x \approx 0.187$ are measured, i.e. an approximately four times larger spreading in lateral than in vertical direction. This is consistent with previous investigations of three-dimensional wall jets although even larger ratios have been reported in the past, e.g. by Davis & Winarto (1980). Providing an explanation for the large lateral spreading rate, Launder & Rodi (1983) consider the curl of the Reynolds equation, yielding an expression for the rate of increase of streamwise vorticity

$$\frac{\mathrm{D}\omega_x}{\mathrm{D}t} = \underbrace{\omega_x \frac{\partial u}{\partial x}}_{\mathrm{A}} + \underbrace{\omega_y \frac{\partial u}{\partial y}}_{\mathrm{B}} + \underbrace{\omega_z \frac{\partial u}{\partial z}}_{\mathrm{C}}$$
$$+ \underbrace{\frac{\partial^2}{\partial y \partial z}\left(\overline{w^2} + \overline{v^2}\right) + \frac{\partial^2 \overline{vw}}{\partial y^2} - \frac{\partial^2 \overline{vw}}{\partial z^2}}_{\mathrm{D}} + \underbrace{\nu\left(\frac{\partial^2 \omega_x}{\partial y^2} + \frac{\partial^2 \omega_x}{\partial z^2}\right)}_{\mathrm{E}}. \tag{3.6}$$

Term A accounts for streamwise stretching and can be expected to have a damping effect since $\partial u/\partial x$ is mostly negative. Terms D and E represent the contributions of the Reynolds stress field and viscous diffusion respectively. The magnitude of the latter is at least an order of magnitude smaller than the other terms while the Reynolds stresses are assumed to reinforce the effect of vortex-line bending reflected in terms B and C. These can be rewritten as

$$\omega_y \frac{\partial u}{\partial y} + \omega_z \frac{\partial u}{\partial z} = \frac{\partial u}{\partial z}\frac{\partial v}{\partial x} - \frac{\partial u}{\partial y}\frac{\partial w}{\partial x}. \tag{3.7}$$

As pointed out by Launder & Rodi (1983), the two terms on the right of equation 3.7 balance each other in the case of free axisymmetric jets. For wall jets, however, asymmetry arises from the no-slip condition. We consider the inner layer in the half-plane where $z > 0\,\mathrm{mm}$ and assume that $w > v$ and $\partial u/\partial y \gg \partial u/\partial z$. Thus, the second term on
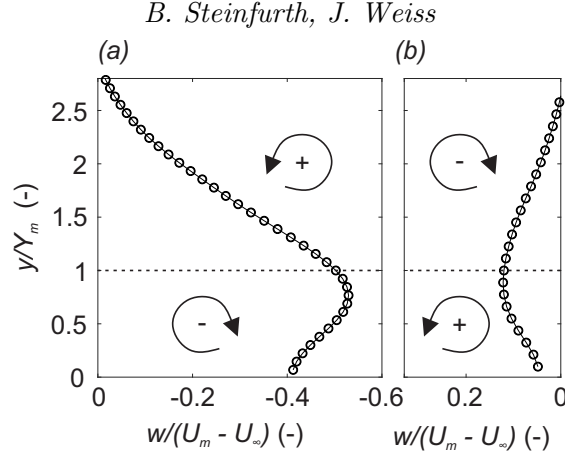
B. Steinfurth, J. Weiss

FIGURE 7. Profiles of spanwise velocity component w at $x = 300\,\text{mm}$ in $z > 0\,\text{mm}$ half-plane at the location of maximum w; (a) $U_\infty = 20\,\text{m/s}$ and (b) zero cross-flow ($U_\infty = 0\,\text{m/s}$); sign of streamwise vorticity amplification through vortex-line bending highlighted for inner and outer layer of wall jets

the right of equation 3.7 is dominant. Furthermore, $\partial w/\partial x$ is negative, leading to an overall positive source of streamwise vorticity amplification. In the outer layer, the sign of $\partial u/\partial y$ changes, which results in a negative source term. As a consequence, streamwise vorticity of opposite signs is enforced in the inner and outer layer, essentially leading to a strengthened outward-directed velocity component in the region $y \approx Y_m$ that is associated with increased lateral spreading. Satisfying mass conservation, this should be compensated by a re-direction of streamlines and an inward-directed flow in wall-normal direction. Such characteristics are indeed confirmed by PIV measurements at $x = 300\,\text{mm}$ in the absence of a cross-flow, figure 6 (f), also exhibiting a remarkable similarity to the velocity field of a three-dimensional wall jet computed by Kebede (1982) using a linear eddy-viscosity model.

Being the focus point of this study, we now turn our attention to the wall jet in cross-flow for which cross-section velocity fields are shown in the left column of figure 6. Clearly, the expansion in wall-normal and spanwise direction is much smaller than for the case of zero cross-flow. In fact, a slight lateral contraction is observed during the development stage between $x = 50\,\text{mm}$ and $x = 150\,\text{mm}$. It is also apparent that the flow is directed towards the symmetry plane ($z = 0\,\text{mm}$), meaning that w is of opposite sign compared to the case discussed above. Analogous to the classical wall jet without an external stream, the lateral spreading (here, lack thereof) can be explained by assessing the vortex-line bending terms B and C in equation 3.7. Now, w is negative, hence $\partial w/\partial x$ is positive (the velocity magnitude decays with increasing outlet distance). As a result, the source terms for the inner and outer layer are of opposite sign compared to the wall jet in quiescent surroundings, and the consequence of the self-amplifying process is that surrounding fluid from the boundary layer is entrained into the wall jet through mean fluid motion.

The mechanism of streamwise vorticity amplification through vortex-line bending is illustrated in figure 7 where spanwise velocity profiles measured at an outlet distance of $x = 300\,\text{mm}$ are shown for the cases with and without cross-flow. Both profiles are extracted from the locations where $|w|$ reaches its maximum in the $z > 0\,\text{mm}$ half-plane, i.e. where positive values indicate outward-directed flow.

It is confirmed that the spanwise component is of opposite sign throughout the presented velocity profiles and indeed throughout the half-plane (not shown here). The
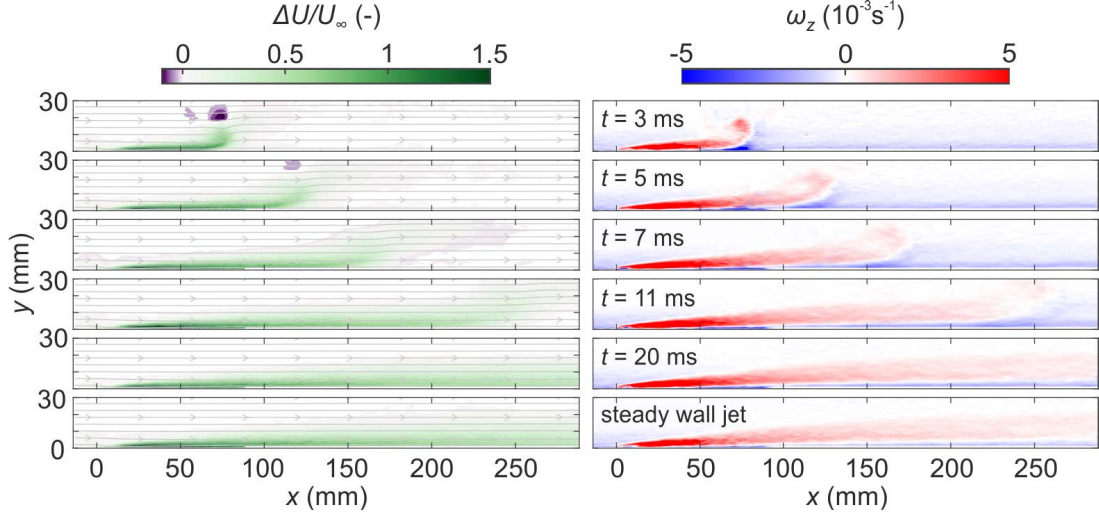
FIGURE 8. Time series of gain in streamwise velocity due to starting wall jets at $R = 0.67$ (left) and mean spanwise vorticity (right)

maximum magnitude is reached at approximately Y_m where $\partial u / \partial y$, and thus the vorticity amplification, changes its sign.

We conclude that the presence of a co-flowing cross-flow fundamentally changes the spreading characteristics of steady wall jets. Specifically, streamwise vorticity with an opposite sense of rotation is produced in the case of an external stream, leading to the amplification of inward-directed lateral flow. This mechanism opposes the jet expansion in spanwise direction through turbulent diffusion, apparently cancelling one another as a negligible overall spreading rate is measured. These findings are consistent with the 'directing influence' of a cross-flow stated by Narasimha *et al.* (1973) and explain the applicability of scalings laws determined for the two-dimensional flow to jet properties inside the symmetry plane of the finite-span jets addressed in the current study.

3.2. *Starting finite-span wall jet*

Next, we consider the case where the jet emission is started at a defined time instant, which was realised by opening the fast-switching valve at $t = t_0 = 0$ s. The practical consideration that such a t_0 also exists for experiments of steady jets addressed above suggests that 'approximate self-similarity' may also be observed for starting wall jets provided the flow is assessed after a sufficiently long time duration. The main objective in this sub-section is to determine this time delay or, from a different perspective, identify the region inside the leading part of starting wall jets where the scaling method introduced above is not applicable.

Figure 8 contains information on velocity fields during the starting process based on phase-locked PIV measurements. Contour plots of the steady wall jets are also shown in the bottom row for reference. The presented quantities are the same as in figure 3 but only the medium velocity ratio wall jet ($R = 0.67$) is shown.

Following the fluid emission, a leading vortex develops. This flow structure is associated with an accumulation of spanwise vorticity close to the jet propagation front, inducing a gain in near-wall velocity as well as a slight deficit in the outer layer. As shown by the authors through tomographic reconstructions of the three-dimensional flow field (Steinfurth & Weiss 2021c,a), the leading vortex has the shape of a half-ring in the case of finite-span outlet slots. As this vortex half-ring propagates downstream, it quickly
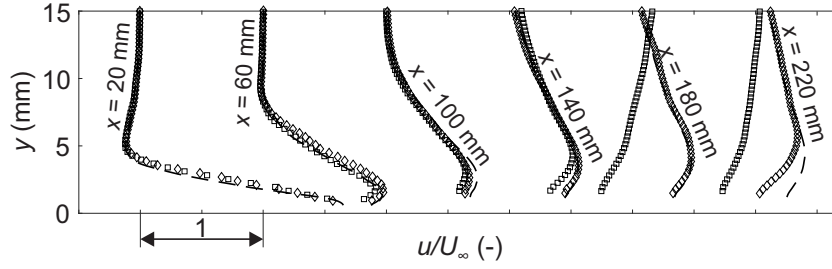
FIGURE 9. Wall-normal velocity profiles for $R = 0.67$, $--$ steady wall jet, $\square$ starting wall jet at $t = t_0 + 7\,\text{ms}$, $\diamond$ starting wall jet at $t = t_0 + 11\,\text{ms}$

diffuses due to viscous shearing. It is important to note that the spreading rate near the propagation front is larger than in the trailing wall-attached jet, i.e. peak jet velocities U_m are found in greater wall distance. Apart from the leading vortex, however, the wall jet appears to exhibit similar characteristics as the steady wall jet addressed above.

A more detailed comparison between starting and steady wall jets is enabled by velocity profiles presented in figure 9. Along with the steady configuration (dashed line), profiles are shown for the $R = 0.67$ starting jet at $t = 7\,\text{ms}$ and $t = 11\,\text{ms}$ at different streamwise locations. Referring to figure 8, it can be noted that the propagation front is located at approximately $x \approx 170\,\text{mm}$ and $x \approx 250\,\text{mm}$ for these two time steps. Therefore, unforced boundary-layer profiles can be seen at the two locations of largest outlet distance for the former time instant. For $t = 11\,\text{ms}$, on the other hand, the wall jet already imposes an effect at $x = 220\,\text{mm}$ inasmuch as the streamwise velocity reaches values approaching those found for the steady wall jet inside the outer wall jet layer. The same is not true for the near-wall region where a smaller velocity is measured. In locations that have been passed by the propagation front, however, a good agreement between velocity profiles can be noted.

We conclude that wall jets trailing the leading vortex ring generated by the sudden initiation of fluid exhibit practically identical velocity profiles as those measured in steady wall jets where the starting process has no influence on the flow. It is therefore reasonable to assume that similarity behaviour, shown to be at hand for the steady configuration, also exists for certain regions of starting wall jets.

In order to quantitatively define flow regions where 'approximate self-similarity' may be applicable, more information regarding the convection and growth of the propagation front is required. As a means to reveal the leading vortex ring, a series of finite-time Lyapunov exponent (FTLE) fields are shown in figure 10. Large values of this quantity indicate an attracting material line (A), governing the displacement of boundary-layer fluid along the propagation front. The diffusion of the leading vortex structure also becomes apparent, which is associated with a growth in streamwise and wall-normal direction. Figure 10 also contains diagrams of U_m and Y_m extracted for the same time steps. As was already inferred from evaluating the velocity profiles presented in figure 9, jet parameters approach values associated with steady wall jets in the flow region between outlet and leading part of the jet. Across the propagation front (with increasing x), larger values of Y_m can be noted. Recall that Y_m points to locations inside the free stream in the unforced boundary-layer where the maximum velocity is $U_m/U_\infty = 1$. The onset of deviation between instantaneous Y_m curves and the steady case are highlighted by dashed verticals, nicely coinciding with the trailing ends of vortex structures revealed by FTLE fields.

Based on these observations, the time-dependent extent of the leading vortex region can be determined by defining threshold values applied to curves of starting wall jets
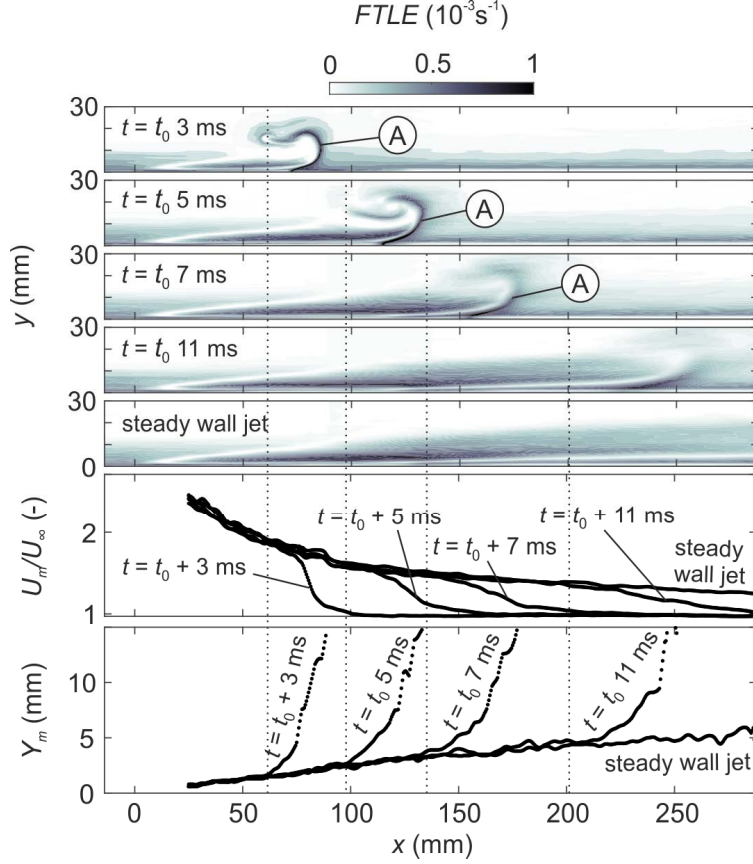
FIGURE 10. Time series of finite-time Lyapunov exponent field for starting wall jet at $R = 0.67$; peak jet velocities with respective wall distance for the same time-steps shown in the two bottom diagrams

at different time instants. Here, we define the downstream end of the leading vortex as the location where $U_m = 1.03U_\infty$ whereas a deviation of 10% with respect to the steady wall jet half-width was chosen to identify the upstream boundary. Computing the locations given by these thresholds for various time-steps, information on the convection and expansion of the wall jet leading part is obtained (figure 11). Separated by the resulting linear curves, three regions of the flow field can be identified in the space-time-diagrams. Not yet reached by the propagation front, behaviour associated with the unforced boundary-layer can be expected inside the area highlighted in light grey. The leading part of the jet resides in regions highlighted in dark grey. Further upstream, U_m and Y_m are identical to corresponding values of the steady wall jet to within the thresholds stated above.

It is immediately apparent that the two curves diverge for all velocity ratios, confirming the longitudinal expansion of the jet leading part mentioned above. Although larger convective velocities are measured for increased velocity ratios, there appears to be a strong dependence on $U_\infty = 20\,\mathrm{m/s}$ as well. This suggests the application of the velocity ratio R as a scaling parameter, which was also proven to be a good choice to describe the evolution of main wall jet properties above. And indeed, the curves of time-dependent locations enclosing the jet leading part collapse reasonably well (diagram in the right of figure 11), indicating convective velocities of $U_{c,1} = 1.48RU_\infty$ and $U_{c,2} = 1.82RU_\infty$ for the boundaries of the jet leading part.

We will now use these approximations to identify the flow regions highlighted in
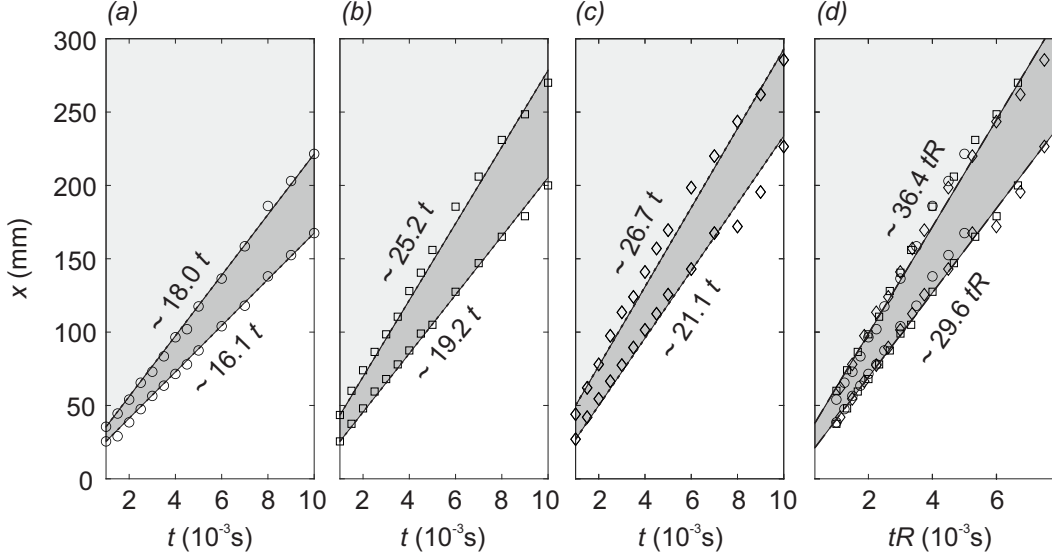
B. Steinfurth, J. Weiss

FIGURE 11. Time-dependent locations of leading part boundaries for starting jets of different velocity ratios; (a) $R = 0.5$, (b) $R = 0.67$, (c) $R = 0.75$ and (d) locations for all velocity ratios scaled with R

figure 11, i.e. the boundary-layer unaffected by wall jets as well as the leading and trailing jet parts for various time steps during the starting process. For PIV data, yielding U_m, Y_m and $Y_{m/2}$, the convective velocities simply define intervals of x. For wall-shear stress measurements, where the number of temporal samples by far exceeds the number of sensors, we use $U_{c,1}$ and $U_{c,2}$ to compute residence times of the wall jet regions at the respective sensor locations. The scaled jet properties, along with the power law expressions determined for steady wall jets above (solid line), are presented in figure 12. Symbols coloured in light grey indicate the unforced boundary-layer while dark grey circles represent the jet leading part and black is used for the trailing wall jet.

As was hypothesised above, there is indeed a wall jet region during the starting process with characteristics identical to those of steady wall jets. The scatter observed for black circles is not larger than that for the steady-blowing case. Deviations from the power law fit are again due to an insufficient local momentum excess. Furthermore, we conclude that the approximate convective velocities are suited to determine the flow region where the scaling suggested by ZW93 can be applied. A distinct departure from the 'approximately self-similar' behaviour is noted across the leading vortex region.

3.3. Stopping finite-span wall jet

Attention is now turned to the case where fluid emission is terminated at $\tilde{t} = 0$ s. Prior to that time instant, the flow field is identical to that of a steady wall jet addressed above.

A time series of the velocity fields directly subsequent to the end of the jet emission is presented in figure 13. Again, only the medium velocity ratio $R = 0.67$ is considered, for which the gain in streamwise velocity (left column) and the spanwise vorticity (right column) are shown.

Immediately following the jet emission phase, a stopping vortex is generated near the outlet. This flow structure has been observed previously by Steinfurth & Weiss (2021a) and was explained as a consequence of radial entrainment at the jet trailing part due to mass conservation. It is associated with a small-scale strand of positive spanwise vorticity, inducing a slight velocity deficit on its upper part before diffusing quickly.
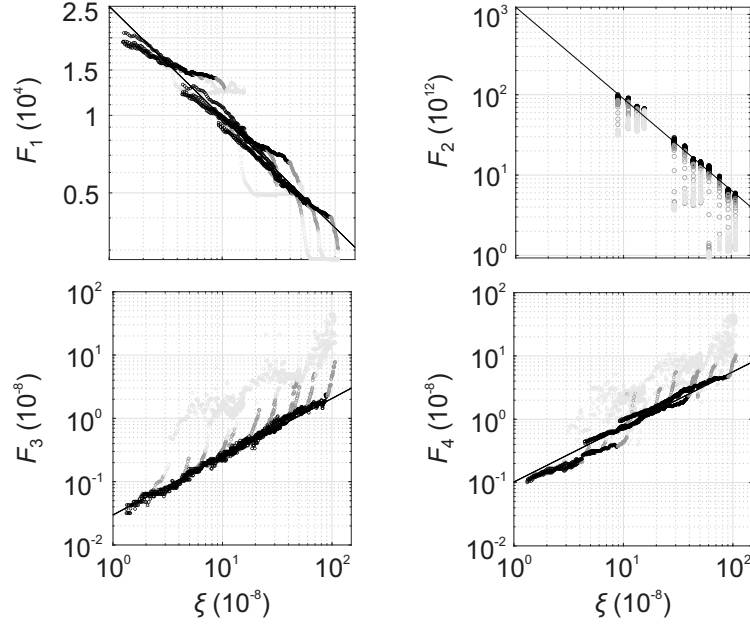
FIGURE 12. Scaled starting wall jet properties for different time instants, black symbols used for region upstream of leading vortex, dark grey for leading vortex and light grey for unforced boundary layer downstream of wall jet
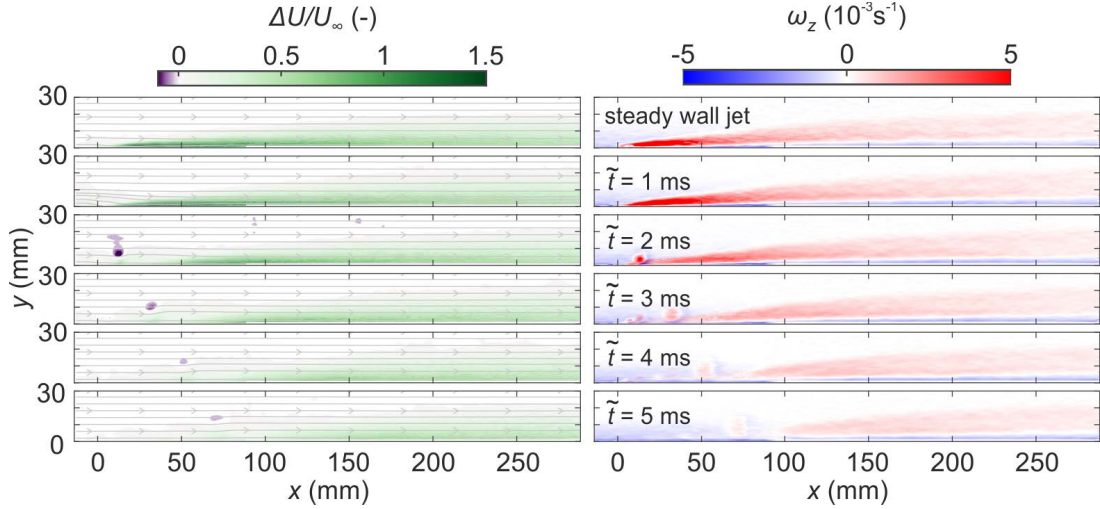
FIGURE 13. Time series of gain in streamwise velocity due to stopping wall jet at $R = 0.67$ (left) and mean spanwise vorticity (right)

Further downstream, however, both the velocity and vorticity fields appear to be very similar to that of the steady jet at a certain distance to the jet trailing part.

This is confirmed by the diagrams presented in figure 14, showing peak jet velocities U_m and corresponding jet widths Y_m during the stopping process. Both parameters again converge to the values measured for the steady wall jet for large x. The jet trailing part, however, represents a deceleration wave where the velocity decreases from U_m found for the steady case to U_∞. At the upstream end of this deceleration wave, the stopping vortex induces a minor local peak in streamwise velocity.

Compared to Y_m, U_m is the more sensitive indicator of the transitional region between deceleration wave and jet with steady characteristics. We will therefore evaluate time-
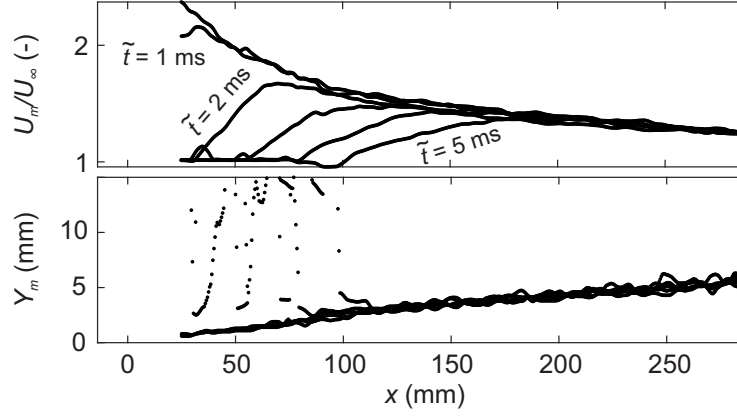
FIGURE 14. Peak jet velocities U_m and respective wall distance Y_m for stopping $R = 0.67$ wall jet at
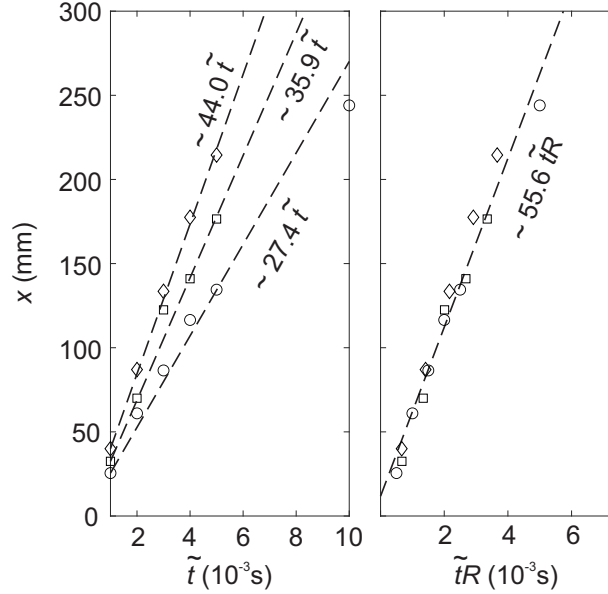
FIGURE 15. Time-dependent locations of trailing jet part for stopping jets of different velocity ratios

dependent U_m distributions to detect the upstream boundary of the 'approximately self-similar' flow region and use the global maximum as the indicating value. This choice is motivated by the monotonous decrease in streamwise direction for the steady wall jet and the empirical observation that both U_m and Y_m curves collapse downstream of the location associated with maximum velocity as shown in figure 14.

The locations of maximum U_m for the three velocity ratios following the jet termination are presented in figure 15. Again, an almost linear dependence can be noted inside the evaluated range. However, the associated velocities are much larger than those for the convection of the leading vortex, approximately separated by a factor of two. Also exceeding local streamwise velocities, it is reasonable to assume that the slopes of these curves are linked to the diffusion of the jet trailing part rather than its convection. Again, the velocity ratio R is applied to collapse the data for different jet velocities, yielding an approximate for the advance of the deceleration wave $U_d = 2.78 R U_\infty$

Based on this velocity, we again identify a region inside the measurement domain that
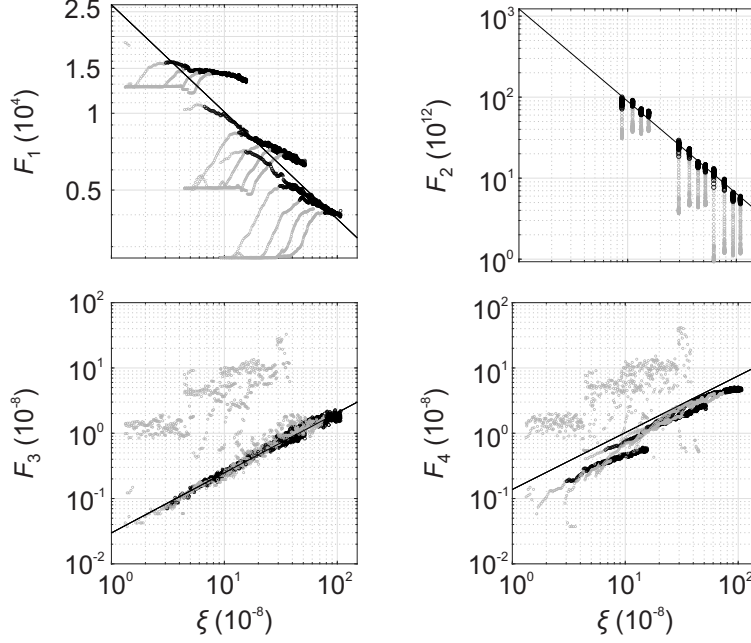
FIGURE 16. Scaled stopping wall jet properties for different time instants, black symbols used for region downstream of deceleration wave, grey for deceleration wave and unforced boundary layer upstream of wall jet

may exhibit behaviour similar to that of the steady wall jets addressed above. Figure 16 contains diagrams of the scaled jet properties with black symbols used for the region downstream of the locations estimated by U_d. Again, both the decay of U_m and τ as well as the jet spreading rate for these regions are in good agreement with the power law expressions established above. Upstream of the jets, the velocity and wall shear-stress decrease as values associated with the free stream are approached across the deceleration wave. This deviation from the 'approximate self-similarity' is adequately captured by employing U_d.

3.4. A model for starting/stopping wall jets

The results presented so far indicate that power law expressions proposed by Narasimha *et al.* (1973) and ZW93 are also applicable to steady wall jets ejected from a finite-span nozzle after minor adjustments (eq. 3.4). Interestingly, a jet structure with such characteristics is also found for unsteady jet velocity programs, upstream of the propagation front (x_p) and downstream of the deceleration wave (x_d), with time-dependent locations given by

$$x_p(t) = U_{c,1}t \tag{3.8}$$

and

$$x_d(t) = U_d\tilde{t} \tag{3.9}$$

where

$$\tilde{t} = \begin{cases} 0\,\mathrm{s}, & \mathrm{if}\, t \leqslant t_{\mathrm{p}} \\ t - t_{\mathrm{p}}, & \mathrm{if}\, t > t_{\mathrm{p}}. \end{cases} \tag{3.10}$$

B. Steinfurth, J. Weiss

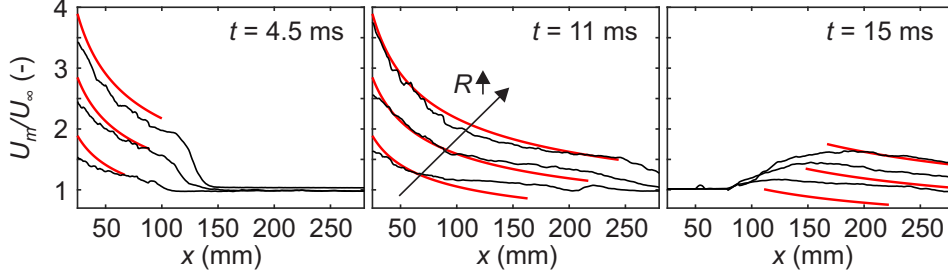FIGURE 17. Measured velocity distributions (black curves) and modelled velocity inside the region between propagation front and deceleration wave (red curves)

Note that the propagation front exists for $t \geqslant 0\,\text{s}$, and the deceleration wave only starts to develop when t equals the pulse duration t_p, i.e. when the fluid emission is stopped.

Now, a simple model for starting/stopping, or pulsed, wall jets can be introduced, predicting U_m, τ, Y_m and $Y_{m/2}$ for outlet distances in the range $x = x_d, \ldots, x_p$. We will now demonstrate the capabilities of this model by comparing the estimated peak jet velocities U_m with the measured velocity distribution for different velocity ratios and a pulse duration of $t_p = 11\,\text{ms}$ (figure 17). Recall that the only input parameters to the modelled velocity distributions (red curves) are the velocity ratios R, the momentum fluxes J and the (constant) kinematic viscosity ν.

The starting process is ongoing for the first two time steps, i.e. the trailing part of the jet is located at $x = 0\,\text{mm}$. A good agreement between modelled and measured velocities can be attested although some deviation is observed for the two smaller velocity ratios at large outlet distances. This is explained by an insufficient excess in kinematic momentum flux preventing the applicability of the concept of 'approximate self-similarity'. In fact, unrealistic maximum velocities $U_m < U_\infty$ are predicted for $R = 0.5$ at $x > 150\,\text{mm}$. At $R = 0.75$, on the other hand, only negligible differences are noted. Furthermore, a good prediction of the jet leading part can be attested as larger rates of velocity decay are found upstream of the predicted jet propagation front, i.e. right of the red curves. Similarly, a good prediction of the decay in U_m is noted for the largest velocity ratio during the stopping process in the jet far-field. Substantial deviations, however, are observed for the smaller velocity ratio as the excess in momentum flux is much smaller than $U_m/U_\infty = 2$, the threshold stated by ZW93.

Finally, we will use the proposed model to estimate the wall shear-stress signals at five locations downstream of the outlet, again considering a pulsed jet with a valve opening time of $t_p = 11\,\text{ms}$ (figure 18). Here, $U_{c,1}$ and U_d are used to determine the time intervals during which the wall jets reside at the sensor locations. Note that the introduced model predicts constant jet properties at given outlet locations for each jet velocity. Therefore, the modelled signals equal horizontals with end points depending on $U_{c,1}$ and U_d.

Since U_d is almost twice as large as $U_{c,1}$, a decreasing length of the wall jet $x_p - x_d$ is predicted as it convects downstream. At $R = 0.5$, this difference is only positive for the first three sensor locations. In other words, complete diffusion of the wall jet is predicted before reaching larger outlet distances. Indeed, no clear plateaus are seen in the signals measured at these locations. For the two larger velocity ratios, small jet lengths are estimated in the jet far-field which is again confirmed by the phase-averaged signals. The actual passage of wall jets inducing quasi-constant wall shear-stress appears to slightly forego the prediction by the model which is simply due to the conservative definition of the 'approximately self-similar' jet region based on the threshold values stated above.
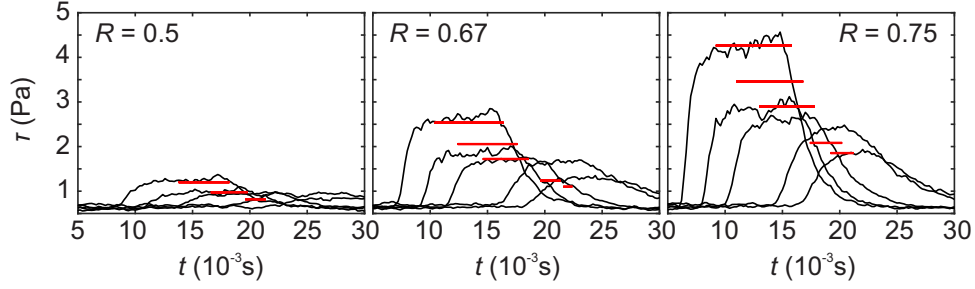
FIGURE 18. Measured wall shear-stress signals (black curves) and predicted wall shera-stress (red curves) at five locations downstream of jet outlet

Nonetheless, a good overall agreement between the modelled and measured wall shear-stress can be attested during the jet passage with deviations not exceeding $\Delta\tau = 0.5\,\mathrm{Pa}$.

4. Conclusions

The main objective of this study was to assess the applicability of scaling laws first established by Narasimha *et al.* (1973) to pulsed finite-span wall jets in a cross-flow. A pulsed-jet actuator was used to generate jets with a constant velocity as well as unsteady velocity programs.

Despite the limited spanwise outlet dimension $L = 20\,\mathrm{mm}$, non-dimensional velocity profiles identical to those of two-dimensional wall jets studied by ZW93 are determined in the centre plane. There is a small discrepancy for the smallest investigated velocity ratio $R = 0.5$, which is in line with empirical observations made by ZW93 suggesting that a certain excess in momentum is required for wall jets to exhibit 'approximate self-similarity'. This was confirmed in the current study where power law expressions similar to those obtained by ZW93 were shown to map the development of the decay in maximum velocity and wall shear-stress as well as the jet spreading rate for larger velocity ratios $R = (0.67, 0.75)$. First established by Narasimha *et al.* (1973), these scaling laws only require knowledge of the gross momentum flux in the outlet plane, the jet velocity ratio and the kinematic viscosity. Previous investigations of finite-span wall jets indicate what Narasimha *et al.* (1973) dubbed 'anomalous behaviour' due to three-dimensional effects (Sforza & Herbst 1970; Newman *et al.* 1972), mainly reflected in enhanced lateral spreading and thus a more rapid velocity decay. However, such characteristics have only been observed in the absence of a cross-flow (Abrahamsson *et al.* 1996; Davis & Winarto 1980). Indeed, the strong lateral spreading for this case was confirmed through PIV measurements up to $x/b = 600$ in the current study but a different picture was revealed when a cross-flow was applied. Here, the spanwise velocity component is directed towards the jet symmetry plane while the wall-normal component is associated with an outward-directed fluid motion. In consequence, a self-amplifying process of streamwise vorticity production that is argued to be responsible for the large lateral spreading rates without an external stream by Launder & Rodi (1983) and George *et al.* (2000) is at hand. However, it is associated with an opposite sense of rotation, essentially countering the lateral spreading of the three-dimensional wall jet in cross-flow. This finding is consistent with what Narasimha *et al.* (1973) referred to as the 'directing influence' of an external stream.

It was then shown that 'approximately self-similar' flow regions also exist in the case of starting and stopping jets where the momentum addition is initiated and stopped abruptly. These regions are enclosed by the leading vortex and the deceleration wave

where the flow properties transition to conditions found in the unforced boundary layer downstream and upstream of the wall jet. The velocities associated with these jet boundaries collapse when scaled with the velocity ratio, which enables a prediction of the time-dependent wall jet region by means of empirical constants. It is worth mentioning that the advance of the deceleration wave is associated with a velocity approximately twice as large as the convective velocity of the jet leading part. Hence, the length of the region with steady jet characteristics decreases once the fluid emission is stopped, which is in agreement with less distinct footprints of wall jets associated with relatively short pulse durations (Steinfurth & Weiss 2021*b*). Based on the empirical constants, a model for wall jet properties is proposed, predicting the space-time interval where the wall jet resides. In this region, the maximum velocity, wall shear-stress and jet half-width can be estimated using the scaling laws obtained for the steady configuration.

This model may prove useful in technical implementations of pulsed wall jets. For instance, forcing parameters may be optimised to ensure a certain momentum addition throughout the control domain in active separation control. However, it is reasonable to assume that wall jets exhibit different advancing velocities in such configurations compared to the zero-pressure-gradient flow addressed in this study. Future work therefore must be aimed at overcoming the empiricism related to the time-dependent wall jet boundaries. A further major finding relevant to technical flows was the lack of a lateral spreading rate, which may be taken into account when designing the location of and spacing between finite-span outlets.

Declaration of interests

The authors report no conflict of interest.

Acknowledgements

REFERENCES

ABRAHAMSSON, H., JOHANSSON, B. & LÖFDAHL, L. 1996 An investigation of the turbulence field in a three-dimensional wall jet. In *Advances in Turbulence VI. Fluid Mechanics and its Applications* (ed. S. Gavrilakis, L. Machiels & P. A. Monkewitz), , vol. 36, pp. 59–89. Dordrecht: Springer.

BAKKE, P. 1957 An experimental investigation of a wall jet. *J. Fluid Mech.* **2**, 467–472.

BRADSHAW, P. & GEE, M. T. 1962 Turbulent wall jets with and without an external stream. *Aeronaut. Res. Counc. R&M* **3252**.

CRAFT, T. J. & LAUNDER, B. E. 2001 On the spreading mechanism of the three-dimensional turbulent wall jet. *J. Fluid Mech.* **435**, 305–326.

DAVIS, M. R. & WINARTO, H. 1980 Jet diffusion from a circular nozzle above a solid plane. *J. Fluid Mech.* **730**, 626–658.

FÖRTHMANN, E. 1934 Über turbulente Strahlausbreitung. *E. Ing. Arch.* **5** (1), 42–54.

GARTSHORE, I. S. & NEWMAN, B. G. 1969 The turbulent wall jet in an arbitrary pressure gradient. *Aeronaut. Quart.* **20** (1), 25–56.

GEORGE, W. K., ABRAHAMSSON, H., ERIKSSON, J., KARLSSON, R. I., LÖDAHL, L. & WOSNIK, M. 2000 A similarity theory for the turbulent plane wall jet without external stream. *J. Fluid Mech.* **425**, 367–411.

GLAUERT, M. B. 1956 The wall jet. *J. Fluid Mech.* **1**, 625–643.

GREENBLATT, D. & WYGNANSKI, I. J. 2000 The control of flow separation by periodic excitation. *Prog. Aerosp. Sci.* **36** (7), 487–545.

KEBEDE, W. 1982 Numerical computations of the 3-dimensional wall jet.

KRUKA, V. & ESKINAZI, S. 1964 The wall-jet in a moving stream. *J. Fluid Mech.* **20** (4), 555–579.

LAI, J. C. S. & LU, D. 1996 Effect of wall inclination on the mean flow and turbulence characteristics in a two-dimensional wall jet. *Int. J. Heat Fluid Flow* **17** (4), 377–385.

LAUNDER, B. E. & RODI, W. 1979 The turbulent wall jet. *Prog. Aerosp. Sc.* **19**, 81–128.

LAUNDER, B. E. & RODI, W. 1983 The turbulent wall jet - Measurements and modeling. *Ann. Rev. Fluid Mech.* **15**, 429–459.

MYERS, G. E., SCHAUER, J. J. & EUSTIS, R. H. 1963 Plane turbulent wall jet flow development and friction factor. *J. Fluid Eng.* **85** (1), 47–53.

NAQAVI, I. Z., TYACKE, J. C. & TUCKER, P. G. 2018 Direct numerical simulation of a wall jet: Flow physics. *J. Fluid Mech.* **852**, 507–542.

NARASIMHA, R., NARAYAN, K. YEGNA & PARTHASARATHY, S. P. 1973 Parametric analysis of turbulent wall jets in still air. *Aeronaut. Quart.* **77** (751), 355–359.

NEWMAN, B. G., PATEL, R. P., SAVAGE, S. B. & TJIO, H. K. 1972 Three-dimensional wall jet originating from a circular orifice. *Aeronaut. Quart.* **23** (3), 188–200.

PAI, B. R. & WHITELAW, J. H. 1971 The prediction of wall temperature in the presence of film cooling. *Int. J. Heat Mass Transfer* **14** (3), 409–426.

PATEL, R. P. 1962 Self preserving, two-dimensional turbulent jets and wall jets in a moving stream. PhD thesis.

SCHWARZ, W. H. & COSART, W. P. 1961 The two-dimensional turbulent wall-jet. *J. Fluid Mech.* **10**, 481–495.

SEBAN, R. A. & BACK, L. H. 1961 Velocity and temperature profiles in a wall jet. *Int. J. Heat Mass Transfer* **3**, 255–265.

SFORZA, P. M. & HERBST, G. 1970 A study of three-dimensional, incompressible, turbulent wall jets. *AIAA J.* **8** (1), 276–282.

SIGALLA, A. 1958 Measurements of skin friction in a plane turbulent wall jet. *Aeronaut. Quart.* **62**, 873–877.

STEINFURTH, B. & WEISS, J. 2020 Vortex rings produced by non-parallel planar starting jets. *J. Fluid Mech.* **903**.

STEINFURTH, B. & WEISS, J. 2021a Boundary-layer control by means of pulsed jets at different inclination angles. *AIAA Journal* **59** (8).

STEINFURTH, B. & WEISS, J. 2021b Development of inclined pulsed jets in an adverse-pressure-gradient crossflow. *AIAA AVIATION 2021 FORUM* **59**.

STEINFURTH, B. & WEISS, J. 2021c Velocity ratio effect on flow structures of non-parallel planar starting jets in cross-flow. *Journal of Fluid Mechanics* **915**.

THOMAS, F. 1963 Untersuchungen über die Grenzschicht an einer Wand stromabwärts von einem Ausblasespalt. In *Abhandlungen der Braunschweigischen Wissenschaftlichen Gesellschaft Band*, , vol. 15, pp. 1–17. Braunschweig: Vieweg.

TOLLMIEN, W. 1926 Berechnung turbulenter Ausbreitungsvorgänge. *ZAMM - J. Appl. Math. Mech.* **6** (6), 468–478.

WEISS, J., JONDEAU, E., GIANI, A., CHARLOT, B. & COMBETTE, P. 2017a Static and dynamic calibration of a MEMS calorimetric shear-stress sensor. *Sensor Actuat. A: Phys.* **265**, 211–216.

WEISS, J., SCHWAAB, Q., BOUCETTA, Y., GIANI, A., GUIGUE, C., COMBETTE, P. & CHARLOT, B. 2017b Simulation and testing of a MEMS calorimetric shear-stress sensor. *Sensor Actuat. A: Phys.* **253**, 210–217.

WEISS, J., STEINFURTH, B., CHAMARD, L., GIANI, A. & COMBETTE, P. 2022 Spectral proper orthogonal decomposition of unsteady wall shear stress under a turbulent separation bubble. *AIAA J.* .

WILLE, R. & FERNHOLZ, H. 1965 Report on the first European Mechanics Colloquium, on the Coanda effect. *J. Fluid Mech.* **24** (4), 801–819.

WYGNANSKI, I., KATZ, Y. & HOREV, E. 1992 On the applicability of various scaling laws to the turbulent wall jet. *J. Fluid Mech.* **234**, 669–690.

22   *B. Steinfurth, J. Weiss*

Zhou, M. D. & Wygnanski, I. 1993 Parameters governing the turbulent wall jet in an external stream. *AIAA J.* **31** (5), 848–853.

4

Critical assessment of methodology

Although utmost attention was paid to limiting the uncertainty of measurement procedures as much as possible, some shortcomings inherent to the methodology could not be avoided. These will be addressed in the following.

4.1 Setting the jet velocity

In the present work, the forcing intensity was varied by adjusting the axial PJA outlet velocity $u_{\text{out}}(t)$. Considering that its signal is governed by the valve position with only two possible states, a square-wave was assumed to be an acceptable representation of $u_{\text{out}}(t)$. Here, the highs and lows are of durations t_{p} and t_{off} corresponding to the intervals where the valve was open and closed, respectively. Assuming that the actuation period is initiated by the opening of the valve at $t = t_0$, the outlet velocity can be formally written as

$$u_{\text{out}}(t) = \begin{cases} u_{\text{jet}}, & \text{if } t_0 \leq t \leq t_{\text{p}} \\ 0\,\text{m/s}, & \text{if } t_{\text{p}} < t \leq t_{\text{p}} + t_{\text{off}}. \end{cases} \tag{4.1}$$

In the research articles presented above, u_{jet} is referred to as the nominal jet velocity that is based on the duty cycle $DC = t_{\text{p}}/(t_{\text{p}} + t_{\text{off}})$, the time-averaged mass flow rate $\dot{m}$, the mass density of the emitted fluid ϱ_{jet} and the outlet area A_{out},

$$u_{\text{jet}} = \frac{1}{DC} \frac{\dot{m}}{\varrho_{\text{jet}} A_{\text{out}}}. \tag{4.2}$$

This definition requires some assumptions that are addressed in the following. First, it is assumed that the jet emission time where $u_{\text{out}} = u_{\text{jet}}$ is identical to the valve opening time. This is not entirely realistic since a deceleration wave already develops as the jet passes through the nozzle downstream of the magnetic valve, resulting in an emission time slightly longer than t_{p} (see figure 2 in **Article 1**). It is also important to note that the maximum specified uncertainty of $\pm15\%$ with regards to the valve opening and closure times directly translates

into an uncertainty of the jet velocity. From our experience, the valve switching characteristic can also change over time due to wear.

Second, the approach relies on the conversion of a constant mass flow into a time-dependent outlet velocity. This was facilitated by providing a reservoir downstream of the mass flow controller and upstream of the actuator (Figure 2.1). The volume of this tank was sufficient to compensate pressure fluctuations induced by the pulsatile ejection of fluid so that the plunger position of the mass flow controller was constant for a given forcing signal. Nonetheless, u_jet may not be completely constant during the ejection phase as a slightly varying velocity can be expected for large pulse durations in particular.

Third, compressibility effects were not taken into account as typical Mach numbers associated with the pulsed jets $Ma < 0.3$ were deemed sufficiently small. In addition, the jet mass density was computed based on the regulated wind tunnel temperature. I abstained from temperature measurements in the jet exit plane as to not affect the outlet profile.

Next, the outlet area of $A_\text{out} = (20 \times 0.5)\,\text{mm}^2$ was defined in a computer-aided design software but slight deviations may occur during 3D printing depending on the orientation of the nozzle in the printer and wear of optical components integrated in this device. However, the uncertainty around this parameter may be marginal as outlet geometries were qualified by means of a thickness gauge (Figure 4.1).
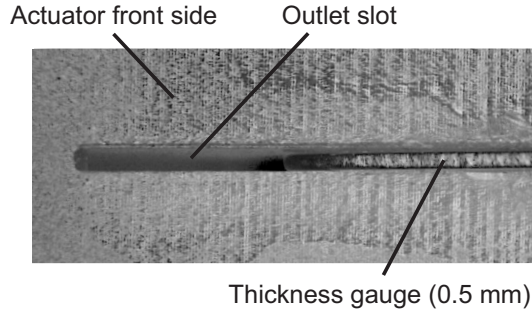

Figure 4.1: Microscope image of actuator outlet, photograph taken by René Halboth

Finally, when more than one actuator was employed to manipulate the flow (**Article 4**), it was assumed that the mass flow coming from the pressure reservoir was evenly distributed to all devices. However, deviations in pressure loss between the flexible connecting tubes may tarnish this assumption.

It can be concluded that a number of potential errors can be ascertained for the procedure of setting the jet velocity. A recent article by Semaan (2020) suggests that the uncertainty of experimentally-measured forcing intensities is indeed significant as even for an optimised setup, the uncertainty of c_μ is approximately 11% [157]. He also shows that for the approach taken in the present work, the uncertainty magnification is predominantly linked with the quality of the mass flow controller. Here, a device with an uncertainty of $\pm(0.5\%\,\text{o.m.v} + 0.1\%\,\text{FS})$ and a full-scale output of $FS = 50\,\text{l}_\text{s}/\text{min}$ was employed, representing a significantly smaller uncertainty than that assumed in the study mentioned above. The analysis and comparison of varied jet velocity configurations justified in the present work is therefore deemed justified.

4.2 Velocity field measurements

The flow fields considered in this thesis are dominated by large gradients in space and time. This gives rise to some challenges for PIV measurements that will be addressed in the following.

Considering that the spatial resolution of measured velocity fields was on the order of the actuator outlet width suggests that there may be non-uniform seeding particle displacement at the scale of interrogation areas in the near-outlet region. To estimate the measurement uncertainty, two parameters need to be considered [158]: first, the particle-image diameter d_τ that is correlated with the width of the displacement-correlation peak even for uniform flows [159]; second, the variation of particle-image displacement $|a|$ within the evaluated interrogation area. Intuitively, the effect of spatial gradients is negligible when $|a| \ll d_\tau$ [160]. For ratios $|a|/d_\tau$ substantially larger than zero (i.e., in the case of strong sub-interrogation gradients), however, the correlation peak amplitude is systematically reduced. For instance, a loss-of-correlation by 25% is already reached at $|a|/d_\tau = 0.66$ [158]. In the current work, even larger ratios occur in the flow regions mentioned above, resulting in an approximate uncertainty up to 25% (only due to spatial gradients) based on the expressions for the bias and random error provided in Ref. [158].

In addition to large spatial gradients, particles may undergo substantial accelerations as they interchange momentum with pulsed jets. As the mass densities associated with jets and seeding particles are not equal, a velocity lag that is proportional to the squared particle diameter d_p occurs [142]. Considering a step change in velocity resembling the initiation of fluid, the response time of a particle of mass density ϱ_p is

$$\tau_\mathrm{p} = d_\mathrm{p}^2 \frac{\varrho_\mathrm{p}}{18\mu} \tag{4.3}$$

where μ is the dynamic viscosity. A typical time response for the seeding particles employed in this work, according to Ref. [161], is $\tau_\mathrm{p} \approx 2\,\mu\mathrm{s}$, which should be compared with a reference time scale τ_ref that reflects the velocity fluctuations along a particle path by computing the Stokes number $Stk = \tau_\mathrm{p}/\tau_\mathrm{ref}$. To assess the particle behaviour during the jet initiation process, one may define this reference time scale as $\tau_\mathrm{ref} = d_\mathrm{out}/u_\mathrm{jet}$ where d_out is the outlet width. Then, acceptable Stokes numbers of $Stk < 10^{-1}$ [162] are only obtained for jet velocities up to $u_\mathrm{jet} = 25\,\mathrm{m/s}$. As typical velocities investigated in this study are much larger, a non-negligible lag velocity can be expected, resulting in a discrepancy between the measured velocity field data and the expected jet velocity as observed in **Article 1**. Since the particle diameter $d_\mathrm{p} \approx 1\,\mu\mathrm{m}$ could not be reduced, the only available counter measure would be to employ a different type of seeding exhibiting shorter time responses, such as silicon dioxide or titanium dioxide, which was refrained from due to health considerations.

In conclusion, it should be noted that the impact of experimental shortcomings explained in this paragraph is limited to certain regions where high spatial and temporal gradients occur. However, this does not affect the quality of measurement data in greater outlet distance upon which the major findings of this work are based.

5

Discussion

In this chapter, I discuss the major results reported in the research articles accompanying this thesis in light of the objectives defined in chapter 1. Thus, emphasis is put on findings that enable progress in the field of active separation control.

5.1 The flow generated by a pulsed-jet actuator

Article 1 was dedicated to the fundamental properties of PJA-generated pulsed jets emitted into quiescent ambience. It was suggested that during the jet initiation, the lateral and axial velocity components are of the same order of magnitude in the near-outlet region. This results in a significant outward-directed deflection of the ejected vorticity layer and substantial entrainment of surrounding fluid. It was argued that this effect is mainly due to the temporary presence of over-pressure inside the jet exit plane, which is indeed required for any non-zero radial velocity from an analytical standpoint [122]. A secondary explanation (that does not disprove the effect of over-pressure) lies in the occurrence of axis-switching. This phenomenon describes the expansion of the vortex ring minor axis while, at the same time, the major axis contracts. Thus, the original minor axis becomes the major axis, and vice versa, and several self-induced deformations may follow in an oscillatory fashion. Axis-switching has been observed in non-circular starting jets [163–165], such as the one addressed in this work. Here, the longer outlet dimension coincides with the original major axis of the vortex ring, and the first transition may be reflected in the observed expansion along the smaller outlet dimension that is particularly noticeable in figure 6(a) of the paper. No second transition is observed in the current study as the oscillation wave-length is known to increase both with the outlet aspect ratio [163, 166] as well as core thickness [130, 167], both of which are relatively large in the present study. It is therefore assumed that vortex rings become incoherent prior to a potential second transition. Overall, axis-switching is known to enhance the entrainment of jets [168, 169], which has recently been shown for the case of a synthetic-jet actuator [170]. This beneficial behaviour appears to be reinforced by the effect of over-pressure in the present work since the lateral expansion of PJA-generated vortex rings is much larger than for those produced in a water tank where the over-pressure effect was assumed to be less significant.

The substantial entrainment discussed above directly results in larger vortex bubble volumes than for other means of vortex ring generation (figure 9 in **Article 1**). Larger vortex dimensions in turn lead to an enhanced added-mass effect that relates to the Lagrangian fluid drift induced by the vortex ring [123], analogous to the motion of a solid body propagating in irrotational flow [171]. To set this large volume of fluid into unsteady vortical motion, a substantial pressure contribution to the overall impulse provided to the flow field is required, suggesting that the generation of a leading vortex ring may indeed be of large relative importance in terms of the manipulation inflicted on the flow field [172]. This was also the primary motivation for assessing the concept of a formation number in the case of PJA-generated jets (**Q1** in chapter 1). However, it was shown that such a time scale is not well-defined in the present context since there is no pinch-off between the leading vortex ring and the trailing jet. Nonetheless, dimensionless pulse durations maximising the vortex ring circulation have been established. They were found to be larger than the value reported by Gharib et al. (1998), which was argued to be the case due to the capability of generating vortex rings with thicker cores (i.e., smaller non-dimensional energies $\alpha = E/(\Gamma^{3/2}I^{1/2})$). The inter-relation between the invariants of motion and the formation number was recently taken up by Krieg & Mohseni (2021) [173]. They argue that pinch-off occurs once the induced convective velocity associated with the vortex ring exceeds a characteristic velocity of the trailing jet. The latter is approximated by the maximum achievable velocity in a fully-developed pipe flow being twice the feeding velocity (i.e., approximately $2u_\text{jet}$). The induced velocity, on the other hand, can be estimated with some simplifications based on the circulation and impulse of the vortex ring so that the following kinematic criterion is suggested for pinch-off:

$$\sqrt{\frac{\varrho\pi\Gamma^3}{4I}} \geq 2u_\text{jet}. \tag{5.1}$$

It follows that the formation number (and vortex ring energy) can be altered by changing the ratio between circulation and impulse which is realised using different nozzle geometries that essentially yield varied outlet velocity profiles in Ref. [173]. Alternatively, a time-dependent feeding velocity can be provided. Thus, an accelerating exit velocity that is adapted to the increasing velocity induced by the vortex ring (left-hand side in equation (5.1)) is shown to result in much thicker vortex rings in the study mentioned above, up to a maximum theoretical thickness associated with Hill's vortex. This proves that limiting non-dimensional vortex ring energies other than $\alpha_\text{lim} \approx 0.33$ introduced in chapter 1 can be produced even in the case of a piston-cylinder setup. Interestingly, a vortex core thickness corresponding to Hill's vortex was also observed in the current study. Indeed, it may be argued that the *axial* component of the jet velocity increases during the jet emission in a similar fashion as the velocity program mentioned above as a certain time response can be expected subsequent to the opening of the valve, compensating the increasing induced velocity of the growing vortex ring and enabling the prolonged process of vorticity feeding presented in **Article 1**. Furthermore, the criterion stated in equation (5.1) provides an explanation as to why the convective velocity associated with elongated slots is lower than for circular vortex rings [133]. Consider a circular outlet with a diameter equal to the width of a slot-like outlet. At a given centreline velocity, the rate of circulation production is similar for both types of outlets. However, the impulse provided

by the slot is much larger due to the larger outlet area, resulting in a substantially reduced convective velocity according to equation (5.1). This theoretical explanation is in line with the observed longer residence time of vortex rings near such outlets and the absence of a pinch-off in the current work and for similar outlet geometries [134].

Although the flow configuration investigated in **Article 1** differs from the scenario usually found in active separation control, some important conclusions can be drawn. First, the pulsatile ejection of fluid by means of a PJA leads to the generation of large-scale vortex rings with high entrainment rates followed by a trailing jet. And second, a pressure contribution arises from the rapid initiation of fluid, affecting the outlet velocity profile and thereby, the effect of pulsed jets on the surrounding flow field.

Article 2 constitutes an intermediate step between the investigation of pulsed jets in quiescent ambience and their inclined introduction into a boundary-layer. Compared to smaller jet emission angles, no momentum flux is directly supplied in the direction of the cross-flow in the case of transverse jets ($\varphi = 90°$). Accordingly, the near-wall flow must be energised by shifting high-momentum fluid, which can be achieved through large-scale vortex structures (i.e., with a function pricinple similar to that of passive vortex generators [174–176] inducing strands of streamwise vorticity that entrain fluid from the outer flow). In fact, comparable flow structures (here, a counter-rotating vortex pair) are found in the trailing part of pulsed jets generated with a PJA (figure 13). A further characteristic of transverse jets is the blocking effect they impose on the flow upstream of the outlet. This leads to a deceleration of the cross-flow that may be desired in some applications [177] but is typically considered detrimental in active separation control. Therefore, I will not attempt to infer direct conclusions regarding the effectivity of PJA-generated pulsed jets injected into a boundary-layer as studied in **Article 2**. However, some further fundamental conclusions regarding the generation of large-scale vortices can be drawn.

It was shown that the topology of eventual vortex structures is governed by the process of vorticity cancellation (boundary-layer vs. jet shear-layer). In the current setup, the vorticity on the windward side of the jet only persisted the interaction with the boundary-layer for velocity ratios larger than a transitional value of $r \approx 4$. However, it is conceivable that this value is specific to the studied combination of the incoming boundary-layer and the outlet width. Even though a larger outlet dimension *a priori* does not result in an enhanced vorticity flux, an increased jet core region may be associated with a reduced decay [178], thereby feeding the shear-layer for a prolonged duration. The findings of **Article 1** also suggest that the vorticity production in the case of a PJA is enhanced through an additional pressure contribution, suggesting that the boundary-layer vorticity may be dominated by choosing operating parameters that result in more substantial over-pressure.

Depending on the velocity ratio being smaller/larger than the transitional value, different vortex structures develop with potential applications briefly mentioned in the following. For sufficiently large velocity ratios, asymmetrical vortex rings are observed. Assuming that their circulation is important to certain applications, such as mixing control or the reattachment of a separated shear-layer, the effect of the pulse duration is revealed in **Article 2**. Consistent with results presented in Ref. [136], the formation time maximising the vortex ring circulation

decreases with the velocity ratio (down to $L/d_{\text{eq}} \approx 7$ for $r \approx 5$). For velocity ratios $r < 4$, on the other hand, hairpin vortices are generated. They contain a region of spanwise vorticity that is convected in the near-wall region which may be beneficial to prevent flow separation as fluid is entrained into the boundary-layer. However, this effect was not specifically addressed in **Article 2**.

The generation of leading vortex structures in a cross-flow is revisited in **Article 3** but here, emphasis is put on the influence of the inclination/emission angle φ. It is shown that vortex rings are only produced for $\varphi = 60°$ and relatively large velocity ratios. Otherwise, pulsed jets attach to the wall where they form a vortex half-ring by rolling up in the boundary-layer. It is therefore concluded that the eventually developing flow structure depends on the capability of pulsed jets to follow the turning angle that is equal to φ. This capability in turn arises from a disbalance of static pressure between the windward and leeward side of the jet, loosely ascribed to the Coandă effect [179]. Looking at this from a different perspective, the jet does not attach to the wall when the suction effect induced on the windward side is sufficiently strong. However, vorticity is only produced on this side for relatively large velocity ratios (**Article 2**). Hence, wall-attached jets are observed for smaller jet velocities in the case of the larger turning angle. No such bifurcation behaviour is found for $\varphi = 30°$ where wall jets are generated independent of the velocity ratio.

A major finding presented in **Article 3** is that the near-wall flow is energised more effectively in the case of wall-attached jets. The smaller emission angle of $\varphi = 30°$ can therefore be considered more appropriate for active separation control, and there is no obvious caveat with choosing even smaller angles that may ensure the wall attachment to a greater extent even in the case of an adverse pressure gradient (in fact, it was shown in **Article 5** that the jet characteristics in some outlet distance are independent of the nozzle geometry).

It was then argued that the over-pressure effect, already discussed in relation to **Article 1**, also enhances the impulse supplied to the flow as an additional source term

$$I_{\text{p}} = \int\limits_{0}^{t_{\text{p}}} \int\limits_{A_{\text{out}}} (p - p_\infty)\mathrm{d}A\mathrm{d}t \tag{5.2}$$

arises. Since the pressure contribution was shown to be substantial, it should be taken into account when assessing the control authority associated with PJAs. This could be realised by incorporating equation (5.2) in the momentum coefficient,

$$c_\mu(t) = \frac{I_{u,\text{jet}}(t) + I_{\text{p}}(t)}{qL_{\text{c}}}, \tag{5.3}$$

which was already suggested for under- and over-expanded jets [180]. However, no attempt has been made in the current work to quantify $I_p(t)$, and it should be noted that its experimental determination is anything but trivial. Two possible approaches can be envisaged. First, the time-dependent pressure distribution in the jet exit plane can be determined by considering the jet kinematics according to Krieg & Mohseni (2013):

$$p(r) = p_\infty - \frac{\varrho}{2}v(r)^2 + \varrho \int\limits_r^{R_\infty} \left(u\frac{\partial v}{\partial x} + \frac{\partial v}{\partial t} \right) \mathrm{d}\bar{\omega} \tag{5.4}$$

where r is the radial coordinate and $\bar{\omega}$ is a dummy variable for the radius of integration. Hence, pressure distributions can be inferred from the velocity gradient field. However, an accurate measurement of the velocity gradient field was not possible in the current work due to the millimetre-scale outlet and the lack of scalability of the PJA under consideration. Therefore, a numerical simulation appears to be the only reliable approach to obtaining the pressure distribution.

An alternative method lies in the measurement of the gross impulse due to over-pressure. To this end, the actuator must be mounted on a scale that measures the thrust due to the jet emission which can be related to the impulse supplied to the flow. This procedure was followed by Krueger & Gharib (2003) to measure the impulse per pulsed jet generated with a piston-cylinder setup (Figure 5.1). They noted that for stroke ratios smaller than the formation number (i.e., $L/D < 4$), the total impulse increases by an extent that is larger than can be explained based on the ejected momentum flux. For larger L/D, on the other hand, the slope is reduced as no further increase of the vortex size is achieved and the relative contribution attributed to the acceleration of entrained and added mass through the leading vortex ring is marginalised with increasing length of the trailing jet.
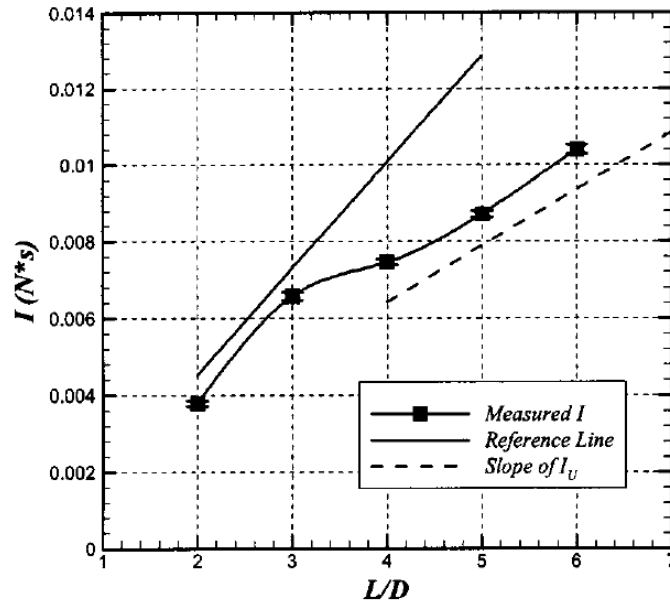

Figure 5.1: Impulse supplied to the flow by pulsatile ejection of different amounts of fluid, based on figure in Ref. [172]

Similarly, the (time-dependent) thrust exerted by a PJA can be measured. However, the experimental procedure is complicated by relatively small expected forces on the order of a couple of milli-Newton and the required sub-millisecond temporal resolution. The former aspect at least can be handled by considering multiple PJAs, for instance installed in a model and mounted on a balance as suggested in [103].

Finally, it is worth mentioning that, to some degree, the over-pressure effect discussed above is linked to the function principle of PJAs where the flow duct is periodically blocked for certain durations. During this time, the fluid is slowed down upstream of the valve and a pressure compatible with the requirement to accelerate a certain amount of mass once the valve is opened develops. A comparable acceleration of fluid is typically not at hand for fluidic devices. Hence, I assume that the over-pressure effect is less significant for these types of actuators. Synthetic-jet actuators, on the other hand, are known to exhibit an over-pressure phenomenon similar to the one observed in the current work [181, 182].

To summarise the results of the first part of this thesis, the flow generated with the specific device under consideration was shown to be characterised by a leading vortex structure. Despite the slot-like outlet geometry, this vortex has an almost spherical shape in the absence of a cross-flow due to substantial lateral expansion rates. When injected into an external stream, pulsed jets either penetrate through the boundary-layer, generating asymmetrical vortex rings, or attach to the wall where vortex half-rings can be observed. It was argued that the latter type of flow structure, occurring at small jet emission angles, is better suited to prevent boundary-layer separation. Here, the energisation of the near-wall flow is driven by three mechanisms (**Q2** in chapter 1). First, low-momentum fluid is shifted away from the wall through the leading vortex half-ring. Second, the wall jet enhances the momentum flux. And third, high-momentum fluid from the outer flow is entrained towards the wall on the jet trailing part. The amount of fluid required to generate maximum-circulation vortex structures corresponds to equivalent stroke ratios of $\mathcal{O}(L/d_{\mathrm{eq}}) = 10$ for all configurations. In the second part of this thesis, it was assessed whether this time scale may prove useful in the choice of actuation parameters.

5.2 Guidelines for active separation control

While the first part of this work was dedicated to shedding some light on the fundamental properties of PJA-generated jets, the focus was shifted to issues that may be considered more relevant to separation control applications in the second part.

In **Article 4**, implications of adjusting the two time scales defining the forcing signal (t_{p} and t_{off}) were addressed. In combination with the jet velocity, these parameters govern the control authority as well as the mass flow consumption. It was shown that knowledge of two flow-inherent threshold values is required to reliably control boundary-layer separation in the current setup. First, c_μ must be set sufficiently large as to completely eliminate the region of reverse-flow at the downstream end of the control domain. And second, t_{off} must be chosen so that the characteristic separation time is not exceeded because otherwise, reverse flow invariably occurs (independent of c_μ). It is important to note that these two criteria do not define the pulse duration t_{p}. In fact, the observed strict dependence of the control authority on the well-established parameter c_μ raises doubts regarding the usefulness of a time scale that governs the maximum vortex circulation identified in the first part of this thesis. It was even shown that particularly small pulse durations have a negligible, or even adverse, effect on the pressure distribution, which was explained by the importance of the trailing wall jet (**Q2**).

The approach proposed in **Article 4** is primarily based on the finding that the boundary-layer relaxation process is governed by a constant time scale (**Q3** in chapter 1), which is consistent with findings reported in Ref. [87]. It is worth noting that the exploitation of this characteristic separation time may not necessarily require the specific perturbations generated with a PJA. In fact, the only precondition is the possibility to adjust t_{off} which may be readily facilitated by synthetic-jet and also plasma actuators. Even for sweeping-jet devices, a time delay between the momentum addition to a given location can be established. Hence, adopting the approach established in **Article 4** would essentially result in an adjustment of the (mass flow-dependent) sweeping frequency which may enable efficiency enhancements for these devices as well.

The results presented in **Article 4** also suggest that the control authority is not explicitly governed by the reduced forcing frequency, confirming the relative insensitivity towards this parameter previously determined for pulsed-jet actuation [44]. This can be explained by the PJA operation principle that does not rely on the excitation of flow-inherent instabilities for which a reduced frequency of $F_{\text{opt}}^+ = 1$ has been suggested [95]. In fact, the investigated scenario does not involve a separated shear-layer at the location of momentum addition as the target is to prevent boundary-layer separation in the first place. For this type of configuration, even larger frequencies have been suggested in the literature [25], which was not confirmed in the present work where the desired control authority was also reached at substantially lower frequencies ($F^+ < 1$).

An important issue not addressed in much detail is the occurrence of high dynamical loads that may be viewed detrimental in technical applications. These arise from two contributors: first, the periodic generation of thrust due to jet ejection; second, fluctuations of the pressure distribution due to the manipulation of the flow field. The latter source in particular is enforced by increasing t_{off} (or reducing the actuation frequency). Seifert et al. (1996) showed that lift oscillations on the order of $\pm 3\%$ may occur on a NACA 0015 airfoil due to periodic excitation, which they considered 'not large'. However, more subtantial fluctuations (up to 50%) have been reported recently in the case of single-pulse jets generated with a PJA for the same type of airfoil [183]. The pulse delay for the latter scenario can be regarded as $t_{\text{off}} \to \infty$, hinting at the significance of the time delay between pulses for the control of dynamic loads. Future implementations must therefore weigh up the benefits associated with mass flow savings and the need to limit transient loads.

Furthermore, the efficiency assessment carried out in **Article 4** was solely based on the mass flow consumption. A further energy source, namely the pressure supply, was not considered. Indeed, the following dilemma unfolds: at constant c_μ, mass flow can be saved by reducing the duty cycle. At the same time, the required supply pressure increases. In other words, the beneficial effects associated with low duty cycles presented in **Article 4** invariably come at the expense of a larger supply pressure. Again, this issue must be revisited taking into account the specific boundary conditions of the application in question. It should also be noted that fluidic actuators tend to require a smaller supply pressure while synthetic-jet actuators do not need a pressure supply at all.

Finally, **Article 5** was dedicated to establishing models for PJA-generated wall jets. The motivation from a separation control perspective lies in the finding that this flow structure may be considered the major contributor to the overall control authority as shown in **Article 4**. As the primary finding, it was noted that the scaling laws established for quasi-2D wall jets can be adapted to the flow under consideration in the present work. Thus, power law constants could be established, describing the spreading rate as well as the decay in jet velocity and wall shear-stress inside the pulsed wall jet. Its propagation and diffusion in turn were shown to be scalable with a velocity ratio parameter that has previously been used to describe shear-layer characteristics [184–186].

The applicability of scaling laws initially introduced in Ref. [187] was explained by a lack of lateral spreading that was observed when jets were injected into a cross-flow in the current setup. In fact, measurements indicate a distinct inward-directed mean velocity component on both sides of the jet. As to why the lateral velocity component changes sign at the end of the jet development region, no explanation is given in **Article 5**. However, the negligible transverse expansion means that the near-wall flow is only affected downstream of the jet outlet confirming results presented in **Article 3**. This may have important implications in terms of the actuator spacing in separation control, considering that a more distinct spreading rate can be expected to enable larger actuator spacings [101]. This aspect, and also the interaction between adjacent pulsed jets, should therefore be addressed in the future.

Modelling the jet diffusion, as suggested in **Article 5**, also helps to understand why the impact of pulsed jets associated with relatively small amounts of fluid is negligible in greater outlet distance, especially for small $t_{\rm p}$ [188]. Once the jet emission is stopped, the deceleration wave begins to advance with a velocity much larger than the propagation front. Therefore, the length of the wall jet, equalling the distance between these two locations, quickly decreases. This observation can lay the ground for a supplementary criterion for the pulse duration, ensuring the arrival of a non-diffused wall jet at a given outlet distance. However, a number of issues need to be resolved to render this method a practical guideline in active separation control. Thus, the effect of an adverse pressure gradient needs to be taken into account as it is easy to envisage that the empirical constants for the advancing velocities determined in **Article 5** are affected by this boundary condition. The same applies to the time delay between pulses as a shorter $t_{\rm off}$ can be expected to enhance the convective velocity.

To summarise the second part of this thesis, guidelines for the choice of actuation parameters have been established. The control authority was primarily governed by the mean momentum input, which debunked our initial hypothesis based on the assumption that the effectivity is mainly driven by large-scale leading vortices. Instead, the trailing wall-attached jet was shown to be of overriding importance in terms of the control authority, demanding a pulse duration that exceeds the characteristic formation time of the leading vortex. As the second time scale, the duration between successive pulses needs to be adapted to the characteristic separation time of the flow. Considerable proof has been presented that these guidelines lead to systematic and substantial mass flow savings when the duty cycle is reduced. I therefore hope that the findings presented in this work pave the way for more efficient separation control applications in the future.

References

[1] G. V. Lachmann. **Boundary layer and flow control**. **1**. Pergamon Press, Oxford, 1961.

[2] G. V. Lachmann. **Boundary layer and flow control**. **2**. Pergamon Press, Oxford, 1961.

[3] M. G. el Hak and D. M. Bushnell. **Separation control: Review**. *J. Fluids Eng.*, **113**(1):5–30, 1991. `doi:10.1115/1.2926497`.

[4] R. L. Simpson. **Turbulent boundary-layer separation**. *Annu. Rev. Fluid Mech.*, **21**:205–232, 1989. `doi:10.1146/annurev.fl.21.010189.001225`.

[5] L. Prandtl. **Über Flüssigkeitsbewegung bei sehr kleiner Reibung**. *Verhandlungen des III. Internationalen Mathematiker-Kongresses*, pages 484–491, 1904.

[6] L. Prandtl. **The mechanics of viscous fluids**. In W. F. Durand, editor, *Aerodynamic Theory*, **3**, pages 759–760. Springer, Berlin, 1935.

[7] H. Schlichting. **Einige neuere Ergebnisse über Grenzschichtbeeinflussung**. In T. von Kármán, editor, *Advances in Aeronautical Sciences: Proceedings of the First International Congress in the Aeronautical Sciences*, **2**, pages 563–586. Pergamon Press, London, 1959.

[8] E. Truckenbrodt. **Ein einfaches Näherungsverfahren zum Berechnen der laminaren Reibungsschicht mit Absaugung**. *Forschg. Ing.-Wes.*, **22**:147–157, 1956.

[9] C. V. Seal and C. R. Smith. **The control of turbulent end-wall boundary layers using surface suction**. *Exp. Fluids*, **27**:484–496, 1999. `doi:10.1007/s003480050373`.

[10] W.-L. Chen, H. Li, and H. Hu. **An experimental study on a suction flow control method to reduce the unsteadiness of the wind loads acting on a circular cylinder**. *Exp. Fluids*, **55**, 2014. `doi:10.1007/s00348-014-1707-7`.

[11] E. D. Poppleton. **Boundary layer control for high lift by suction of the leading-edge of a 40 degree swept-back wing**. *Tech. Rep. RM 2897. ARC.*, 1955.

[12] M. A. Karim and M. Acharya. **Suppression of dynamic stall vortices over pitching airfoils by leading-edge suction**. *AIAA J.*, **32**:1647–1655, 1994. `doi:10.2514/3.12155`.

[13] M. Alrefai and M. Acharya. **Controlled leading-edge suction for management of unsteady separation pitching airfoils.** *AIAA J.*, **43**:2327–2336, 1996. `doi:10.2514/3.13398`.

[14] H. Atik, C.-Y. Kim, L. L. van Dommelen, and J. D. A. Walker. **Boundary-layer separation control on a thin airfoil using local suction**. *J. Fluid Mech.*, **535**:415–443, 2005. `doi:10.1017/S002211200500501X`.

[15] D. Greenblatt, K. B. Paschal, C.-S. Yao, J. Harris, N. W. Schaeffler, and A. E. Washburn. **Experimental investigation of separation control part 1: Baseline and steady suction**. *AIAA J.*, **44**:2820–2830, 2006. `doi:10.2514/1.13817`.

REFERENCES

[16] L. B. GRATZER. **Analysis of transport applications for high-lift schemes**. In P. E. COLIN AND J. WILLIAMS, editors, *GARD Course on Assessment of Lift Augmentation Devices*. Rhode-Saint-Genese, 1971.

[17] W. H. BALL. **Tests of wall blowing concepts for diffuser boundary layer control**. In *20th Joint Propulsion Conference*, 1984. `doi:10.2514/6.1984-1276`.

[18] J. P. JOHNSTON AND M. NISHI. **Vortex generator jets - Means for flow separation control**. *AIAA J.*, **28**(6):989–994, 1990. `doi:10.2514/3.25155`.

[19] G. V. SELBY, J. C. LIN, AND F. G. HOWARD. **Control of low-speed turbulent separated flow using jet vortex generators**. *Exp. Fluids*, **12**:394–400, 1992. `doi:10.1007/BF00193886`.

[20] S. D. PETERSON AND M. W. PLESNIAK. **Flow structure and skin friction in the vicinity of a streamwise-angled injection hole fed by a short pipe**. *Exp. Fluids*, **43**:627–638, 2007. `doi:10.1007/s00348-007-0350-y`.

[21] F. COLETTI, M. J. BENSON, J. LING, C. J. ELKINS, AND J. K. EATON. **Turbulent transport in an inclined jet in crossflow**. *Int. J. Heat Fluid Flow*, **43**:149–160, 2013. `doi:10.1016/j.ijheatfluidflow.2013.06.001`.

[22] F. S. HENRY AND H. H. PEARCEY. **Numerical model of boundary-layer control using air-jet generated vortices**. *AIAA J.*, **32**(12):2415–2425, 1994. `doi:10.2514/3.12308`.

[23] C. KÜPPER AND F. S. HENRY. **Numerical study of air-jet vortex generators in a turbulent boundary layer**. *Appl. Math. Mod.*, **27**(5):359–377, 2003. `doi:10.1016/S0307-904X(02)00138-5`.

[24] I. WYGNANSKI. **Boundary layer and flow control by periodic addition of momentum**. In *4th Shear Flow Control Conference*, 1997. `doi:10.2514/6.1997-2117`.

[25] D. GREENBLATT AND I. J. WYGNANSKI. **The control of flow separation by periodic excitation**. *Prog. Aerosp. Sci.*, **36**(7):487–545, 2000. `doi:10.1016/S0376-0421(00)00008-7`.

[26] G. B. SCHUBAUER AND H. SKRAMSTAD. **Laminar boundary-layer oscillations and transition on a flat plate**. *J. Res. Natl. Bur. Stand.*, **38**:251–292, 1947. `doi:10.2514/8.1267`.

[27] I. WYGNANSKI AND R. A. PETERSON. **Coherent motion in excited free shear flows**. *AIAA J.*, **25**(2):201–213, 1987. `doi:10.2514/3.9610`.

[28] S. CROW AND F. CHAMPAGNE. **Orderly structure in jet turbulence**. *J. Fluid Mech.*, **48**:547–591, 1971. `doi:10.1017/S0022112071001745`.

[29] C.-M. HO AND L.-S. HUANG. **Subharmonics and vortex merging in mixing layers**. *J. Fluid Mech.*, **119**:443–473, 1982. `doi:10.1017/S0022112082001438`.

[30] C. O. PASCHEREIT, I. WYGNANSKI, AND H. E. FIEDLER. **Experimental investigation of subharmonic resonance in an axisymmetric jet**. *J. Fluid Mech.*, **283**:365–407, 1995. `doi:10.1017/S0022112095002369`.

[31] F. G. COLLINS AND J. ZELENEVITZ. **Influence of sound upon separated flow over wings**. *AIAA J.*, **13**(3):408–410, 1975. `doi:10.2514/3.49717`.

[32] M. NISHIOKA, M. ASAI, AND S. YOSHIDA. **Control of flow separation by acoustic excitation**. *AIAA J.*, **28**(11):1909–1915, 1990. `doi:10.2514/3.10498`.

[33] K. B. M. Q. ZAMAN. **Effect of acoustic excitation on stalled flows over an airfoil**. *AIAA J.*, **30**(6):1492–1499, 1992. `doi:10.2514/6.1990-4009`.

[34] F. TINAPP AND W. NITSCHE. **Separation control on a high-lift configuration by periodic excitation**. In *Notes on Numerical Fluid Mechanics III*, **77**, pages 42–49. Vieweg Verlag, Braunschweig, 2002.

[35] R. C. Chang. **Forcing level effects of internal acoustic excitation on the improvement of airfoil performance**. *J. Aircr.*, **29**(5):823–829, 1992. `doi:10.2514/3.46252`.

[36] T. E. Oyler and W. E. Palmer. **Exploratory investigation of pulse blowing for boundary layer control**. *Report No. NR 72H-12*, 1972.

[37] S. F. Tardu. **Active control of near-wall turbulence by local oscillating blowing**. *J. Fluid Mech.*, **439**:217–253, 2001. `doi:10.1017/S0022112001004542`.

[38] X. Q. Cheng, Z. X. Qiao, X. Zhang, M. Quadrio, and Y. Zhou. **Skin-friction reduction using periodic blowing through streamwise slits**. *J. Fluid Mech.*, **920**, 2021. `doi:10.1017/jfm.2021.439`.

[39] R. D'Andrea, R. L. Behnken, and R. M. Murray. **Active control of an axial flow compressor via pulsed air injection**. 1996. Technical Report.

[40] M. Staats. *Active flow control on a highly loaded compressor cascade with periodic nonsteady outflow conditions*. PhD thesis, Technische Universität Berlin, 2021.

[41] F. Tinapp. *Aktive Kontrolle der Strömungsablösung an einer Hochauftriebs-Konfiguration*. PhD thesis, Technische Universität Berlin, 2001.

[42] R. Petz and W. Nitsche. **Active separation control on the flap of a two-dimensional generic high-lift configuration**. *J. Aircr.*, **44**(3):865–874, 2007. `doi:10.2514/1.25425`.

[43] M. Bauer. *Design and application of a fluidic actuator system for high-lift flow control*. PhD thesis, Technische Universität Berlin, 2015.

[44] F. Haucke. *Aktive Strömungskontrolle zur Effizienzsteigerung von Hochauftriebskonfigurationen*. PhD thesis, Technische Universität Berlin, 2016.

[45] A. Seifert, A. Darabi, and I. Wygnanski. **Delay of airfoil stall by periodic excitation**. *J. Aircr.*, **33**(4):691–698, 1996. `doi:10.2514/3.47003`.

[46] B. Nishri and I. Wygnanski. **Effects of periodic excitation on turbulent flow separation from a flap**. *AIAA J.*, **36**(4):547–556, 1998. `doi:10.2514/2.428`.

[47] T. Suzuki, T. Colonius, and S. Pirozzoli. **Vortex shedding in a two-dimensional diffuser: Theory and simulation of separation control by periodic mass injection**. *J. Fluid Mech.*, **520**:187–213, 2004. `doi:10.1017/S0022112004001405`.

[48] J. Dandois, E. Garnier, and P. Sagaut. **Numerical simulation of active separation control by a synthetic jet**. *J. Fluid Mech.*, **574**:25–58, 2007. `doi:10.1017/S0022112006003995`.

[49] R. B. Kotapati, R. Mittal, O. Marxen, F. Ham, D. You, and L. N. Cattafesta III. **Nonlinear dynamics and synthetic-jet-based control of a canonical separated flow**. *J. Fluid Mech.*, **654**:65–97, 2010. `doi:10.1017/S002211201000042X`.

[50] D. Postl, W. Balzer, and H. F. Fasel. **Control of laminar separation using pulsed vortex generator jets: Direct numerical simulations**. *J. Fluid Mech.*, **667**:81–109, 2011. `doi:10.1017/jfm.2011.34`.

[51] D. M. Luchtenburg, B. Günther, B. R. Noack, R. King, and G. Tadmor. **A generalized mean-field model of the natural and high-frequency actuated flow around a high-lift configuration**. *J. Fluid Mech.*, **623**:283–316, 2009. `doi:10.1017/S0022112008004965`.

[52] R. Becker, R. King, R. Petz, and W. Nitsche. **Adaptive closed-loop separation control on a high-lift configuration using extremum seeking**. *AIAA J.*, **45**(6), 2007. `doi:10.2514/1.24941`.

REFERENCES

[53] T. Duriez, V. Parezanović, J.-C. Laurentie, C. Fourment, J. Delville, J. P. Bonnet, L. Cordier, B. R. Noack, M. Segond, M. Abel, N. Gautier, J. L. Aider, C. Raibaudo, C. Cuvier, M. Stanislas, and S. L. Brunton. **Closed-loop control of experimental shear flows using Machine Learning**. In *7th AIAA Flow Control Conference*, 2014. `doi:10.2514/6.2014-2219`.

[54] L. Henning and R. King. **Robust multivariable closed-loop control of a turbulent backward-facing step flow**. *J. Aircr.*, **44**(1):201–208, 2007. `doi:10.2514/1.22934`.

[55] N. Gautier and J.-L. Aider. **Control of the separated flow downstream of a backward-facing step using visual feedback**. *Proc. R. Soc.*, **469**(2160), 2013. `doi:10.1098/rspa.2013.0404`.

[56] S. L. Brunton, B. R. Noack, and P. Koumoutsakos. **Machine Learning for fluid mechanics**. *Annu. Rev. Fluid Mech.*, **52**:477–508, 2020. `doi:10.1146/annurev-fluid-010719-060214`.

[57] J. D. Mclean, J. D. Crouch, R. Stoner, S. Sakurai, G. E. Seidel, W. Feifel, and H. Rush. **Study of the application of separation control by unsteady excitation to civil transport aircraft**. In *NASA/CR-1999-209338*, Boeing Commercial Airplane Group, Seattle, Washington, 1999.

[58] M. Meyer, W. Machunze, and M. Bauer. **Towards the industrial application of active flow control in civil aircraft - An active highlift flap**. In *32nd AIAA Applied Aerodynamics Conference*, 2014. `doi:10.2514/6.2014-2401`.

[59] E. Moreau. **Airflow control by non-thermal plasma actuators**. *J. Phys. D: Appl. Phys.*, **40**(3):605–636, 1996. `doi:10.1088/0022-3727/40/3/s01`.

[60] D. Greenblatt, T. Schneider, and C. Y. Schüle. **Mechanism of flow separation control using plasma actuation**. *Phys. Fluids*, **24**(7), 2012. `doi:10.1063/1.4733399`.

[61] T. N. Jukes and K.-S. Choi. **On the formation of streamwise vortices by plasma vortex generators**. *J. Fluid Mech.*, **733**(370-393), 2013. `doi:10.1017/jfm.2013.418`.

[62] A. Cutler. **High-frequency pulsed combustion actuator experiments**. *AIAA J.*, **49**(9):1943–1950, 2011. `doi:10.2514/1.J050876`.

[63] L. N. Cattafesta and M. Sheplak. **Actuators for active flow control**. *Annu. Rev. Fluid Mech.*, **43**(1):247–272, 2011. `doi:10.1146/annurev-fluid-122109-160634`.

[64] F. Ostermann. *Fundamental properties of a spatially oscillating jet emitted by a fluidic oscillator*. PhD thesis, Technische Universität Berlin, 2018.

[65] B. L. Smith and A. Glezer. **The formation and evolution of synthetic jets**. *Phys. Fluids*, **10**(9), 1998. `doi:10.1063/1.869828`.

[66] J. M. Kirshner and S. Katz. *Design theory of fluidic components*. Academic Press Inc, 1975.

[67] S. W. Angrist. **Fluid control devices**. *Sc. Amer.*, **211**(6):80–89, 1964.

[68] J. W. Gregory, J. P. Sullivan, and S. Raghu. **Visualization of jet mixing in a fluidic oscillator**. *J. Vis.*, **8**(2):169–176, 2005. `doi:10.1007/BF03181660`.

[69] M. N. Tomac and J. W. Gregory. **Internal jet interactions in a fluidic oscillator at low flow rate**. *Exp. Fluids*, **55**(5), 2014. `doi:10.1007/s00348-014-1730-8`.

[70] C. E. Spyropoulos. **A sonic oscillator**. In *Proceedings of the Fluid Amplification Symposium*, pages 27–52, 1964.

[71] W. Gaylord and V. Carter. **Flueric temperature-sensing oscillator design**. HDL TR-1428, DTIC accession number AD0689444, Harry Diamond Laboratories, Washington, D.C., 1969.

[72] J. W. Gregory and M. N. Tomac. **A review of fluidic oscillator development and application for flow control**. In *43rd Fluid Dynamics Conference, AIAA*, 2013. `doi:10.2514/6.2013-2474`.

[73] D. E. Culley, M. M. Bright, P. S. Prahst, and A. J. Strazisar. **Active flow separation control of a stator vane using embedded injection in a multistage compressor experiment**. *J. Turbomach.*, **126**(1):24–34, 2004. `doi:10.1115/1.1643912`.

[74] R. Seele, P. Tewes, R. Woszidlo, M. A. McVeigh, N. J. Lucas, and I. J. Wygnanski. **Discrete sweeping jets as tools for improving the performance of the V-22**. *J. Aircr.*, **46**(6):2098–2106, 2009. `doi:10.2514/1.43663`.

[75] C. Cerretelli and K. Kirtley. **Boundary layer separation control with fluidic oscillators**. *J. Turbomach.*, **131**(4):1–9, 2009. `doi:10.1115/1.3066242`.

[76] H.-J. Schmidt, R. Woszidlo, C. N. Nayeri, and C. O. Paschereit. **Separation control with fluidic oscillators in water**. *Exp. Fluids*, **58**:1–17, 2017. `doi:10.1007/s00348-017-2392-0`.

[77] B. Steinfurth, A. Berthold, S. Feldhus, F. Haucke, and J. Weiss. **Increasing the aerodynamic performance of a Formula Student race car by means of active flow control.** *SAE Int. J. Adv. Curr. Pract. Mob.*, **1**(3), 2019. `doi:10.4271/2019-01-0652`.

[78] A. Glezer and M. Amitay. **Synthetic jets**. *Annu. Rev. Fluid Mech.*, **34**:503–529, 2002. `doi:10.1146/annurev.fluid.34.090501.094913`.

[79] R. Holman, Y. Utturkar, R. Mittal, B. L. Smit, and L. Cattafesta. **Formation criterion for synthetic jets**. *AIAA J.*, **43**(10):2110–2116, 2005. `doi:10.2514/1.12033`.

[80] T. van Buren, E. Whalen, and M. Amitay. **Vortex formation of a finite-span synthetic jet: High Reynolds numbers**. *Phys. Fluids*, **26**(1), 2014. `doi:10.1063/1.4859895`.

[81] J. Wu, X.-Y. Lu, A. G. Denny, M. Fan, and J.-M. Wu. **Post-stall flow control on an airfoil by local unsteady forcing**. *J. Fluid Mech.*, **371**:21–58, 1998. `doi:10.1017/S0022112098002055`.

[82] M. Amitay, D. R. Smith, V. Kibens, D. E. Parekh, and A. Glezer. **Aerodynamic flow control over an unconventional airfoil using synthetic jet actuators**. *AIAA J.*, **39**(3):361–370, 2001. `doi:10.2514/2.1323`.

[83] C. Lee, G. Hong, Q. P. Ha, and S. G. Mallinson. **A piezoelectrically actuated micro synthetic jet for active flow control**. *Sens. Actuator A Phys.*, **108**(1-3):168–174, 2003. `doi:10.1016/S0924-4247(03)00267-X`.

[84] M. Ciuryla, Y. Liu, J. Farnsworth, C. Kwan, and M. Amitay. **Flight control using synthetic jets on a Cessna 182 model**. *J. Aircr.*, **44**(2):642–653, 2012. `doi:10.2514/1.24961`.

[85] K. McManus and J. Magill. **Separation control in incompressible and compressible flows using pulsed jets**. In *27th AIAA Fluid Dynamics Conference*, 1996. `doi:10.2514/6.1996-1948`.

[86] D. Williams, D. Cornelius, and C. Rowley. **Supersonic cavity response to open-loop forcing**. In R. King, editor, *Active Flow Control*, pages 230–243. Springer, Berlin, 2007.

[87] J. P. Bons, R. Sondergaard, and R. B. Rivir. **The fluid dynamics of LPT blade separation control using pulsed jets**. *J. Turbomach.*, **124**:77–85, 2002. `doi:10.1115/1.1425392`.

[88] J. Ortmanns, M. Bitter, and C. J. Kähler. **Dynamic vortex structures for flow-control applications**. *Exp. Fluids*, **44**:397–408, 2008. `doi:10.1007/s00348-007-0442-8`.

[89] M. Ibrahim, R. Kunimura, and Y. Nakamura. **Mixing enhancement of compressible jets by using unsteady microjets as actuators**. *AIAA J.*, **40**(4), 2002. `doi:10.2514/2.1700`.

[90] J. Choi, A. Annaswamy, H. Lou, and F. Alvi. **Active control of supersonic impingement tones using steady and pulsed microjets**. *Exp. Fluids*, **41**(6):841–855, 2006. `doi:10.1007/s00348-006-0189-7`.

REFERENCES

[91] R. Viard, A. Talbi, P. Pernod, V. Preobrazhensky, and A. Merlen. **Magnetostatic microvalve for high momentum rate pulsed jet generation**. *Proc. Chem.*, **1**(1):421–424, 2009. `doi:10.1016/j.proche.2009.07.105`.

[92] P. Pernod, V. Preobrazhensky, A. Merlen, O. Ducloux, A. Talbi, L. Gimeno, R. Viard, and N. Tiercelin. **MEMS magneto-mechanical microvalves (MMMS) for aerodynamic active flow control**. *J. Magn. Magn. Mater.*, **322**:1642–1646, 2010. `doi:10.1016/j.jmmm.2009.04.086`.

[93] R. Viard, A. Talbi, C. Ghouila-Houri, A. Kourta, A. Merlen, and P. Pernod. **Magneto-mechanical micro-valve for active flow control**. *Sens. Actuator A Phys.*, **316**, 2020. `doi:10.1016/j.sna.2020.112387`.

[94] D. Greenblatt, B. Nishri, A. Darabi, and I. Wygnanski. **Some parameters affecting stall control with particular emphasis on dynamic stall**. In *30th AIAA Fluid Dynamics Conference*, 1999. `doi:10.2514/6.1999-3504`.

[95] I. Wygnanski. **The variables affecting the control of separation by periodic excitation**. In *2nd AIAA Flow Control Conference*, 2004. `doi:10.2514/6.2004-2505`.

[96] A. Seifert, T. Bachar, D. Koss, M. Shepshelovich, and I. Wygnanski. **Oscillatory blowing: A tool to delay boundary layer separation**. *AIAA J.*, **31**(11):2052–2060, 1993. `doi:10.2514/3.49121`.

[97] D. A. Compton and J. P. Johnston. **Streamwise vortex production by pitched and skewed jets in a turbulent boundary layer**. *AIAA J.*, **30**(3), 1992. `doi:10.2514/3.10967`.

[98] I. M. Milanovic and K. B. M. Q. Zaman. **Fluid dynamics of highly pitched and yawed jets in crossflow**. *AIAA J.*, **42**(5):874–882, 2004. `doi:10.2514/1.2924`.

[99] Y.-Y. Feng, Y.-P. Song, and R. E. Breitenthal. **Model of the trajectory of an inclined jet in incompressible crossflow**. *AIAA J.*, **56**(2):458–464, 2018. `doi:10.2514/1.J056181`.

[100] R. Woszidlo. *Parameters governing separation control with sweeping jet actuators*. PhD thesis, The University of Arizona, 2011.

[101] C. Otto, P. Tewes, J. C. Little, and R. Woszidlo. **Comparison between fluidic oscillators and steady jets for separation control**. *AIAA J.*, **57**(12):5220–5228, 2019. `doi:10.2514/1.J058081`.

[102] P. Poisson-Quinton. **Recherches théoriques et expérimentales sur le contrôl de couche limits**. In *International Congress of Applied Mechanics*, 1948.

[103] J. S. Attinello. **Design and engineering features of flap blowing installations**. In G. V. Lachmann, editor, *Boundary layer and flow control*, **1**. Pergamon Press, 1961.

[104] D. Oster, I. Wygnanski, B. Dziomba, and H. Fiedler. **The effect of initial conditions on the two-dimensional turbulent mixing layer**. In H. Fiedler, editor, *Structure and Mechanics of Turbulence*. Springer, 1978.

[105] F.-B. Hsiao, R.-N. Shyu, and R. C. Chang. **High angle of attack airfoil performance improvement by internal acoustic excitation**. *AIAA J.*, **32**(3):655–657, 1994. `doi:10.2514/3.12034`.

[106] A. Seifert, S. Eliahu, D. Greenblatt, and I. Wygnanski. **Use of piezoelectric actuators for airfoil separation control**. *AIAA J.*, **36**(8):1535–1537, 1998. `doi:10.2514/2.549`.

[107] M. Amitay, V. Kibens, D. Parekh, and A. Glezer. **The dynamics of flow reattachment over a thick airfoil controlled by synthetic jet actuator**. In *37th Aerospace Sciences Meeting and Exhibit*, 1999. `doi:10.2514/6.1999-1001`.

[108] K. R. McManus, P. B. Joshi, H. H. Legner, and S. J. Davisl. **Active control of aerodynamic stall using pulsed jet actuators**. In *26th AIAA Fluid Dynamics Conference*, 1996. `doi:10.2514/6.1995-2187`.

[109] K. D. Hipp, M. M. Walker, S. I. Benton, and J. P. Bons. **Control of poststall airfoil using leading-edge pulsed jets**. *AIAA J.*, **55**(2), 2017. doi:10.2514/6.2016-1822.

[110] A. Vakilii. **Review of vortical flow utilization**. In *16th Aerodynamic Ground Testing Conference*, 1990. doi:10.2514/6.1990-1429.

[111] K. Shariff and A. Leonard. **Vortex rings**. *Annu. Rev. Fluid Mech.*, **24**:235–279, 1992. doi:10.1146/annurev.fl.24.010192.001315.

[112] D. I. Pullin. **Vortex ring formation at tube and orifice openings**. *Phys. Fluids*, **25**(3):401–403, 1979. doi:10.1063/1.862606.

[113] N. Didden. **On the formation of vortex rings: Rolling-up and production of circulation**. *Z. Angew. Math. Phys.*, **30**:101–116, 1979. doi:10.1007/BF01597484.

[114] D. Auerbach. **Experiments on the trajectory and circulation of the starting vortex**. *J. Fluid Mech.*, **183**:185–198, 1987. doi:10.1017/S0022112087002593.

[115] M. Gharib, E. Rambod, and K. Shariff. **A universal time scale for vortex ring formation.** *J. Fluid Mech.*, **360**:121–140, 1998. doi:10.1017/S0022112097008410.

[116] K. Mohseni and M. Gharib. **A model for universal time scale of vortex ring formation**. *Phys. Fluids*, **10**(10), 1998. doi:10.1063/1.869785.

[117] M. Rosenfeld, E. Rambod, and M. Gharib. **Circulation and formation number of laminar vortex rings**. *J. Fluid Mech.*, **376**:297–318, 1998. doi:10.1017/S0022112098003115.

[118] R. Sau and K. Mahesh. **Passive scalar mixing in vortex rings**. *J. Fluid Mech.*, **582**:449–461, 2007. doi:10.1017/S0022112007006349.

[119] P. S. Krueger, J. O. Dabiri, and M. Gharib. **The formation number of vortex rings in uniform background coflow**. *J. Fluid Mech.*, **556**:1271–1281, 2006. doi:10.1017/S0022112006009347.

[120] C. O'Farrell and J. O. Dabiri. **Pinch-off of non-axisymmetric vortex rings**. *J. Fluid Mech.*, **740**:61–96, 2014. doi:10.1017/jfm.2013.639.

[121] M. Nitsche and R. Krasny. **A numerical study of vortex ring formation at the edge of a circular tube**. *J. Fluid Mech.*, **276**:139–161, 1994. doi:10.1017/S0022112094002508.

[122] M. Krieg and K. Mohseni. **Modelling circulation, impulse and kinetic energy of starting jets with non-zero radial velocity**. *J. Fluid Mech.*, **719**:488–526, 2013. doi:10.1017/jfm.2013.9.

[123] J. O. Dabiri. **Note on the induced Lagrangian drift and added-mass of a vortex**. *J. Fluid Mech.*, **547**:105–113, 2006. doi:10.1017/S0022112005007585.

[124] P. S. Krueger. **An over-pressure correction to the slug model for vortex ring circulation**. *J. Fluid Mech.*, **545**:427–443, 2005. doi:10.1017/S0022112005006853.

[125] I. Choutapalli, A. Krothapalli, and J. H. Arakeri. **An experimental study of an axisymmetric turbulent pulsed air jet**. *J. Fluid Mech.*, **631**:23–63, 2009. doi:10.1017/S0022112009007009.

[126] L. A. Ruiz, R. W. Whittlesey, and J. O. Dabiri. **Vortex-enhanced propulsion**. *J. Fluid Mech.*, **668**:5–32, 2011. doi:10.1017/S0022112010004908.

[127] A. B. Olcay and P. S. Krueger. **Momentum evolution of ejected and entrained fluid during laminar vortex ring formation**. *Theor. Comp. Fluid Dyn.*, **24**:465–482, 2010. doi:10.1007/s00162-009-0173-y.

[128] K. Bremhorst and P. G. Hollis. **Velocity field of an axisymmetric pulsed, subsonic air jet**. *AIAA J.*, **28**(12):2043–2049, 1990. doi:10.2514/3.10520.

REFERENCES

[129] S. C. SHADDEN, J. O. DABIRI, AND J. E. MARSDEN. **Lagrangian analysis of fluid transport in empirical vortex ring flows**. *Phys. Fluids*, **18**(4), 2006. `doi:10.1063/1.2189885`.

[130] F. F. GRINSTEIN. **Self-induced vortex ring dynamics in subsonic rectangular jets**. *Phys. Fluids*, **7**(10):2519–2521, 1995. `doi:10.1063/1.868699`.

[131] F. F. GRINSTEIN AND C. R. DEVORE. **Dynamics of coherent structures and transition to turbulence in free square jets**. *Phys. Fluids*, **8**(5):1237–1251, 1996. `doi:10.1063/1.868895`.

[132] J. J. AI, S. C. M. YU, A. W.-K. LAW, AND L. P. CHUA. **Vortex dynamics in starting square water jets**. *Phys. Fluids*, **8**(5), 2005. `doi:10.1063/1.1823532`.

[133] Y. D. AFANASYEV. **Formation of vortex dipoles**. *Phys. Fluids*, **18**, 2006. `doi:10.1063/1.2182006`.

[134] G. PEDRIZZETTI, F. DOMENICHINI, AND G. TONTI. **On the left ventricular vortex reversal after mitral valve replacement**. *Ann. Biomed. Eng.*, **38**(3):769–773, 2010. `doi:10.1007/s10439-010-9928-2`.

[135] C. O'FARRELL AND J. O. DABIRI. **Perturbation response and pinch-off of vortex rings and dipoles**. *J. Fluid Mech.*, **704**:280–300, 2012. `doi:10.1017/jfm.2012.238`.

[136] R. SAU AND K. MAHESH. **Dynamics and mixing of vortex rings in crossflow**. *J. Fluid Mech.*, **604**:389–409, 2008. `doi:10.1017/S0022112008001328`.

[137] Y. K. CHANG AND A. D. VAKILI. **Dynamics of vortex rings in crossflow**. *Phys. Fluids*, **7**(7):1583–1597, 1995. `doi:10.1063/1.868545`.

[138] A. EROGLU AND R. E. BREIDENTHAL. **Structure, penetration, and mixing of pulsed jets in crossflow**. *AIAA J.*, **39**(3):842–850, 2001. `doi:10.2514/2.1351`.

[139] H. JOHARI. **Scaling of fully pulsed jets in crossflow**. *AIAA J.*, **44**(11):842–850, 2006. `doi:10.2514/1.18929`.

[140] D. C. MCCORMICK. **Boundary layer separation control with directed synthetic jets**. In *38th Aerospace Sciences Meeting and Exhibit*, 2000. `doi:10.2514/6.2000-519`.

[141] M. HECKLAU, D. P. SALAZAR, AND W. NITSCHE. **Influence of the actuator jet angle on the reattachment process with pulsed excitation**. *Notes on Numerical Fluid Mechanics and Multidisciplinary Design*, **121**, 2010.

[142] M. RAFFEL, C. E. WILLERT, F. SCARANO, C. J. KÄHLER, AND S. T. WERELEY. *Particle image velocimetry - A practical guide*. Springer, Cham, Switzerland, 3 edition, 2018.

[143] J. KASTEN, C. PETZ, I. HOTZ, H.-C. HEGE, B. R. NOACK, AND G. TADMOR. **Lagrangian feature extraction of the cylinder wake**. *Phys. Fluids*, **22**, 2010. `doi:10.1063/1.3483220`.

[144] F. LEKIEN AND S. D. ROSS. **The computation of finite-time Lyapunov exponents on unstructured meshes and for non-Euclidean manifolds**. *Chaos*, **20**, 2010. `doi:10.1063/1.3278516`.

[145] K. MULLENERS AND M. RAFFEL. **Dynamic stall development**. *Exp. Fluids*, **54**(1469), 2013. `doi:10.1007/s00348-013-1469-7`.

[146] S. N. GADDE AND S. VENGADESANI. **Lagrangian coherent structures in tandem flapping wing hovering**. *J. Bionic Eng.*, **14**:307–316, 2017. `doi:10.1016/s1672-6529(16)60399-2`.

[147] G. HALLER. **Distinguished material surfaces and coherent structures in three-dimensional fluid flows**. *Physica D*, **149**:248–277, 2001. `doi:10.1016/S0167-2789(00)00199-8`.

[148] G. HALLER. **Lagrangian coherent structures from approximate velocity data**. *Phys. Fluids*, **14**(6):1851–1861, 2002. `doi:10.1063/1.1477449`.

[149] B. Steinfurth and F. Haucke. **Coherent structures in the actively controlled wake of a high-lift configuration**. *AIAA J.*, **56**(10):1–9, 2018. `doi:10.2514/1.J057094`.

[150] H. Akima. **A new method of interpolation and smooth curve fitting based on local procedures.** *J. ACM*, **17**(4):589–602, 1970. `doi:10.1145/321607.321609`.

[151] A. M. Mancho, D. Small, S. Wiggins, and K. Idel. **Computation of stable and unstable manifolds of hyperbolic trajectories in two-dimensional, aperiodically time-dependent vector fields**. *Physica D*, **182**:188–222, 2003. `doi:10.1016/S0167-2789(03)00152-0`.

[152] C. Garth, F. Gerhardt, X. Tricoche, and H. Hagen. **Efficient computation and visualization of coherent structures in fluid flow applications**. *IEEE Trans. Vis. Comput. Graph.*, **13**, 2007. `doi:10.1109/TVCG.2007.70551`.

[153] S. L. Brunton and C. W. Rowley. **Fast computation of finite-time Lyapunov exponent fields for unsteady flows**. *Chaos*, **20**, 2010. `doi:10.1063/1.3270044`.

[154] S. Barakat, C. Garth, and X. Tricoche. **Interactive computation and rendering of finite-time Lyapunov exponent fields**. *IEEE Trans. Vis. Comput. Graph.*, **18**, 2012. `doi:10.1109/tvcg.2012.33`.

[155] C. Conti, D. Rossinelli, and P. Koumoutsakos. **GPU and APU computations of finite-time Lyapunov exponent fields**. *J. Comput. Phys.*, **231**, 2012. `doi:10.1016/j.jcp.2011.10.032`.

[156] M. P. Rockwood, T. Loiselle, and M. A. Green. **Practical concerns of implementing a finite-time Lyapunov exponent analysis with under-resolved data**. *Exp. Fluids*, **60**, 2019. `doi:10.1007/s00348-018-2658-1`.

[157] R. Semaan. **The uncertainty of the experimentally-measured momentum coefficient**. *Exp. Fluids*, **61**, 2020. `doi:10.1007/s00348-020-03076-5`.

[158] J. Westerweel. **On velocity gradients in PIV interrogation**. *Exp. Fluids*, **44**:831–842, 2008. `doi:10.1007/s00348-007-0439-3`.

[159] R. J. Adrian. **Statistical properties of particle image velocimetry measurements in turbulent flow**. In R. J. A. et al., editor, *Laser anemometry in fluid mechanics*, **3**, pages 115–129. Lisbon, 1988.

[160] R. D. Keane and R. J. Adrian. **Optimization of particle image velocimeters. I. Double pulsed systems**. *Mea. Sci. Technol.*, **1**(11):1202–1215, 1992. `doi:10.1088/0957-0233/1/11/013`.

[161] D. Ragni, F. Schrijer, B. W. van Oudheusden, and F. Scarano. **Particle tracer response across shocks measured by PIV**. *Exp. Fluids*, **50**(1), 2011. `doi:10.1007/s00348-010-0892-2`.

[162] M. Samimy and S. K. Lele. **Motion of particles with inertia in a compressible free shear layer**. *Phys. Fluids*, **3**(8):1915–1923, 1991. `doi:10.1063/1.857921`.

[163] R. J. Arms and F. R. Hama. **Localized-induction concept on a curved vortex and motion of an elliptic vortex ring**. *Phys. Fluids*, **8**(4), 1965. `doi:10.1063/1.1761268`.

[164] H. Viets and P. M. Sforza. **Dynamics of bilaterally symmetric vortex rings**. *Phys. Fluids*, **15**(2), 1972. `doi:10.1063/1.1693899`.

[165] M. R. Dhanak and B. D. E. Bernadinis. **The evolution of an elliptic vortex ring**. *J. Fluid Mech.*, **109**:189–216, 1981. `doi:10.1017/S0022112081001006`.

[166] Y. Oshima, N. Izutsu, K. Oshima, and A. K. M. F. Hussain. **Bifurcation of an elliptic vortex ring**. *Fluid Dyn. Res.*, **3**(1–4):133–139, 1988. `doi:10.1016/0169-5983(88)90056-1`.

[167] M. Cheng, J. Lou, and T. T. Lim. **Evolution of an elliptic vortex ring in a viscous fluid**. *Phys. Fluids*, **28**(3), 2016. `doi:10.1063/1.4944059`.

REFERENCES

[168] C.-M. Ho and E. Gutmark. **Vortex induction and mass entrainment in a small-aspect-ratio elliptic jet**. *J. Fluid Mech.*, **179**:383–405, 1987. `doi:10.1017/S0022112087001587`.

[169] W. Wang, C. Pan, and J. Wang. **Quasi-bivariate variational mode decomposition as a tool of scale analysis in wall-bounded turbulence**. *Exp. Fluids*, **59**, 2018. `doi:10.1007/s00348-017-2450-7`.

[170] J. C. Straccia and J. A. N. Farnsworth. **Axis switching in low to moderate aspect ratio rectangular orifice synthetic jets**. *Phys. Rev. Fluids*, **6**, 2021. `doi:10.1103/PhysRevFluids.6.054702`.

[171] C. Darwin. **Note on hydrodynamics**. *Math. Proc. Cambr. Phil. Soc.*, **49**:342–354, 1953. `doi:10.1017/S0305004100028449`.

[172] P. S. Krueger and M. Gharib. **The significance of vortex ring formation to the impulse and thrust of a starting jet**. *Phys. Fluids*, **15**(5):1271–1281, 2003. `doi:10.1063/1.1564600`.

[173] M. Krieg and K. Mohseni. **A new kinematic criterion for vortex ring pinch-off**. *Phys. Fluids*, **33**, 2021. `doi:10.1063/5.0033719`.

[174] H. H. Pearcey. **Shock-induced separation and its prevention**. In G. V. Lachmann, editor, *Boundary layer and flow control*, **2**, pages 1170–1344. Pergamon, New York, 1961.

[175] F. T. Smith. **Theoretical prediction and design for vortex generators in turbulent boundary layers**. *J. Fluid Mech.*, **270**:91–132, 1994. `doi:10.1017/S0022112094004210`.

[176] A. Seshagiri, E. Cooper, and L. W. Traub. **Effects of vortex generators on an airfoil at low Reynolds numbers**. *J. Aircr.*, **46**(1):116–122, 2009. `doi:10.2514/1.36241`.

[177] D. Keisar, A. Garzozi, M. Shoham, and D. Greenblatt. **Development and evaluation of a fluidic facemask for COVID-19 transmission mitigation**. *OSF Prepr.*, 2022.

[178] J. Mi, R. C. Deo, and G. J. Nathan. **Characterization of turbulent jets from high-aspect-ratio rectangular nozzles**. *Phys. Fluids*, **17**(6), 2005. `doi:10.1063/1.1928667`.

[179] R. Wille and H. Fernholz. **Report on the first European Mechanics Colloquium, on the Coanda effect**. *J. Fluid Mech.*, **24**(4):801–819, 1965. `doi:10.1017/S0022112065001702`.

[180] M. W. Kelly. **Analysis of some parameters used in correlating blowing-type boundary-layer control data**. In *NASA report, RM A56F12*, 1956.

[181] M. Krieg, A. Pitty, M. Salehi, and K. Mohseni. **Optimal thrust characteristics of a synthetic jet actuator for application in low speed maneuvering of underwater vehicles**. In *Proceedings of OCEANS 2005 MTS/IEEE*, **3**, pages 2342–2347, 2005. `doi:10.1109/OCEANS.2005.1640115`.

[182] M. Krieg and K. Mohseni. **Pressure and work analysis of unsteady, deformable, axisymmetric, jet producing cavity bodies**. *J. Fluid Mech.*, **769**:337–368, 2015. `doi:10.1017/jfm.2015.120`.

[183] A. Carusone, C. Sicot, J.-P. Bonnet, and J. Borée. **Transient dynamical effects induced by single-pulse fluidic actuation over an airfoil**. *Exp. Fluids*, **62**, 2021. `doi:10.1007/s00348-020-03108-0`.

[184] G. Brown and A. Roshko. **On density effects and large structure in turbulent mixing layers**. *J. Fluid Mech.*, **64**(4):775–816, 1974. `doi:10.1017/S002211207400190X`.

[185] P. A. Monkewitz and P. Huerre. **Influence of the velocity ratio on the spatial instability of mixing layers**. *Phys. Fluids*, **25**(7):1137–1143, 1982. `doi:10.1063/1.863880`.

[186] M. J. Day, W. C. Reynolds, and N. N. Mansour. **Parametrizing the growth rate influence of the velocity ratio in compressible reacting mixing layers**. *Phys. Fluids*, **10**(10):2686–2688, 1998. `doi:10.1063/1.869786`.

[187] R. Narasimha, K. Y. Narayan, and S. P. Parthasarathy. **Parametric analysis of turbulent wall jets in still air**. *Aeronaut. Quart.*, **77**(751):355–359, 1973. `doi:10.1017/S0001924000041324`.

[188] B. Steinfurth and J. Weiss. **Development of inclined pulsed jets in an adverse-pressure-gradient crossflow.** *AIAA AVIATION 2021 FORUM*, **59**, 2021. `doi:10.2514/6.2021-2837`.